

Newcastle University

NUCLEATION, GROWTH AND DISSOLUTION OF FACETED SINGLE CRYSTALS

Aatika Khatoon Rizvi

A thesis submitted in accordance with the requirements for the degree of
Engineering Doctorate in Biopharmaceutical Process
Development
(EngD Chemical Engineering)

School of Engineering

January 2020

This thesis is dedicated to my father.

“Indeed, to God we belong and to God we shall return.”

May his soul rest in peace.

Abstract

The crystallisation and dissolution (non-sink) behaviour from the solution phase is studied for some selected pharmaceutical representative materials, notably urea and paracetamol, and is interrelated to an assessment of surface chemistry of the crystal habit facets.

The inclusion of a small amount of biuret, a known decomposition impurity of urea, is found to increase the solution metastable zone. Polythermal analysis is consistent with a concentration dependence of the nucleation behaviour of both the pure and the doped systems associated with the mechanism changing from progressive to instantaneous with increasing concentration, with a concomitant decrease in the interfacial tension and a significant increase in nucleation rate of the doped system, from $9.22\text{-}20.48$ to $9.25\text{-}67.73\text{ nm}^{-3}\cdot\text{s}^{-1}$, and decrease in the critical nucleus size. The crystal habit of urea in solution is found to be dominated by the $\{110\}$ and smaller polar $\{111\}$ capping faces resulting in the $\{-1-1-1\}$ not being observed. The mean crystal growth rates of the $\{110\}$ and $\{111\}$ faces are found to increase with respect to supersaturation with $\{111\}$ exhibiting a greater level of increase than $\{110\}$. The addition of biuret to the solution is found to have a greater effect on retarding the growth of $\{111\}$ compared to $\{110\}$, resulting in a more compact morphology. Rationalising this behaviour with computational molecular modelling studies reveals stronger additive binding on $\{111\}$ compared to $\{110\}$.

The mean crystal dissolution rates of $\{110\}$ and $\{111\}$ faces of urea in ethanolic solutions are found to increase with respect to the degree of undersaturation, with the dissolution behaviour being mechanistically consistent with the growth behaviour. The mean crystal dissolution rates of both faces in acetonitrile are very similar to each other, and to the dissolution rate of the $\{110\}$ face in ethanol. The dissolution rate of the $\{111\}$ face in ethanol is found to be faster than that of the other faces. Rationalising this behaviour with computational molecular modelling reveals a higher wetting energy of $\{111\}$ compared to $\{110\}$. Dissolution modelling based on the experimental data, were consistent with boundary layer thicknesses of $0.5\mu\text{m}$ and $0.3\mu\text{m}$ for the same undercoolings for ethanol and acetonitrile, respectively. These values are smaller than expected but are consistent with modelling data.

The relative solubilities of paracetamol are higher in acetonitrile than in fed state simulated intestinal fluid (FeSSIF). The crystal habit of paracetamol in solution is

found to exhibit five equivalent morphologically significant faces, giving rise to a prismatic crystal. The mean crystal dissolution rates of these faces are found to increase with respect to degree of undersaturation in acetonitrile, with the dissolution rates of all faces being very similar. The mean crystal dissolution rate of these faces is found to increase with respect to temperature in FeSSIF, with the dissolution rates of the faces being similar. The dissolution rates in acetonitrile and FeSSIF are rationalised through prediction of the intermolecular interactions. Dissolution modelling revealed the boundary layer thicknesses to be $0.3\mu\text{m}$ and $0.1\mu\text{m}$ for acetonitrile and FeSSIF, respectively. This might reflect the greater number of binding sites of water compared to acetonitrile, as well as the assumption that water is a representative probe for FeSSIF.

The importance of this work in enhancing the quality of dissolution testing is also highlighted, notably, the utility of relating dissolution properties at the single particle level to the same material as it progresses throughout the drug product processing cycle.

Acknowledgements

Firstly, I would like to say a very big thank you to my supervisors, Prof. Kevin Roberts and Dr. Toshiko Izumi for their endless support, guidance and encouragement throughout my EngD. I have been extremely lucky to have supervisors that cared for not only my work, but also my wellbeing, and for that I am forever grateful. I am also very sorry that you had to read over my thesis during your Christmas holidays, and I will try and make it up to you both.

I would also like to thank the many colleagues and friends I have met at the University of Leeds, in particular, Dr. Thomas Turner, Dr. Ian Rosbottom, Dr. Diana Camacho Corzo, Dr. CaiYun Ma, Dr. Hien Nguyen, Dr. Jonathan Pickering and Dr. Nornizar Anuar, for their helpful discussions, advice and guidance throughout my time at Leeds.

I would like to extend my gratitude to the materials science and crystallisation teams at Pfizer, Sandwich, particularly, Dr Ivan Marziano, Dr, Klimentina Pencheva, and Dr. Radoslav Penchev, for always being willing to provide help and guidance whenever needed. I would also like to thank the many friends I made whilst at Pfizer, for making my placement experience unforgettable, particularly, Krystan, James, Chloe, Rand, Sadia, Aidan, Inese and JP. I would also like to thank my housemates Val and Tas for their patience, the fun times, and the endless supply of food.

Finally, this thesis would not have been possible without the constant love, support and encouragement from my mum, sisters and husband, to whom I am forever grateful.

Table of Contents

Abstract	i
Acknowledgements	iii
Table of Contents	v
List of Tables	x
List of Figures	xiv
Nomenclature and Abbreviations	xxi
Chapter 1: Introduction	1
1.1 Research Background	2
1.2 Aims and Objectives	7
1.3 Project Management	8
1.4 Scope of Thesis	8
References	12
Chapter 2: Theoretical Background on Crystallography and the Crystallisation Process	15
2.1 Introduction	16
2.2 Crystallography	16
2.2.1 Lattice, Unit Cell and Crystal Systems	16
2.2.2 Bravais Lattice	18
2.2.3 Miller Indices and Planes	20
2.2.4 Symmetry	23
2.3 Crystal Chemistry and Polymorphism	24
2.3.1 Crystal Chemistry	24
2.3.2 Polymorphism	25
2.4 Crystal Morphology and Habit	26
2.5 Crystallisation	27
2.5.1 Solubility	27
2.5.2 Supersaturation	28
2.5.3 Nucleation	31
2.5.4 Crystal Growth	33
2.5.5 Dissolution	36
2.6 Closing Remarks	39
References	40
Chapter 3: Theoretical Background of Nucleation, Growth and Dissolution	42

3.1 Introduction	43
3.2 Nucleation Theories	43
3.2.1 Classical Nucleation Theory	43
3.2.2 Two-Step Nucleation	45
3.2.3 Isothermal Analysis	46
3.2.4 Assessment using Polythermal Methodology	47
3.3 Crystal Growth Rates	50
3.4 Prediction of Crystal Growth Mechanisms	51
3.5 Crystal Growth Theories	53
3.5.1 Surface Energy	53
3.5.2 Diffusion Theory	53
3.6 Techniques for Studying Crystal Growth.....	55
3.6.1 FBRM	55
3.6.2 AFM.....	56
3.6.3 Optical Microscopy	57
3.7 Dissolution Models.....	58
3.7.1 Noyes-Whitney	59
3.7.2 Hixson-Crowell	60
3.7.3 Hintz-Johnson	61
3.7.4 Model Selection.....	62
3.8 Choice of Crystallisation System	62
3.8.1 Urea	63
3.8.2 Paracetamol	65
3.9 Closing Remarks	66
References	68
Chapter 4: Materials and Methods	73
4.1 Introduction	74
4.2 Materials	74
4.2.1 Supplied Materials.....	74
4.2.2 Preparation of FeSSIF.....	74
4.3 Experimental Methodology	75
4.3.1 Solubility Determination.....	75
4.3.2 Polythermal Crystallisation	75
4.3.3 Single Crystal Growth and Dissolution	77

4.3.4 Noyes-Whitney and Hintz-Johnson Model Calculations	81
4.4 Computational Methodology	82
4.4.1 Geometry Optimisation.....	82
4.4.2 COSMOthermX	84
4.4.3 VisualHabit Systsearch	84
4.5 Conclusions	86
References	87
Chapter 5: Solubility, Nucleation and Growth of Urea in the Presence and Absence of Biuret	89
5.1 Introduction	90
5.2 Solubility	91
5.3 Polythermal Crystallisation.....	93
5.3.1 MSZW Urea in Absolute Ethanol.....	94
5.3.2 MSZW Urea and 1%w/w Biuret in Absolute Ethanol	96
5.4 Nucleation Kinetics using KBHR Methodology	101
5.4.1 Nucleation Kinetics of Urea in Absolute Ethanol	101
5.4.1.1 Progressive Nucleation Kinetics for Urea in Absolute Ethanol	103
5.4.1.2 Instantaneous Nucleation Kinetics for Urea in Absolute Ethanol.....	105
5.4.2 Nucleation Kinetics of Urea and 1%w/w Biuret in Absolute Ethanol.....	106
5.4.2.1 Progressive Nucleation Kinetics for Urea and 1%w/w Biuret in Absolute Ethanol.....	109
5.4.2.2 Instantaneous Nucleation Kinetics for Urea and 1%w/w Biuret in Absolute Ethanol	110
5.5 Growth Rate as a Function of Solution Environment, Predicted Growth Mechanism and Kinetics	112
5.5.1 Growth Rate of Urea Single Crystals as a Function of Solution Environment	112
5.5.2 Predicted Growth Mechanism and Kinetics	117
5.5.3 Calculated Growth Mechanism and Kinetics	118
5.6 Surface Characterisation and Effect of Impurity.....	120
5.6.1 {110}.....	122
5.6.2 {111} and {-1-1-1}.....	124
5.6.3 Comparison of Surface Interactions	127
5.7 Conclusions	130
References	132
Chapter 6: Dissolution of Urea Single Crystals.....	134

6.1 Introduction	135
6.2 Dissolution of Urea in Absolute Ethanol.....	135
6.2.1 Face Specific Dissolution Rate.....	136
6.2.2 Intermolecular Interactions of Urea with Absolute Ethanol	139
6.3 Dissolution Model Predictions for Urea in Ethanol	144
6.3.1 Noyes-Whitney and Hintz-Johnson	145
6.3.2 Comparison of Models with Experimental Data.....	153
6.3.3 Modification of Dissolution Models	155
6.4 Dissolution of Urea in Acetonitrile	159
6.4.1 Face Specific Dissolution Rate.....	159
6.4.2 Intermolecular Interactions of Urea with Acetonitrile	162
6.5 Dissolution Model Predictions for Urea in Acetonitrile	167
6.5.1 Noyes-Whitney and Hintz-Johnson	167
6.5.2 Comparison of Models with Experimental Data.....	175
6.5.3 Modification of Dissolution Models	177
6.6 Comparison of Urea Dissolution in Ethanol and Acetonitrile.....	180
6.7 Conclusions	182
References	184
Chapter 7: Dissolution of Paracetamol Single Crystals	185
7.1 Introduction	186
7.2 Solubility of Paracetamol	186
7.3 Surface Characterisation of Paracetamol	190
7.4 Dissolution of Paracetamol in Acetonitrile.....	191
7.4.1 Face Specific Dissolution Rate.....	192
7.4.2 Intermolecular Interactions of Paracetamol with Acetonitrile	194
7.5 Dissolution Model Predictions for Paracetamol in Acetonitrile	200
7.5.1 Noyes-Whitney and Hintz-Johnson	200
7.5.2 Comparison of Models with Experimental Data.....	208
7.6 Dissolution of Paracetamol in FeSSIF	213
7.6.1 Face Specific Dissolution Rate.....	213
7.6.2 Intermolecular Interactions of Paracetamol with FeSSIF.....	215
7.7 Dissolution Model Predictions for Paracetamol in FeSSIF.....	219
7.7.1 Noyes-Whitney and Hintz-Johnson	220
7.7.2 Comparison of Models with Experimental Data.....	227

7.8 Conclusions	232
References	234
Chapter 8: Conclusions and Future Work	235
8.1 Introduction	236
8.2 Conclusions of this Study.....	236
8.2.1 Solubility, Nucleation and Growth of Urea in the Presence and Absence of Biuret.....	236
8.2.2 Surface Characterisation of Urea with Biuret	238
8.2.3 Dissolution of Urea Single Crystals	239
8.2.4 Dissolution of Paracetamol Single Crystals.....	240
8.3 Review of Thesis Aims and Objectives.....	241
8.4 Suggestions for Future Work	242
References	246
Appendices.....	247

List of Tables

Table 2.1: The seven crystal systems with geometries.

Table 2.2: Seven crystal systems separated into Bravais lattices.

Table 3.1: Growth mechanism predicted by values of α

Table 3.2: Urea polymorphs with unit cell parameters.

Table 3.3: Paracetamol polymorphs with unit cell parameters

Table 4.1: The force fields used to determine the optimised geometry.

Table 5.1: Solubility of urea in ethanol obtained from literature.

Table 5.2: Calculated activity coefficient using van't Hoff equation.

Table 5.3: MSZW obtained for urea in ethanol at different concentrations.

Table 5.4: MSZW for urea and biuret in ethanol at different concentrations.

Table 5.5: A comparison of enthalpies and entropies of crystallisation and dissolution of ideal solubility, urea in ethanol, and urea and biuret in ethanol.

Table 5.6: Dissolution and crystallisation temperatures obtained from the polythermal method and calculated values of the critical undercooling and relative critical undercooling for urea in ethanol.

Table 5.7: Calculated progressive nucleation kinetics for urea in ethanol.

Table 5.8: Calculated instantaneous nucleation kinetics for urea in ethanol.

Table 5.9: Dissolution and crystallisation temperatures obtained from the polythermal method and calculated values of the critical undercooling and relative critical undercooling for urea and 1% w/w biuret in ethanol.

Table 5.10: Calculated progressive nucleation kinetics for urea and 1% w/w biuret in ethanol.

Table 5.11: Calculated instantaneous nucleation kinetics for urea with biuret in ethanol.

Table 5.12: An example of the experimental crystal images obtained at the initial and final time points for urea in ethanol and urea and 1% w/w biuret in ethanol at each supersaturation.

Table 5.13: Experimental mean growth rates and standard deviations obtained from crystal growth experiments of urea in ethanol and urea and 1% w/w biuret in ethanol.

Table 5.14: α -factor ranges with their corresponding growth mechanism.

Table 5.15: Calculated α -factors, anisotropy factor and predicted growth mechanism for the {110} and {111} faces of urea.

Table 5.16: Calculated growth mechanisms for the {110} and {111} surfaces of urea with and without the addition of biuret in the system.

Table 5.17: The total interaction energy of urea and biuret with each face under consideration.

Table 5.18: The calculated adsorption energies and surface coverages of biuret on the {110} and {111} faces of urea.

Table 6.1: Experimental mean retreat rates and standard deviations obtained for urea in ethanol.

Table 6.2: An example of the experimental crystal images obtained at the initial and final time points for urea in ethanol at each undersaturation.

Table 6.3: The calculated wetting energies of the {110} and {111} faces of urea.

Table 6.4: An example of the Noyes-Whitney calculation, at an undersaturation of 0.05, with a boundary layer equal to 50% of the volume equivalent diameter.

Table 6.5: The calculated mass loss rate using the Noyes-Whitney equation, with a boundary layer equal to 50% of the volume equivalent diameter.

Table 6.6: The calculated mass loss rate using the Noyes-Whitney equation, with a boundary layer equal to 25% of the volume equivalent diameter.

Table 6.7: The calculated mass loss rate using the Noyes-Whitney equation, with a boundary layer equal to 10% of the volume equivalent diameter.

Table 6.8: The calculated mass loss rate using the Noyes-Whitney equation, with a boundary layer equal to 1% of the volume equivalent diameter.

Table 6.9: An example of the Hintz-Johnson calculation, at an undersaturation of 0.05.

Table 6.10: The calculated mass loss rate using the Hintz-Johnson equation.

Table 6.11: An example of the calculation of actual mass loss as a function of time, at an undersaturation of 0.05.

Table 6.12: The percentage difference between values of experimental mass loss and calculated mass loss.

Table 6.13: An example of the Noyes-Whitney calculation with a fixed boundary layer parameter of 0.5 μ m.

Table 6.14: The percentage difference between values of experimental mass loss and calculated mass loss with a fixed boundary layer.

Table 6.15: Experimental mean retreat rates and standard deviations obtained for urea in acetonitrile.

Table 6.16: An example of the experimental crystal images obtained at the initial and final time points for urea in ethanol at each undersaturation

Table 6.17: The calculated wetting energies of the {110} and {111} faces of urea.

Table 6.18: An example of the Noyes-Whitney calculation, at an undersaturation of 0.05, with a boundary layer equal to 50% of the volume equivalent diameter.

Table 6.19: The calculated mass loss rate using the Noyes-Whitney equation, with a boundary layer equal to 50% of the volume equivalent diameter.

Table 6.20: The calculated mass loss rate using the Noyes-Whitney equation, with a boundary layer equal to 25% of the volume equivalent diameter.

Table 6.21: The calculated mass loss rate using the Noyes-Whitney equation, with a boundary layer equal to 10% of the volume equivalent diameter.

Table 6.22: The calculated mass loss rate using the Noyes-Whitney equation, with a boundary layer equal to 1% of the volume equivalent diameter.

Table 6.23: An example of the Hintz-Johnson calculation, at an undersaturation of 0.05.

Table 6.24: The calculated mass loss rate using the Hintz-Johnson model.

Table 6.25: An example of the calculation of actual mass loss as a function of time, at an undersaturation of 0.05

Table 6.26: The percentage difference between values of experimental mass loss and calculated mass loss.

Table 6.27: An example of the Noyes-Whitney calculation with a fixed boundary layer parameter of 0.3 μ m.

Table 6.28: The percentage difference between values of experimental mass loss and calculated mass loss with a fixed boundary layer.

Table 6.29: A comparison of the wetting energies of {110} and {111} surfaces of urea with ethanol and acetonitrile.

Table 7.1: Solubilities of paracetamol in acetonitrile, water and FeSSIF.

Table 7.2: Calculated activity coefficients of paracetamol in acetonitrile, water and FeSSIF.

Table 7.3: Experimental mean retreat rates and standard deviations obtained for paracetamol in acetonitrile.

Table 7.4: An example of the experimental crystal images obtained at the initial and final time points for paracetamol in acetonitrile at each undersaturation.

Table 7.5: An example of the Noyes-Whitney calculation, at an undersaturation of 0.05, with a boundary layer equal to 50% of the volume equivalent diameter.

Table 7.6: The calculated mass loss rate using the Noyes-Whitney equation, with a boundary layer equal to 50% of the volume equivalent diameter

Table 7.7: The calculated mass loss rate using the Noyes-Whitney equation, with a boundary layer equal to 25% of the volume equivalent diameter.

Table 7.8: The calculated mass loss rate using the Noyes-Whitney equation, with a boundary layer equal to 10% of the volume equivalent diameter.

Table 7.9: The calculated mass loss rate using the Noyes-Whitney equation, with a boundary layer equal to 1% of the volume equivalent diameter.

Table 7.10: An example of the Hintz-Johnson calculation, at an undersaturation of 0.05.

Table 7.11: The calculated mass loss rate using the Hintz-Johnson model.

Table 7.12: An example of the calculation of actual mass loss as a function of time, at an undersaturation of 0.05.

Table 7.13: The percentage difference between values of experimental mass loss and calculated mass loss.

Table 7.14: An example of the Noyes-Whitney calculation with a fixed boundary layer parameter of $0.3\mu\text{m}$.

Table 7.15: The percentage difference between values of experimental mass loss and calculated mass loss with a fixed boundary layer.

Table 7.16: Experimental mean retreat rates and standard deviations obtained for paracetamol in FeSSIF.

Table 7.17: An example of the experimental crystal images obtained at the initial and final time points for paracetamol in FeSSIF at each temperature.

Table 7.18: An example of the Noyes-Whitney calculation, at a temperature of 30°C , with a boundary layer equal to 50% of the volume equivalent diameter.

Table 7.19: The calculated mass loss rate using the Noyes-Whitney equation, with a boundary layer equal to 50% of the volume equivalent diameter.

Table 7.20: The calculated mass loss rate using the Noyes-Whitney equation, with a boundary layer equal to 25% of the volume equivalent diameter.

Table 7.21: The calculated mass loss rate using the Noyes-Whitney equation, with a boundary layer equal to 10% of the volume equivalent diameter.

Table 7.22: The calculated mass loss rate using the Noyes-Whitney equation, with a boundary layer equal to 1% of the volume equivalent diameter.

Table 7.23: An example of the Hintz-Johnson calculation, at a temperature of 30°C .

Table 7.24: The calculated mass loss rate using the Hintz-Johnson model.

Table 7.25: An example of the calculation of actual mass loss as a function of time, at a temperature of 30°C .

Table 7.26: The percentage difference between values of experimental mass loss and calculated mass loss.

Table 7.27: An example of the Noyes-Whitney calculation with a fixed boundary layer parameter of $0.1\mu\text{m}$.

Table 7.28: The percentage difference between values of experimental mass loss and calculated mass loss with a fixed boundary layer.

List of Figures

Figure 1.1: Hypothetical particles with different shapes whilst still having the same volume equivalent diameter.

Figure 1.2: The scope of the EngD thesis

Figure 2.1: The size and shape of the unit cell specified by means of the lengths a , b and c of the three independent edges, and three angles α , β and γ between these edges.

Figure 2.2: The coordinates of an atom at the centre of the unit cell written as $(\frac{1}{2}, \frac{1}{2}, \frac{1}{2})$.

Figure 2.3: Miller indices of crystal planes: (a) (100), (b) (200), (c) (300), (d) (0k0), (e) (00l).

Figure 2.4: Miller indices of crystal planes: (a) (110), (b) (101), (c) (011).

Figure 2.5: Miller indices of crystal planes: (a) (110) and $(\bar{1}\bar{1}0)$ (b) $(\bar{1}\bar{1}0)$ and $(\mathbf{1}\bar{1}0)$, (c) projection down the c -axis showing the equivalent planes.

Figure 2.6: A schematic showing (a) monotropic polymorph and (b) enantiotropic polymorph where T_0 denotes the transition temperature.

Figure 2.7: The region below the solubility curve is undersaturated, and the region above the metastable zone edge is supersaturated. The region in the middle is the metastable zone width.

Figure 2.8: The crystal growth process (Kossel's model). (Mullin, 2001)
A: Flat surfaces B: Steps C: Kinks D: Surface-adsorbed growth units E: Edge vacancies F: Surface vacancies

Figure 2.9: A schematic of the Burton, Cabrera and Frank growth mechanism.

Figure 2.10: A schematic of the birth and spread growth mechanism.

Figure 2.11: A schematic of the rough interface growth mechanism.

Figure 2.12: A schematic diagram showing the (a) BCF growth mechanism, and (b) B&S growth mechanism and (e) RIG growth mechanism at (c) the expected crystal growth mechanisms as a function of supersaturation. Additionally, (d) the transition between the BCF, B&S and RIG mechanisms are shown.

Figure 2.13: The Biopharmaceutical Classification System.

Figure 3.1: FBRM probe tip (left) and chord measurement (right).

Figure 3.2: A schematic showing how the two categories of dissolution models incorporate mass transfer.

Figure 3.3: A representation of the Nernst-Brunner model

Figure 3.4: The molecular structure of urea

Figure 3.5: The decomposition process of urea to form biuret.

Figure 3.6: The crystal morphology and habit of urea

Figure 3.7: The molecular structure of paracetamol

Figure 3.8: The crystal morphology of paracetamol at (a) lower supersaturation and (b) higher supersaturation

Figure 4.1: An example of the temperature profile and crystallisation and dissolution temperatures obtained.

Figure 4.2: The instrumentation used for single crystal growth and dissolution experiments.

Figure 4.3: A schematic showing centre-to-face measurements to determine growth rates.

Figure 4.4: A schematic showing how the crystal was divided, allowing for the calculation of Heron's formula

Figure 4.5: The unit cell of urea

Figure 4.6: The unit cell of paracetamol

Figure 4.7: An example of the result of the grid search applied and the white and coloured tetrahedrons found.

Figure 5.2: A comparison of solubility data obtained from experimentation with solubility data obtained from literature.

Figure 5.3: A comparison of the solubility data of urea in ethanol obtained from experimentation with the calculated ideal solubility in van't Hoff coordinates.

Figure 5.4: An example of the MSZW results obtained from Crystal 16.

Figure 5.5: Crystallisation and dissolution temperatures of urea in ethanol allowing for the determination of the MSZW at all concentrations used.

Figure 5.6: Crystallisation and dissolution temperatures of urea and biuret in ethanol allowing for the determination of MSZW at all concentrations used.

Figure 5.7: Crystallisation and dissolution temperatures for urea in ethanol, and urea and biuret in ethanol in van't Hoff coordinates.

Figure 5.8: Plot of q vs μ_c in ln-ln coordinates for urea in ethanol at concentrations of 0.04 g/mL, 0.046 g/mL, 0.050 g/mL, 0.058 g/mL, and 0.066 g/mL.

Figure 5.9: An example of curve fittings obtained from Origin Pro for progressive nucleation data obtained using the polythermal method.

Figure 5.10: plot of q vs μ_c in ln-ln coordinates for urea and 1% w/w biuret in ethanol at concentrations of 0.04 g/mL, 0.046g/mL, 0.05 g/mL, 0.058 g/mL and 0.066g/mL.

Figure 5.11: An example of curve fittings obtained from Origin Pro for progressive nucleation data for urea and 1% w/w biuret in ethanol.

Figure 5.12: The relationship between growth rate and supersaturation for the {110} and {111} faces of urea in a pure system and with an additive in the system.

Figure 5.13: The unit cell of urea showing growth in the {110} direction and {111} direction, respectively.

Figure 5.14: Molecular packing of the (a) {110}, (b) {111} and (c) {-1-1-1} surfaces of urea.

Figure 5.15: An example of the grid search applied to determine interactions of biuret with the {110} surface.

Figure 5.16: Removal of the grid applied to show the varying degrees of biuret interaction with the {110} surface.

Figure 5.17: The strongest interaction of biuret with the {110} surface, with hydrogen bonding depicted.

Figure 5.18: The top 100 interactions of biuret with the {110} surface, broken down into hydrogen bonding, van der Waals and electrostatic interactions.

Figure 5.19: An example of the grid search applied to determine interactions of biuret with the {111} surface.

Figure 5.20: Removal of the grid applied to show the varying degrees of interaction of biuret with the {111} surface.

Figure 5.21: The strongest interaction of biuret with the {111} surface, with hydrogen bonding depicted.

Figure 5.22: The top 100 interactions of biuret with the {111} surface, broken down into hydrogen bonding, van der Waals and electrostatic interactions.

Figure 5.23: The top 100 interactions of biuret with the polar opposite {-1-1-1} surface, broken down into hydrogen bonding, van der Waals and electrostatic interactions.

Figure 5.24: Comparison of the total energy interactions of both {110} and {111} surfaces under consideration, along with the {-1-1-1} surface.

Figure 5.24: A breakdown of interaction energies into hydrogen bonding (■), dispersive van der Waals bonding (■) and electrostatic bonding (■) of urea and biuret with each surface under consideration.

Figure 5.255: Interactions of biuret with the {110} and {111} surface, respectively, as determined by Singh and Tiwari through molecular dynamic simulations.

Figure 6.1: The relationship between dissolution rate and undersaturation for the {110} and {111} faces of urea in ethanol

Figure 6.2: A comparison between growth and dissolution rates of the {110} and {111} faces of urea in ethanol.

Figure 6.3: An example of the grid search applied to determine interactions of ethanol with the {110} surface.

Figure 6.4: Removal of the grid applied to show the varying degrees of ethanol interaction with the {110} surface.

Figure 6.5: The strongest interaction of ethanol with the {110} surface, with hydrogen bonding depicted.

Figure 6.6: The top 100 interactions of ethanol with the {110} surface, broken down into hydrogen bonding, van der Waals and electrostatic interactions.

Figure 6.7: The strongest interaction of ethanol with the {111} surface, with hydrogen bonding depicted.

Figure 6.8: The top 100 interactions of ethanol with the {111} surface, broken down into hydrogen bonding, van der Waals and electrostatic interactions.

Figure 6.9: The top 100 interactions of ethanol with the {-1-1-1} surface, broken down into hydrogen bonding, van der Waals and electrostatic interactions.

Figure 6.10: A comparison of the total energy interactions of {110} and {111} surfaces under consideration, along with the {-1-1-1} surface.

Figure 6.11: The relationship between the mass loss of a crystal of urea and the degree of undersaturation calculated using the Noyes-Whitney equation, with a boundary layer equal to 50% of the volume equivalent diameter.

Figure 6.12: The relationship between the mass loss of a crystal of urea and the degree of undersaturation calculated using the Noyes-Whitney equation, with a boundary layer equal to 25% of the volume equivalent diameter.

Figure 6.13: The relationship between the mass loss of a crystal of urea and the degree of undersaturation calculated using the Noyes-Whitney equation, with a boundary layer equal to 25% of the volume equivalent diameter.

Figure 6.14: The relationship between the mass loss of a crystal of urea and the degree of undersaturation calculated using the Noyes-Whitney equation, with a boundary layer equal to 25% of the volume equivalent diameter.

Figure 6.15: The relationship between the mass loss of a crystal of urea and the degree of undersaturation calculated using the Hintz-Johnson model.

Figure 6.16: A comparison between the experimental mass loss and calculated mass losses using Noyes-Whitney and Hintz-Johnson.

Figure 6.17: Comparison between the experimental mass loss and calculated values with a fixed boundary layer.

Figure 6.18: The relationship between dissolution rate and undersaturation of the {110} and {111} face of urea in acetonitrile.

Figure 6.19: The strongest interaction of acetonitrile with the {110} surface, with hydrogen bonding depicted.

Figure 6.20: The top 100 interactions of acetonitrile with the {110} surface, broken down into hydrogen bonding, van der Waals and electrostatic interactions.

Figure 6.21: The strongest interaction of acetonitrile with the {111} surface, with hydrogen bonding depicted.

Figure 6.22: The top 100 interactions of acetonitrile with the {111} surface, broken down into hydrogen bonding, van der Waals and electrostatic interactions.

Figure 6.23: The top 100 interactions of acetonitrile with the $\{-1-1-1\}$ surface, broken down into hydrogen bonding, van der Waals and electrostatic interactions.

Figure 6.24: Comparison of the total energy interactions of both $\{110\}$ and $\{111\}$ surfaces, along with the $\{-1-1-1\}$ surface.

Figure 6.25: The relationship between the mass loss of a crystal of urea and the degree of undersaturation calculated using the Noyes-Whitney equation, with a boundary layer equal to 50% of the volume equivalent diameter.

Figure 6.26: The relationship between the mass loss of a crystal of urea and the degree of undersaturation calculated using the Noyes-Whitney equation, with a boundary layer equal to 25% of the volume equivalent diameter.

Figure 6.27: The relationship between the mass loss of a crystal of urea and the degree of undersaturation calculated using the Noyes-Whitney equation, with a boundary layer equal to 10% of the volume equivalent diameter.

Figure 6.28: The relationship between the mass loss of a crystal of urea and the degree of undersaturation calculated using the Noyes-Whitney equation, with a boundary layer equal to 1% of the volume equivalent diameter.

Figure 6.29: The relationship between the mass loss of a crystal of urea and the degree of undersaturation calculated using the Hintz-Johnson model.

Figure 6.30: A comparison between the experimental mass loss and calculated mass losses using Noyes-Whitney and Hintz-Johnson.

Figure 6.31: Comparison between the experimental mass loss and calculated values with a fixed boundary layer.

Figure 6.32: A comparison of the total interaction energies of $\{110\}$ and $\{111\}$ surfaces with ethanol and acetonitrile.

Figure 6.33: A comparison of the dissolution rates of $\{110\}$ and $\{111\}$ surfaces of urea in ethanol and acetonitrile.

Figure 7.1: A comparison of the solubilities of paracetamol in acetonitrile, water and FeSSIF.

Figure 7.2: A comparison of the ideal solubility of paracetamol, calculated using van't Hoff equation, with solubilities in the three solvents.

Figure 7.3: The (a) $\{011\}$, (b) $\{100\}$, (c) $\{110\}$, (d) $\{201\}$ and (e) $\{001\}$ surfaces of paracetamol

Figure 7.4: The relationship between dissolution rate and undersaturation for the faces of paracetamol in acetonitrile.

Figure 7.5: The strongest interaction of acetonitrile with the $\{011\}$ surface, with hydrogen bonding depicted.

Figure 7.6: The top 100 interactions of acetonitrile with the $\{011\}$ surface, broken down into hydrogen bonding, van der Waals and electrostatic interactions.

Figure 7.7: The strongest interaction of acetonitrile with the (a) $\{100\}$, (b) $\{110\}$ and (c) $\{201\}$ surfaces of paracetamol, with hydrogen bonding depicted.

Figure 7.8: The top 100 interactions of acetonitrile with the {100} surface, broken down into hydrogen bonding, van der Waals and electrostatic interactions.

Figure 7.9: The top 100 interactions of acetonitrile with the {110} surface, broken down into hydrogen bonding, van der Waals and electrostatic interactions.

Figure 7.10: The top 100 interactions of acetonitrile with the {201} surface, broken down into hydrogen bonding, van der Waals and electrostatic interactions.

Figure 7.11: A comparison of the total energy interactions of acetonitrile with all surfaces of paracetamol.

Figure 7.12: The relationship between the mass loss of a crystal of paracetamol and the degree of undersaturation calculated using the Noyes-Whitney equation, with a boundary layer equal to 50% of the volume equivalent diameter.

Figure 7.13: The relationship between the mass loss of a crystal of paracetamol and the degree of undersaturation calculated using the Noyes-Whitney equation, with a boundary layer equal to 25% of the volume equivalent diameter.

Figure 7.14: The relationship between the mass loss of a crystal of paracetamol and the degree of undersaturation calculated using the Noyes-Whitney equation, with a boundary layer equal to 10% of the volume equivalent diameter.

Figure 7.15: The relationship between the mass loss of a crystal of paracetamol and the degree of undersaturation calculated using the Noyes-Whitney equation, with a boundary layer equal to 1% of the volume equivalent diameter.

Figure 7.16: The relationship between the mass loss of a crystal of paracetamol and the degree of undersaturation calculated using the Hintz-Johnson model

Figure 7.17: A comparison between the experimental mass loss and calculated mass losses using Noyes-Whitney and Hintz-Johnson.

Figure 7.18: Comparison between the experimental mass loss and calculated values with a fixed boundary layer.

Figure 7.19: The relationship between dissolution rate and temperature for the faces of paracetamol in FeSSIF.

Figure 7.20: The strongest interaction of water with the {001} surface of paracetamol, with hydrogen bonding depicted.

Figure 7.21: The top 100 interactions of water with the {001} surface, broken down into hydrogen bonding, van der Waals and electrostatic interactions.

Figure 7.22: The strongest interactions of water with the (a) {011}, (b) {100} and (c) {201} surfaces, with hydrogen bonding depicted.

Figure 7.23: The top 100 interactions of water with the (a) {011}, (b) {100} and (c) {201} surfaces, broken down into hydrogen bonding, van der Waals and electrostatic interactions

Figure 7.24: A comparison of the total energy interactions of water with all surfaces of paracetamol.

Figure 7.25: The relationship between the mass loss of a crystal of paracetamol and the temperature calculated using the Noyes-Whitney equation, with a boundary layer equal to 50% of the volume equivalent diameter.

Figure 7.26: The relationship between the mass loss of a crystal of paracetamol and the temperature calculated using the Noyes-Whitney equation, with a boundary layer equal to 25% of the volume equivalent diameter.

Figure 7.27: The relationship between the mass loss of a crystal of paracetamol and the temperature calculated using the Noyes-Whitney equation, with a boundary layer equal to 10% of the volume equivalent diameter.

Figure 7.28: The relationship between the mass loss of a crystal of paracetamol and the temperature calculated using the Noyes-Whitney equation, with a boundary layer equal to 1% of the volume equivalent diameter.

Figure 7.29: The relationship between the mass loss of a crystal of paracetamol and the degree of undersaturation calculated using the Hintz-Johnson model.

Figure 7.30: A comparison between the experimental mass loss and calculated mass losses using Noyes-Whitney and Hintz-Johnson.

Figure 7.31: Comparison between the experimental mass loss and calculated values with a fixed boundary layer.

Figure 8.1: Calibration Plot for Paracetamol in HPLC

Figure 8.2: An example of a Paracetamol peak in HPLC.

Nomenclature and Abbreviations

a:	activity coefficient
a_1 :	dimensionless thermodynamic parameter
a_2/b :	dimensionless thermodynamic parameter
A:	pre-exponential factor
A_c :	surface area of crystal
A_1 :	growth parameter in B&S model
A_2 :	growth parameter in BCF model
c:	solution concentration
c_s :	solubility
c_t :	bulk concentration
C_0 :	concentration of crystallites
c^* :	equilibrium saturation concentration
d:	dimensionality of crystal growth
D:	diffusion coefficient
D_{volume} :	volume equivalent diameter
E_{cr} :	total crystallisation energy
E_{sl} :	total energy in slice of crystal face
G:	overall growth rate
h:	boundary layer thickness
i^* :	number of molecules within critical nucleus radius
J:	nucleation rate
J_M :	mass flux
k_n :	nucleus shape factor
k_p :	proportionality constant
k_v :	crystallite growth shape factor
k_B :	Boltzmann constant
k_G :	growth rate constant
k_{MT} :	mass transfer coefficient
K_J :	nucleation rate constant
K_G :	growth rate constant
L:	characteristic dimension
L_1 :	molar heat of fusion
m, n:	crystallite growth exponents
M_c :	mass of crystal

MW _s :	molecular weight of solute
M:	mass
N _{det} :	detectable number of crystallites
N ₀ :	number of particles
q:	cooling rate
q ₀ :	free parameter in $\mu_c(q)$ dependence for progressive and instantaneous nucleation
r:	radius
r*:	critical nucleus radius
r _H :	molecular radius of solute
R:	ideal gas constant
R _G :	growth rate
S:	supersaturation ratio
t:	time
T:	temperature
T _{cryst} :	crystallisation temperature
T _{diss} :	dissolution temperature
T _e :	equilibrium temperature
T _M :	melting temperature
V:	volume
x:	mole fraction
x _d :	diffusion layer
x _{ideal} :	mole fraction at the ideal solubility
x _{eq} :	mole fraction of solute
α:	volume shape factor
α _{det} :	relative volume of crystals at detection point
β:	crystal surface shape factor
γ _{eff} :	effective interfacial tension
Γ:	shape factor
ΔG:	overall excess free energy
ΔG _s :	surface excess free energy
ΔG _v :	volume excess free energy
ΔH _f :	molar enthalpy of fusion
ΔH _d :	enthalpy of dissolution
ΔS _d :	entropy of dissolution

ΔT_c :	critical undercooling
λ :	molecular latent heat of crystallisation
μ :	viscosity of solvent
μ_c :	relative critical undercooling
v_0 :	molecular volume
ξ :	surface entropy factor
ρ_s :	density of solute
σ :	relative supersaturation
σ^s :	solution relative supersaturation
τ :	induction time
ACN:	acetonitrile
AFM:	atomic force microscopy
API:	Active Pharmaceutical Ingredient
ATR-FTIR:	attenuated total reflectance – Fourier transform infrared
BCF:	Burton, Cabrera and Frank mechanism
BCS:	biopharmaceutical classification system
BFDH:	Bravais, Friedel, Donnay and Harker
B&S:	birth and spread
CCD:	charge-coupled device
CLD:	chord-length distribution
EtOH:	ethanol
Exp:	experimental
FBRM:	focussed beam reflectance measurement
FeSSIF:	fed state simulated intestinal fluid
HPLC:	high performance liquid chromatography
H-bond:	hydrogen bonding
H-J:	Hintz-Johnson
KHBR:	Kashchiev-Borissova-Hammond-Roberts
MSZW:	metastable zone width
N-W:	Noyes-Whitney
RIG:	rough interface growth
US:	undersaturation
UV:	ultraviolet
vdW:	van der Waals

Chapter 1: Introduction

1.1 Research Background

Active Pharmaceutical Ingredients (API's) exist as mainly crystalline materials, the particle size and shape of which can influence their physical and chemical properties, manufacturing and processability. They are usually manufactured by batch processing and are purified through crystallisation. The crystallisation process is broken into two fundamental processes – nucleation and crystal growth – both of which can exhibit behaviour which is unpredictable, hence proving to be difficult processes to control. As a result of this, as well as their complex molecular chemistry, many API's can have anisotropic crystal structures, which has a great influence not only crystal growth, but also on crystal dissolution. (Blagden et al., 2007)

The nucleation process requires a supersaturated solution in order to take place, which allows for the formation of crystal nuclei. This process has been widely studied since Ostwald's proposed rule of stages in 1897, providing an explanation for the existence of multiple solid forms of a crystal, and the crystallisation kinetics of these metastable forms. (Ostwald, 1897; Turner, 2015) Ostwald proposed that the most kinetically accessible crystal structure was not the most stable, but actually the least stable form. Metastability and undercooling were also known phenomena at this time, indicating that a barrier to nucleation also existed. (Threlfall, 2003)

Volmer followed this in 1939 with the classical nucleation theory, which states that nucleation is associated with the assembly of molecules through intermolecular interactions. The amount of free energy available in order to obtain this assembly is dependent upon the supersaturation within the solution. These crystallite clusters assembled have the same packing as the resultant crystal structure. However, classical nucleation theory makes a number of assumptions which has resulted in a disagreement between experimental results and theoretical calculations; for example, nuclei are assumed to be perfectly spherical. (Volmer, 1939; Davey et al., 2002)

More recently nucleation kinetic parameters have been determined through the polythermal KBHR (Kashchiev-Borissova-Hammond-Roberts) method (Kashchiev et al., 2010; Kashchiev et al., 2010), where the effect of cooling rate on the relative critical undercooling can be observed. This method has been validated through the determination of crystallisation parameters of methyl stearate from kerosene using both the polythermal and isothermal methodology. (Corzo et al., 2014) Also, this

method has been applied to para-amino benzoic acid to determine key kinetic parameters of an organic compound. (Turner et al., 2016)

The reproducibility of the crystallisation process remains a challenge for pharmaceutical companies for the manufacture of a wide range of API's. (Myerson, 2002; York, 1983) Growth kinetics data are collected on a small scale to allow for optimisation of the crystallisation process, allowing for the understanding and characterisation of the crystal growth process.

Solvent induced nucleation (Turner et al., 2016; Corzo et al., 2014) and growth (Nguyen et al., 2014; Camacho et al., 2017) of crystals in the presence of impurities and additives can dramatically control the growth morphology and kinetics of the crystal further, due to face dependent interactions. Additives have a range of uses during the crystal growth process, for example, they can impede nucleation and growth of crystalline materials by hindering the adsorption of solute molecules, or they can promote the rate of crystallisation by decreasing the surface free energy. (Singh et al., 2015)

The effect of interaction of additives with the growing crystallites is selective enhancement or discouragement of crystal growth on specific faces, which can be used to reduce differences in growth rates of individual crystal faces and reduces anisotropic growth. The appearance of needle- or plate-like crystals is the unwelcome outcome of different growth rates of different crystal faces. (Singh et al., 2015) Growth can be controlled either by acting on the macroscopic conditions or by employing additives capable of hindering the growth of the crystals at a molecular scale. (Salvalaglio et al., 2012)

The use of additives has been widely studied (Sangwal, 1996; Yang et al., 2013; Anwar et al., 2009; Addadi et al., 1985; Weissbuch et al., 1991; Clydesdale et al., 2005; Kubota et al., 1995; Kubota et al., 2000; Sangwal, 2002; Anklam, 2005) to gain computational and theoretical understanding of the interaction between the additive and anisotropic crystal faces. Therefore, it is becoming increasingly clear that solvent induced nucleation and growth of a crystal in the presence of an additive can dramatically alter the nucleation kinetics, growth morphology and growth kinetics of the crystal due to the anisotropic face specific interactions. However, there are very few experimental findings regarding the effect of an additive on the metastable zone width (MSZW), nucleation and growth kinetics of a single crystal.

There have been limited experimental kinetic studies on the nucleation and growth of individual faces of spontaneously nucleated crystals. This is due to a lack of routine and rapid experimental procedures as the most common techniques applied are aimed at measuring crystal size distribution, which is represented by an average value rather than specific growth rates of individual crystal faces.

Previous studies carried out by Hien et al. (2013) investigated the effect of solvent on face dependent crystal growth rates of ibuprofen. The nucleation kinetics and growth rates of morphologically important faces were obtained and were found to be a function of solvent type and supersaturation. This was also integrated with a molecular scale understanding of the crystal growth process. Additionally, the effect of additive on face specific growth of urea was investigated through molecular dynamics simulations by Singh and Tiwari (2015), who showed that any concentration of additive was found to hinder the growth at varying degrees of all faces investigated. These studies were performed in order to understand, and ultimately control, the crystal growth process.

Most commercial particle size instruments calculate crystal size in terms of volume equivalent diameter, i.e. the diameter of a sphere with the same volume as the particle. This method is satisfactory for a crystal with diameters that are approximately equal, for example, roughly cubic/spherical crystals; however, for crystals with anisotropic habits, the results can be confusing.



Figure 26.1: Hypothetical particles with different shapes whilst still having the same volume equivalent diameter. (Hien et al., 2014)

Therefore, molecular scale understanding of the crystal nucleation and growth process is necessary in order to enable the choice of suitable solvents or tailor-made additives.

Additionally, growth models have been derived which combine the diffusion of growth units within a solution, and the incorporation of these units into the crystal surface, using the analogy of a circuit. These models have been applied to the growth of methyl stearate crystals in different solvents (Camacho et al., 2017), allowing for the

determination of key growth parameters and the rate limiting step in the crystal growth process. These results have provided a key insight into the crystallisation process and the effect of different solutions on this.

Whilst nucleation and growth mechanisms have, in comparison, been widely studied, it has been generally assumed that the crystal growth process, is the inverse of the crystal dissolution process, where dissolution is defined as “the release and diffusion of pharmaceutical molecules from the particle surface into the surrounding fluid medium”. (Wang et al., 2012) Additionally, it has also been considered that the dissolution process is faster than the growth process, due to the dissolution process being solely mass transfer limited, whereas the growth process is dependent on both mass transfer and the incorporation of the molecule into the crystal surface. However, very limited experimental studies have been carried out on the dissolution process in order to prove or disprove either of these assumptions. (Hubbard, 2002)

The dissolution rate of a pharmaceutical dosage form can strongly influence bioavailability, therefore there is significant interest in predicting, designing and controlling the dissolution of API's during the development stages. Dissolution testing is an important analytical tool in drug product development, manufacturing and quality assessment, as the objectives of dissolution testing include characterisation and screening of an API, the establishment of an in-vitro-in-vivo relationship of the drug product, and quality control in order to ensure a consistent product. (Liu et al., 2013)

Dissolution models were designed in order to predict the bioperformance of an API based on in-vitro information. In order to do this, a number of general assumptions were made:

1. All classical particle dissolution models were developed for spherical particles.
2. The surfaces of the particles were all considered to have a homogeneous dissolution rate.
3. The driving force for dissolution was considered to be directly proportional to the level of undersaturation in the solution.

However, real pharmaceutical crystals are anisotropic with different functional chemistry's on the faces of the crystal; therefore the expectation would be that the faces would exhibit different wetting and dissolution properties. (Pedersen et al.,

1976) Additionally, the shape of the crystal would influence the total surface area and as a result, this would have an effect on the dissolution rate. (Pickering et al.) Raghavan et al. (2002) investigated this anisotropic effect on dissolution, by determining the kinetics of dissolution of lactose. It was found that the shape of lactose differed considerably during the dissolution process, and with this change, particles of the same material but different shapes also exhibited different dissolution behaviour.

Additionally, the development of most dissolution models considered the dissolution of particles under sink conditions, which is defined in European Pharmacopoeia as the volume of dissolution medium that is at least 3-10x the saturation volume. (Council of Europe, 2008; Liu et al., 2013) Therefore, the dissolution process would be expected to be very fast in these conditions. However, local concentrations of API in solution in the region of dissolving particles could be close to that of a saturated solution, i.e. non-sink conditions. Therefore, the dissolution of API crystals in a solution environment which is close to that of the solubility limit would be expected to have a correlation with the overall bioperformance of the API.

The scenario outlined above sets the framework for this EngD research, which involves the prediction and determination of nucleation and growth mechanisms and kinetic parameters, allowing for the ultimate goal of controlling the crystallisation growth process. The experimental and molecular modelling work was developed in order to understand the effect of crystallisation conditions, for example, supersaturation and the inclusion of an additive, on the crystallisation process. Following on from this, the reverse process of dissolution allowed for the explicit determination of a correlation between the growth and dissolution processes. This EngD research also involves the determination of the dissolution rates of anisotropic particles of API, along with a review of the most applicable dissolution models to establish the validity of dissolution model calculations in predicting bioperformance of API's. All experimental work is rationalised through molecular modelling research, highlighting specific interactions between anisotropic faces with their different surface chemistry's and different solvent environments.

Within this EngD research, urea was selected as a model material for measuring the nucleation and growth mechanisms and kinetic parameters, and face specific dissolution rate, as urea has a widely known morphology, with distinct

morphologically important faces. Additionally, urea also has a tailor-made additive, biuret, which has been extensively studied computationally. Paracetamol was also selected as a model API for determining face-specific dissolution rates, due to the ease of crystallisation of paracetamol, allowing for the replication, and hence calculated prediction, of a 'real-life' dissolution process in biorelevant media.

1.2 Aims and Objectives

The research question at the core of this EngD study is:

What is the influence of solution environment on the nucleation, growth and dissolution of anisotropic crystals, at the single crystal level, and can these interactions be predicted through computational or empirical modelling?

This aim can be obtained through the delivery of the following objectives:

1. Characterising and comparing solution behaviour of urea in ethanol and urea with biuret in ethanol as a function of supersaturation.
2. Investigation of the role of additive and concentration of solution on crystallisation nucleation kinetics through the application of the polythermal methodology.
3. Determination of the influence of an additive on the crystal growth kinetics and growth mechanism of individual crystal faces as a function of supersaturation.
4. Rationalisation of experimental growth data through morphological analysis of crystal surface chemistry's and intermolecular interactions of crystal habit faces under consideration.
5. Studying crystal dissolution kinetics of individual crystal habit faces as a function of undersaturation, temperature and solvent type.
6. Comparison of experimental dissolution data with predictive dissolution models to assess the reliability of predicted data, and make amendments to predictive dissolution models if necessary.
7. Studying scale-up of single crystal dissolution to powder dissolution and compare predictive models to experimental data of powders, and make amendments to dissolution models if necessary.
8. Develop a work-flow to scale-up single crystal dissolution to pharmaceutical powder dissolution in order to predict bioperformance of a pharmaceutical compound in non-sink conditions.

1.3 Project Management

This EngD has been carried out as a research project as part of the EPSRC funded Centre for Doctoral Training in Biopharmaceutical Process Development (Newcastle University, 2019). This was a collaborative project with the EPSRC Centre for Doctoral Training in Complex Particulate Products and Processes (CP3) at the University of Leeds (University of Leeds, 2019) and Pfizer, under the guidance of Professor Kevin J. Roberts at the University of Leeds and Dr. Toshiko Izumi at Pfizer, along with Professor Adam Harvey and Dr. Chris O'Malley at Newcastle University. This EngD has also been carried out in association with the Advanced Digital Design of Pharmaceutical Therapeutics (ADDoPT) project. (ADDoPT, 2019)

The experimental work for this research was carried out at the Centre for Doctoral Training in CP3 at the University of Leeds, and at Pfizer, Sandwich. Assessment of the polythermal technique for analysing nucleation kinetics in Chapter 5 was carried out with guidance from Dr. Thomas Turner and Dr. Diana Camacho Corzo. Single crystal growth and dissolution data in Chapters 5, 6 and 7 were obtained and analysed with guidance from Dr. Ian Rosbottom, Dr. Diana Camacho Corzo, Dr. Ivan Marziano and Dr. CaiYun Ma. Morphological and intermolecular interaction data outlined in Chapters 5, 6 and 7 were collected with guidance from Dr. Klimentina Pencheva, Dr. Radoslav Penchev, Dr. Jonathan Pickering, Dr. Thai Thu Hien Nguyen, and Dr. Nornizar Anuar.

Part of this research has been presented at the Sixth European Conference on Crystal Growth (ECCG6) in Varna, Bulgaria, and at the 13th International Workshop on Crystal Growth and Organic Materials (CGOM13) in Seoul, South Korea. Poster presentations have been attached in Appendices D1 and D2, titled '*The Influence of Solution Environment on the Nucleation Kinetics and Growth Mechanism of Urea*' and '*The Influence of Solution Environment on the Face-Specific Retreat Rates that are Associated with the Dissolution of Urea Single Crystals*', respectively. A publication titled '*The Influence of Solution Environment on the Nucleation and Growth of Urea*' has been submitted to the Journal of Crystal Growth and Design.

1.4 Scope of Thesis

This thesis is made up of 8 chapters, where each chapter concludes with an individual references section.

Chapter 1 establishes the research background of the thesis, presenting an introduction to the research, along with the research question, and outlining the aims and objectives of the project. This chapter concludes with an outline of the thesis structure.

Chapter 2 presents a literature review covering the fundamental theoretical concepts of the crystallisation process, from solubility and supersaturation, through to nucleation, growth, dissolution and characterisation.

Chapter 3 presents a more comprehensive literature review on nucleation theories and measurement of nucleation kinetics, along with crystal growth mechanisms and kinetics. The measurement techniques used to determine crystal growth are also reviewed, and the development of dissolution models are discussed.

Chapter 4 provides a description of the materials used for experimental and computational research, and outlines the methodologies associated with both experimental and computational techniques used for this research.

Chapter 5 presents the results of solubility analysis of urea, along with the determined nucleation kinetics and mechanisms for urea in ethanol and urea with biuret in ethanol. The mean crystal growth rates of the {110} and {111} faces as a function of supersaturation and with and without the influence of additive are also presented. The rationalisation of this data through morphological analysis and intermolecular interactions is also presented.

Chapter 6 presents the mean crystal dissolution rates of the {110} and {111} faces of urea as a function of undersaturation, along with a comparison of the growth and dissolution rates under the same conditions. Additionally, the dissolution rates of urea as a function of solvent are presented, along with a breakdown of intermolecular interactions in order to rationalise the data obtained. Finally, experimental dissolution data is compared with the data obtained from predictive dissolution models, along with a modification of the predictive models in order to obtain better dissolution predictions.

Chapter 7 presents the results of the mean crystal dissolution rates of paracetamol as a function of solvent and biorelevant media, along with a breakdown of the intermolecular interactions in order to rationalise the dissolution behaviour. The experimental dissolution data is also compared with the data obtained from predictive

models, along with the modifications proposed in Chapter 6, to assess the reliability of the models to allow for predictions of dissolution in in-vivo conditions.

Chapter 8 highlights the key outcomes of this research, along with suggestions for future work allowing for this research to be expanded upon to a larger scale.

The scope of this thesis is presented schematically in Figure 1.2.

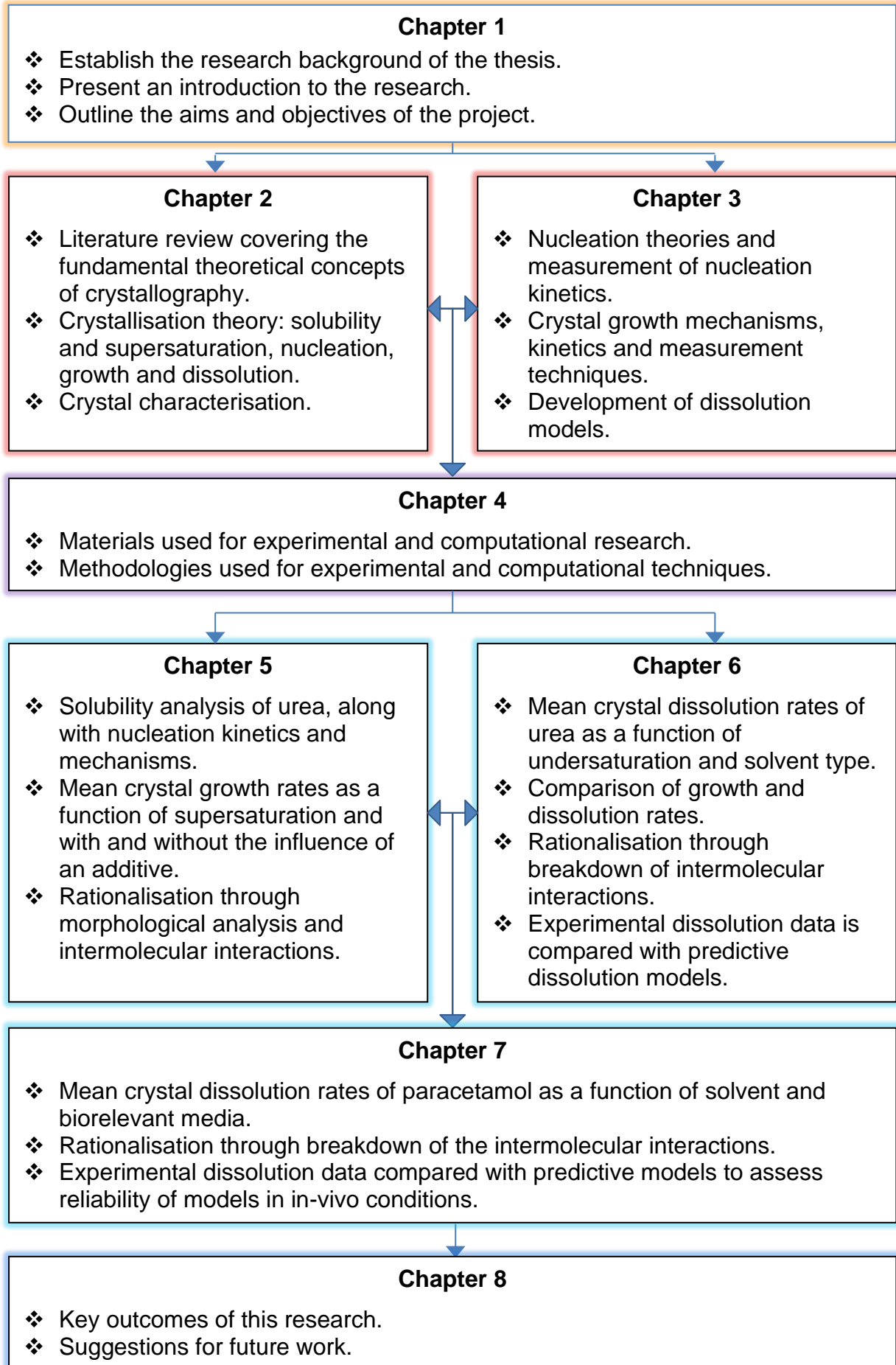


Figure 1.2 The scope of the EngD thesis.

References

- Addadi, L.; Berkovitch-Yellin, Z.; Weissbuch, I.; van Mil, J.; Shimon, L. J. W.; Lahav, M.; Leiserowitz, L. Growth and Dissolution of Organic Crystals with “Tailor-Made” Inhibitors – Implications in Stereochemistry and Materials Science. *Angew. Chem. Int. Ed.* **1985**. 24 (6), 466-485.
- ADDoPT 2019: <https://www.addopt.org/>
- Anklam, M. R.; Firoozabadi, A. An Interfacial Energy Mechanism for the Complete Inhibition of Crystal Growth by Inhibitor Adsorption. *J. Chem. Phys.* **2005**. 123 (14), 144708-1 – 144708-12.
- Anwar, J.; Boateng, P. K.; Tamaki, R.; Odedra, S. Mode of Action and Design rules for Additives that Modulate Crystal Nucleation. *Angew. Chem. Int. Ed. Engl.* **2009**. 48 (9), 1596-1600.
- Blagden, N.; de Matas, M; Gavan, P. T.; York, P. Crystal Engineering of Active Pharmaceutical Ingredients to Improve Solubility and Dissolution Rates. *Adv. Drug Deliv. Rev.* **2007**. 59 (7), 617-630.
- Camacho, D. M.; Roberts, K. J.; Muller, F.; Thomas, D.; More, I.; Lewtas. K. Morphology and Growth of Methyl Stearate as a Function of Crystallisation Environment. *Cryst. Growth Des.* **2017**. 17 (2), 563-575.
- Clydesdale, G.; Thomson, G. B.; Walker, E. M. A Molecular Modelling Study of the Crystal Morphology of Adipic Acid and Its Habit Modification by Homologous Impurities. *Cryst. Growth Des.* **2005**. 5 (6), 2154-2163.
- Corzo, D. M. C.; Borissova, A.; Hammond, R. B.; Kashchiev, D.; Roberts, K. J.; Lewtas, K.; More, I. Nucleation Mechanism and Kinetics from the Analysis of Polythermal Crystallisation Data: Methyl Stearate from Kerosene Solutions. *CrystEngComm.* **2014**. 16 (6), 974-991.
- Council of Europe. European Pharmacopeia 6.1: Supplement. 6th Edition. **2008**. 3479-3481.
- Davey, R. J., Allen, K., Blagden, N., Cross, W. I., Lieberman, H. F., Quayle, M. J., Righini, S., Seton, L., Tiddy, G. J. T. Crystal Engineering – Nucleation, the Key Step. *CrystEngComm.* **2002**. 4 (47), 257-264.
- Hubbard, A. T. Encyclopedia of Surface and Colloid Science (Volume 1). **2002**. CRC Press
- Kashchiev, D.; Borissov, A.; Hammond, R. B.; Roberts, K. J. Effect of Cooling Rate on the Critical Undercooling for Crystallisation. *J. Cryst. Growth.* **2010**. 312 (5), 698-704.

- Kashchiev, D.; Borissova, A.; Hammond, R. B.; Roberts, K. J. Dependence of the Critical Undercooling for Crystallisation on the Cooling Rate. *J. Phys. Chem.* **2010**. 114 (16), 5441-5446.
- Kubota, N.; Mullin, J. W. A Kinetic Model for Crystal Growth from Aqueous Solution in the Presence of Impurity. *J. Cryst. Growth.* **1995**. 152 (3), 203-208.
- Kubota, N.; Yokota, M.; Mullin, J. W. Combined Influence of Impurity Concentration and Supersaturation on Crystal Growth. *J. Cryst. Growth.* **2000**. 212 (3), 480-488.
- Liu, P., De Wulf, O., Heikkila, T., van Veen, B., Kiesvaara, J., Hirvonen, J., Peltonen, L., Laaksonen, T. Dissolution Studies of Poorly Soluble Drug Nanosuspensions in Non-Sink Conditions. *AAPS Pharm. Sci. Tech.* **2013**. 14(2), 748-756.
- Myerson, A. *Handbook of industrial crystallization.* **2002**: Butterworth-Heinemann.
- Newcastle University, BBTC, 2019: <https://www.ncl.ac.uk/bbtc/>
- Nguyen, T. T. H. Influence of Crystallisation Environment on the Nucleation and Growth of Single Crystals of (RS)-Ibuprofen. **2013**. PhD thesis. University of Leeds.
- Nguyen, T. T. H.; Hammond, R. B.; Roberts, K. J.; Marziano, I.; Nichols, G. Precision Measurement of the Growth Rate and Mechanism of Ibuprofen {001} and {011} as a Function of Crystallisation Environment. *CrystEngComm.* **2014**. 16 (21), 4568-4586.
- Ostwald, W. Studies on Formation and Transformation of Solid Materials. *Z. Phys. Chem.* **1897**. 22, 289-330.
- Pedersen, P. V., Brown, K. F. Theoretical Isotropic Dissolution of Non-Spherical Particles. *J. Pharm. Sci.* **1976**. 65(10), 1437-1442.
- Pickering, J., Kathyola, T., Nguyen, T. H., Ramachandran, V., Soufian, M., Hammond, R. B., Roberts, K. J., Pencheva, K., Ticehurst, M. A Comparative Study of the Experimental and Theoretical Dissolution Kinetics of Ibuprofen in Ethanol. (*Submitted J. Pharm. Sci.*)
- Raghavan, S. L., Ristic, R. I., Sheen, D. B., Sherwood, J. N. Dissolution Kinetics of Single Crystals of α -Lactose Monohydrate. *J. Pharm. Sci.* **2002**. 91(10), 2166-2174.
- Salvalaglio, M.; Vetter, T.; Giberti, F.; Mazzotti, M.; Parrinello, M. Uncovering Molecular Details of Urea Crystal Growth in the Presence of Additives. *J. Am. Chem. Soc.* **2012**. 134 (41), 17221-17233.
- Sangwal, K. Effects of Impurities on Crystal Growth Processes. *Prog. Cryst. Growth and Charact.* **1996**. 32 (1-3), 3-43.
- Sangwal, K. On the Nature of Supersaturation Barriers Observed During the Growth of Crystals from Aqueous Solutions Containing Impurities. *J. Cryst. Growth.* **2002**. 242 (1-2), 215-228.

Singh, M. K.; Tiwari, V. S. Uncovering the Mode of Action of Solvent and Additive Controlled Crystallisation of Urea Crystal: A Molecular-Scale Study. *Cryst. Growth Des.* **2015**. 15 (7), 3220-3234.

Turner, T. D. Molecular Self-Assembly, Nucleation Kinetics and Cluster Formation Associated with Solution Crystallisation. **2015**. PhD Thesis. University of Leeds.

Turner, T. D.; Corzo, D. M. C.; Toroz, D.; Curtis, A.; Dos Santos, M. M.; Hammond, R. B.; Lai, X.; Roberts, K. J. The Influence of Solution Environment on the Nucleation Kinetics and Crystallisability of Para-Aminobenzoic Acid. *Phys. Chem. Chem. Phys.* **2016**. 18 (39), 27507-27520.

Threlfall, T. Structural and Thermodynamic Explanations of Ostwald's Rule. *Org. Proc. Res. Dev.* **2003**. 7 (6), 1017-1027.

University of Leeds, CP3, 2019: <https://particulates.leeds.ac.uk/>

Volmer, M. Kinetik der phasenbildung. **1939**. Dresden & Leipeg, Steinkoff.

Wang, Y. Abrahamsson, B., Lindfors, L., Bresseur, J. G. Comparison and Analysis of Theoretical Models for Diffusion Controlled Dissolution. *Mol. Pharmaceutics*. **2012**. 9 (5), 1052-1066.

Weissbuch, I.; Addadi, L.; Leiserowitz, L. Molecular Recognition at Crystal Interfaces. *Science*. **1991**. 253 (5020), 637-645.

Yang, X.; Qian, G.; Duan, X.; Zhou, X. Impurity Effect of L-Valine on L-Alanine Crystal Growth. *Cryst. Growth Des.* **2013**. 13 (3), 1295-1300.

York, P. Solid State Properties of Powders in the Formulation and Processing of Solid Dosage Forms. *Int. J. Pharm.* **1983**. 14 (1), 1-28.

Chapter 2: Theoretical Background on Crystallography and the Crystallisation Process

2.1 Introduction

The principal theoretical background of crystallography and the crystallisation process are described in this chapter, with a focus on solubility, crystal nucleation and growth, morphology and polymorphism, and crystal dissolution. A comprehensive understanding of crystal nucleation and growth allows for the ability to incorporate additives into the crystallisation process in order to manipulate crystal morphologies, hence influencing the physical and chemical properties of the crystal. Further to crystal nucleation and growth, which have been widely studied, the theory of crystal dissolution has been focussed upon, allowing for the ability to understand the behaviour of active pharmaceutical ingredients in relation to a drug product formulation.

This chapter starts with an overview of crystallography, focussing on crystal systems, Bravais lattices and Miller indices and planes, followed by solubility and supersaturation to outline the onset of the crystallisation process. Finally, an overview of nucleation, growth and dissolution theory will be presented.

2.2 Crystallography

Crystallography is the science of determining the highly ordered arrangement of atoms in a three dimensional structure – the crystalline solid. This crystalline solid consists of a rigid arrangement of ions, atoms or molecules, which have distinguishing locations specific to the substance being crystallised. The regularity of this arrangement results in the substance having a specific shape or morphology as the crystal grows. Crystals of a particular substance have similar shapes however two crystals formed under the same conditions will very rarely be completely identical in shape and size. (Borchard-Ott et al., 2011)

2.2.1 Lattice, Unit Cell and Crystal Systems

The repetition of a parallelepiped from one lattice point to another generates the lattice, where a lattice point is an arrangement in space of isolated points in a regular pattern, showing the positions of atoms, molecules or ions in the structure of a crystal. The generating parallelepiped is called the unit cell. If the exact arrangement of atoms within one unit cell is known, then the atomic arrangement for the whole crystal is known. (Sands, 1969)

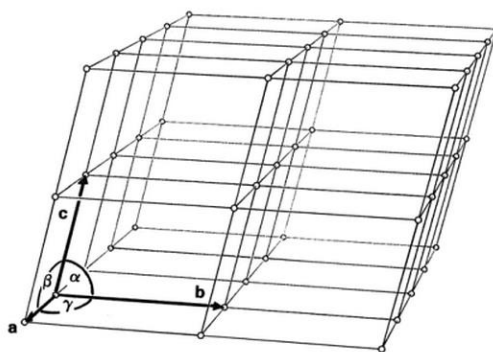


Figure 2.1: The size and shape of the unit cell specified by means of the lengths a , b and c of the three independent edges, and three angles α , β and γ between these edges. (Sands, 1969)

The positions of the atoms described in terms of crystallographic axes are defined by the three basis vectors – referred to as the a -, b - and c - axes. The lattice coordinates are used as units, and the atomic positions are given in terms of fractional coordinates, x , y , and z which describe fractions of the lattice constants, a , b and c respectively. (Massa, 2000)

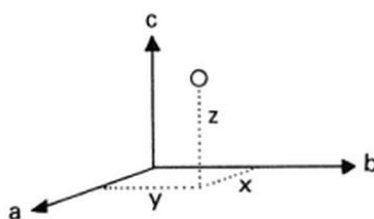


Figure 2.2: The coordinates of an atom at the centre of the unit cell written as $(\frac{1}{2}, \frac{1}{2}, \frac{1}{2})$. (Massa, 2000)

In addition to three dimensional periodicity, the most important property of crystals is their symmetry. For example, if there is a mirror plane in the crystal normal to the b -axis, it follows that a - and c - axes must lie in this plane and hence be perpendicular to the b -axis. If a three-fold rotation axis lies parallel to the c -axis, this implies that the angle between a and b (γ) must be 120° . The full consideration gives rise to seven crystal possibilities, also known as the seven crystal systems. They are distinguished from one another by their shape – the geometry of the lattice that is required by the underlying symmetry elements. (Massa, 2000)

Table 2.1: The seven crystal systems with geometries.

Crystal System	Axes Length	Angle Between Axes
Cubic	$a = b = c$	$\alpha = \beta = \gamma = 90^\circ$
Trigonal	$a = b = c$	$\alpha = \beta = \gamma \neq 90^\circ$
Tetragonal	$a = b \neq c$	$\alpha = \beta = \gamma = 90^\circ$
Hexagonal	$a = b \neq c$	$\alpha = \beta = 90^\circ, \gamma = 120^\circ$
Orthorhombic	$a \neq b \neq c$	$\alpha = \beta = \gamma = 90^\circ$
Monoclinic	$a \neq b \neq c$	$\alpha = \beta = 90^\circ \neq \gamma$
Triclinic	$a \neq b \neq c$	$\alpha \neq \beta \neq \gamma \neq 90^\circ$

2.2.2 Bravais Lattice

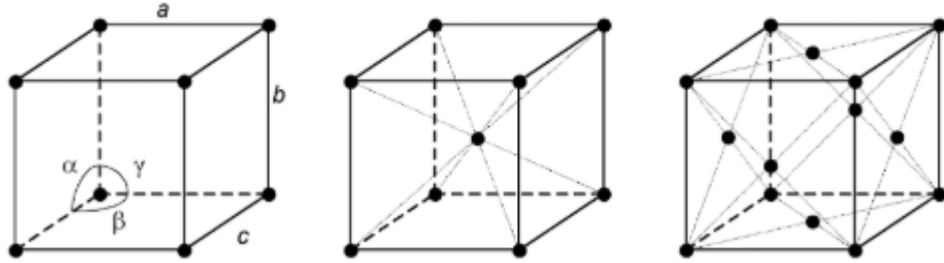
A special property of a crystal lattice is that the lattice points are identical; therefore if there is an atom at or near one point, there must be an identical atom at the same position relative to every other lattice point. There are fourteen different ways to arrange lattice points. These are constructed as three separate types (Carter and Norton, 2013):

- Primitive (P) lattices: one lattice point per unit cell
- Body-centred (I) lattices: a lattice point at the corners and one in the centre of the cell.
- Face-centred (A, B, C or F) lattices: a lattice point at the corners and others at one (A, B or C) or all three (F) of the faces.

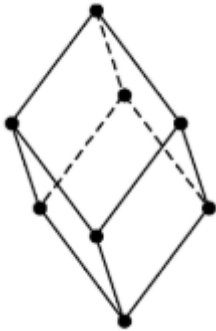
All of the Bravais lattices are presented in Table 2.2, separated into their crystal systems.

Table 2.2: Seven crystal systems separated into Bravais lattices. (Carter et al., 2013)

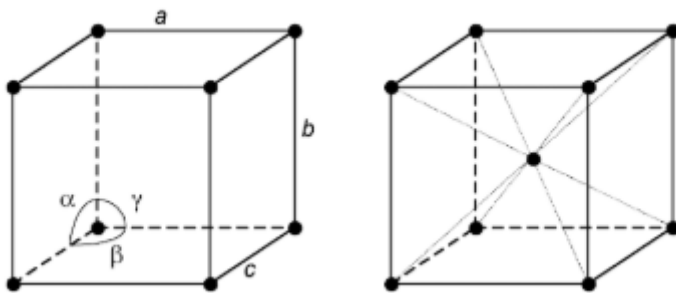
Cubic symmetry: has three Bravais lattices, the primitive cubic cell, the body-centred cubic cell, and the face-centred cubic cell, shown respectively.



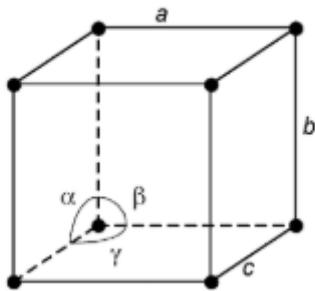
Trigonal symmetry: only has one Bravais lattice, the primitive trigonal unit cell.



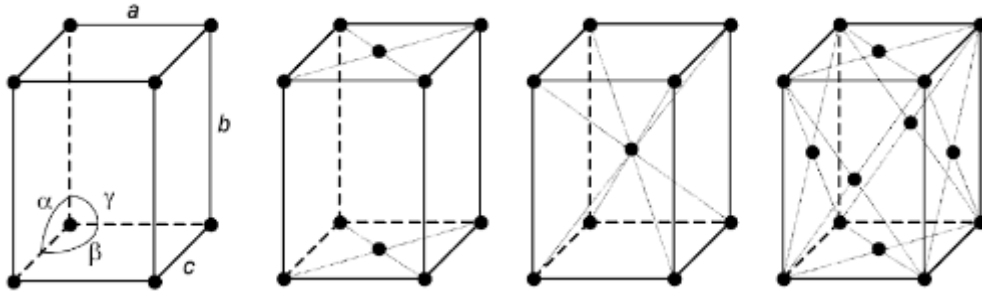
Tetragonal symmetry: has two Bravais lattices, the primitive tetragonal unit cell, and the body-centred tetragonal unit cell, shown respectively.



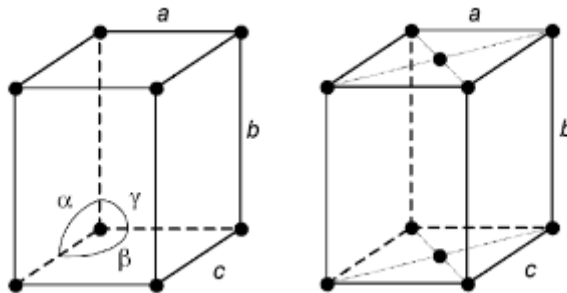
Hexagonal symmetry: only has one Bravais lattice, the primitive hexagonal unit cell.



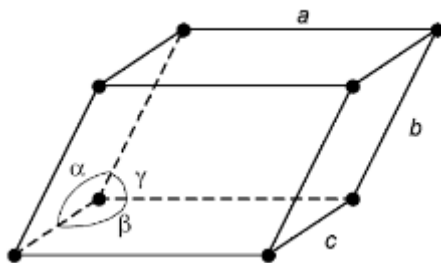
Orthorhombic symmetry: has four Bravais lattices, the primitive orthorhombic cell, the base-centred orthorhombic cell, the body-centred orthorhombic cell and the face-centred orthorhombic cell.



Monoclinic symmetry: has two Bravais lattices, the primitive monoclinic cell and the base-centred monoclinic cell.



Triclinic symmetry: only has one Bravais lattice: the primitive triclinic cell.



2.2.3 Miller Indices and Planes

Miller indices are used for the identification of the surfaces of a crystal structure. They are denoted by the letters h , k and l to represent a set of parallel planes, and the values of h , k and l are the inverse of the fractions of a unit cell edge, where they intersect the edge. The edges of the unit cell are denoted by a , b and c , therefore if a plane lies parallel to any of these edges, but does not intersect this edge, it is given the index "0".

For example, a facet plane that intersects the a - axis of the unit cell, but lies parallel to the b - and c - axes would be denoted by the Miller indices (100) , therefore (100)

represents a set of identical planes all separated by the distance “ $1a$ ”. A plane parallel to this Miller indices that intersects the “ a ” edge of the unit cell in the middle, at $a/2$, would have a Miller indices of (200) . Similarly, a plane parallel to the (100) index that intersects the “ a ” edge of the unit cell at $a/3$, would have a Miller indices of (300) .

Any general plane that is parallel to the (100) Miller indices would be denoted as $(h00)$. Additionally, any general plane parallel to the “ a ” and “ c ” unit cell edges, but intersecting the “ b ” unit cell edge would be denoted by the Miller indices $(0k0)$, and any general plane parallel to the “ a ” and “ b ” unit cell edges and intersecting the “ c ” unit cell edge would be denoted by the Miller indices $(00l)$. (Tilley, 2013)

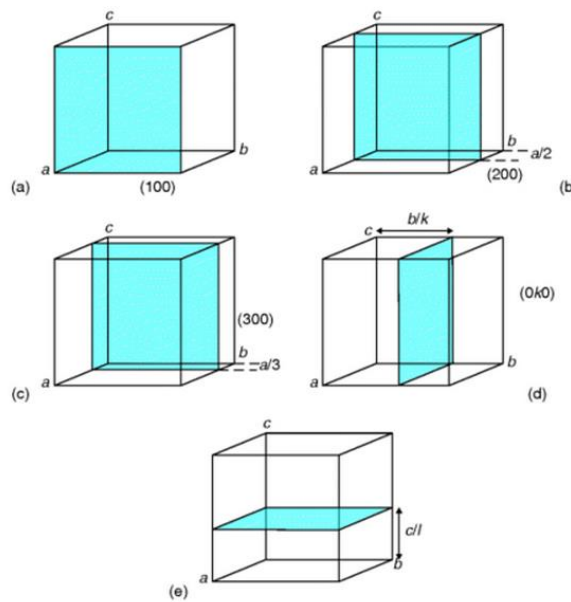


Figure 2.3: Miller indices of crystal planes: (a) (100) , (b) (200) , (c) (300) , (d) $(0k0)$, (e) $(00l)$. (Tilley, 2013)

Additionally, any general plane that cuts two edges and lies parallel to a third is denoted by the Miller indices $(hk0)$, $(0kl)$ or $(h0l)$.

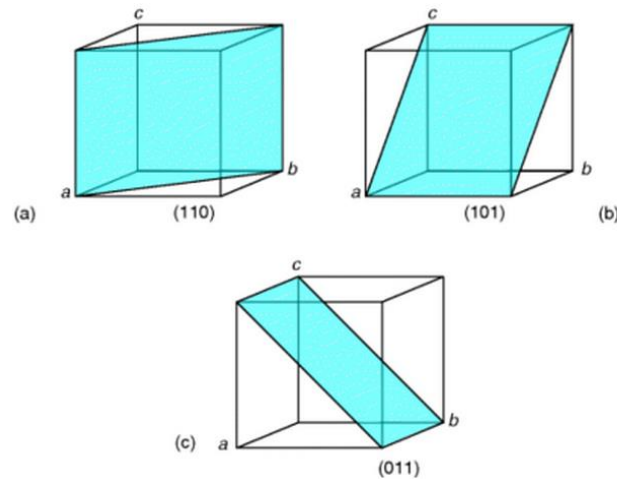


Figure 2.4: Miller indices of crystal planes: (a) (110), (b) (101), (c) (011). (Tilley, 2013)

Intersections of a plane within a unit cell can be negative as well as positive. Therefore, to distinguish between these, negative intersections are denoted with a bar above the number, and are related to planes which have a positive Miller indices. For example, a plane with a positive Miller indices of (110) is also related to a similar plane which is perpendicular to the “b” unit cell edge at a positive intersection but is also perpendicular to the “a” unit cell edge at a negative intersection. This plane would have the Miller indices $(\bar{1}10)$. The (110) plane also has two other related planes, one of which is opposite to the plane mentioned previously, i.e. perpendicular to the “b” unit cell edge at a negative intersection and also perpendicular to the “a” unit cell edge at a positive intersection which can be denoted with the Miller indices $(1\bar{1}0)$. The final related plane has both the “a” unit cell edge and the “b” unit cell edge at a negative intersection, which is denoted with the Miller indices $(\bar{1}\bar{1}0)$. As the position of the axes of the unit cell is arbitrary, the Miller indices of planes can be considered equivalent. For example, $(\bar{1}\bar{1}0)$ is equivalent to (110) and $(1\bar{1}0)$ is considered equivalent to $(\bar{1}10)$. (Tilley, 2013)

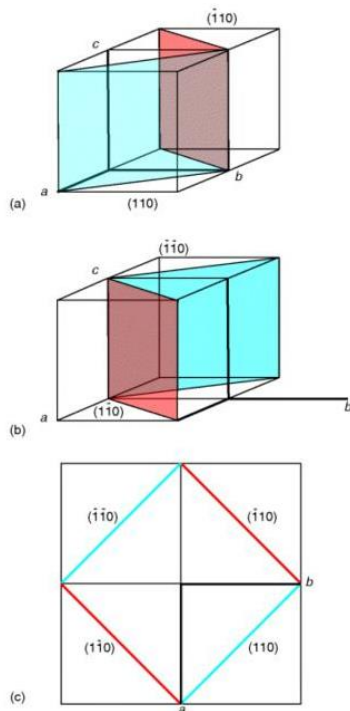


Figure 2.5: Miller indices of crystal planes: (a) (110) and $(\bar{1}\bar{1}0)$ (b) $(\bar{1}\bar{1}0)$ and (110) , (c) projection down the c -axis showing the equivalent planes. (Tilley, 2013)

2.2.4 Symmetry

Symmetry is an important property in crystallisation as a crystal consists of ions, atoms or molecules which are repeated regularly in three dimensional space. This known as translational symmetry, and is an inherent property of all crystals. Due to this translational symmetry, the physical and chemical properties of crystals are defined. The most important symmetry operations are outlined below (Mullin, 2001):

- **Rotations:** The international standard of notation for rotational symmetry is as follows – an ‘ f ’-fold axis of rotational symmetry will be specified by ‘ f ’. For example, a 2-fold axis of rotational symmetry will be denoted with ‘2’. Rotational symmetry will usually be denoted by an integer (either 1, 2, 3 or 4).
- **Mirror Planes:** Mirror planes can either be parallel or perpendicular and are denoted by ‘ m ’. For example, ‘ f ’ m means an ‘ f ’-fold rotation axis with a parallel mirror plane and ‘ f ’/ m means a ‘ f ’-fold rotation axis with a perpendicular mirror plane.
- **Inversion:** an inversion centre is denoted with an ‘ i ’, and it relates pairs of points or objects which are equidistant from and on opposite sides of a central point. This central point is called an inversion centre.

- Rotation Inversion: This is denoted by a bar, for example ' \bar{f} ', meaning the crystal is brought back onto itself with an ' f '-fold rotation, followed by an inversion. Therefore, ' $\bar{2}$ ' means the crystal has a 2-fold rotation followed by an inversion.

2.3 Crystal Chemistry and Polymorphism

2.3.1 Crystal Chemistry

In order to understand crystal chemistry and intermolecular interactions within crystal structures, knowledge of the nature of chemical bonds is necessary. There are five types of chemical bonding (Kutty et al., 2001):

1. Ionic bonding
2. Covalent bonding
3. Metallic bonding
4. Van der Waals bonding
5. Hydrogen bonding

Ionic bonding occurs when electrons are transferred from one atom to another, resulting in positively or negatively charged ions. These ions are held together by electrostatic or coulombic forces, which are equal in all directions. Therefore, ionic bonding is non-directional so the geometry of the molecule is not specific by the chemical bonding.

Covalent bonding occurs when the outer electrons of two atoms are shared between both atoms. Unlike ionic bonding, there is no transference of electrons from one atom to another. The sharing of electrons results in a rigid structure due to the definite geometric configuration.

Metallic bonding occurs when electrons are delocalised and are considered to constitute an electron cloud. The negatively charged electron cloud encloses the positively charged nuclei of the atom.

Van der Waals forces are weaker intermolecular interactions and are always present, long-range forces that may be attractive or repulsive. These interactions bring molecules together through momentary alignment or orientation. These interactions can be from different origins – dipole-dipole, induced dipoles, London dispersive

forces of attraction, or repulsion prevailing between molecules without permanent dipoles.

Hydrogen bonding occurs when a hydrogen atom bonded covalently to another atom is attracted by an electronegative atom, for example, oxygen, nitrogen or fluorine, from a neighbouring molecule. As a result of this, the hydrogen atom is located between the two atoms. Hydrogen bonding is stronger than van der Waals forces of interaction, however both are weaker than covalent or ionic bonding.

The types of bonding occurring within a crystal structure has an impact upon the chemical and physical properties of the crystal, for example, surface properties, melting point and polymorphism.

2.3.2 Polymorphism

Polymorphism, according to McCrone's definition is the "*ability of any element or compound to crystallise as more than one distinct chemical species*" (Bernstein et al., 2001), and is a very common and significant problem within the pharmaceutical industry. This is because different crystal arrangements of the same element or compound will have different inter- and intra-molecular interactions, therefore polymorphs will have different physical and chemical properties, for example, solubility, melting point and chemical stability.

According to Ostwald's rule, it is not the most stable polymorph which is initially obtained, but the least stable polymorph, with the highest amount of free energy, which then transforms to the next most stable polymorph, until the most stable polymorph with the least amount of free energy is formed. (Hilfiker et al., 2006)

There are two types of polymorphism – monotropic and enantiotropic. Monotropic polymorphism occurs when one form of the substance is stable over the entire temperature range up to the melting point, therefore there is no reversible polymorphic transformation below the melting point. Enantiotropic polymorphism, on the other hand, occurs when one form of the substance changes into another upon heating, and the process is reversed when the substance is cooled. (Moody, 2013) Therefore, there is a reversible transition point at some temperature below the melting point of either polymorphic form. As a result of this, both polymorphs have a definitive range of temperatures over which they are in the thermodynamically stable solid phase.

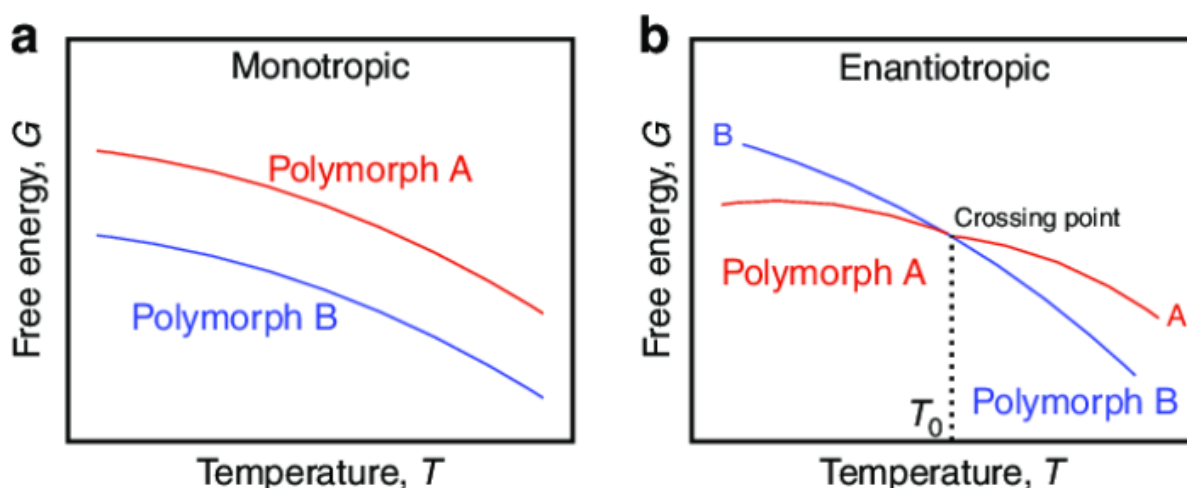


Figure 2.6: A schematic showing (a) monotropic polymorph and (b) enantiotropic polymorph where T_0 denotes the transition temperature. (Li et al., 2018)

Metastable polymorphic forms are undesirable during pharmaceutical processing, as the processing conditions may result in a polymorphic transition, i.e. the formation of a more stable polymorphic form. As polymorphs have different physical and chemical properties, for example, solubility, bioavailability and stability, the performance of a pharmaceutical product is dependent upon the polymorph. Additionally, a change in polymorphic form can also lead to a change in crystal habit, which can affect the compaction and flow properties of the powder.

2.4 Crystal Morphology and Habit

Crystal morphology defines the external shape and appearance of the crystal. The external habit of a crystal is controlled, not only by its internal structure, but by the conditions at which the crystal grows. Crystal habit is governed by the slowest growing faces.

The habit of a crystal can be affected by the polymorphic form being crystallised, the presence of a solvent, or the presence of impurities, which are often added deliberately. Imposter molecules may be incorporated into growing crystal lattice to impede the growth of specific faces, which dominates crystal habit. (Jones, 2002) A quantitative description of a crystal means knowing the crystal faces present, their relative area, the lengths of the areas in three directions, the angles between the faces and the shape factor of the crystal. (Myerson, 1993)

The polymorphic form, rate of growth, the solvent used, and the impurities present can all have a major impact on crystal habit. The habit of crystals obtained from

industrial crystallisation processes can have a major impact on a number of important properties relating to slurry and the dry product. It will affect the rheological properties of the suspension, the filtration or centrifugation efficiency, the bulk density of the solid and the flow properties of the solid.

Crystal habit can vary dramatically with the rate of crystal growth and nucleation. Very rapid crystallisation processes can often produce amorphous-appearing materials (with no visible faces) that are actually crystalline. This is the result of the rapidity of the growth process, with all faces growing so rapidly they disappear.

Changes in the solvent used or the presence of an impurity can also profoundly affect crystal habit. In recent years, great strides have been made in developing a quantitative understanding of habit modification. The impurity or solvent can hinder the growth of a face by sterically hindering the attachment of additional molecules. Additives can also be tailor made to substitute into the crystal lattice in only certain faces, thus blocking growth and altering the morphology. (Myerson, 1993)

The prediction and control of crystal habit by the appropriate selection of solvent or addition of impurity is an area of great current interest with potential for great impact on industrial crystallisation.

2.5 Crystallisation

The crystallisation process is viewed as a two-step process involving the dissolution of the active pharmaceutical ingredient, and changing some attribute of the system, for example, temperature, pH, or solvent content, in order to induce crystallisation. The crystallisation process is used to produce high purity products from solutions containing significant amounts of impurities with comparatively low energy input. (Blacker and Williams, 2011)

2.5.1 Solubility

At a given temperature and pressure, there is a maximum amount of solute that can dissolve in a given amount of solvent. When this maximum is reached, the solution is said to be saturated. The amount of solute required to make a saturated solution at a given condition is called the solubility. (Blacker and Williams, 2011) In other words, solubility provides the concentration at which the solid solute and the liquid solution are at equilibrium. This allows the calculation of maximum yield of product crystals

accompanying a change of state from one concentration to another in which crystals form. (Myerson, 1993)

In an ideal solution, the amount of energy required to break solute-solute interactions in addition to the amount of energy required to break solvent-solvent interactions is equal to the amount of energy required to make solute-solvent interactions. To estimate solubility behaviour in an ideal solution, the van't Hoff relationship can be used (Coulson et al., 2002):

$$\ln x_{ideal} = \frac{\Delta H_f}{RT} \left(\frac{T}{T_M} - 1 \right) \quad (2.1)$$

Where x_{ideal} is the mole fraction at the ideal solubility of the solute, ΔH_f is the molar enthalpy of fusion of the pure solute, R is the ideal gas constant, T is temperature and T_M is the melting temperature of the pure solute. If the solution is found to exhibit non-ideal behaviour, the enthalpy and entropy of dissolution can be calculated through another expression of the van't Hoff equation:

$$\ln x = -\frac{\Delta H_d}{RT} + \frac{\Delta S_d}{R} \quad (2.2)$$

Where x is the mole fraction of the solute in solution, and ΔH_d and ΔS_d are the enthalpy of dissolution and the entropy of dissolution respectively. The mole fraction at the ideal solubility of the solute can be related to the non-ideal behaviour of the solution through the activity coefficient, a , through the following equation:

$$a = \frac{x_{ideal}}{x} \quad (2.3)$$

If the calculated activity coefficient is greater than 1, forces of attraction between solute-solute molecules are favoured over forces of attraction between solute-solvent molecules. A solution can exhibit behaviour different to that of an ideal solution due to either enthalpic or entropic factors, or both. This can be determined through the comparison of van't Hoff plots – if the gradients of the lines differ, the deviation from an ideal solution is due to both enthalpic and entropic factors. However, if the lines are parallel, the deviation from ideal behaviour is only due to entropic factors.

2.5.2 Supersaturation

Crystallisation is a rate process, meaning the time required for crystallisation depends on a driving force. In the case of crystallisation, the driving force is called

supersaturation. A solution in which the solute concentration exceeds the equilibrium (saturation) solute concentration at a given temperature is known as a supersaturated solution. Supersaturated solutions are metastable, implying that crystallisation will ultimately occur, albeit after time has elapsed, but that process is inhibited by a kinetic barrier. (Myerson, 1993)

The degree of supersaturation may be expressed by (Coulson et al., 2002):

$$\Delta c = c - c^* \quad (2.4)$$

Where c and c^* are the solution concentration and equilibrium saturation value respectively. The supersaturation ratio, S , and the relative supersaturation, σ , are then:

$$S = \frac{c}{c^*} \quad (2.5)$$

$$\sigma = \frac{\Delta c}{c^*} = S - 1 \quad (2.6)$$

Whilst the fundamental driving force for crystallisation, the true thermodynamic supersaturation, is the difference in chemical potential, in practice, supersaturation is generally expressed in terms of solution concentration. (Coulson et al., 2002)

The metastability of a solution decreases as supersaturation increases. Every solution has a maximum amount that it can be supersaturated before it becomes unstable. The zone between the saturation curve and this unstable boundary is called the metastable zone and is where all crystallisation operations occur.

In practice, the practical limits of the metastable zone vary as a function of conditions for a given substance. This is because the presence of dust and dirt, the cooling rate employed, solution history and the use of agitation can all aid in the formation of nuclei and decrease the metastable zone.

In general, there are two types of measurement for the determination of the metastable limit. In the first method, solutions are cooled to a given temperature rapidly, and the time required for crystallisation is measured. When this time becomes short, then the effective metastable limit has been approached. A second method is to cool the solution at some rate, and observe the temperature where the first crystals form. The temperature at which crystals are first observed will vary with the cooling rate used. (Myerson, 1993)

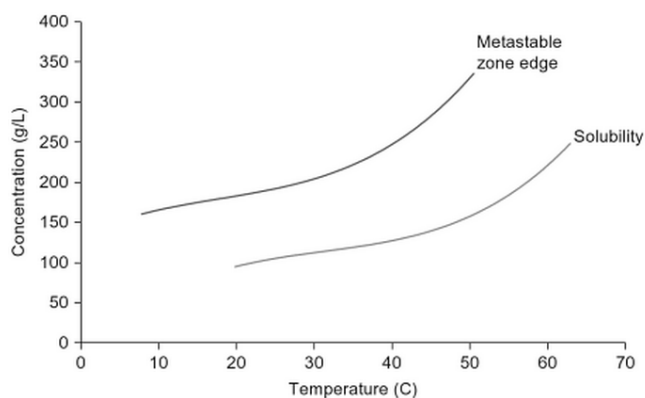


Figure 2.7: The region below the solubility curve is undersaturated, and the region above the metastable zone edge is supersaturated. The region in the middle is the metastable zone width. (Blacker and Williams, 2011)

When plotting concentration against temperature, three regions are found.

- A stable or undersaturated region where crystal growth is not favoured.
- A metastable region where the solution is supersaturated to a degree and where crystallisation will take place after a time.
- An unstable region where the solution is more supersaturated and where spontaneous crystallisation with no time delay is expected.

Within the metastable zone, the nucleation stage is quite controlled and crystals are able to grow with a steady supply of solute molecules without the formation of other nuclei. The metastable zone width should be large enough to provide a stable region for crystal growth, but not so large that it leads to a barrier for growth. In the unstable region, controlled crystal growth to macroscopic dimensions is not possible. Thus, in this region, depending on the degree of supersaturation, very small crystal particles will be produced, also known as fines. Therefore crystallisers are normally operated away from the edge of the effective metastable zone, due to the formation of fines. Fines cause filtration problems and are usually not wanted in the final product.

The metastable zone width is the difference between the temperature of dissolution and that of crystallisation. It needs to be carefully characterised and understood to produce optimal crystals. Very high cooling rates of the solution may result in an unwanted outcome, for example, the formation of a metastable polymorph, precipitations of an amorphous phase or formations of a colloidal dispersion. (Blacker and Williams, 2011)

The most common method applied for supersaturation generation is cooling crystallisation. Cooling crystallisation is usually the preferred method of crystallisation because of its relative ease of control and scale up. The most important factor among cooling crystallisation is the cooling rate. If the cooling rate is high, the mixture will precipitate very quickly in order to avoid excess levels of supersaturation, and control over the properties of the crystallising solid will be very limited. Also, the rapid formation of the crystallising solid can cause solvent or other impurity molecules to be included in the solid. There are three types of cooling profiles that are normally used (Blacker and Williams, 2011):

- Natural – this is characterised by an initial steep cooling rate followed by a much slower cooling rate in the latter stages, which can result in poor quality crystals being formed. This method is not generally used.
- Linear – this can be used very efficiently if the rate is adjusted to suit the purposes of the crystallisation. A steep linear cooling rate can be used to generate small particles as primary nucleation will predominate as a means to rapidly decrease supersaturation. This method of cooling crystallisation is useful as it can be easily transferred to a different plant or vessel.
- Cubic – this is where an initial slow period of cooling is followed by a steep cooling period. This profile is optimal for crystallisation because the initial slow cooling rate prevents the mixture from reaching excessive supersaturation levels and allowed the existing supersaturation to deplete via crystallisation.

Cooling crystallisation is usually applied for moderately or highly soluble substances when the slope of the solubility-temperature curve is positive and sufficiently steep. Usually a temperature range is preferred where the slope of the solubility curve is the steepest, as a relatively large amount of solid is formed for a given degree of cooling.

The main limitation of the cooling method is that the yield is limited by the solubility of the compound at the lowest temperature. Such a limitation can sometimes be circumvented if the solution that leaves the crystalliser can be recycled to an upstream unit operation. (Lewis et al., 2015)

2.5.3 Nucleation

Nucleation, associated with the formation of three dimensional clusters, plays a key role in defining particle size, polymorphic form and crystallinity. At the nucleation

stage, small clusters of solute molecules are formed. Some of these clusters may grow sufficiently to form stable nuclei and subsequently form crystals. Others fail to reach adequate dimensions before they dissolve again. (Blacker and Williams, 2011)

Nucleation is a complex event, since nuclei may be generated by many different mechanisms. Most nucleation classification schemes distinguish between primary nucleation – in the absence of crystals, and secondary nucleation – in the presence of crystals. Primary nucleation is based on sequences of bimolecular collisions and interactions in a supersaturated fluid that result in the build-up of lattice structured bodies which may or may not achieve thermodynamic stability. Such primary nucleation is known as homogeneous.

Primary nucleation may also be initiated by suspended particles of foreign substances, and this mechanism is general referred to as heterogeneous nucleation. In industrial crystallisation, most primary nucleation is almost certainly heterogeneous, in that it is induced by foreign solid particles invariably present in working solutions. Although the mechanism of heterogeneous nucleation is not fully understood, it probably begins with adsorption of the crystallising species on the surface of solid particles, thus creating apparently crystalline bodies, larger than critical nucleus size, which then grow into macro-crystals. (Coulson et al., 2002)

Although it is an idealised case, homogeneous nucleation is useful in that it a full derivation of the parameters important in nucleation theory and provides a useful benchmark for the process. using this as a basis, the more representative heterogeneous nucleation case can be considered a modification as it is when nucleation is induced by other particles, which are able to act as structural templates by lowering the interfacial tension to encourage nucleation within the metastable zone, so reducing induction time. (Blacker and Williams, 2011)

Secondary nucleation can only take place if crystals of the species under consideration are already present. Since this is usually the case in industrial crystallisers, secondary nucleation has a profound influence on virtually all industrial crystallisation processes. (Coulson et al., 2002) A seed of the appropriate type, shape or size can be used as a template for the secondary nucleation. Seeding can be used to initiate crystallisation away from the metastable zone during the cooling process. By using well-defined seeding protocol, batch to batch variability is reduced, as homogeneous seeding can be used to control crystallinity, particle size distribution

and purity. However, caution is needed when using dry-milled powder seeds, as they may have suffered mechanical damage which could impede regrowth or encourage impurity ingress. (Blacker and Williams, 2011)

Secondary nucleation is a significant problem in industrial crystallisation, where an aggressive environment for soft particles is provided by their interaction with mechanical elements such as reactor surfaces, pumps, baffles, stirrers etc. This results in the production of attrition fragments, which have a growth rate less than that produced by homogeneous nucleation. Such dispersion in growth rates can result in a product with a variable particle size distribution, leading to problems in downstream processing, including issues with isolation, drying, particle flow and variability in product performance attributes such as content uniformity. (Blacker and Williams, 2011)

2.5.4 Crystal Growth

Following nucleation, crystal growth is the next stage in the crystallisation process. Crystal growth from solution occurs through the generation of supersaturation, and is affected by the solvent used and possible impurities within the solution.

The main steps involved in crystal growth are (Dhanaraj et al., 2010; Pethrick, 2007):

1. Mass transport of the solute molecules to the boundary layer and diffusion through this boundary layer between the solution and crystal surface, enabled by a concentration driving force.
2. Adsorption of the solute molecule onto the crystal surface.
3. Diffusion of the solute molecule over the crystal surface until an energetically favourable site is found to incorporate the solute molecule, allowing for integration of the molecule into the crystal surface.

The Kossel model states that the crystal surface is made up of layers, incorporating faces, steps and kink sites. Additionally, the surface will have loosely adsorbed growth units, as well as sites which are vacant. As a result of this, growth units will be most easily incorporated into the crystal surface at a kink site. However, a growth unit reaching a crystal surface is not integrated into the lattice immediately. Instead, it adsorbs onto a step site, and moves along to a kink site where it is finally incorporated.

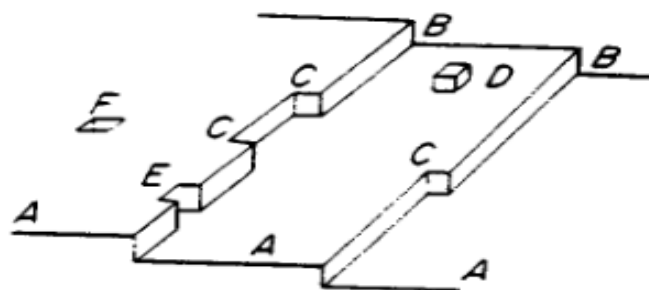


Figure 2.8: The crystal growth process (Kossel's model). (Mullin, 2001)

A: Flat surfaces B: Steps C: Kinks D: Surface-adsorbed growth units E: Edge vacancies F: Surface vacancies

One of the major drawbacks of the Kossel model is that once sufficient growth units have been incorporated into the kink sites allowing for the formation of step sites, resulting in the formation of sufficient step sites and hence a crystal face, the generation of new kink sites and steps would require a high level of supersaturation. (Vere, 2013)

Crystals grown from solution typically exhibit regular planar facets characterised by their Miller indices. Although appearing flat to the naked eye, these crystalline surfaces are rarely so at the molecular level. Surface roughness provides ample sites for surface integration. Due to these different crystal facets having different surface chemistries, the growth of each of these facets is expected to be different. Generally speaking, faster growing surfaces with smaller relative areas are most likely to be prone to surface roughening and, for example, fast growing needle-shaped crystals may tend to incorporate impurities selectively at their facet ends if the growth process on these interfaces is not carefully enough controlled. (Blacker et al., 2011)

The development of measurement techniques intended to define face specific crystal growth rates, allowed for the establishment of three crystal growth mechanisms to explain these growth rates under differing supersaturation conditions.

1. Screw Dislocation Mechanism (Vere, 2013) (Burton et al, 1951): This mechanism was developed by Burton, Cabrera and Frank (BCF) showing how the emergence of screw dislocations at a crystal surface would act as continuous generators of kink and step sites. This would result in the possibility of continuous growth taking place at much lower supersaturations. The resulting growth rate expression for the BCF mechanism is given by:

$$R_G = A\sigma^2 \tanh\left(\frac{B}{\sigma}\right) \quad (2.7)$$

Where A and B are temperature-dependent constants.

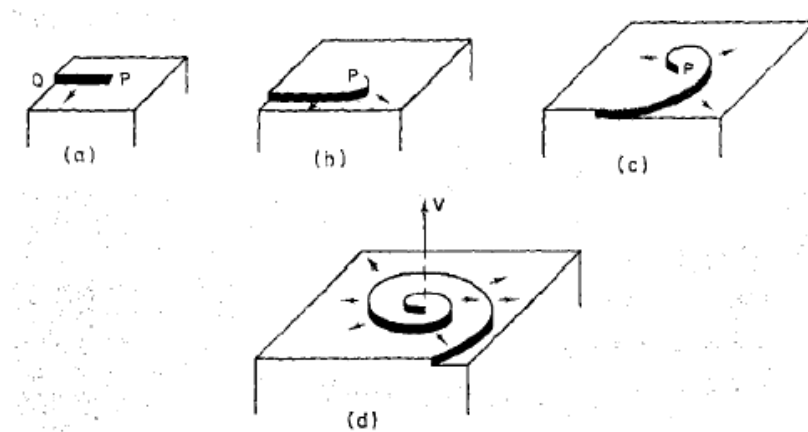


Figure 2.9: A schematic of the Burton, Cabrera and Frank growth mechanism. (Blacker et al., 2011)

2. Birth and Spread Mechanism (Lewis, 2015): The birth and spread (B&S) model is a layer growth model that is also referred to as the two-dimensional nucleation model. The step source is from the formation of two-dimensional nuclei on the crystal surface, which grow into islands by spreading laterally along the crystal surface. An island can either grow and cover the whole surface area before a new island is formed on top of it (also known as the mononuclear model). Or, more realistically, islands can nucleate all over the surface and incorporate the new incomplete layers formed by laterally spreading islands. Two dimensional nucleation can only occur if the supersaturation in solution is sufficient enough to overcome the two dimensional nucleation barrier. This supersaturation generally occurs at a higher supersaturation than that needed for the screw dislocation mechanism. The relationship between growth and supersaturation for the B&S mechanism is given by:

$$R_G = A_1 \sigma^{\frac{5}{6}} \exp\left(\frac{A_2}{\sigma}\right) \quad (2.8)$$



Figure 2.10: A schematic of the birth and spread growth mechanism. (Blacker et al., 2011)

3. Rough Interface Growth Mechanism (Pethrick, 2007; Myerson, 1993): At high supersaturation, the rough interface growth (RIG) mechanism occurs, where the crystal grows without the presence of well-defined surface layers at the

interface. The rough interface is characterised by the presence of numerous step and kink sites. Due to this rough surface, the approaching growth units are provided with numerous binding positions, therefore growth on these surfaces is fast and continuous as every growth unit arriving at the interface immediately finds an integration site. As a result of this, RIG has a linear dependence on supersaturation, defined as:

$$R_G = A\sigma \quad (2.9)$$



Figure 2.11: A schematic of the rough interface growth mechanism. (Blacker et al., 2011)

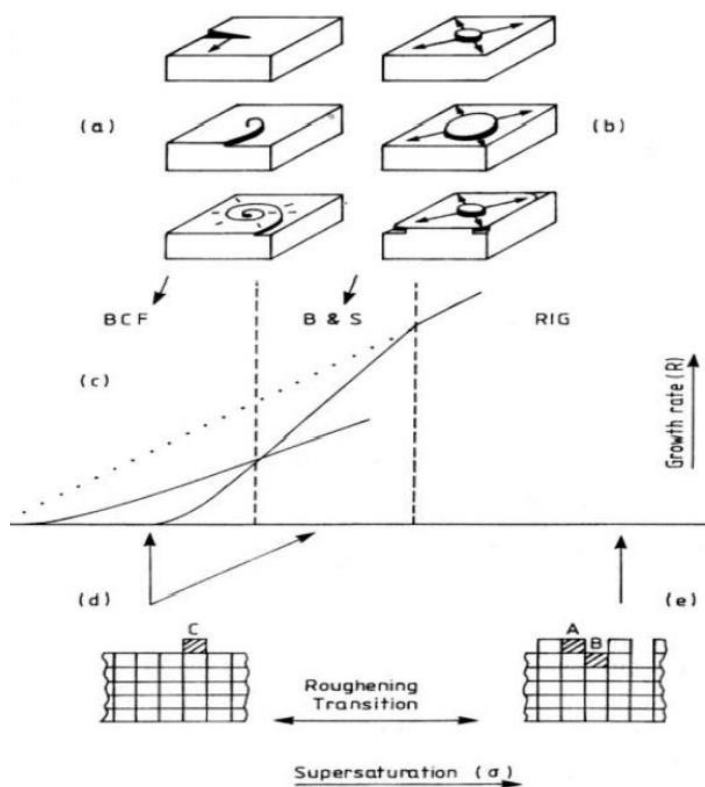


Figure 2.12: A schematic diagram showing the (a) BCF growth mechanism, and (b) B&S growth mechanism and (e) RIG growth mechanism at (c) the expected crystal growth mechanisms as a function of supersaturation. Additionally, (d) the transition between the BCF, B&S and RIG mechanisms are shown. (Blacker et al., 2011)

2.5.5 Dissolution

Dissolution is defined as the “release and diffusion of pharmaceutical molecules from the particle surface into the surrounding fluid medium.” (Hubbard, 2002) Generally, there is no conceptual difference between crystal growth and crystal dissolution in

the crystal-solution system. The two processes are believed to be reverse processes, therefore crystal dissolution can be considered to be crystal growth in an undersaturated solution, with net fluxes of ions or molecules in the opposite direction.

During dissolution, constituent units are more accessible to the solvent molecules, particularly the units at the edges and corners of the crystal. Therefore, the rate of the dissolution process is determined by the transport of molecules away from the crystal surface. The solution is said to be saturated when it contains a solute at the limit of its solubility, considering the conditions of temperature and pressure. The rate at which the drug dissolves from the solid may be used to predict the drug release rate from the therapeutic system. The higher the solubility, the more rapid the rate of dissolution when no chemical reaction is involved. (Hubbard, 2002; Bruschi, 2015)

Dissolution testing is an important analytical tool in drug product development, manufacturing and quality assessment, playing various roles during the life cycle of the dosage form. Objectives of dissolution testing include characterisation and formulation screening of API, establishing an in-vitro in-vivo relationship, and quality control to keep product consistency. (Liu et al., 2013)

Dissolution testing with a demonstrated predictability for in-vivo performance can be used to request a waiver of bioequivalency studies from regulatory authorities, significantly reducing development time and costs by avoiding lengthy and expensive clinical trials. Dissolution tests provide a measure of the extent and rate of drug release from a dosage form into an aqueous medium under a specific set of test conditions. The drug release profile obtained is a result of a combination of properties of API, formulation design, manufacturing process and the chemical and mechanical environment of the test method selected to monitor drug release. (Khadka et al., 2014)

The bioavailability of an orally administered drug depends primarily on its solubility in the gastrointestinal tract and its permeability across cell membranes. This forms the basis for the biopharmaceutical classification system (BCS) outlined in Figure 2.13.

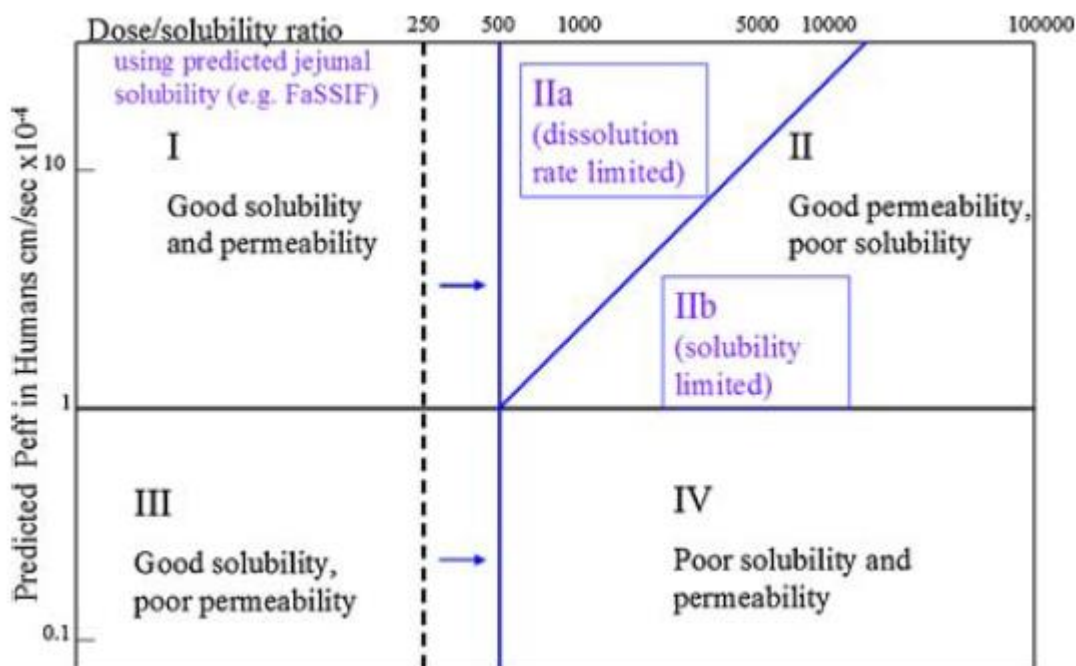


Figure 2.13: The Biopharmaceutical Classification System. (Butler et al., 2010)

The adsorption of drug from the gastrointestinal tract is largely controlled by the dissolution rate and solubility, which determine how fast a drug reaches its maximum concentration in the luminal intestinal fluid, and intestinal permeability, which relates to the rate at which the dissolved drug will cross the intestinal wall to reach the portal blood circulation. (Butler et al., 2010)

In drug discovery, the number of insoluble drug candidates has increased in recent years – poor aqueous solubility and dissolution in gastrointestinal fluids being a limiting factor to in-vivo bioavailability. Therefore, in-vitro dissolution is recognised as very important in drug development. (Khadka et al., 2014)

The dissolution of a solid in a liquid may be regarded as being composed of two consecutive strategies (Aulton, 2013):

1. Interfacial reaction: the liberation of solute molecules from the solid phase to the liquid phase. It involves a phase change so that molecules of solid become molecules of solute in the solvent in which crystals are dissolving.
2. Solute molecules must migrate through the boundary layers surrounding the crystal to the bulk of solution.

Boundary layers are static or slow moving layers of liquid that surround all solid surfaces. Mass transfer takes place more slowly through these static or slow moving

layers that inhibit the movement of solute molecules from the surface of the solid to the bulk solution. During diffusion, the concentration of the solution in the boundary layer changes from being saturated at the crystal surface to being equal to that of the bulk solution at its outermost limit. (Aulton, 2013) Therefore, local concentrations of API's that have low solubility could get close to that of a saturated solution in the region of dissolving particles, resulting in non-sink conditions. In the European Pharmacopoeia, sink conditions are defined as the volume of dissolution medium that is at least 3-10x the saturation volume. (Liu et al., 2013)

The pharmaceutical industry employs the use of mathematical models for the dissolution of immediate-release drugs, however dissolution under non-sink conditions complicates the mathematical derivation. (Qiu et al., 2009)

2.6 Closing Remarks

This chapter presents the fundamental concepts of crystallography and stages of the crystallisation process upon which the basis for this research lies. A summary of important concepts were provided on ideal solubility, nucleation and growth which provide a basis for the research carried out and discussed in Chapter 5. A summary of the dissolution concepts in relation to pharmaceutical compounds, which provide a basis for the research carried out in Chapters 6 and 7. This chapter reviews important aspects in crystal science and engineering such as the importance of polymorphism, size of crystal, and effects of crystallisation conditions.

References

- Aulton, M. E. *Aulton's Pharmaceuticals: The Design and Manufacture of Medicines*. **2013**. Elsevier Health Sciences.
- Bernstein, J., J. M. Bernstein. *Polymorphism in Molecular Crystals*. **2002**. Clarendon Press.
- Blacker, A. J., M. T. Williams. *Pharmaceutical Process Development: Current Chemical and Engineering Challenges*. **2011**. Cambridge: RSC.
- Borchardt-Ott, W. R. O. Gould. *Crystallography: An Introduction*. **2011**. Germany: Springer.
- Bruschi, M. L. *Strategies to Modify the Drug Release from Pharmaceutical Systems*. **2015**. Woodhead Publishing.
- Burton, W. K., N. Cabrera, F. C. Frank. The Growth of Crystals and the Equilibrium Structure of their Surfaces. *Philos. T. R. Soc. A*. **1951**. 243(866), 299-358.
- Butler, J. M., J. B. Dressman. The Developability Classification System: Application of Biopharmaceutics Concepts to Formulation Development. *J. Pharm. Sci.* **2010**. 99(12), 4940-4954.
- Carter, C. B. M. G. Norton. *Ceramic Materials: Science and Engineering*. **2013**. New York: Springer.
- Coulson, J. M., J. F. Richardson, J. H. Harker, J. R. Backhurst. *Coulson and Richardson's Chemical Engineering: Particle Technology and Separation Processes*. **2002**. Butterworth-Heinemann.
- Dhanaraj, G., Byrappa, K., Prasad, V., Dudley, M. *Springer Handbook of Crystal Growth*. **2010**. Springer Science & Business Media.
- Hilfiker, R. *Polymorphism: In the Pharmaceutical Industry*. **2006**. John Wiley & Sons.
- Hubbard, A. T. *Encyclopedia of Surface and Colloid Science (Volume 1)*. **2002**. CRC Press.
- Khadka, P., Ro, J., Kim, H., Kim, I., Kim, J. T., Cho, J. M., Yun, G., Lee, J. Pharmaceutical Particle Technologies: An Approach to Improve Drug Solubility, Dissolution and Bioavailability. *Asian J. Pharm. Sci.* **2014**. 9(6), 304-306.
- Kutty, T. R. N., J A. K. Tareen. *Fundamentals of Crystal Chemistry*. **2001**. University Press.
- Lewis, A., M. Seckler, H. Kramer, G. von Rosmalen. *Industrial Crystallisation: Fundamentals and Applications*. **2015**. UK: Cambridge University Press.

Li, L., Salamonczyk, M., Shadpour, S., Zhu, C., Jakli, A., Hegmann, T. An Unusual Type of Polymorphism in a Liquid Crystal. *Nat. Commun.* **2018**. 9(1), 1-8.

Liu, P., De Wulf, O., Heikkila, T., van Veen, B., Kiesvaara, J., Hirvonen, J., Peltonen, L., Laaksonen, T. Dissolution Studies of Poorly Soluble Drug Nanosuspensions in Non-Sink Conditions. *AAPS Pharm. Sci. Tech.* **2013**. 14(2), 748-756.

Massa, W. *Crystal Structure Determination*. **2000**. New York: Springer.

Moody, B. *Comparative Inorganic Chemistry*. **2013**. Elsevier.

Mullin, J.W. *Crystallisation*. **2001**. Oxford: Butterworth-Heinemann.

Myerson, A. S. *Handbook of Industrial Crystallisation*. **1993**. Boston; London: Butterworth-Heinemann.

Pethrick, R. A. *Polymer Structure Characterisation: From Nano to Macro Organisation*. **2007**. Royal Society of Chemistry.

Qiu, Y., Y. Chen, G. G. Z. Zhang, L. Liu, W. Porter. *Developing Solid Oral Dosage Forms: Pharmaceutical Theory and Practice*. **2009**. Academic Press.

Sands, D. E. *Introduction to Crystallography*. **1969**. New York: W. A. Benjamin.

Tilley, R. J. D. *Understanding Solids: The Science of Materials*. **2013**. UK: Wiley.

Vere, A. W. *Crystal Growth: Principles and Progress*. **2013**. Springer Science & Business Media.

Chapter 3: Theoretical Background of Nucleation, Growth and Dissolution

3.1 Introduction

The physical properties of active pharmaceutical ingredients play a significant role when formulating into drug products. Therefore, a thorough understanding of the nucleation, growth and dissolution processes of active pharmaceutical ingredients are required, in order to understand their behaviour in the differing environments of each process, for example, the effect of super- or undersaturation, solvent and presence of impurity.

This chapter starts with an introduction to classical nucleation theory, and moves onto more modern approaches to studying nucleation and determination of nucleation mechanisms and kinetic parameters. Following on from nucleation, the determination of crystal growth rates have been presented, along with methods used in order to predict growth mechanisms. Additionally, more recent methods used to determine crystal growth kinetics have been presented. Finally, dissolution theories have been presented along with empirical models used to calculate dissolution in varying solution environments.

3.2 Nucleation Theories

3.2.1 Classical Nucleation Theory

The formation of a stable crystal nucleus within a homogeneous fluid is not known with any degree of certainty. This is because not only do the constituent molecules have to coagulate, without re-dissolving, but they also have to become orientated into a fixed lattice. The number of molecules in a stable crystal nucleus can vary from approximately ten to several thousand. If the nucleus grows beyond a certain critical size, it becomes stable under the average conditions, thereby stopping the process of re-dissolving.

The classical theory of nucleation stemming from the works of Gibbs (1948), Volmer (1939), Becker and Doring (1935) is based on the condensation of a vapour to a liquid, and this may be extended to crystallisation from melts and solutions.

The overall excess free energy, ΔG , between a small solid particle of solute (assumed for simplicity to be a sphere of radius 'r') and the solute in solution is equal to the sum of the surface excess free energy, ΔG_s , and the volume excess free energy ΔG_v . Therefore, ΔG_s is defined as the excess free energy between the

surface of the particle and the bulk of the particle, and ΔG_v is defined as the excess free energy between a very large particle and the solute in solution. ΔG_s is a positive quantity, the magnitude of which is proportional to r^2 , and in a supersaturated solution, ΔG_v is a negative quantity proportional to r^3 . (Mullin, 2000)

$$\Delta G = \Delta G_s + \Delta G_v = 4\pi r^2 \gamma_{eff} + \frac{4}{3}\pi r^3 \Delta G_v \quad (3.1)$$

In this equation, ΔG_v is the free energy change of the transformation per unit volume and γ is the interfacial tension, i.e. between the developing crystalline surface and the supersaturated solution in which it is located.

ΔG_s and ΔG_v depend differently on 'r' so the free energy of formation, ΔG , passes through a maximum. This maximum value, ΔG_{crit} , corresponds to the critical nucleus, r_c :

$$\Delta G_{crit} = \frac{16\pi\gamma_{eff}^3}{3(\Delta G_v)^2} = \frac{4\pi\gamma_{eff}r^{*2}}{3} \quad (3.2)$$

The critical size ' r^* ' represents the minimum size of a stable nucleus, therefore, particles smaller than this size will dissolve in order to achieve a reduction in free energy. The nucleation rate, J, is a useful way of expressing the number of nuclei formed per unit time per unit volume:

$$J = A \exp \left[-\frac{16\pi\gamma_{eff}^3 v_0^2}{3k_B^3 T^3 (\ln S)^2} \right] \quad (3.3)$$

In this equation, A is a pre-exponential factor, v_0 is the molecular volume, S is supersaturation, k_B is the Boltzmann constant and T is temperature. This shows that the three main variables governing the rate of nucleation are the temperature, degree of supersaturation and interfacial tension. (Mullin, 2000)

Classical theories of homogeneous nucleation all utilise the concept of a clustering mechanism, however, they do not agree on the effect of supersaturation on the size of a critical nucleus. However, these differences have not been resolved due to the difficulty experienced in attempting to investigate nucleation in an impurity free system, which is practically impossible. (Kashchiev, 2000)

Classical nucleation theory is based on a few major assumptions (Erdemir et al., 2009):

1. Clusters are modelled as spherical droplets having uniform densities. Density is independent of droplet size. For crystallisation from solution, this assumption implies that the building blocks are ordered, therefore molecular arrangement of the nucleus is equal to that of a large crystal.
2. Growth of clusters take place by addition of one monomer at a time. Additionally, clusters are at rest and do not undergo translational, vibrational or rotational motion.
3. Clusters are incompressible and the vapour surrounding them is an ideal gas with a constant pressure. Formation of clusters does not change the vapour state.
4. Nucleation rate is time-dependent, therefore classical nucleation theory is considered in terms of steady-state kinetics i.e. a linear increase of the number of nuclei formed with time.

3.2.2 Two-Step Nucleation

The two-step nucleation theory was first supported by ten Wolde and Frenkel (1997) who reported Monte-Carlo simulations of homogeneous nucleation. They observed the formation of a highly disordered liquid droplet which was then followed by the formation of a crystalline nucleus inside the droplet. As a consequence of this, the nucleation rate was increased by many orders of magnitude.

This theory has been supported by a variety of experimental studies. Dynamic and static light scattering studies in the nucleation of lysozyme crystals showed that monomers rapidly aggregate in the initial stage of the crystallisation process, which progressively restructure into compact structures at later stages of the crystallisation process. (Georgalis et al., 1997) Differential scanning calorimetry analysis of supersaturated lysozyme solution revealed an unstable structure formed just after the preparation of the solution transforms into a more structured aggregate just before the end of the induction period. (Igarashi et al., 2006) Additionally, numerous small-angle scattering studies on the nucleation of proteins also suggest that the first observable nuclei in solution are droplet-like that rearrange to form more compact structures. (Pontoni et al., 2004)

Small-angle X-ray scattering has also been utilised to directly study the nucleation of glycine from aqueous solutions, and results indicated that glycine dimers were

engaged in mass fractal aggregates in supersaturated solutions, which transformed into surface fractal structures prior to nucleation. This transformation was attributed to the organisation of liquid-like clusters into ordered lattice structures. (Chattopadhyay et al., 2005)

3.2.3 Isothermal Analysis

Nucleation kinetics parameters have recently been derived through the use of induction time measurements, by observing crystallisation at a specified temperature and supersaturation. (ter Horst et al., 2011) Induction time is defined as the time taken after supersaturation is reached within a solution and the appearance of crystallites. The appearance of crystallites are usually determined through the turbidity of the solution. This is considered sufficient representation of the determination of the presence of crystallites, however in reality, the initial formation of crystallites will be too small to be detected through this turbidity measurement. Therefore, the occurrence of crystal growth has to take place before turbidity of the solution can be detected.

The existence of this induction time is in disagreement with the assumptions of the classical nucleation theory as mentioned in Section 3.2, steady state kinetics are assumed in classical nucleation theory where the assumption is that nucleation occurs as soon as supersaturation is achieved.

Nucleation kinetics have been assessed various times through isothermal analysis, using a number of organic materials, e.g. butyl paraben (Yang et al., 2013), isonicotinamide (Kulkarni et al., 2013) and para-aminobenzoic acid (Sullivan et al., 2014). Isothermal analysis has been used to determine solvent effect on interfacial tensions, nucleation rates in a solvent, and the relationship between solution chemistry and attachment frequency for the three aforementioned organic materials, respectively.

Induction time measurements as a function of supersaturation can be related through the following expression (Corzo et al., 2014):

$$\ln \tau = \left[\frac{16\pi\gamma_{eff}^3 v_0^2}{3k^3 T^3 (\ln S)^2} \right] - \ln A \quad (3.4)$$

Induction time, τ , in this equation, is therefore inversely proportional to the rate of nucleation. If a spherical critical nucleus is assumed, the critical nucleus radius r^* and number of molecules i^* within the critical nucleus radius can be calculated using the following equations:

$$r^* = \frac{2\gamma_{eff}v_0}{kT \ln S} \quad (3.5)$$

$$i^* = \frac{4\pi(r^*)^3}{3v_0} \quad (3.6)$$

3.2.4 Assessment using Polythermal Methodology

Nucleation kinetics parameters and crystallite growth information have more recently been studied using a polythermal method due to a connection between the metastable zone width and the properties of the crystallite. An approach by Kashchiev-Borissova-Hammond-Roberts (KBHR) allows the determination of nucleation mechanisms within a solution, as well as the kinetics associated with the nucleation process. (Kashchiev et al., 2010; Kashchiev et al., 2010)

The KBHR methodology allows for nucleation kinetics determination through the analysis of MSZW data, by extrapolating the measured T_{diss} values to $0^\circ\text{C}/\text{min}$ cooling rate to determine T_e , the equilibrium temperature. These values can then be used to calculate the critical undercooling (ΔT_c), which allows for the calculation of relative critical undercooling (μ_c).

$$\Delta T_c = T_e - T_c \quad (3.7)$$

Where T_e is the equilibrium temperature and T_c is the temperature of crystallisation. The critical undercooling (ΔT_c) can then be used to calculate the relative critical undercooling (μ_c):

$$\mu_c = \frac{\Delta T_c}{T_e} \quad (3.8)$$

The linear dependence of relative critical undercooling (μ_c) on the cooling rate, q , in \ln - \ln coordinates, and the assessment of the gradient of the slope allows for the establishment of nucleation mechanism – whether progressive or instantaneous. A gradient >3 is indicative of progressive nucleation mechanism, where nuclei are continuously formed in the presence of already growing nuclei, over a longer period of time. A gradient <3 is indicative of the instantaneous nucleation mechanism, where

all nuclei are formed instantaneously at the beginning of the nucleation process, and at any point in time the solution will contain a fixed number of nuclei of the same size, with the assumption that all nuclei will grow at the same rate.

In order to analyse the data further to determine nucleation kinetics, the following inequalities must be met:

$$\mu_c < 0.1 ; a\mu_c < 1 \quad (3.9)$$

Where a can be calculated through the following formula:

$$a = \frac{\lambda}{k_B T_e} \quad (3.10)$$

Where λ is the molecular latent heat of crystallisation and k_B is the Boltzmann constant.

If progressive nucleation is found to be governing the process, the data is further analysed to determine the effective interfacial tension, the critical nucleus radius and the nucleation rate. In order to determine nucleation kinetics for a progressive nucleation mechanism, the dependence of μ_c on q can be described through N_{det} , the number of crystallites at the detection point:

$$\ln(q) = \ln(q_0) + a_1 \ln(\mu_c) - \frac{a_2}{(1-\mu_c)\mu_c^2} \quad (3.11)$$

Where q_0 , a_1 and a_2 are free parameters, and can be found through the following equations:

$$q_0 = \frac{VK_J T_e}{N_{det} 2b} \quad (3.12)$$

Where V is the volume of the solution, and K_J is the nucleation rate constant.

$$a_1 = 3 \quad (3.13)$$

$$a_2 = b = \frac{k_n v_0^2 \gamma_{eff}^3}{k T_e \lambda^2} \quad (3.14)$$

Where k_n is the nucleus shape factor - $16\pi/3$ for spherical nuclei and 32 for cubic nuclei - v_0 is the volume occupied by a solute molecule in the crystal and γ_{eff} is the effective interfacial tension. The nucleation rate, J , can then be calculated through the following equation:

$$J = K_j e^{\frac{-b}{(1-\mu_c)\mu_c^2}} \quad (3.15)$$

Determination of the effective interfacial tension also allows for the calculation of the critical nucleus radius, r^* , and the number of molecules in the critical nucleus, i^* , through the following equations:

$$r^* = \frac{2\gamma_{eff}v_0}{\lambda\mu_c} \quad (3.16)$$

$$i^* = \frac{2bkT_e}{\lambda\mu_c^3} \quad (3.17)$$

If instantaneous nucleation is found to be the nucleation mechanism governing the process, the rate limiting step of the process and the concentration of nuclei can be calculated through further data analysis. In order to determine nucleation kinetics for the instantaneous nucleation mechanism, the dependence of μ_c on q can be found through the following equation:

$$\ln(q) = \ln(q_0) + (n + 1) \ln u_c \quad (3.18)$$

This equation allows for the calculation of the parameter q_0 , which is also related to the concentration of crystallites, C_0 , and the dimensionless relative volume of crystals at the detection point, α_{det} , through the following equation:

$$q_0 = \left[\frac{k_v C_0}{(n+1)^d \alpha_{det}} \right]^{\frac{1}{md}} (a)^n K_G T_e \quad (3.19)$$

Where k_v is the crystallite growth shape factor, $2A_0$, calculated using the cross-sectional area A_0 for needle-like crystals. n and m are crystallite growth exponents which are related to the growth mechanism, where $n=1$ corresponds to growth mediated by the diffusion of solute towards the crystal or across the crystal/solution interface, and $n=2$ corresponds to growth mediated through the presence of screw dislocations in the crystallite. The value of m ranges between 0.5 and 1, where $m=0.5$ corresponds to growth controlled by undisturbed diffusion of the solute to the crystal surface and $m=1$ corresponds to growth controlled by diffusion of the solute through a stagnant layer around the crystallite. The value of d is the dimensionality of crystallites growth which corresponds to 1 for needle-like crystals, 2 for disks or plates or 3 for cubes or spheres. K_G is the overall growth rate of the crystal.

This polythermal approach was recently applied to methyl stearate from kerosene, allowing for the determination of nucleation kinetics parameters such as interfacial tension, which was further validated by the isothermal methodology. (Corzo et al., 2014) Additionally, the method was applied to para-aminobenzoic acid allowing for the determination of interfacial tension in different solvents, as well as determining that a change in the nucleation mechanism takes place with an increase in concentration. (Turner, 2015) Therefore, as a result of this, key kinetic parameters, as well as an insight into the mechanisms related to nucleation and growth of a solute within a solvent can be determined.

3.3 Crystal Growth Rates

Crystals grow by the advance of the individual faces present in the crystal. In general, each face will grow at a different rate and the relative growth rates of different faces determine crystal habit or shape. Faster faces tend to grow out of the crystal and so those faces which govern the morphology, and hence, habit of the crystal are the slower growing faces. Therefore, it is important to define the specific growth rate that is to be measured. The particular growth rate that is most suitable depends on the purpose of experimentation.

Many different experimental techniques have been employed to facilitate crystal growth measurements. The single crystal growth techniques, which can focus on individual face growth rates, are predominantly used for fundamental studies relating to growth mechanisms. Measurements made on populations of crystals are useful for determining overall mass transfer rates under controlled conditions, and for observing size-dependent growth or growth rate dispersion. (Mullin, 2001)

There is no simple or generally accepted method of expressing the growth rate of a crystal, since it has a complex dependence on temperature, supersaturation and agitation. However, for carefully defined conditions, crystal growth rates may be expressed as a mass deposition rate ($\text{kg}\cdot\text{m}^{-2}\cdot\text{s}^{-1}$), a mean linear velocity ($\text{m}\cdot\text{s}^{-1}$), or an overall linear growth rate ($\text{m}\cdot\text{s}^{-1}$).

There are three main ways of expressing the growth rate of a crystal or populations of crystals. (Garside et al., 2002)

1. Face growth rate: This is the velocity of advance of crystallographic faces, and is measured perpendicular to the face. This is the only growth rate that is

directly related to fundamental theories of crystal growth based on mechanistic descriptions of the crystal growth process, mentioned previously in Section 2.5.4. In order to measure this velocity, it is necessary to observe and measure individual faces of a crystal.

- Overall mass growth rate: This is best expressed as the total mass flux to the crystal surface, R_G ($\text{kg}\cdot\text{m}^{-2}\cdot\text{s}^{-1}$) and is averaged over the whole crystal. For a crystal of mass M_C and surface area A_C , the total mass flux is given by:

$$R_G = \frac{1}{A_C} \cdot \frac{dM_C}{dt} \quad (3.20)$$

If faceted growth rates (V_{hkl}) and areas (A_{hkl}) of all faces of a crystal are known R_G can also be expressed as a summation of all the faces present.

$$R_G = \frac{\rho_C}{A_C} \sum V_{hkl} A_{hkl} \quad (3.21)$$

Overall mass growth rate is particularly valuable for yield calculations and design purposes, particularly batch systems.

- Overall linear growth rate (G) is defined as the rate of change of a characteristic dimension (L) of the crystal and has dimensions of velocity:

$$G = \frac{dL}{dt} \quad (3.22)$$

The value of 'G' depends on the specific characteristic dimension and it is important to define this dimension. 'G' and ' R_G ' can be related as follows:

$$R_G = \frac{3\alpha}{\beta} \cdot \rho_C \cdot G \quad (3.23)$$

Where α is the volume shape factor and β is the crystal surface shape factor. For spheres and cubes $\beta/\alpha = 6$.

The overall linear growth rate is widely used in population balance theory and therefore in design procedures for continuous crystallisers.

3.4 Prediction of Crystal Growth Mechanisms

A surface entropy factor was used by Jackson in order to characterise the crystal surface or interface structure at the molecular level. This surface entropy factor can be used to predict the growth mechanism of a crystal facet. (Elwenspoek, 1986; Jackson, 1958; Jackson et al., 1958; Jackson, 1967; Bennema et al., 1977)

$$\alpha = \xi \frac{L_1}{RT} = \xi \frac{\Delta H}{RT} = \xi \frac{\Delta S}{R} \quad (3.24)$$

In this equation, L_1 is the molar heat of fusion for the melt growth calculation, and in the case of crystal growth from solution, L must be replaced by enthalpy of dissolution. ξ is the surface entropy factor and $\xi = E_{sl}/E_{cr}$ with E_{sl} being the total energy in the slice of the crystal face and E_{cr} being the total crystallisation energy. ΔH is the enthalpy of the phase transition and ΔS is the entropy of phase transition.

Values of α have been predicted for specific systems, thereby making it possible to define the growth mechanisms by which the system under consideration will grow. This has led to a simplification of the expression, resulting in (Davey, 1986):

$$\alpha = \xi \left(\frac{\Delta H_f}{RT} - \ln X_{eq} \right) \quad (3.25)$$

In this equation, ΔH_f is the heat of fusion and X_{eq} is the mole fraction of the solute calculated for the supersaturation that growth occurs, for a given solvent and temperature, T .

Larger values of α correspond to a smoother crystal surface, therefore as α increases the growth process changes from a continuous process to a layer mechanism. As the strength of interactions between solute and solvent increase, resulting in an increase in solubility, this results in a decrease in α -factor. Therefore, an acceleration in growth would be expected, resulting in rough interface growth.

Estimates have been made based on Monte Carlo simulations of α values at which changes in growth mechanism occur. These show that if α is less than approximately 3, the interface is rough and continuous growth occurs, while values greater than approximately 4 correspond to substantially smooth interfaces and layer growth mechanisms. (Bennema et al., 1973) According to Davey (1982), the growth mechanism predicted by values of α are presented in Table 3.1.

Table 3.1: Growth mechanism predicted by values of α .

α -Factor Range	Predicted Growth Mechanism
$\alpha < 2$	The interface is rough and all growth units can be incorporated onto the growing surface. This corresponds to rough interface growth (RIG)
$2 < \alpha < 5$	The interface is smoother, and the most probable mode of growth is B&S.
$\alpha > 5$	The surface becomes very smooth, and generally proceeds by screw dislocation. This corresponds to BCF growth.

3.5 Crystal Growth Theories

There are two main crystal growth theories, based on surface energy and diffusion.

3.5.1 Surface Energy

Surface energy theories are based on the assumption that the shape of a crystal is dictated by the minimum surface energy, i.e. the growth of a crystal in a supersaturated medium develops an “equilibrium” ensuring that the whole crystal has a minimum total surface free energy. Therefore, as crystal growth takes place, it maintains its morphology. (Dhanaraj et al., 2010)

However, there is no general acceptance of surface energy theories of crystal growth, due to the failure to explain the well-known effects of supersaturation and solution on crystal growth rates of faces, which, in practice, results in smaller faster-growing faces being eliminated from the morphology of the crystal.

3.5.2 Diffusion Theory

The origin of diffusion theories dates back to the work of Noyes and Whitney in 1897, who considered that the deposition of solid on the face of a growing crystal was a diffusion-controlled process. They also assumed that the dissolution process was the reverse of the crystallisation process, and that crystallisation and dissolution rates were governed by a concentration gradient between the solid surface and the bulk of the solution.

A considerable modification was made to the diffusion theory of crystal growth by Berthoud (1912) and Valetton (1924) who suggested there are two steps in the mass deposition process (Murthy, 1994):

1. Solute molecules are transported from the bulk of the fluid phase to the solid surface.
2. Solute molecules arrange themselves into the crystal lattice.

A further modification was made to this theory by Camacho (2017) who made an analogy of these two steps to a circuit, stating that as these two effects act consecutively, they must share this driving force, therefore the effect with the larger resistance will be rate-determining. This allowed for the growth rate of a crystal face with time (G) to be expressed as:

$$G = \frac{1}{\frac{1}{k'_{MT}} + \frac{1}{R}} \sigma \quad (3.26)$$

In this equation R is the crystal growth rate, σ^s is the solution's relative supersaturation at the interface, and k'_{MT} is related to the coefficient of mass transfer within the bulk of solution, k_{MT} , through the following equation:

$$k'_{MT} = \frac{k_{MT} C_e MW_s}{\rho_s} \quad (3.27)$$

Where C_e is the solubility equilibrium concentration, MW_s is the molecular weight of the solute, and ρ_s is the density of the solute.

Specific models describing the kinetics on the crystal surface can be inserted into equation (3.26) as 'R' would depend on the mechanism with which the growth units will be attached to the crystal surface. This results in the following power-law, B&S and BCF equations, respectively:

$$G = \frac{1}{\frac{1}{k'_{MT}} + \frac{1}{k_G(\sigma)^{r-1}}} \sigma \quad (3.28)$$

Where G (m/s) is the dependence of growth rate on the supersaturation, σ ; k_G is the growth rate constant, and r is a growth exponent which is considered a good approximation for the BCF growth mechanism when $1 < r < 2$.

$$G = \frac{1}{\frac{1}{k'_{MT}} + \frac{1}{k_G(\sigma)^{-\frac{1}{6}} \exp\left(\frac{A_1}{\sigma}\right)}} (\sigma) \quad (3.29)$$

$$G = \frac{1}{\frac{1}{k_{MT}} + \frac{1}{k_G(\sigma) \tanh\left(\frac{A_2}{\sigma}\right)}} (\sigma) \quad (3.30)$$

Where A_1 and A_2 are thermodynamic parameters.

3.6 Techniques for Studying Crystal Growth

There are a number of techniques that have been previously employed in order to study crystal growth rates. The most common techniques are focussed beam reflectance measurement (FBRM), atomic force microscopy (AFM) and optical light microscopy techniques. These techniques have been discussed in more detail, as different techniques are used in order for different applications.

3.6.1 FBRM

Focused beam reflectance measurement measures a chord length distribution (CLD) which is a function of the number, size and shape of particles under investigation. FBRM uses a focused beam of laser light, which rotates at high speed and propagates into the particle suspension to be measured. As this light scans across a particle or particle structure passing in front of the probe window, light is scattered in all directions. The light scattered back towards the probe is used to measure a chord length of the given particle. The length of the scanned chord is determined in the electronics of the system, and transferred into a chord length distribution histogram. Thus, the chord length distribution provides online particle count and particle dimension information. (Worlitschek, 2005)

Typically, many thousands of chords are measured per second, providing a robust measurement that is sensitive to the change in size or number of particles under investigation. Unlike, for example, optical turbidity or laser diffraction, FBRM does not depend on the presence of a threshold nuclei concentration before a nucleation event is detected – as soon as one particle is in the detectable size range, it will be detected. (Barrett and Glennon, 2002)

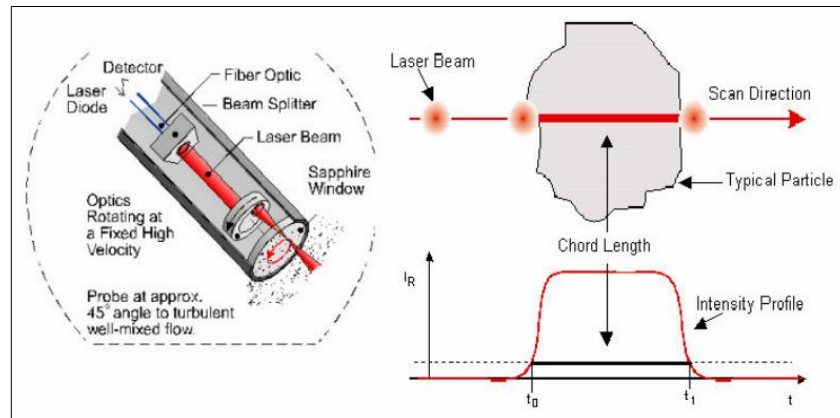


Figure 3.1: FBRM probe tip (left) and chord measurement (right). (Worlitschek and de Buhr, 2005)

FBRM integrated with ATR-FTIR can provide a real-time measurement of dimension and the number of crystals for the nucleation rate and crystal growth rate measurements as a function of supersaturation. Additionally, it can be used for determining growth kinetics and growth mechanisms. For example, Markande et al. (2009) used FBRM and an in-line process refractometer for monitoring aqueous crystallisation of dextrose monohydrate to evaluate the kinetic constants from the growth and nucleation as a function of supersaturation.

Although FBRM is a commonly used technique for determining the crystal growth and particle size, it does not provide any information on the shape of the crystal.

3.6.2 AFM

Binnig and Rohrer shared the Nobel Prize for inventing a scanning tunnelling microscope and discovered that it can image individual surface atoms with unprecedented resolution. This led to the invention of other similar microscopes, resulting in the atomic force microscope being one of the most successful of these new devices.

The concept of using a force to image a surface can be applied to both magnetic and electrostatic forces, as well as interatomic interactions between the tip of the microscope and the sample. Regardless of the origin of the force, all force microscopes have the same five essential components:

1. A sharp tip mounted on a soft cantilever spring.
2. A way of sensing the cantilever's direction.

3. A feedback system to monitor and control the deflection, and hence, the interaction force as a result.
4. A mechanical scanning system that moves the sample with respect to the tip.
5. A display system that converts the measured data into an image.

AFM has been applied in studying the growth of crystals in solution, where data can be recorded as a topological image and presented in various ways. AFM has successfully been used to investigate the crystallisation of proteins, barium nitrate, calcite and viruses. (Rugar et al., 1990)

3.6.3 Optical Microscopy

Optical microscopes, often referred to as light optical microscope is a type of microscope that uses visible light and a system of lenses to magnify images of small samples. Optical microscopes are the oldest design of microscope and were possibly designed in the 17th century. Historically, optical microscopes were easy to develop and are popular because they use visible light, so samples may be directly observed by eye. Digital microscopes that use charge-coupled device (CCD) cameras to examine a sample, show the resulting image directly on a computer screen, negating the need for eyepieces. (Gianfrancesco, 2016)

Optical microscopy employs a series of objective lenses and a visible light to magnify the images of a sample. Microscopy techniques equipped with a video camera and commercial image capturing and analysis software has been employed numerous times to measure in situ the velocity of the moving step and the growth rate of individual faces during the growth process.

For example, Davey et al. (1976) studied the effect of supersaturation on the growth of the (100) face of ammonium dihydrogen phosphate, and the growth kinetics of the (001) and (100) face of urea in two cases in 1974: pure solution and with the presence of biuret as an impurity. More recently, Nguyen et al. (2014) employed optical microscopy to study the effects of solvents on the crystal morphology and growth mechanisms of ibuprofen. Finally, as well as being used for the study of crystal growth, Pickering et al. utilised optical microscopy to study the face specific dissolution rates of the dominant (001) and (011) faces of ibuprofen in ethanol.

Therefore, optical light microscopy has been successfully employed for the study of the dissolution process of single crystals, as well as the crystallisation process, particularly with a focus on the morphologically significant facets of single crystals.

3.7 Dissolution Models

Dissolution models are designed to predict bioperformance of active pharmaceutical ingredients based on in-vitro information. In order to do this, a number of general assumptions have been made.

1. All particles are spherical.
2. Surfaces of particles have a homogeneous dissolution rate.
3. The driving force for dissolution is directly proportional to the level of undersaturation in the solution.

However, in practice, dissolution varies on a face specific basis and characterisation is required of specific edges of each individual particle, resulting in a more complex mass transfer process. Current dissolution models are divided into two categories depending on how they incorporate mass transfer:

1. Models which envisage a boundary layer with a purely diffusion-controlled rate-limiting process operating across a boundary layer and into the bulk solution.
2. Models which envisage surface renewal or disruption of the solid/solution interface due to hydrodynamic processes occurring in the solution.

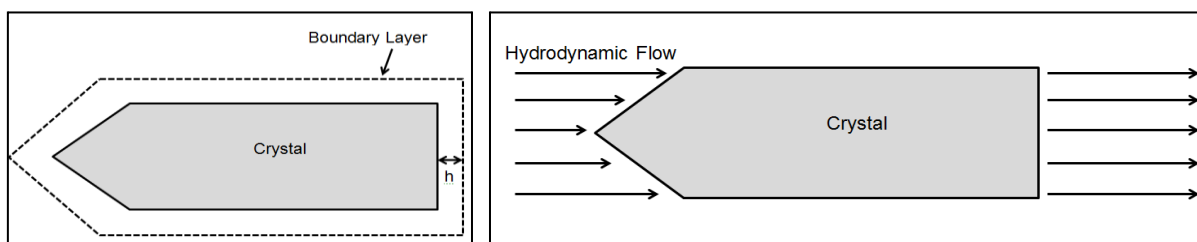


Figure 3.2: A schematic showing how the two categories of dissolution models incorporate mass transfer.

Due to conditions of the single crystal experimental dissolution process which has been studied for this research, where dissolution occurs in a stagnant solution, diffusion-controlled mass transfer models have been focussed on, spanning from the

first established model by Noyes and Whitney (1897) to more modern derivations of this model.

3.7.1 Noyes-Whitney

The Noyes-Whitney equation was derived based on Fick's first law of diffusion, which directly correlates flux with the concentration gradient, and can be expressed as (Fick, 1855; Krishna et al., 2008; Seipmann et al., 2013):

$$J_M = -D \cdot \frac{dc}{dx_d} \quad (3.31)$$

In this equation, J_M is the mass flux, D is the diffusion coefficient, and dc/dx is the change in concentration over the diffusion layer ' x_d '. The negative sign in this equation indicates a decrease in concentration. This equation can also be expressed as a rate of mass transfer (dM/dt):

$$\frac{dM}{dt} = -D \cdot A_c \cdot \frac{dc}{dx} \quad (3.32)$$

In this equation, A_c is the surface area of the dissolving particle.

Noyes and Whitney determined there was a directly proportional relationship between the rate at which a solute dissolves in solution and the difference between the solubility of the substance and the bulk concentration:

$$\frac{dC}{dt} = k_p (C_s - C_t) \quad (3.33)$$

In this equation, dC/dt is the dissolution rate, k_p is a proportionality constant, c_s is the solubility of the substance and c_t is the bulk concentration.

Nernst and Brunner further modified the Noyes-Whitney equation, adding a boundary layer thickness between the dissolving particle and the bulk of the solution, h , giving the following expression:

$$\frac{dM}{dt} = \frac{D \cdot A_c}{h} (C_s - C_t) \quad (3.34)$$

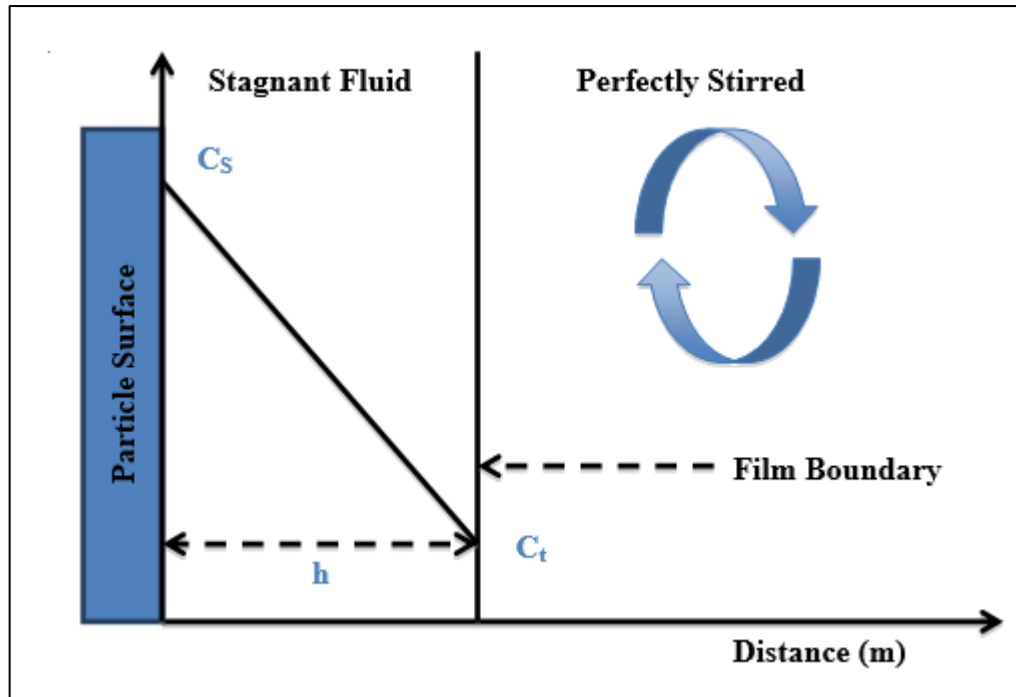


Figure 3.3: A representation of the Nernst-Brunner model (Krishna et al., 2008)

According to the Stokes-Einstein equation, the diffusion coefficient is related to the viscosity of the solvent, μ , through the following equation (Einstein, 1905; Higuchi and Hiestand, 1963):

$$D = \frac{k_B \cdot T}{6\pi\mu r_H} \quad (3.35)$$

Where k_B is the Boltzmann constant, T is temperature, and r_H is the molecular radius of the solute.

3.7.2 Hixson-Crowell

Following on from the derivation from Nernst-Brunner, in 1931, Hixson and Crowell investigated the dependency of the rate of dissolution on surface area and concentration. They identified that agitation, surface area and concentration are the major determining factors in the rate of dissolution. As a result, Hixson and Crowell derived what is more commonly known as the 'cube root law' which can be expressed as:

$$M_t^{1/3} = M_0^{1/3} - k_{1/3}t \quad (3.36)$$

In this equation, $M_t^{1/3}$ is the mass of solute at any time 't', $M_0^{1/3}$ is the initial mass of solute and $k_{1/3}$ is the cube root dissolution constant.

Hixson and Crowell made the following assumptions for this derivation.

1. The dissolving particles are spherical in nature and the shape does not change over time.
2. The solution is agitated and faces of the crystal/particle are subject to the same amount of agitation.
3. The difference in dissolution rates between the crystal faces was considered negligible.

Building on the work carried out by Hixson and Crowell, Higuchi and Hiestand (1963), and Niebergall and Goyan (1963) also derived 'root models', however unlike Hixson-Crowell, they both defined a boundary layer thickness, albeit in different ways. Higuchi and Hiestand considered the boundary layer thickness to be equal to or greater than the particle radius, whereas Niebergall and Goyan assumed the boundary layer thickness to be directly proportional to the square root of the diameter of the particle.

Due to the system being agitated in these models, and on the basis of the dissolution process being under sink conditions, for the purposes of this study these models were not considered for the calculation of the dissolution rate.

3.7.3 Hintz-Johnson

In 1989, Hintz and Johnson described the derivation and utilisation of a dissolution rate model for polydisperse powders under non-sink conditions. In this derivation, they used a Noyes-Whitney type expression and defined the surface area, assuming that the particles were monodisperse spheres, as:

$$A_C = 4\pi r_t^2 N_0 \quad (3.37)$$

In this equation, r_t is the radius at any time, 't', and N_0 is the number of particles present initially.

In order to calculate the Noyes-Whitney equation, a calculated diffusion layer thickness was determined by intrinsic dissolution studies of a drug from a compressed disk. Based on these results, Hintz and Johnson defined the boundary layer thickness as being equal to the particle radius up to the point the particle radius becomes 30 μ m. For particles with radii larger than 30 μ m, the boundary layer thickness was considered to remain a constantly value of 30 μ m.

In 1999, Wang and Flanagan followed on from this derivation, however they stated that the boundary layer thickness did not vary with particle size but remained constant. However, as Wang and Flanagan considered dissolution under sink conditions, their derivation was not considered relevant to this study.

3.7.4 Model Selection

The limitation with all of the models mentioned previously is that they consider a spherical particle shape, however most API's are expected to be anisotropic. Dali and Carstensen (1995) studied the effect of change in the shape factor of "real" crystals using a model geometry of a parallelepiped in non-sink conditions. In order to determine the surface area, they proposed the following expression:

$$A_C = \Gamma \cdot V^{\frac{2}{3}} \quad (3.38)$$

Where Γ is the shape factor.

Therefore, for this study, the Noyes-Whitney and Hinz-Johnson model assumptions were determined to be the most relevant and hence were calculated to determine the predicted mass loss of a single crystal. However, rather than calculate the surface area based on spherical assumptions, in order to gain a more realistic prediction, the Dali and Carstensen equation was incorporated into the model calculations.

Another major limitation of all models discussed, is their inconsistency in the treatment of the boundary layer thickness between the particle surface and the bulk of the solution. Some models envisage a boundary layer that is a function of the particle size, others envisage a boundary layer which is a fixed width. This disagreement between models has been explored to determine the characterisation of a boundary layer, and values which allow for the consistent prediction of the mass loss of a single crystal.

3.8 Choice of Crystallisation System

The following section will focus on molecules that this research is based on, urea and paracetamol. This will provide the background knowledge on the molecules and an introduction to the crystal chemistry.

3.8.1 Urea

Urea is a commodity chemical which is mainly used in the fertiliser and plastics industries on account of its high nitrogen content. However, smaller quantities are also used to make polyurethanes, pharmaceuticals, toothpaste and cosmetics. Most commonly within the pharmaceutical industry, it is used for dermatological purposes, as it contains proteolytic properties which can disrupt protein connections between corneocytes and effect a breaking down of amino acids. Urea can also act as a humectant and can improve barrier function. Urea is employed most frequently for a wide range of conditions ranging from keratosis pilaris to hyperkeratosis and callosities to xerosis. It can also be used for the treatment of infections, particularly infected wounds and ulcers, ears and tooth sockets. (Parish and Parish, 2009)

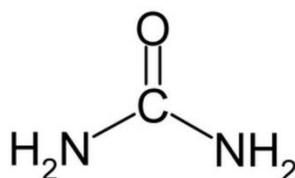


Figure 3.4: The molecular structure of urea

Urea has a number of polymorphs and up to five have been reported. The most stable form at ambient conditions is form I, which has a tetragonal structure and a space group of $P4_21m$, and has been extensively studied. Two other forms exist at higher pressures, forms III and IV, which have orthorhombic structures with space group $P2_12_12_1$. Another high pressure polymorph, form V, has been found. The full list of urea polymorphs together with unit cell parameters and references (where available) have been provided in Table 3.2.

Table 3.2: Urea polymorphs with unit cell parameters.

Ref Code	Polymorph	a	b	c	α	β	γ	Z	Space group	Reference
UREAXX	I	5.66	5.66	4.72	90	90	90	2	$P4_21m$	Sklar et al. (1961)
UREAXX32	III	3.62	8.27	8.84	90	90	90	4	$P2_12_12_1$	(Roszak et al., 2017)
UREAXX32	IV	3.41	7.36	4.65	90	90	90	2	$P2_12_12_1$	
-	V	-	-	-	-	-	-	4	$Pm\bar{c}n$	

The crystal habit of urea, when grown from pure solutions, is as long needles with

varying length: breadth ratios ranging from 10:1 to 50:1. Crystals of urea exhibit three dominant morphological faces – {110}, {111} and {001}, which in turn affect the crystal habit of urea depending on crystallisation conditions. Urea crystals mostly have a needle-like morphology dominated by the {110} face, with smaller {111} and {001} capped faces. The {001} face can also be morphologically insignificant when crystallised under certain conditions. Biuret is a known decomposition impurity of urea that acts as a crystal habit modifier. (Davey et al., 1986; Piana and Gale, 2005)

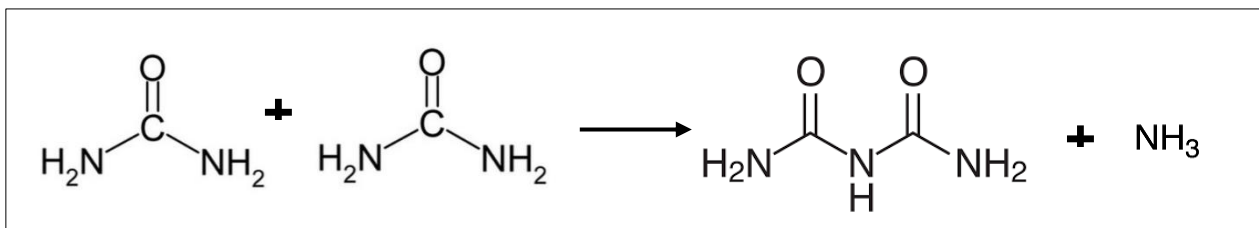


Figure 3.5: The decomposition process of urea to form biuret.

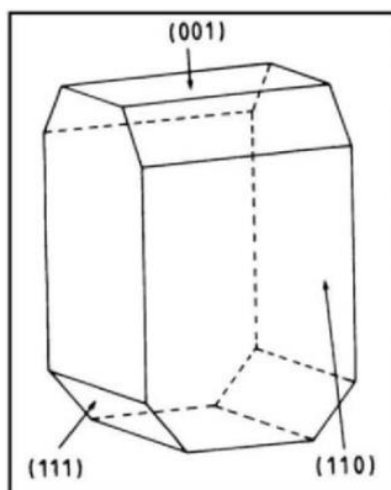


Figure 3.6: The crystal morphology and habit of urea. (Docherty et al., 1993)

Crystals of urea exhibit different morphologies depending on both the nature of the solvent and the presence of additives. Urea crystals grown from water present the well-known needle shape, which exposes the {001} and {110} faces. Crystals grown from methanol exhibit the {110} and {111} faces, causing the crystal morphology to have sharp tips, instead of flat tips, however in ethanol crystal morphologies are generally shorter showing morphologies in the {110} and {111} faces, and less so with {001} face. Adding an additive, such as biuret which selectively binds to faces of urea, results in a considerably larger number of crystal habits. (Salvalaglio et al., 2012)

As a result of this, urea was considered to be the ideal molecule to study before expanding research into a pharmaceutical molecule, paracetamol.

3.8.2 Paracetamol

Paracetamol is a molecular organic compound and was launched as a drug product in 1956. It has grown to become the most widely accepted over the counter analgesic and antipyretic in the world. It is commonly used for the relief of headaches and other minor aches and pains. It is a major ingredient in numerous cold and flu remedies, and it is also used as an intermediate in the manufacture of azo dyes and photographic materials. (Wang, 2011)

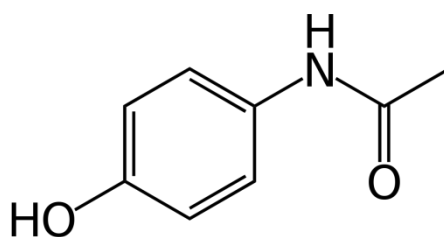


Figure 3.7: The molecular structure of paracetamol

Paracetamol is known to have three polymorphs, a stable form I which has a monoclinic structure, a metastable form II which has an orthorhombic structure, and an unstable form III, which also has an orthorhombic structure. The most stable polymorphs, form I and II, can be obtained easily and their crystal structures are well-known. Crystals of the orthorhombic, less stable, room temperature form III are difficult to grow and need a special recipe to crystallise. The full list of paracetamol polymorphs together with unit cell parameters and references has been provided in Table 3.3.

Table 3.3: Paracetamol polymorphs with unit cell parameters.

Ref Code	Polymorph	a	b	c	α	β	γ	Z	Space group	Reference
HXACAN01	I	12.93	9.40	7.10	90	115.9	90	4	P2 ₁ /a	(Haisa et al., 1976)
HXACAN	II	11.81	17.16	7.39	90	90	90	8	Pcab	(Haisa et al., 1974)
HXACAN40	III	11.84	8.57	14.82	90	90	90	8	Pca2	(Reiss et al., 2017)

Previous studies show morphological variations of monoclinic Paracetamol. These studies show a possible temperature dependence on the growth kinetics, a slight solvent effect and a prominent supersaturation dependence on the morphology of monoclinic Paracetamol. Predictions of Paracetamol morphology show the formation of a prismatic morphology, where $\{100\}$, $\{001\}$, $\{110\}$, $\{011\}$ and $\{201\}$ faces show approximately equivalent morphological importance. (Sudha et al., 2014)

However, although all of the aforementioned faces are observed experimentally, real crystals show a $\{110\}$ dominance at low supersaturations, giving way to an increasing $\{001\}$ dominance as supersaturation is increased. This change is also accompanied by a change of habit, from columnar to plate-like. The morphology of paracetamol crystals grown from water in comparison with organic solvents is also different as crystals grown in water have a columnar morphology a dominant $\{110\}$ face, however crystals grown in organic solvents show $\{001\}$ as the dominant face, and have a more prismatic morphology.

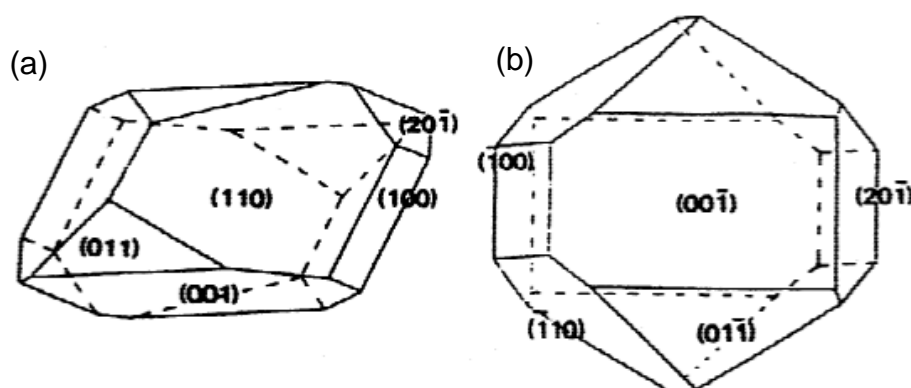


Figure 3.8: The crystal morphology of paracetamol at (a) lower supersaturation and (b) higher supersaturation. (Finnie et al., 2001; Prasad et al., 2001)

Paracetamol was considered a model pharmaceutical compound to study in this research, as it does not have many polymorphic forms, the morphology has been extensively studied, and it is classed as a BCS Class I compound, i.e. highly soluble and highly permeable. (Dressman et al., 2001)

3.9 Closing Remarks

This chapter reviews and outlines the many methods that can be used to determine nucleation, growth and dissolution. The use of optical microscopy techniques, along with methods used to calculate growth and dissolution kinetics have been discussed

in detail in this chapter, which have been used in this EngD research. This EngD study was focussed on the nucleation and hence crystallisation of urea. This makes up a proportion of the subject of this EngD thesis, along with a focus on the dissolution of urea and paracetamol. The experimental and computational work carried out in detail for this research, which has a fundamental basis in this chapter, has been presented in Chapter 4.

References

- Barrett, P., B. Glennon. Characterising the Metastable Zone Width and Solubility Curve Using Lasentec FBRM and PVM. *Chem. Eng. Res. Des.* **2002**. 80(7), pp799-805.
- Becker, R., W. Doring. Kinetische Behandlung der Keimbildung in übersättigten Dämpfen. *Annalen der Physik.* **1935**. 24, 719-752.
- Bennema, P., G. Gilmer, P. Hartman. Crystal Growth: An Introduction. *North-Holland, Amsterdam.* **1973**. 78(11), 1276.
- Bennema, P., J. P. van der Eerden. Crystal Growth from Solution: Development in Computer Simulation. *J. Cryst. Growth.* **1977**. 42(0), 201-213.
- Berthoud, A. *J. Chem. Phys.* **1912**. 10, 624.
- Binnig, G., H. Rohrer, C. Gerber, E. Weibel. 7x7 Reconstruction on Si(111) Resolved in Real Space. *Phys. Rev. Lett.* **1983**. 50(2), 120-123.
- Camacho, D. M.; Roberts, K. J.; Muller, F.; Thomas, D.; More, I.; Lewtas, K. Morphology and Growth of Methyl Stearate as a Function of Crystallisation Environment. *Cryst. Growth Des.* **2017**. 17 (2), 563-575.
- Chattopadhyay, S., D. Erdemir, J. M. B. Evans, J. Ilavsky, H. Amenitsch, C. U. Segre, A.S. Myerson. SAXS Study of the Nucleation of Glycine Crystals from a Supersaturated Solution. *Cryst. Growth Des.* **2005**. 5(2), 523-527.
- Corzo, D. M. C.; Borissova, A.; Hammond, R. B.; Kashchiev, D.; Roberts, K. J.; Lewtas, K.; More, I. Nucleation Mechanism and Kinetics from the Analysis of Polythermal Crystallisation Data: Methyl Stearate from Kerosene Solutions. *CrystEngComm.* **2014**. 16(6), 974-991.
- Dali, M. V., J. T. Carstensen. Effect of Change in Shape Factor of a Single Crystal on Its Dissolution Behaviour. *Pharm. Res.* **1995**. 13 (1), 155-162.
- Davey, R. and J. Mullin, Growth of the {100} faces of ammonium dihydrogen phosphate crystals in the presence of ionic species. *J. Cryst. Growth.*, **1974**. 26(1): p. 45-51.
- Davey, R. The Role of the Solvent in Crystal Growth from Solution. *J. Cryst. Growth.* **1986**. 76(3), 637-644.
- Davey, R., S. J. Jancic (Ed), E. J. de Jong (Ed). The Role of Additives in Precipitation Processes. *Industrial Crystallisation 81.* **1982**. North-Holland Publishing Co.
- Davey, R., W. Fila, and J. Garside, The influence of biuret on the growth kinetics of urea crystals from aqueous solutions. *J. Cryst. Growth.*, **1986**. 79(1): p. 607-613. 7.

Dhanaraj, G., Byrappa, K., Prasad, V., Dudley, M. *Springer Handbook of Crystal Growth*. **2010**. Springer Science & Business Media.

Docherty, R., K. J. Roberts, V. Saunders, S. Black, R. J. Davey. Theoretical Analysis of the Polar Morphology and Absolute Polarity of Crystalline Urea. *Faraday Discuss.* **1993**. 95

Dressman, J., J. Butler, J. Hempenstall, C. Reppas. The BCS: Where do we go from here? *Pharmaceutical Technology*. **2001**. 68-76.

Einstein, A. On the Movement of Small Particles Suspended in Stationary Liquids Required by Molecular-Kinetic Theory of Heat. *Annalen der Physik*. **1905**. 17, 549-560.

Elwenspoek, M. Comment on the α -factor of Jackson for Crystal Growth from Solution. *J. Cryst. Growth*. **1986**. 78(2), 353-356.

Fick, A. On Liquid Diffusion. *Philosophical Magazine – Series 4*. **1855**. 10(63), 30-39.

Finnie, S., K. V. R. Prasad, D. B. Sheen, J. N. Sherwood. Microhardness and Dislocation Identification Studies on Paracetamol. *Pharmaceutical Research*. **2001**. 18(5), 674-681.

Garside, J., A. Mersmann, J. Nyvlt. *Measurement of Crystal Growth and Nucleation Rates*. **2002**. IChemE – Technology & Engineering.

Georgalis, Y., P. Umbach., J. Raptis, W. Saenger. Lysozyme Aggregation Studied by Light Scattering. I. Influence of Concentration and Nature of Electrolytes. *Acta Crystallogr., Sect. D: Biol. Crystallogr.* **1997**. 53, 691–702.

Gianfrancesco, A. D. *Materials for Ultra-Supercritical and Advanced Ultra-Supercritical Power Plants*. **2016**. Woodhead Publishing.

Gibbs, J. W. *Collected Works, Volume 1: Thermodynamics*. **1948**. Yale University Press: New Haven.

Haisa, M., S. Kashino, H. Maeda. The Orthorhombic Form of p-Hydroxyacetanilide. *Acta Cryst.* **1974**. 2510-2512.

Haisa, M., S. Kashino, R. Kawai, H. Maeda. The Monoclinic Form of p-Hydroxyacetanilide. *Acta Cryst.* **1976**. 1283-1285.

Higuchi, W.I., E. N. Hiestand, Dissolution Rates of Finely Divided Drug Powders II. *J. Pharm. Sci.* **1963**. 52 (2), 162-164.

Hintz, R. J., K. C. Johnson. The Effect of Particle Size Distribution on Dissolution Rate and Oral Absorption. *Int. J. Pharm.* **1989**. 51(1), 9-17.

Hixson, A.W., J. H, Crowell. Dependence of Reaction Velocity upon Surface and Agitation I – Theoretical Consideration. *Ind. Eng. Chem. Res.* **1931**. 23(8), 923 – 931.

Igarashi, K., M. Azuma, J. Kato, H. Ioshima. The Initial Stage of Crystallization of Lysozyme: A Differential Scanning Calorimetric (DSC) Study. *J. Cryst. Growth*. **2006**. 204, 181–200.

Jackson, K. A. *Liquid Metals and Solidification*. **1958**. American Society for Metals, Cleveland, OH.

Jackson, K. A., H. S. Peiser (Ed). *Crystal Growth*. **1967**. Pergamon, Oxford.

Jackson, K. A., R. H. Doremus (Ed), B. W. Roberts (Ed), D. Turnbull (Ed). *Growth and Perfection of Crystals*. **1958**. Wiley-New York.

Kashchiev, D.; Borissov, A.; Hammond, R. B.; Roberts, K. J. Effect of Cooling Rate on the Critical Undercooling for Crystallisation. *J. Cryst. Growth*. **2010**. 312 (5), 698-704.

Kashchiev, D.; Borissova, A.; Hammond, R. B.; Roberts, K. J. Dependence of the Critical Undercooling for Crystallisation on the Cooling Rate. *J. Phys. Chem*. **2010**. 114 (16), 5441-5446.

Krishna, R., L. Yu. *Biopharmaceutics Applications in Drug Development*. **2008**. Springer.

Kulkarni, S. A., S. S. Kadam, H. Meekes, A. I. Stankiewicz, J. H. ter Horst. Crystal Nucleation Kinetics from Induction Times and Metastable Zone Widths. *Cryst. Growth Des*. **2013**. 13(6), 2435-2440.

Markande, A., A. Nezzal, J. Fitzpatrick, L. Aerts. Investigation of the Crystallisation Kinetics of Dextrose Monohydrate using in-situ Particle Size and Supersaturation Monitoring. *Particul. Sci. Technol*. **2009**. 27(4), 373-388.

Mullin, J.W. *Crystallisation*. **2001**. Oxford: Butterworth-Heinemann.

Murthy, M. S. Theory of Crystal Growth in Phase Transformations: Precipitation of Barium Sulphate. *Chem. Eng. Sci*. **1994**. 49(14), 2389-2393.

Nguyen, T. T. H.; Hammond, R. B.; Roberts, K. J.; Marziano, I.; Nichols, G. Precision Measurement of the Growth Rate and Mechanism of Ibuprofen {001} and {011} as a Function of Crystallisation Environment. *CrystEngComm*. **2014**. 16, 4568-4586.

Niebergall, P. J., G. Milosovich, J. E. Goyan. Dissolution Rate Studies II. Dissolution of Particles Under Conditions of Rapid Agitation. *J. Pharm. Sci*. **1963**. 52(3), 236-241.

Noyes, A. A., W. R. Whitney. The Rate of Solution of Solid Substances in their Own Solutions. *J. Am. Chem. Soc*. **1897**. 19(12), 930-934.

Parish, J., L. Parish. The Use of Urea in Contemporary Dermatology. *J. Am. Acad. Dermatol*. **2009**. 60(3).

Piana, S., J. D. Gale. Understanding the Barriers to Crystal Growth: Dynamical Simulation of the Dissolution and Growth of Urea from Aqueous Solution. *J. Am. Chem. Soc.* **2005**. 127(6), 1975-1982.

Pickering, J., Kathyola, T., Nguyen, T. H., Ramachandran, V., Soufian, M., Hammond, R. B., Roberts, K. J., Pencheva, K., Ticehurst, M. A Comparative Study of the Experimental and Theoretical Dissolution Kinetics of Ibuprofen in Ethanol. (Submitted *J. Pharm. Sci.*)

Pontoni, D., T. Narayanan, A. R. Rennie. Nucleation and Growth Kinetics of Colloidal Silica. *Prog. Colloid Polym. Sci.* **2004**. 123, 227–230.

Prasad, K. V. R., D. B. Sheen, J. N. Sherwood. Fracture Property Studied of Paracetamol Single Crystals Using Microindentation Techniques. *Pharm. Res.* **2001**. 18(6), 867-872.

Reiss, C. A., J. B. van Mechelen, K. Goubitz, R. Peschar. Reassessment of Paracetamol Orthorhombic Form III and Determination of a Novel Low-Temperature Monoclinic Form III-m from Powder Diffraction Data. *Acta Cryst.* **2018**. 392-399.

Rozak, K., A. Katrusiak. Giant Anomalous Strain between High-Pressure Phases and the Mesomers of Urea. *J. Phys. Chem.* **2017**. 121(1), 778-784.

Rugar, D., P. Hansma. Atomic Force Microscopy. *Phys. Today.* **1990**. 23-30.

Salvalaglio, M., T. Vetter, F. Giberti, M. Mazzotti, M. Parrinello. Uncovering Molecular Details of Urea Crystal Growth in the Presence of Additives. *J. Am. Chem. Soc.* **2012**. 134(41), 17221-17233.

Seipmann, J., F. Seipmann. Mathematical Modelling of Drug Dissolution. *Int. J. Pharm.* **2013**. 453(1), 12-24.

Sklar, N., M. E. Senko, B. Post. Thermal Effects in Urea: the Crystal Structure at -140°C and at Room Temperature. *Acta Cryst.* **1961**. 14, 716-720.

Sudha, C., K. Srinivasan. Understanding the Effect of Solvent Polarity on the Habit Modification of Monoclinic Paracetamol in terms of Molecular Recognition at the Solvent Crystal Interface. *Cryst. Res. Technol.* **2014**. 49(11), 865-872.

Sullivan, R. A., R. J. Davey, G. Sadiq, G. Dent, K. R. Back, J. H. ter Horst, D. Toroz, R. B. Hammond. Revealing the Roles of Desolvation and Molecular Self-Assembly in Crystal Nucleation from Solution: Benzoic and p-Aminobenzoic Acids. *Cryst. Growth Des.* **2014**. 14(5), 2689-2696.

ten Wolde, P. R.; D. Frenkel. Enhancement of Protein Crystal Nucleation by Critical Density Fluctuations. *Science.* **1997**. 277, 1975–1978.

ter Horst, J. H., S. Jiang. Crystal Nucleation Rates from Probability Distributions of Induction Times. *Cryst. Growth Des.* **2011**. 11(1), 256-261.

Turner, T. D. Molecular Self-Assembly, Nucleation Kinetics and Cluster Formation Associated with Solution Crystallisation. **2015**. PhD Thesis. University of Leeds.

Valeton, J. J. P. *Wachstum and Auflosung der kristalle*. **1923**.

Volmer, M. Kinetic der Phasenbildung, Steinkopff, Leipzig. **1939**.

Wang, I. C., M. J. Lee, D. Y. Seo, H. E. Lee, Y. Choi, W. S. Kim, C. S. Kim, M. Y. Jeong, G. J. Choi. Polymorph Transformation in Paracetamol Monitored by in-line NIR Spectroscopy During a Cooling Crystallisation Process. *AAPS Pharm. Sci. Tech.* **2011**. 12(2), 764-770.

Wang, J., D. R. Flanagan. General Solution for Diffusion-Controlled Dissolution of Spherical Particles. 1. Theory. *J. Pharm. Sci.* **1999**. 88 (7), 731-738.

Worlitschek, J., J. de Buhr (Mettler Toledo). *Crystallisation Studies with Focussed Beam Reflectance Measurement and MultiMax*. **2005**.

Yang, H., C. Rasmuson. Nucleation of Butyl Paraben in Different Solvent. *Cryst. Growth Des.* **2013**. 13(10),4226-4238.

Chapter 4: Materials and Methods

4.1 Introduction

This chapter describes the materials used in this study along with the modelling and experimental methodologies employed to deliver the aims and objectives of this work. An overview of the materials used for experimentation has been presented, followed by the molecular modelling and experimental methodologies. These include the determination of interaction energies, solubility determination, polythermal nucleation kinetics studies, measurement of face specific growth mechanism and kinetics, measurement of face specific dissolution, and the calculation of dissolution models.

4.2 Materials

4.2.1 Supplied Materials

Urea was obtained from Acros Organics (purity = 99%, melting point 131-135°C), and Acetaminophen was obtained from Sigma Aldrich (98-102% assay, melting point 168-172°C). Both materials were used as supplied. The solvents used for this study were ethanol (absolute) supplied by Fisher Scientific UK and acetonitrile (>95%) supplied by Fisher Scientific UK. Sterilised, deionised water was supplied by the Pfizer laboratory.

4.2.2 Preparation of FeSSIF

Fed State Simulated Intestinal Fluid was prepared for single crystal dissolution experimentation. For this, acetic acid (glacial) was obtained from Sigma Aldrich, sodium hydroxide pellets ($\geq 97\%$) were obtained from Sigma Aldrich, sodium chloride (99.5-100.5%) was obtained from Sigma Aldrich, and SIF powder composed of sodium taurocholate (70.3-77.7%) and soybean lecithin (24.8-27.4%), was obtained from biorelevant.com. In order to prepare blank FeSSIF and FeSSIF media, the following recipe was used (Biorelevant, 2019):

4.04g of sodium hydroxide pellets, 11.874g of sodium chloride and 8.65g of glacial acetic acid, were added to 0.9L of sterilised, deionised water in a stirred beaker at room temperature and left to dissolve. The pH of this solution was then checked using a pH metre to ensure that a pH of 5 has been obtained. 100mL of sterilised water was then added to the solution and stirred for the preparation of 1L of blank

FeSSIF. Blank FeSSIF had an expiration of one month at room temperature, up to 37°C.

To prepare FeSSIF media, 50mL of blank FeSSIF was added to stirred beaker at room temperature. 1.12g of SIF powder was added to the beaker and left for the contents to dissolve. 50mL of blank FeSSIF was then added to this solution and stirred for the preparation of FeSSIF media. FeSSIF media had an expiration of 48 hours at room temperature or up to 37°C.

4.3 Experimental Methodology

4.3.1 Solubility Determination

To estimate solubility behaviour in an ideal solution, the van't Hoff relationship was used outlined previously in equations (2.1) – (2.3).

4.3.2 Polythermal Crystallisation

4.3.2.1 Instrumentation

Experiments were carried out in a Technobis (2019) Crystal 16 unit. The unit consists of multiple reactors in a 4x4 orientation, allowing for 16 vials holding 1mL solution. Vials are separated into 4 blocks, which can be heated and cooled separately through the combination of Peltier heated aluminium blocks and a water bath heating and cooling system. The 4 blocks can be individually programmed to follow a particular temperature profile, and each vial was magnetically stirred using stirrer bars. MSZW data was collected through the changes in solution turbidity as a function of temperature and cooling rate.

4.3.2.2 Sample Preparation

Two sets of samples of urea in absolute ethanol were prepared at 0.40g, 0.46g, 0.50g, 0.58g and 0.66g per 10mL at a 1mL scale, with 0.0040g, 0.0046g, 0.0050g, 0.0058g, and 0.0066g of biuret (1%w/w) added to one set of samples. Both urea and biuret were weighed into crystal 16 vials using a balance accurate to 5 decimal places, and 1mL of absolute ethanol was added after weighing to form solutions.

4.3.2.3 Methodology and Data Analysis

Both sets of solutions were heated and cooled according to a programmable cycle from -5°C - 60°C . The rates of heating and cooling applied to the solution were 0.5, 1, 2 and $5^{\circ}\text{C}/\text{min}$, with the solutions being constantly stirred at 700rpm using magnetic stirrers. The solutions were held at the maximum and minimum temperature for an hour in order to ensure homogeneity of the solution, and this temperature cycle was repeated four times to obtain average values for the crystallisation and dissolution temperatures, T_{cryst} and T_{diss} respectively.

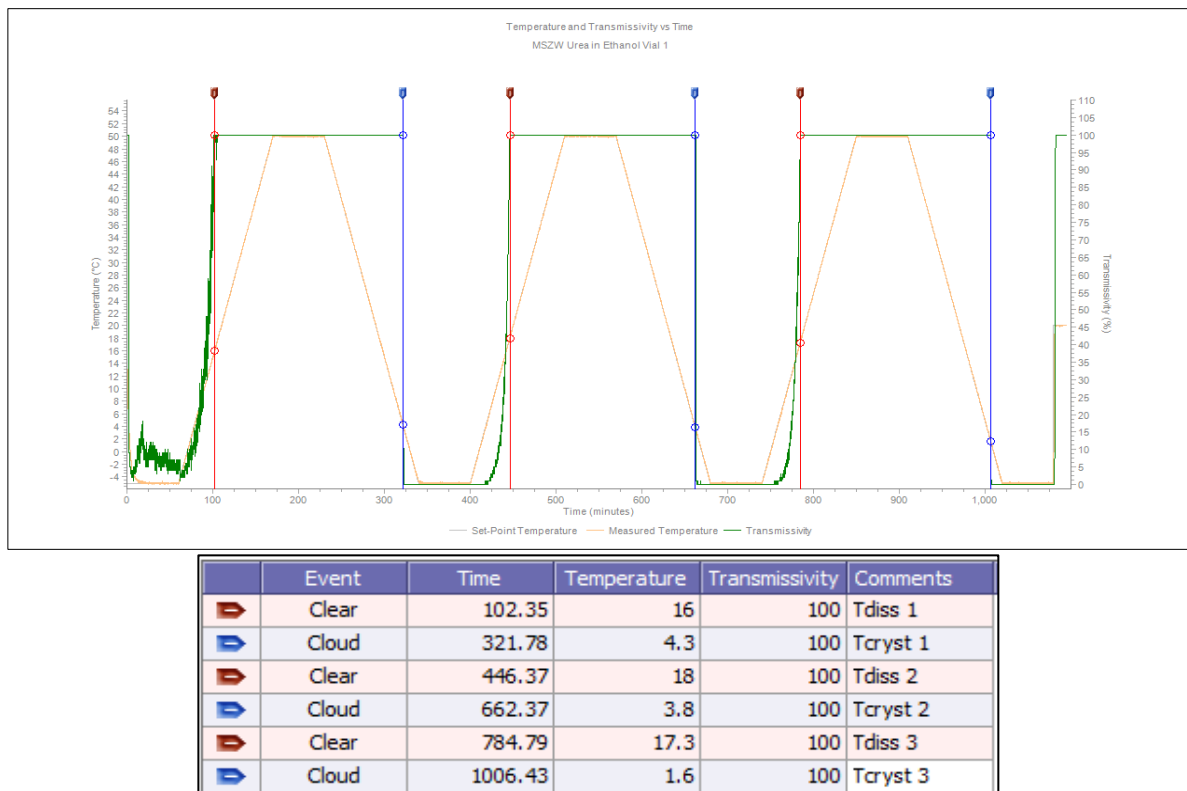


Figure 4.1: An example of the temperature profile and crystallisation and dissolution temperatures ($^{\circ}\text{C}$) obtained, with respect to time (minutes).

T_{diss} was determined through the turbidity profile of the solution, when transmittance through the solution reached 100%. Similarly, T_{cryst} was also determined through the turbidity profile when the transmittance dropped from 100%, indicating the appearance of crystals in the solution. Values of T_{cryst} and T_{diss} were then plotted as a function of cooling rate, and fitted to a linear trend to allow for the determination of the equilibrium MSZW, through the extrapolation of the linear trend to a cooling rate

of 0°C/min. The equilibrium MSZW was then calculated as the difference between T_{diss} and T_{cryst} at the infinitely slow cooling rate.

4.3.3 Single Crystal Growth and Dissolution

4.3.3.1 Instrumentation

Growth and dissolution rates were measured at a 0.5mL scale size as a function of supersaturation and undersaturation, respectively. This was carried out through the use of a Zeiss (2019) Axiovert 100 inverted optical microscope integrated with a Lumenera (2019) Infinity 3 digital camera. This was connected to a PC with Infinity Analyze software allowing for image capture and analysis during the growth and dissolution process. Crystals were grown or dissolved in 0.5mL UV cuvette cell, which was immersed in a shallow cell of water (Turner, 2019), the temperature of which was controlled by a Huber (2019) Ministat 240 fitted with a CC3 controller.

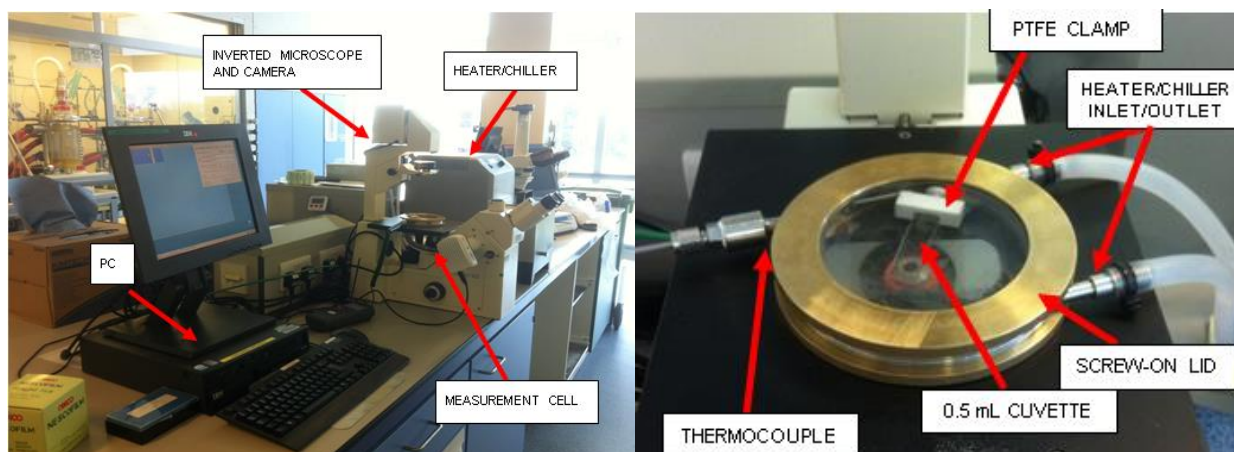


Figure 4.2: The instrumentation used for single crystal growth and dissolution experiments.

4.3.3.2 Crystal Growth Sample Preparation

Two samples of urea in absolute ethanol were prepared by weighing 1g of solute using a balance accurate to 5 decimal places. 1%w/w biuret (0.01g) was added to one sample, and both samples were dissolved in 20mL of absolute ethanol to form solutions.

4.3.3.3 Single Crystal Growth Rate Methodology and Data Analysis

The pure solution containing urea in ethanol was heated to 60°C using a stirrer plate and magnetic stirrer to ensure homogeneity and that urea had completely dissolved

in the solvent. The solution was then transferred to the 0.5mL UV cuvette cell using a pipette, and the cuvette was then sealed using Nescofilm and fixed to the bottom of the measurement cell using a PTFE clamp to ensure the cuvette didn't move within the cell when images were being taken during the growth process. Water was circulated around the measurement cell at constant temperatures of 18, 20, 21, 23, 25 and 27°C in order to maintain a specific level of supersaturation within the cell. The growth process at each temperature was repeated five times, in order to obtain average values for the growth rate of a single crystal at a particular supersaturation. Infinity Analyze software was used to capture a sequence of images of the growing single crystals at specified time points (from 40 seconds to 4 minutes) depending on the level of supersaturation. This methodology was repeated for the solution containing biuret.

The growth rates of the $\{110\}$ and $\{111\}$ faces were measured as centre to face distances, perpendicular to the edge of the crystal face being measured. Facet identification of these faces was determined by comparing the experimental morphology obtained with Figure 3.6. This distance was then plotted as a function of time to determine the growth rate for each individual face. The mean growth rate, along with the standard deviation, was then calculated from the five single crystals analysed at one supersaturation.

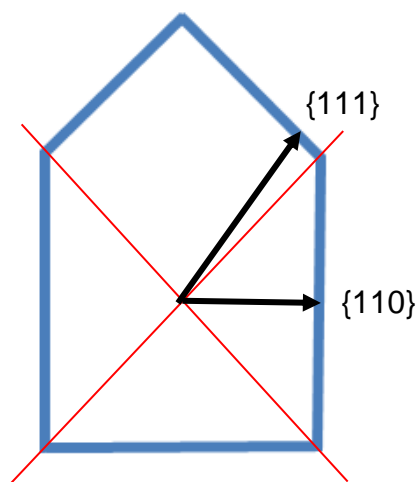


Figure 4.3: A schematic showing centre-to-face measurements to determine growth rates.

4.3.3.4 Single Crystal Dissolution Sample Preparation

A sample of urea in absolute ethanol was prepared by weighing 1.25g of solute using a balance accurate to 5 decimal places. This was then dissolved in 25mL of absolute ethanol to form a solution. A sample of urea in acetonitrile was prepared by weighing

0.145g of solute and dissolving it in 25mL of acetonitrile to form a solution. A sample of paracetamol in acetonitrile was prepared by weighing 0.52g of solute and dissolving it in 20mL of acetonitrile to form a solution. A sample of paracetamol in water was prepared by dissolving 0.348g of solute and dissolving it in 20mL of water.

4.3.3.5 Single Crystal Dissolution Rate Methodology and Data Analysis

The solution containing urea in ethanol was heated to 60°C using a stirrer plate and magnetic stirrer to ensure homogeneity and that urea had completely dissolved in the solvent. The solution was then transferred to the 0.5mL UV cuvette cell using a pipette, and the cuvette was sealed using Nescofilm. The solution was allowed to cool naturally to ambient temperature to induce nucleation and left for 3 hours to allow crystals to grow. Once crystals had formed inside the cuvette, it was fixed to the bottom of the measurement cell using a PTFE clamp to ensure the cuvette didn't move within the cell when images were being taken during the dissolution process. Water was circulated around the measurement cell at constant temperatures of 31, 33, 35, 36, 38, 39, 41, 42, 43 and 45°C in order to maintain a specific level of undersaturation within the cell. The dissolution process at each temperature was repeated five times in order to obtain average values for the dissolution rate of a single crystal at a particular undersaturation.

In order to grow crystals of urea in acetonitrile, the aforementioned process was repeated. However, to maintain the desired level of undersaturation for urea in acetonitrile within the cuvette, water was circulated around the measurement cell at constant temperatures of 32, 34, 36, 38, 40, 41, 43, 44, 46 and 48°C. The dissolution process at each temperature was repeated five times to obtain average values for the dissolution rate of a single crystal of urea in acetonitrile at a particular undersaturation.

Similarly, paracetamol crystals were grown in acetonitrile using the same process and in order to maintain the desired level of undersaturation for paracetamol in acetonitrile within the cuvette, water was circulated around the measurement cell at constant temperatures of 32, 34, 36, 37 and 39°C. The dissolution process at each temperature was repeated five times to obtain average values for the dissolution rate of a single crystal of paracetamol in acetonitrile at each undersaturation.

For the dissolution of paracetamol single crystals in FeSSIF, firstly paracetamol crystals were grown in water using the same process, however rather than leaving the solution of paracetamol in water to grow for 3 hours, it was found that after 3 hours very little growth occurred, therefore the solution was left overnight in the cuvette to allow the single crystals to grow to an appropriate size. Water was then removed from the cuvette, ensuring that the crystals stayed within the cuvette, and was replaced with FeSSIF media and re-sealed using Nescofilm. The cuvette was then placed inside the measurement cell and water was circulated through to ensure constant temperatures of 30, 33, 37 and 40°C. These temperatures are within the minimum and maximum viable temperatures for the use of FeSSIF media.

The dissolution rates of the faces under consideration were measured as centre to face distances, perpendicular to the edge of the crystal face being measured. Facet identification for paracetamol was determined by comparing experimental morphologies obtained with Figure 3.8. This distance was then plotted as a function of time to determine the dissolution rate for each individual face. The mean dissolution rate was then calculated from the five crystals analysed at one undersaturation or temperature.

In order to determine the surface area of a crystal for calculation of the dissolution models, the flat surface of the crystal was divided into irregular polygons. Through the use of Heron's formula, the surface area of the crystal could be determined. (Hammond et al., 2006)

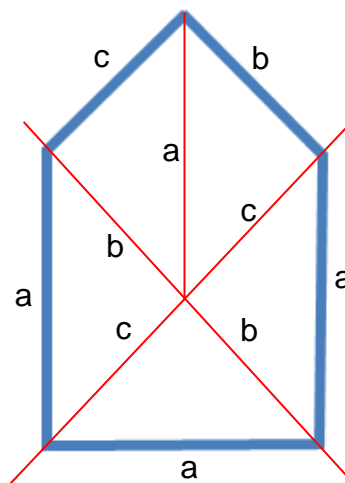


Figure 4.4: A schematic showing how the crystal was divided, allowing for the calculation of Heron's formula.

$$p = \frac{a+b+c}{2} \quad (4.4)$$

$$A_c = \sqrt{p(p-a)(p-b)(p-c)} \quad (4.5)$$

Where a, b and c are the sides of the triangle and p is its semi-perimeter.

4.3.4 Noyes-Whitney and Hintz-Johnson Model Calculations

The Noyes-Whitney equation that was calculated is outlined below (Fick, 1855; Krishna et al., 2008; Seipmann et al., 2013):

$$\frac{dm}{dt} = \frac{A_c D}{h} (C_s - C_t) \quad (4.6)$$

$$D = \frac{k_B T}{6\pi\mu r_H} \quad (4.7)$$

In order to determine the mass loss calculated by the Noyes-Whitney dissolution model, first the surface area of the initial single crystal was determined through the use of Heron's formula, outlined in Section 4.3.3. Additionally, the average morphology ratio of the {110} and {111} face was determined for the initial single crystal. This ratio was input into VisualHabit (Pickering et al., 2017), and used to determine the shape factor of the crystal. The volume of the initial single crystal could then be calculated using the following formula:

$$Volume = \left(\frac{A_c}{\Gamma}\right)^{\frac{3}{2}} \quad (4.8)$$

The diffusion coefficient was then calculated, where viscosity of the solution was assumed to be the same as that of the solvent, therefore the viscosities of ethanol, acetonitrile and water was obtained from literature. An assumption was made that the viscosity of FeSSIF was the same as that of water, as water was the majority component of FeSSIF. Viscosities were obtained from Anton-Paar (2019).

The radius of the solute molecule was calculated through the unit cell parameters of the molecule (Sklar et al., 1961), where the assumption was made that the molecule was spherical. Therefore, in order to calculate the radius of urea, the following method was used:

$$a = 5.662\text{\AA}$$

$$b = 5.662\text{\AA}$$

$$c = 4.716\text{\AA}$$

molecules per unit cell = 2

volume of one molecule = $(5.662 \times 5.662 \times 4.716) / 2 = 75.6 \text{ \AA}^3$

Assuming that the molecule is spherical:

$$75.6 = \frac{4}{3}\pi r^3$$

$$r_H = 2.62 \text{ \AA}$$

The boundary layer thickness was assumed to be between 1%-50% of the volume equivalent diameter, therefore the Noyes-Whitney equation was calculated at regular intervals between these values, firstly with a boundary layer thickness 50% of the volume equivalent diameter and then with boundary layer thicknesses which were 25%, 10% and 1% of the volume equivalent diameter. The volume equivalent diameter was calculated using the following formula:

$$D_{volume} = \left(\frac{6}{\pi} V_{particle} \right)^{\frac{1}{3}} \quad (4.9)$$

4.4 Computational Methodology

Computational methodologies were applied in order to analyse the interactions between urea and biuret, paracetamol, and the solvents used for growth and dissolution experiments.

4.4.1 Geometry Optimisation

Before interactions between molecules can be determined, the geometries of the molecules under consideration have to be optimised, meaning an arrangement has to be found whereby the forces existing between atoms are acceptably close to zero. Therefore, the molecular structure for an isolated urea molecule was downloaded from the Cambridge Crystallographic Data Centre [CCDC] (2019) database (Refcode: UREAXX) and imported into Materials Studio (Version 7.0). (Biovia, 2019)

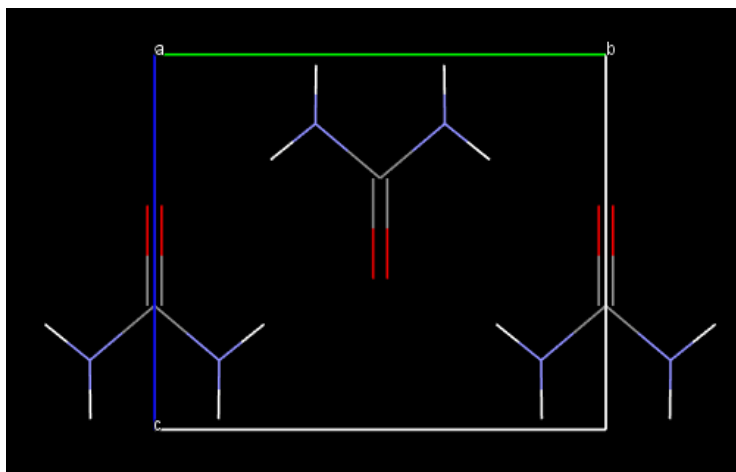


Figure 4.5: The unit cell of urea

Bonding between the atoms was calculated and the unit cell was rebuilt. Various combinations of forcefields were selected in order to determine the optimum geometry, as outlined in Table 4.1:

Table 4.1: The force fields used to determine the optimised geometry.

Force field	Charges	Summation Method	
		Electrostatic	Van der Waals
COMPASS	Force field Assigned	Ewald	Atom Based
COMPASS II	Force field Assigned	Ewald	Atom Based
pcff	Force field Assigned	Ewald	Atom Based
Dreiding	QEq	Ewald	Atom Based
Dreiding	Gasteiger	Ewald	Atom Based

The geometry is considered optimised when the density change of the unit cell is within 10% and the change in cell parameters is within 5%. Additionally, automatic parameters should not have been used in order to carry out the geometry optimisation calculations. This process was repeated for paracetamol using the CCDC Refcode: HXACAN01.

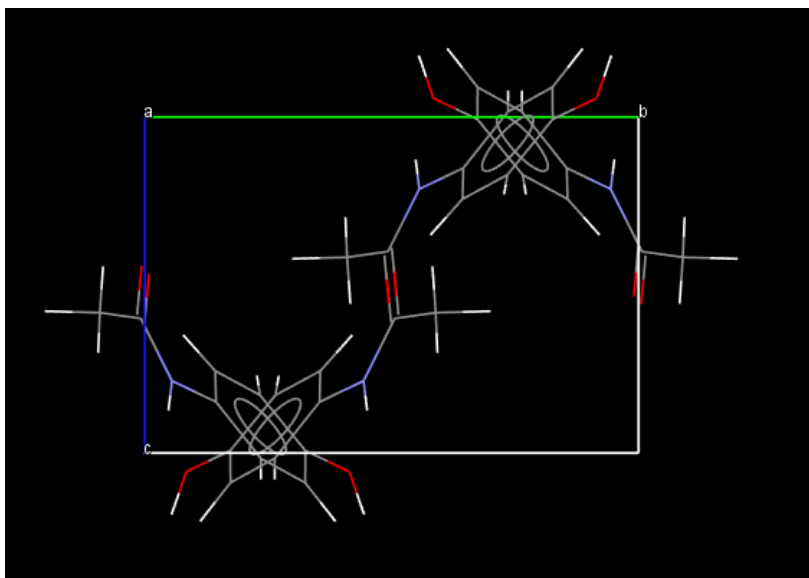


Figure 4.6: The unit cell of paracetamol

4.4.2 COSMOthermX

COSMOthermX (Cosmologic, 2019) was implemented to calculate the wetting energies of surfaces under consideration for urea with respect to the solvents used, allowing for the determination of the ability of the solvent to maintain contact with the solid surface.

After geometry optimisation has been carried out, the surface for which wetting energies are to be calculated is specified in a new atomistic file, and built under a vacuum slab. The surface is then further optimised using GGA-PBE functional calculations developed by Perdew, Burke and Enzerhorf (1996), and DNP basis set in DMol3 (Delley, 2000). These calculations generated the optimised surface to be exported to the COSMOthermX software package, and the “Conductor-Like Screening Model” (Klamt et al., 1993) was used to calculate the wetting energy of surfaces of urea with ethanol and acetonitrile.

4.4.3 VisualHabit Systsearch

Systematic surface search in the Mercury VisualHabit software package (Pickering et al., 2017) was used to calculate the interaction energies between a probe molecule and the crystal surface. These interaction energies are determined through the placement of a probe in a grid on or above the surface of the crystal. A .cif file was imported into VisualHabit and the morphology calculated using BFDH (Bravais (1866), Friedel (1907), Donnay and Harker (1937)) prediction.

The predicted faces were then selected in the VisualHabit software package, in order to carry out the systematic search. The solvent probe was selected to determine the interaction of the solvent probe with the selected surface of the crystal. The probe was rotated through a series of rotational spaces of Euler angles to allow for the determination of the interaction energy, and this was depicted through a series of grid points. The placement of the grid points were defined as 15 in the 'X' direction, 5 in the 'Y' direction and 5 in the 'Z' direction. The interaction energies were calculated using the Dreiding atomic force field calculated using the Gasteiger method.

(Pickering et al., 2017) (Gasteiger and Marsili, 1978) (Gasteiger and Marsili, 1980) This force field allowed for the separation of interactions into hydrogen bonding, dispersive van der Waals, and electrostatic interactions.

The grid through which calculations were carried out was specified to cover one unit cell, however the surface itself was built of multiple unit cells in order to minimise edge effects. A minimum interaction energy was defined as -2 kcal/mol to discard interactions which can be considered negligible. Coloured tetrahedrons in the grid are defined as having interaction energies greater than the defined value, and white tetrahedrons are defined as the probe having a negligible interaction with the surface. This grid was found to be acceptable when the grid rows closest and furthest away from the surfaces both contained white tetrahedrons only.

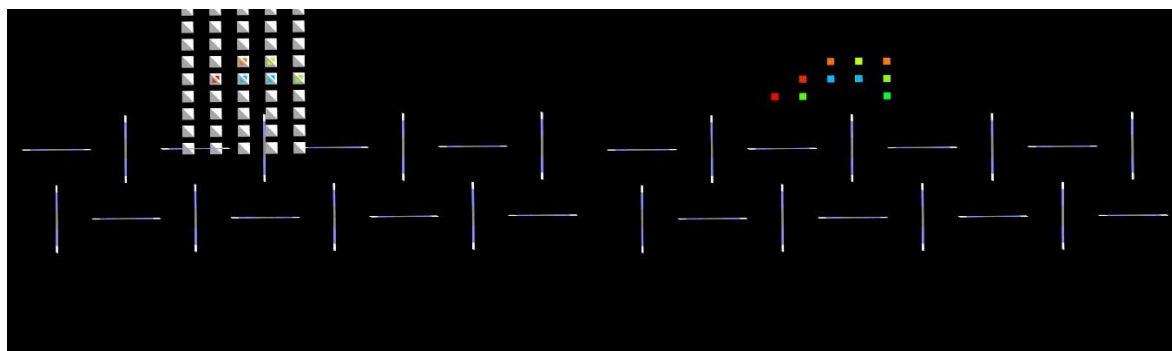


Figure 4.7: An example of the result of the grid search applied and the white and coloured tetrahedrons found.

The VisualHabit Systsearch calculation is a simple calculation method to determine the most energetically favourable, therefore the most stable interaction of the probe molecule with the surface; however the method is based on the following assumptions (Ramachandran et al., 2015):

1. The crystal lattice is perfect and does not contain any defects.

2. The surface of the crystal can be represented by termination of the bulk lattice.
3. The probe molecule is considered rigid, and any changes to the probe molecule due to interactions with the surface are not taken into account.
4. Any charges on the probe molecule are not taken into account.
5. Intra-molecular interactions are not taken into consideration.
6. Solvent effects are not explicitly taken into account, for example, the wetting energy of a solvent with a particular surface may be higher however for the purposes of this calculation all energies are considered equal.

4.5 Conclusions

This chapter presents the materials used for this research, alongside the instrumentation and experimental methodologies employed. Additionally, an outline of the computational methodologies have also been presented.

The experimental method for analysing the solubility of a solution has been presented, as well as the instrumentation, methodology and analysis for the determination of MSZW. Additionally, the experimental method for the determination of the effect of an additive on face specific crystal growth rates carried out in a 0.5mL cuvette cell has been presented. Finally, the experimental method for the measurement of face specific dissolution rates in ethanol, acetonitrile and FeSSIF has been outlined, along with the preparation method for FeSSIF.

The computational methodology employed for the determination of the wetting energies of the crystal faces under consideration has been outlined. In addition, the method for calculating the intermolecular interactions between the solvent molecule and the surface of the crystal face has been presented.

References

- Anton-Paar. **2019**. <https://wiki.anton-paar.com/en/acetonitrile/>
- Anton-Paar. **2019**. <https://wiki.anton-paar.com/uk-en/ethanol/>
- Anton-Paar. **2019**. <https://wiki.anton-paar.com/uk-en/water/>
- Biorelevant. **2019**. <https://biorelevant.com/>
- Biovia. **2019**. <https://www.3dsbiovia.com/products/collaborative-science/biovia-materials-studio/>
- Bravais, A. *Etudes Cristallographiques*. **1866**. Paris: Gauthier Villars
- CCDC. **2019**. <https://www.ccdc.cam.ac.uk/>
- Cosmologic. **2019**. <http://www.cosmologic.de/products/cosmotherm.html>
- Coulson, J. M., J. F. Richardson, J. H. Harker, J. R. Backhurst. *Coulson and Richardson's Chemical Engineering: Particle Technology and Separation Processes*. **2002**. Butterworth-Heinemann.
- Delley, B., From molecules to solids with the DMol approach. *J. Chem. Phys.* **2000**. 113 (18), 7756-7764
- Donnay, J. D. H., D. Harker. *Am. Mineral.* **1937**. 22, 463.
- Fick, A. On Liquid Diffusion. *Philosophical Magazine – Series 4*. **1855**. 10(63), 30-39.
- Friedel, G. *Bull. Soc. Franc. Mineral.* **1907**. 30, 326.
- Gasteiger, J., M. Marsili. A New Model for Calculating Atomic Charges in Molecules. *Tetrahedron Lett.* **1978**. 19(34), 3181-3184.
- Gasteiger, J., M. Marsili. Iterative Partial Equalization of Orbital Electronegativity – A Rapid Access to Atomic Charges. *Tetrahedron Lett.* **1980**. 36(22), 3219-3228.
- Hammond, R. B., K. Pencheva, K. J. Roberts. A Structural-Kinetic Approach to Model Face Specific Solution/Crystal Surface Energy Associated with the Crystallisation of Acetyl Salicylic Acid from Supersaturated Aqueous/Ethanol Solution. *Cryst. Growth & Design*. **2006**. 6(6), 1324-1334.
- Huber. **2019**. https://www.huber-online.com/en/product_datasheet.aspx?no=2016.0005.01
- Klamt, A., G. Schüürmann. COSMO: a new approach to dielectric screening in solvents with explicit expressions for the screening energy and its gradient. *J. Chem. Soc., Perkin Trans. 2*. **1993**. (5), 799-805.
- Krishna, R., L. Yu. *Biopharmaceutics Applications in Drug Development*. **2008**. Springer.

Lumenera. **2019**. <https://www.lumenera.com/>

Perdew, J.P., K. Burke, and M. Ernzerhof. Generalized gradient approximation made simple. *Phys. Rev. Lett.* **1996**. 77(18), 3865-3868.

Pickering, J., R. B. Hammond, V. Ramachandran, M. Soufian, K. J. Roberts. Synthonic Engineering Modelling Tools for Product and Process Design. *Engineering Crystallography: From Molecule to Crystal to Functional Form*. **2017**. NATO: Springer.

Ramachandran, V., D. Murnane, R. B. Hammond, J. Pickering, K. J. Roberts, M. Soufian, B. Forbes, S. Jaffari, G. P. Martin, E. Collins, K. Pencheva. Formulation Pre-Screening of Inhalation Powders Using Computational Atom-Atom Systematic Search Method. *Mol. Pharmaceutics*. **2015**. 12(1), 18-33.

Seipmann, J., F. Seipmann. Mathematical Modelling of Drug Dissolution. *Int. J. Pharm.* **2013**. 453(1), 12-24.

Sklar, N., M. E. Senko, B. Post. Thermal Effects in Urea: the Crystal Structure at -140°C and at Room Temperature. *Acta Cryst.* **1961**. 14, 716-720.

Technobis. **2019**. <https://www.crystallizationsystems.com/crystal16>

Turner, T. D., T. T. H. Nguyen, P. Nicholson, G. Brown, R. B. Hammond, K. J. Roberts, I. Marziano. A Temperature-Controlled Single Crystal Growth Cell for the in-situ Measurement and Analysis of Face Specific Growth Rates. *J. Appl. Cryst.* **2019**. 52(2), 463-467.

Zeiss. **2019**. <https://www.micro-shop.zeiss.com/en/de/>

Chapter 5: Solubility, Nucleation and Growth of Urea in the Presence and Absence of Biuret

5.1 Introduction

Crystallisation behaviour of a solute can be primarily characterised through solubility determination and the kinetic behaviour of a solute with a solvent. Solvent induced nucleation and growth of a crystal in the presence of impurities and additives can dramatically control or alter the solubility, nucleation kinetics and growth morphology and mechanism, due to face dependent interactions.

This chapter aims to explore this and present the solubility data of urea in absolute ethanol as van't Hoff plots to assess the ideal behaviour of the solution. Also presented in this chapter are the results of the metastable zone width of urea in absolute ethanol and urea with the addition of 1% w/w biuret in absolute ethanol, obtained through the slow cooling polythermal method. The cooling rates applied to the solution and the temperatures of undercooling obtained from the polythermal method as a result, were further used to determine if there was a change in nucleation mechanism with the addition of biuret into the solution. Other critical parameters associated with the theory of nucleation, such as the interfacial tension between the nucleus and the solution, the critical nucleus radius needed to ensure crystal growth, and the nucleation rate were determined through the polythermal method, allowing for a comparison between a pure urea system in absolute ethanol and a urea system with biuret additive in absolute ethanol.

Previous studies of the growth of urea with an additive have been conducted through molecular dynamics simulations, however little experimental data has been provided regarding the face-specific growth of urea in the presence of biuret. The determination of the effect of biuret on the growth mechanism of morphologically important faces of urea – {110} and {111} faces – have not been studied, therefore this chapter aims to present the results obtained when face-specific experimental data of a pure urea system in absolute ethanol and a urea system with biuret impurity in absolute ethanol was fitted to growth models to determine the growth mechanism and rate-determining step.

5.2 Solubility

The solubility of urea in absolute ethanol was obtained from literature.

Table 5.1: Solubility of urea in ethanol obtained from literature. (Lee et al., 1972)

Temperature (°C)	6.9	18.2	25.5	35.5	45.4	55.0
Concentration (g urea/100g ethanol)	3.72	4.88	5.84	7.44	9.68	12.44

The solubility data obtained from experimentation was compared with the limited data of urea in absolute ethanol that is available in literature. (Lee et al., 1972; Capuci et al., 2016)

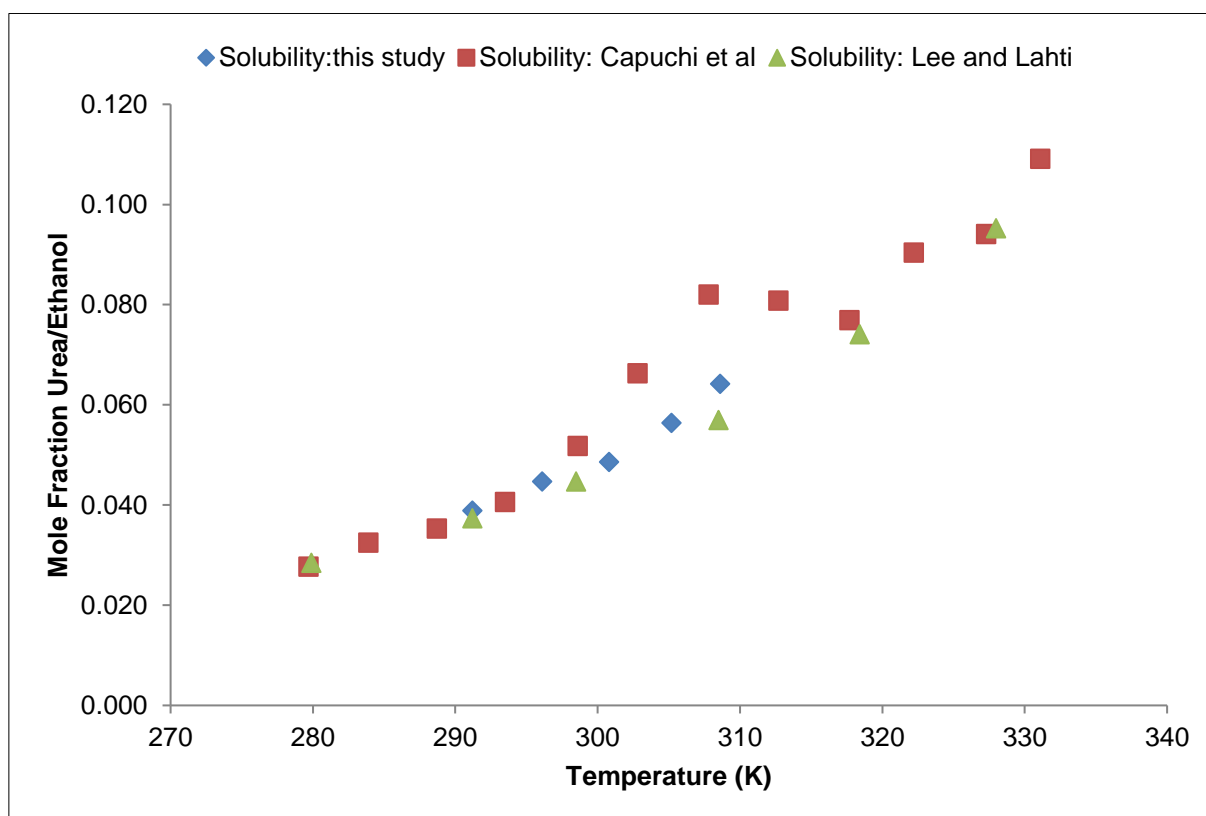


Figure 5.1: A comparison of solubility data obtained from experimentation with solubility data obtained from literature.

The theoretical solubility of urea in absolute ethanol was determined through the van't Hoff equation, assuming ideal solution behaviour, and this was compared to the solubility data obtained from experimentation.

Table 5.2: Calculated activity coefficient using van't Hoff equation.

Temperature (K)	1/T	X _{ideal}	X _{solubility}	Activity coefficient
279.9	0.0036	0.163	0.029	5.710
291.2	0.0034	0.204	0.037	5.460
298.5	0.0034	0.234	0.045	5.234
308.5	0.0032	0.280	0.057	4.902
318.4	0.0031	0.330	0.074	4.445
328.0	0.0030	0.384	0.095	4.020

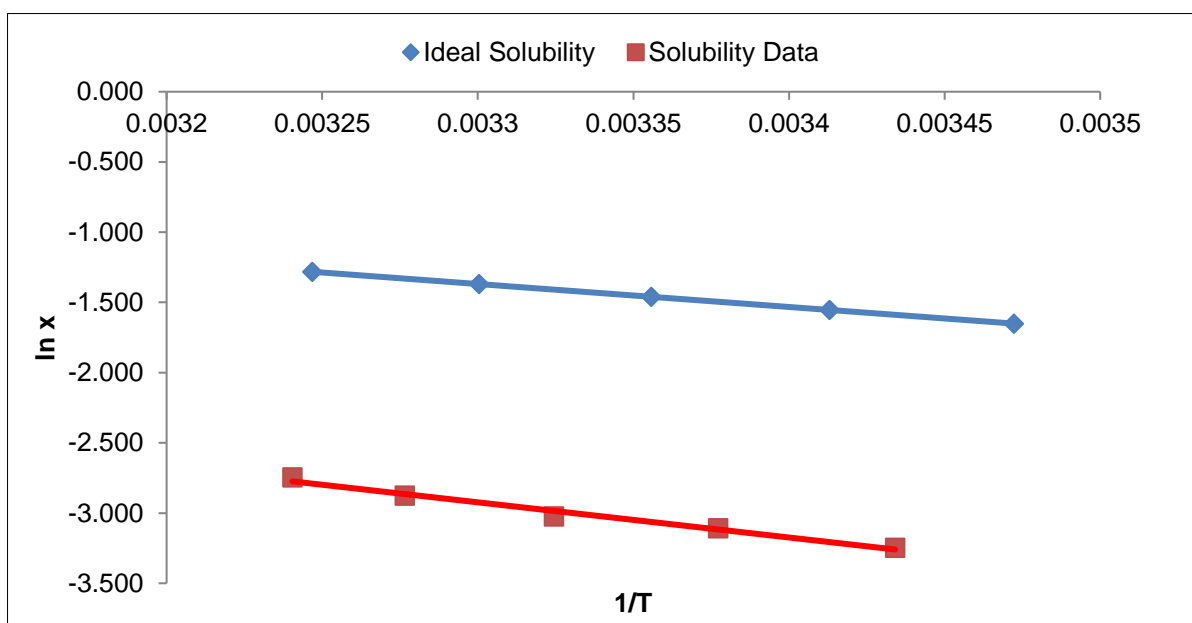


Figure 5.2: A comparison of the solubility data of urea in ethanol obtained from experimentation with the calculated ideal solubility in van't Hoff coordinates.

In an ideal solution, the amount of energy required to break solute-solute interactions in addition to the amount of energy required to break solvent-solvent interactions is equal to the amount of energy required to make solute-solvent interactions. The solubility of urea in absolute ethanol is less than ideal; therefore solute-solute interactions are favoured. This is reinforced through the calculation of the activity coefficient, as the activity coefficient is greater than 1, so forces of attraction between solute-solute molecules would be favoured over forces of attraction between solute-solvent molecules. However, with increasing temperature, the behaviour of urea in absolute ethanol becomes closer to the ideal scenario. A solution can exhibit behaviour different to that of an ideal solution due to either enthalpic or entropic

factors, or both. This can be determined through the comparison of van't Hoff plots – if the gradients of the lines differ, the deviation from an ideal solution would be due to both enthalpic and entropic factors. However, if the lines are parallel, the deviation from ideal behaviour is only due to entropic factors. As the gradients of the lines for urea in absolute ethanol are different, it can be concluded that deviation from ideal behaviour is both enthalpically and entropically driven.

5.3 Polythermal Crystallisation

The slow cooling polythermal crystallisation method was used to determine the metastable zone width (MSZW) of saturated solutions of urea in absolute ethanol at five temperatures (20°C, 25°C, 30°C, 35°C and 40°C). MSZW measurements were taken as a function of four solution heating and cooling rates (0.5°C/min, 1.0°C/min, 2.0°C/min and 5.0°C/min). This experiment was repeated with 1%w/w biuret additive included within the solution, to determine the effect of an additive on MSZW. The complete table for MSZW values for urea in ethanol, and urea with 1% biuret in ethanol have been provided in Appendix A1 and Appendix A2, respectively.

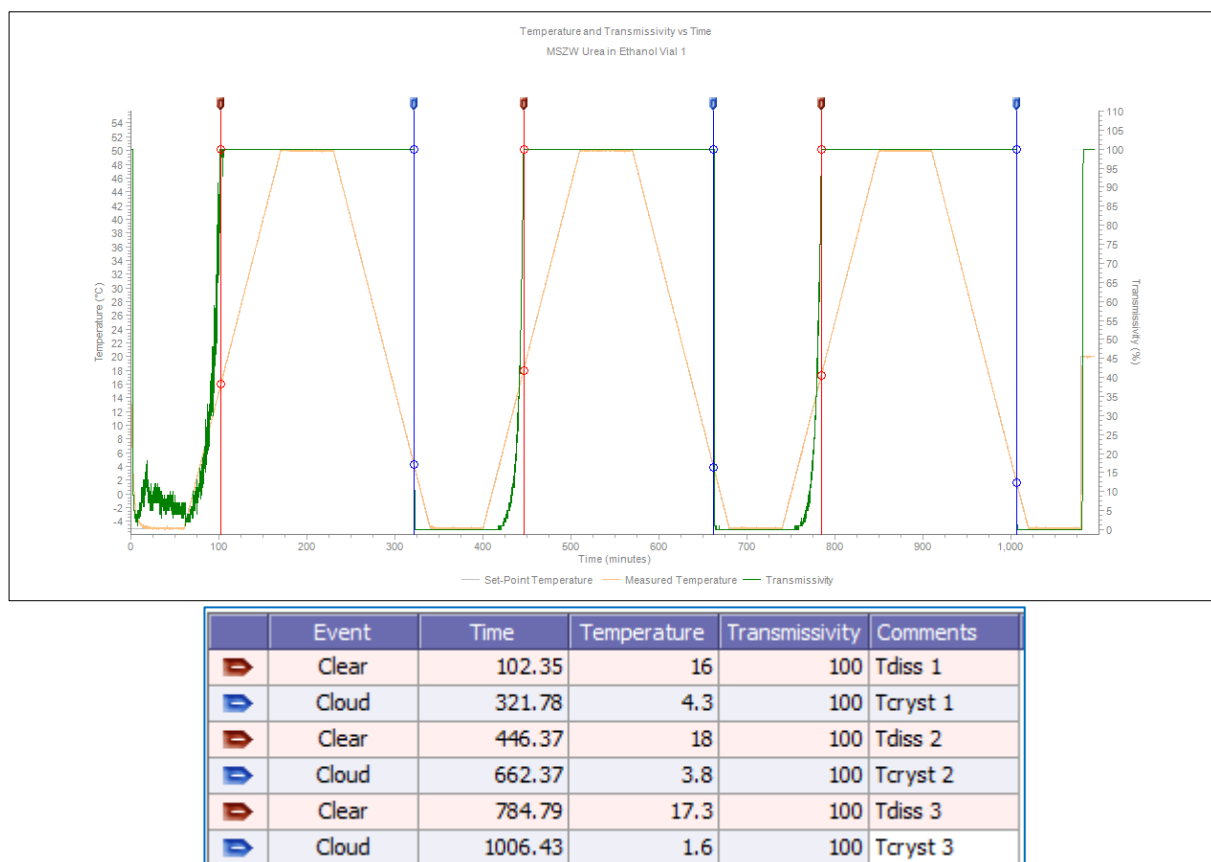
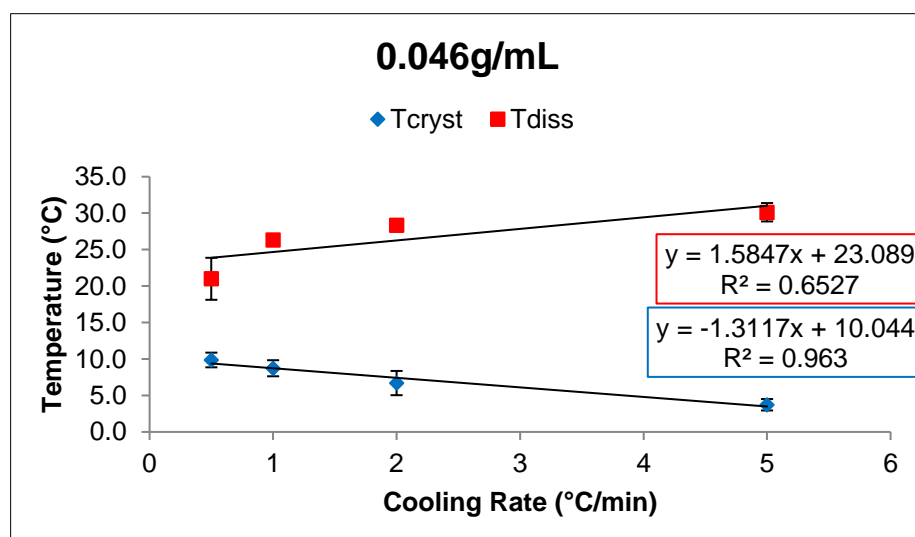
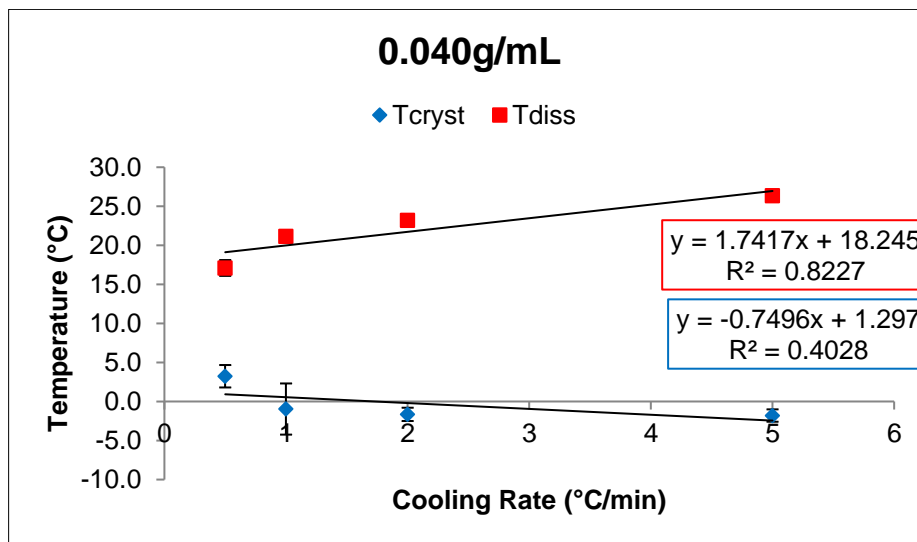


Figure 5.3: An example of the MSZW results obtained from Crystal 16.

5.3.1 MSZW Urea in Absolute Ethanol

Five concentrations of urea in absolute ethanol (0.040g/mL, 0.046g/mL, 0.050g/mL, 0.058g/mL and 0.066g/mL) were used to determine MSZW.



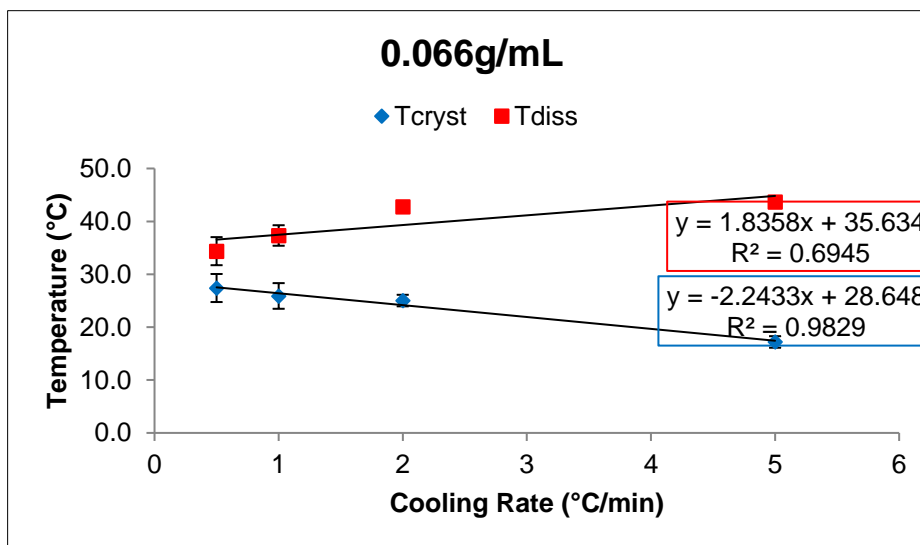
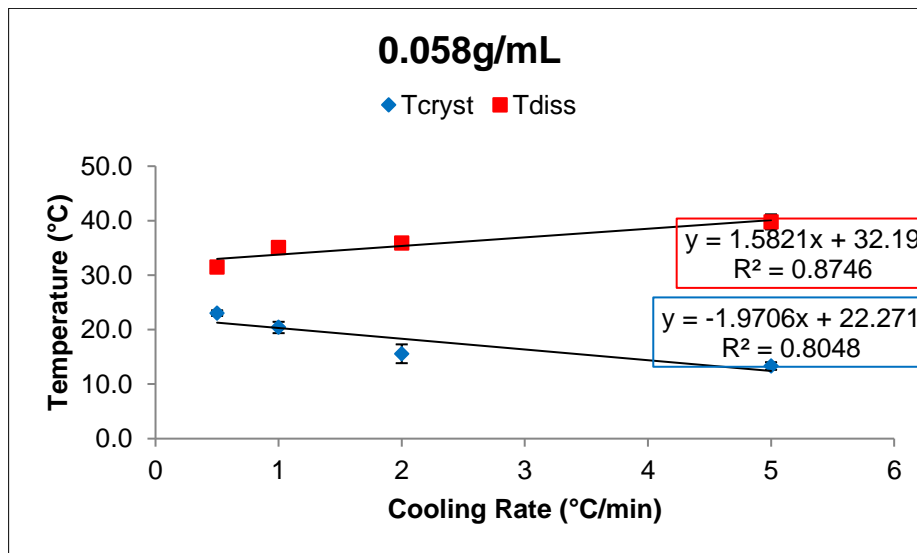
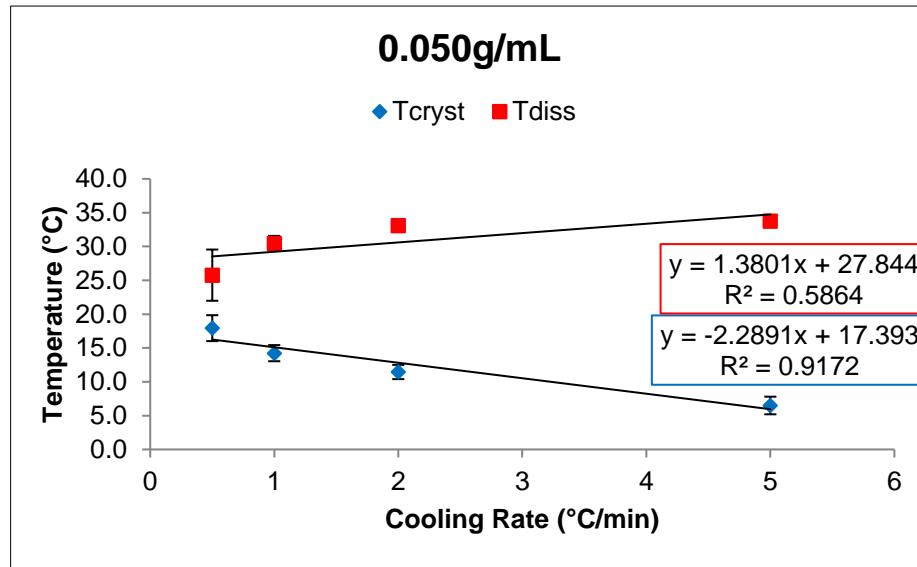


Figure 5.4: Crystallisation and dissolution temperatures of urea in ethanol allowing for the determination of the MSZW at all concentrations used.

The experimental data obtained of temperature vs cooling rate are presented, showing the dependency of the crystallisation and dissolution processes on the heating and cooling rates of the solution. For all concentrations, the crystallisation temperature decreases with increasing cooling rate, whereas the dissolution temperature increases with increasing cooling rate. This is because with a slow cooling rate, the structure of the crystallites in the solution can adapt to the changes of the temperature of solution, resulting in a narrow MSZW, whereas with a higher cooling rate the structure of the crystallites cannot change as rapidly as the changes in temperature of solution, which ultimately results in a much wider MSZW.

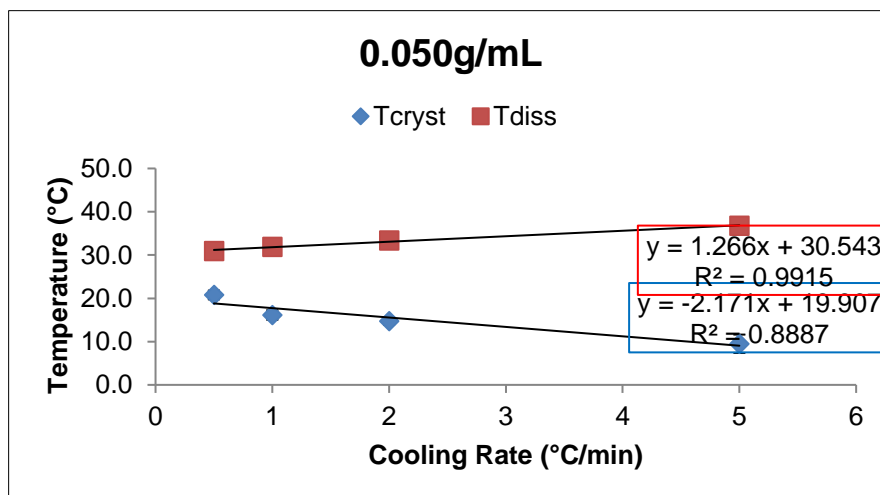
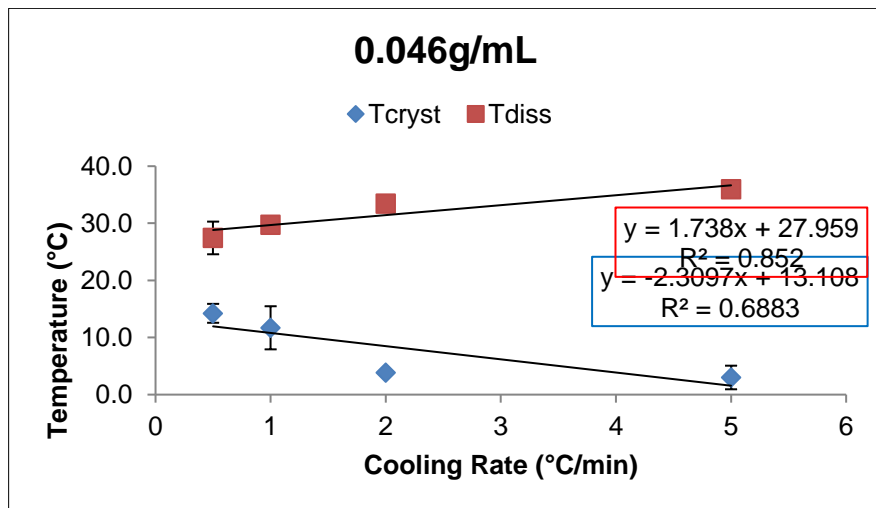
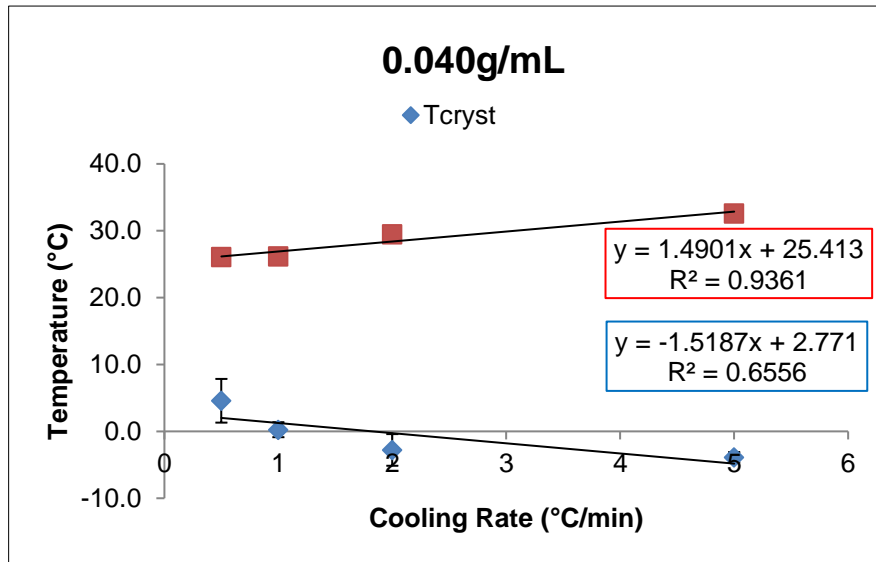
Table 5.3: MSZW obtained for urea in ethanol at different concentrations.

Concentration (g/mL)	T_{cryst} (°C)	T_{diss} (°C)	MSZW (°C)
0.040	1.3	18.2	16.9
0.046	10.0	23.1	13.1
0.050	17.4	27.8	10.4
0.058	22.3	32.2	9.9
0.066	28.6	35.6	7.0

At an infinite cooling rate, with increasing concentration the MSZW decreases. The MSZW is a measure of the stability of the solution – the wider the MSZW the more stable the solution. Therefore, with increasing concentration, supersaturation resulting in the onset of crystallisation is reached at a higher temperature, which would mean an increasingly unstable solution.

5.3.2 MSZW Urea and 1%w/w Biuret in Absolute Ethanol

The same five concentrations of urea along with 1%w/w biuret additive were added to absolute ethanol to determine the effect of additive on MSZW.



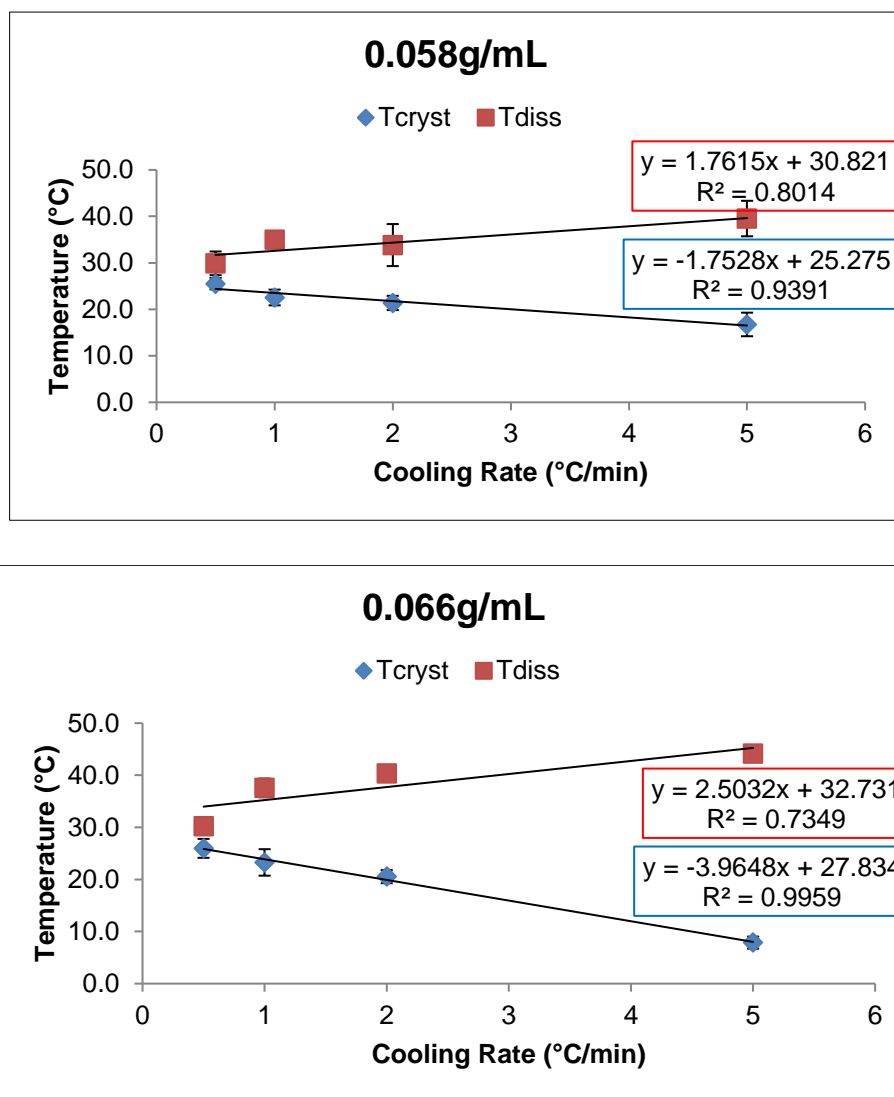


Figure 5.5: Crystallisation and dissolution temperatures of urea and biuret in ethanol allowing for the determination of MSZW at all concentrations used.

The experimental data obtained of temperature vs cooling rate with the addition of biuret are presented, showing the dependency of crystallisation and dissolution processes on the heating and cooling rates, and the effect an additive has on this. For all concentrations, the inclusion of biuret does not affect the observed trend for pure urea in absolute ethanol, where the crystallisation temperature decreases with increasing cooling rate and the dissolution temperature increases with increasing cooling rate. However, at lower concentrations, in comparison with pure urea in absolute ethanol the dissolution temperature of the solution with additive is much higher. Therefore, the addition of biuret at lower concentrations affects solute-solvent interactions.

Table 5.4: MSZW for urea and biuret in ethanol at different concentrations.

Concentration (g/mL)	T_{cryst} (°C)	T_{diss} (°C)	MSZW (°C)
0.040	2.8	25.4	22.6
0.046	13.1	28.0	14.9
0.050	19.9	30.5	10.6
0.058	25.3	30.8	5.5
0.066	27.8	32.7	4.9

At an infinite cooling rate, the addition of biuret does not affect the trend observed for urea in absolute ethanol, where the MSZW decreases with increasing concentration. However, at lower concentrations, the MSZW is much wider, meaning the addition of biuret results in a more stable solution. This further confirms that the addition of biuret affects solute-solvent interactions at lower concentrations. At higher concentrations the effect is much less clear, as the MSZW is narrower with the addition of biuret in comparison with the system without biuret, however the error of measurement could play a role in this. Additionally, at higher concentrations, there is less solvent with respect to solute, which suggests that solvent concentration plays a role in mediating these effects. This work was restricted to one biuret concentration, therefore further work would be needed to at other quantities of biuret and with other solvents to fully quantify this effect.

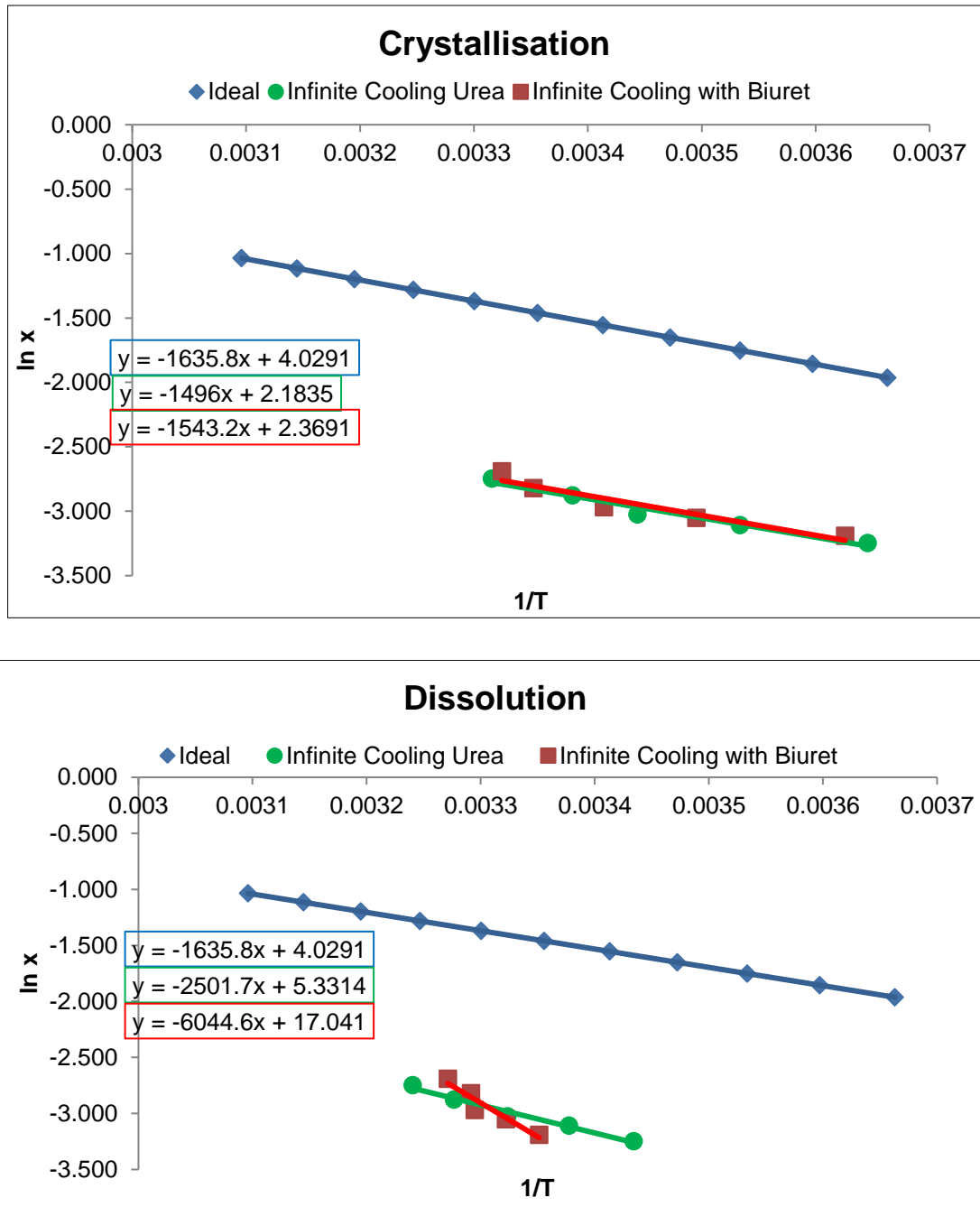


Figure 5.6: Crystallisation and dissolution temperatures for urea in ethanol, and urea and biuret in ethanol in van't Hoff coordinates.

The crystallisation and dissolution temperatures in van't Hoff coordinates for urea in absolute ethanol and urea and 1%w/w biuret in ethanol show that biuret has little to no effect on the crystallisation temperatures of urea at all concentrations; however it does have a great effect on the dissolution temperature of urea.

Table 5.5: A comparison of enthalpies and entropies of crystallisation and dissolution of ideal solubility, urea in ethanol, and urea and biuret in ethanol.

		ΔH_f (kJ/mol)	ΔS_f (J/K)
Crystallisation	Ideal	13.6	33.5
	Urea	12.4	18.2
	Urea & Biuret	12.8	19.7
		ΔH_d (kJ/mol)	ΔS_d (J/K)
Dissolution	Ideal	13.6	33.5
	Urea	20.8	44.3
	Urea & Biuret	50.2	141.7

The values presented in Table 5.5 show that the deviation from ideal behaviour during the crystallisation process are due to entropic factors, and as both systems have comparable entropies of fusion, the crystallisation process is not affected by the addition of biuret. However, during the dissolution process, the deviation from ideal behaviour is due to both enthalpic and entropic factors, and the addition of biuret increases both the enthalpic effect and the entropic effect.

5.4 Nucleation Kinetics using KBHR Methodology

The nucleation mechanism and kinetics were determined using data obtained from polythermal crystallisation, following the analysis procedure for KBHR methodology outlined previously. (Kashchiev et al., 2010; Kashchiev et al., 2010)

5.4.1 Nucleation Kinetics of Urea in Absolute Ethanol

Table 5.6 shows the values obtained from polythermal crystallisation for mean temperatures of dissolution and crystallisation at four cooling rates and five concentrations of urea in absolute ethanol. These values were then used to determine critical undercooling and relative critical undercooling, which can be further used to establish the nucleation mechanism of urea in absolute ethanol.

Table 5.6: Dissolution and crystallisation temperatures obtained from the polythermal method and calculated values of the critical undercooling and relative critical undercooling for urea in ethanol.

Cooling Rate (°C/min)	Conc (g/ml)	Mean T _{diss} (K)	Mean T _{cryst} (K)	T _e	ΔT _c	μ _c	ln q	ln μ _c
0.5	0.040	290.1	276.2	291.2	15.0	0.052	-0.693	-2.966
1		294.3	272.0		19.2	0.066	0.000	-2.719
2		296.2	271.3		19.9	0.068	0.693	-2.683
5		299.3	271.2		20.0	0.069	1.609	-2.678
0.5	0.046	294.0	282.8	296.1	13.3	0.045	-0.693	-3.103
1		299.3	281.7		14.4	0.049	0.000	-3.023
2		301.4	279.7		16.4	0.055	0.693	-2.893
5		303.1	276.7		19.4	0.066	1.609	-2.725
0.5	0.050	298.8	290.9	300.8	9.9	0.033	-0.693	-3.414
1		303.5	287.2		13.6	0.045	0.000	-3.096
2		306.1	284.5		16.3	0.054	0.693	-2.915
5		306.8	279.5		21.3	0.071	1.609	-2.648
0.5	0.058	304.5	296.0	305.2	9.2	0.030	-0.693	-3.502
1		308.1	293.4		11.8	0.039	0.000	-3.253
2		308.9	288.6		16.6	0.054	0.693	-2.912
5		313.0	286.3		18.9	0.062	1.609	-2.782
0.5	0.066	307.4	300.4	308.6	8.2	0.027	-0.693	-3.628
1		310.3	298.9		9.7	0.031	0.000	-3.460
2		315.8	298.0		10.6	0.034	0.693	-3.371
5		316.7	290.2		18.4	0.060	1.609	-2.820

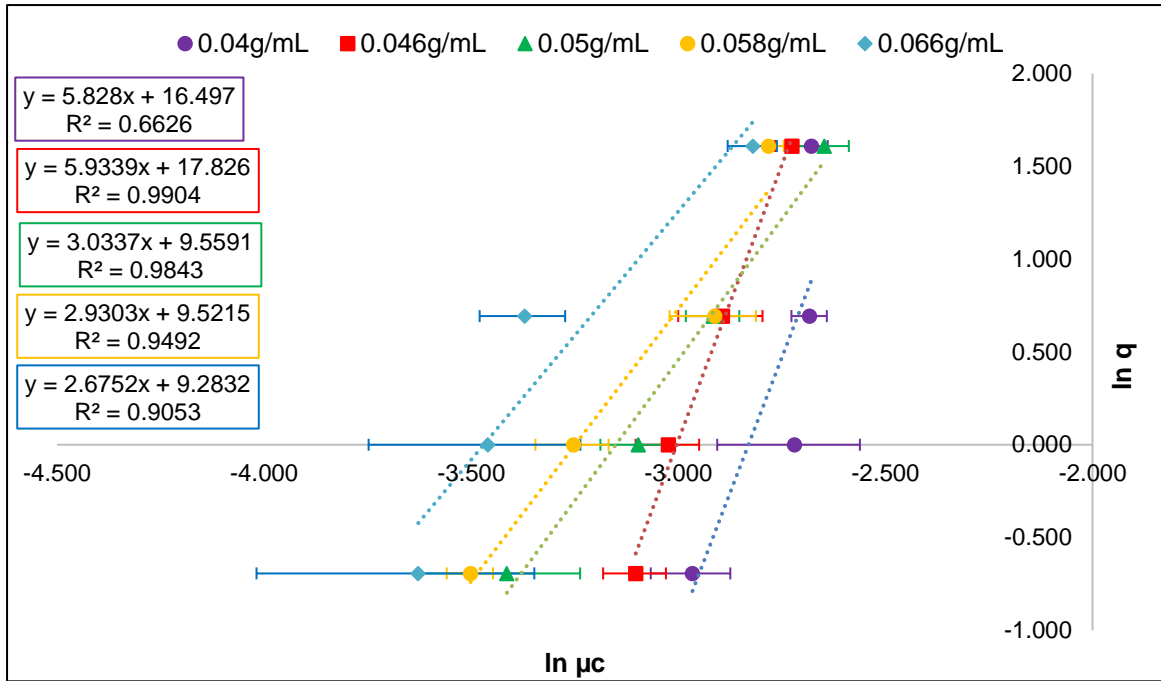
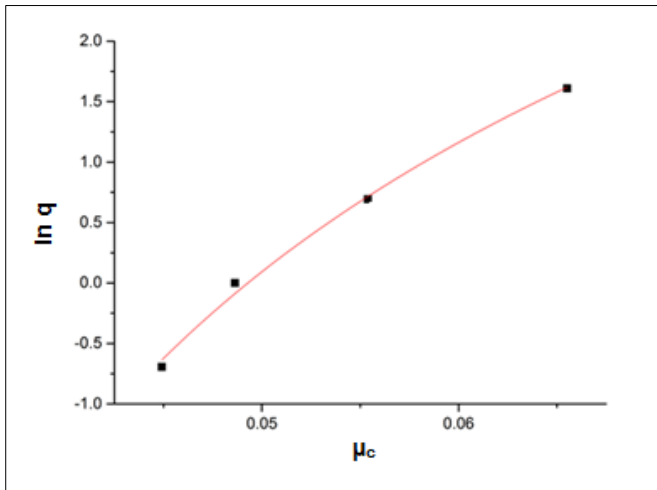


Figure 5.7: Plot of q vs uc in \ln - \ln coordinates for urea in ethanol at concentrations of 0.04 g/mL, 0.046 g/mL, 0.050 g/mL, 0.058 g/mL, and 0.066 g/mL.

The data shows that the gradient for the lower concentrations are greater than 3, therefore the nucleation mechanism at these concentrations was found to be progressive – where crystal nuclei form continuously during nucleation process, resulting in a number of nuclei of different sizes. At higher concentrations however, the gradients are equal to or less than 3, therefore the nucleation mechanism was found to be instantaneous, meaning that all the nuclei would form at the beginning of the nucleation process, and the solution will contain a fixed number of nuclei.

5.4.1.1 Progressive Nucleation Kinetics for Urea in Absolute Ethanol

The nucleation data obtained at lower concentrations of urea in absolute ethanol, which was found to exhibit progressive nucleation, was further analysed to determine nucleation kinetics parameters.



Model	NewFunction (User)		
Equation	A+B*(ln(x))-((C)/((1-x)*(x^2)))		
Reduced Chi-Sqr	0.00576		
Adj. R-Square	0.99405		
		Value	Standard Error
B	A	10.83448	0.15016
	B	3	0
	C	0.00417	3.73054E-4

Figure 5.8: An example of curve fittings obtained from Origin Pro for progressive nucleation data obtained using the polythermal method.

An example of the curve fitting for urea in absolute ethanol is shown in Figure 5.8, where A corresponds to $\ln q_0$, B corresponds to the free parameter a_1 , which was fixed at 3, and C corresponds to a_2 , which is used for the determination of interfacial tension.

v_0 was calculated using unit cell parameters and was determined to be $7.56 \times 10^{-29} \text{ m}^3$, the shape factor was assumed for a spherical nuclei as $kn = 16/3\pi$, and λ was found from literature to be $2.26 \times 10^{-20} \text{ J/molecule}$. Table 5.7 presents values of effective interfacial tension (γ_{eff}), the critical nucleus radius (r^*), the number of molecules in the critical radius (i^*), and the nucleation rate (J).

Table 5.7: Calculated progressive nucleation kinetics for urea in ethanol.

Conc (g/mL)	q	μ_c	$\ln q_0$ [A]	a_1 [B]	a_2 [C]	γ_{eff} (mJ/m ²)	r^* (nm)	i^*	J (1/nm ³ .s)
0.04	0.5	0.052	9.946	3	0.0047	4.652	0.605	12.244	9.22
	1	0.066					0.472	5.838	18.76
	2	0.068					0.456	5.244	20.27
	5	0.069					0.453	5.165	20.48

0.046	0.5	0.045	10.834	3	0.00417	4.495	0.670	16.659	11.44
	1	0.049					0.619	13.126	15.61
	2	0.055					0.543	8.886	23.62
	5	0.066					0.459	5.368	35.22

The results obtained for progressive nucleation kinetics for urea in absolute ethanol, show that with an increase in concentration, the effective interfacial tension decreases. This would be expected as interfacial tension is defined as the work required to create a unit area of interface, and an increased concentration of urea would be expected to reach supersaturation faster. This is also reinforced through the values of critical nucleus radius, number of molecules in the critical radius and the nucleation rate, as a lower interfacial tension results in higher values at the same cooling rate. The values calculated for critical nucleus radius show good agreement with calculated values for other organic molecules, such as aspirin and para-aminobenzoic acid. (Pencheva, 2006; Turner, 2015) Calculating the critical nucleus radius was based on homogeneous nucleation theory, which would underestimate the cluster size as it does not consider heterogeneous nucleation. Hence, caution should be exercised with regards to the values determined. Nonetheless, the trends are unlikely to change hence the trend was focussed on. Additionally, with increasing cooling rate the nucleation rate increases much more at a higher concentration of urea in absolute ethanol, as supersaturation is achieved faster.

5.4.1.2 Instantaneous Nucleation Kinetics for Urea in Absolute Ethanol

The nucleation data obtained at higher concentrations of urea in absolute ethanol, which was found to have an instantaneous nucleation mechanism, were further analysed.

Table 5.8: Calculated instantaneous nucleation kinetics for urea in ethanol.

Conc (g/mL)	K_G (m/s)	$\ln q_0$	$n+1$	n	$k_v (2A_0)$	d	m	C_0
0.05	4.11×10^{-8}	9.5591	3.0337	2.0337	3.56×10^{-9}	1	0.5	5.72×10^{14}
0.058	4.11×10^{-8}	9.5215	2.9303	1.9303	3.56×10^{-9}	1	0.5	4.88×10^{14}
0.066	4.11×10^{-8}	9.2832	2.6752	1.6752	3.56×10^{-9}	1	0.5	4.81×10^{14}

The values of q_0 and $(n+1)$ were obtained from the plot of q vs μ_c in \ln - \ln coordinates. The concentration of nuclei (C_0), therefore, could be calculated through the following assumptions: $d = 1$, $m = 0.5$, $K_G = 4.11 \times 10^{-8}$, $k_v = 3.56 \times 10^{-9}$. The value of d is the dimensionality of crystal growth, and was assumed to be 1 as that corresponds to growth of needle-like crystals, m is a growth exponent for the system and was assumed to be 0.5 to indicate undisturbed diffusion of the solute to the crystal

surface, K_G is the overall growth rate of the crystal, and was determined through single crystal experiments, where an average value of the growth rate was taken. Finally, k_v is the crystallite growth shape factor calculated through $k_v = 2A_0$, where A_0 is the fixed cross sectional area of a needle. The widths of urea crystals were measured, and were found to have a range of 30-55 μm , therefore an average value was taken as an approximation to calculate A_0 .

Values of n are used to determine the rate limiting step of the growing crystallites, for example, if $n = 1$, this is indicative of a system where the growth of a crystallite is rate limited only by the diffusion of the growth unit to the growing crystallite. Also, if $n = 2$, this is indicative of a system where the growth of a crystallite is rate limited by the rearrangement of the solute at the crystal/solution interface. The calculated values of n for all concentrations, presented in Table 5.8, can all be rounded to 2. Therefore, during the nucleation process, the growth of urea crystallites at the concentrations studied is rate limited by the rearrangement of the solute at the crystal/solution interface.

The calculated concentration of nuclei (C_0) decreases with increasing concentration, as presented in Table 5.8, which was also found to be the case for values calculated for para-aminobenzoic acid. Additionally, both organic molecules were found to have the same general trend whereby with decreasing concentration, the system changes nucleation mechanism from an instantaneous mechanism to a progressive mechanism. (Turner, 2015)

5.4.2 Nucleation Kinetics of Urea and 1%w/w Biuret in Absolute Ethanol

The same five concentrations and four cooling rate conditions were repeated to determine nucleation kinetics for urea in absolute ethanol, with the addition of 1%w/w biuret. Table 5.9 shows the values obtained from polythermal crystallisation for mean temperatures of dissolution and crystallisation. These values were then used to determine critical undercooling and relative critical undercooling, which were further used to establish the effect of an additive on the nucleation mechanism and kinetics.

Table 5.9: Dissolution and crystallisation temperatures obtained from the polythermal method and calculated values of the critical undercooling and relative critical undercooling for urea and 1% w/w biuret in ethanol.

Cooling Rate (°C/min)	Conc (g/ml)	Mean T _{diss} (K)	Mean T _{cryst} (K)	T _e	ΔT _c	μ _c	ln q	ln μ _c
0.5	0.040	299.1	277.6	298.4	20.8	0.070	-0.693	-2.662
1		299.2	273.3		25.2	0.084	0.000	-2.474
2		302.5	270.2		28.2	0.094	0.693	-2.360
5		305.6	269.1		29.3	0.098	1.609	-2.322
0.5	0.046	300.4	287.2	301.0	13.8	0.046	-0.693	-3.085
1		302.8	284.7		16.3	0.054	0.000	-2.916
2		306.4	276.9		24.1	0.080	0.693	-2.524
5		309.0	276.0		25.0	0.083	1.609	-2.488
0.5	0.050	303.9	293.8	303.5	9.7	0.032	-0.693	-3.443
1		304.9	289.2		14.3	0.047	0.000	-3.055
2		306.4	287.8		15.7	0.052	0.693	-2.962
5		309.8	282.5		21.0	0.069	1.609	-2.671
0.5	0.058	302.9	298.5	303.8	5.3	0.017	-0.693	-4.053
1		308.0	295.6		8.3	0.027	0.000	-3.606
2		306.8	294.4		9.4	0.031	0.693	-3.473
5		312.5	289.8		14.1	0.046	1.609	-3.074
0.5	0.066	303.2	299.0	305.7	6.7	0.022	-0.693	-3.816
1		310.6	296.3		9.4	0.031	0.000	-3.478
2		313.3	293.5		12.2	0.040	0.693	-3.224
5		317.1	280.9		24.8	0.081	1.609	-2.510

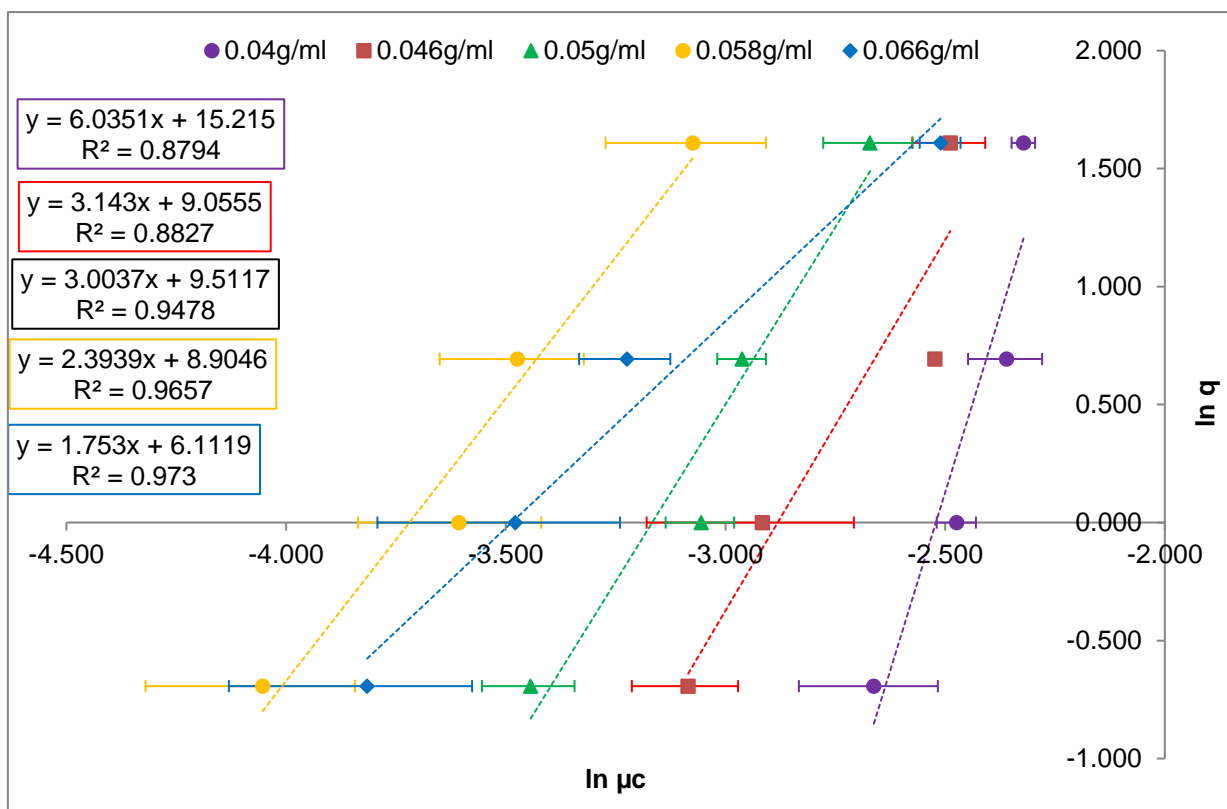


Figure 5.9: plot of q vs μc in \ln - \ln coordinates for urea and 1% w/w biuret in ethanol at concentrations of 0.04 g/mL, 0.046g/mL, 0.05 g/mL, 0.058 g/mL and 0.066g/mL.

The data shows that the gradient for the lowest concentration was greater than 3, therefore the nucleation mechanism at this concentration was found to be progressive. At 0.046g/mL, however, there was a decrease in gradients. From 6-3.1, similar to the gradients obtained for pure urea solutions. Hence, for this reason, although the gradient at 0.046g/mL was slightly larger than 3, it was considered as instantaneous nucleation. At higher concentrations however, the gradients were equal to or less than 3, therefore the nucleation mechanism was found to be instantaneous. Comparing the nucleation mechanism with and without 1%w/w biuret also showed that the addition of biuret altered the nucleation mechanism such that at a lower concentration, the mechanism changes from progressive to instantaneous. It was also found that both systems followed the same general trend, where a decrease in concentration resulted in a change of nucleation mechanism, from instantaneous to progressive. This general trend was also observed for other organic molecules. (Turner, 2015)

5.4.2.1 Progressive Nucleation Kinetics for Urea and 1%w/w Biuret in Absolute Ethanol

The nucleation data which was obtained at 0.04g/mL for urea and 1%w/w biuret in absolute ethanol was further analysed to determine nucleation kinetics, and compare these to that of the system which did not contain biuret to ascertain whether the addition of biuret within the system affects the kinetic parameters of a progressive nucleation mechanism.

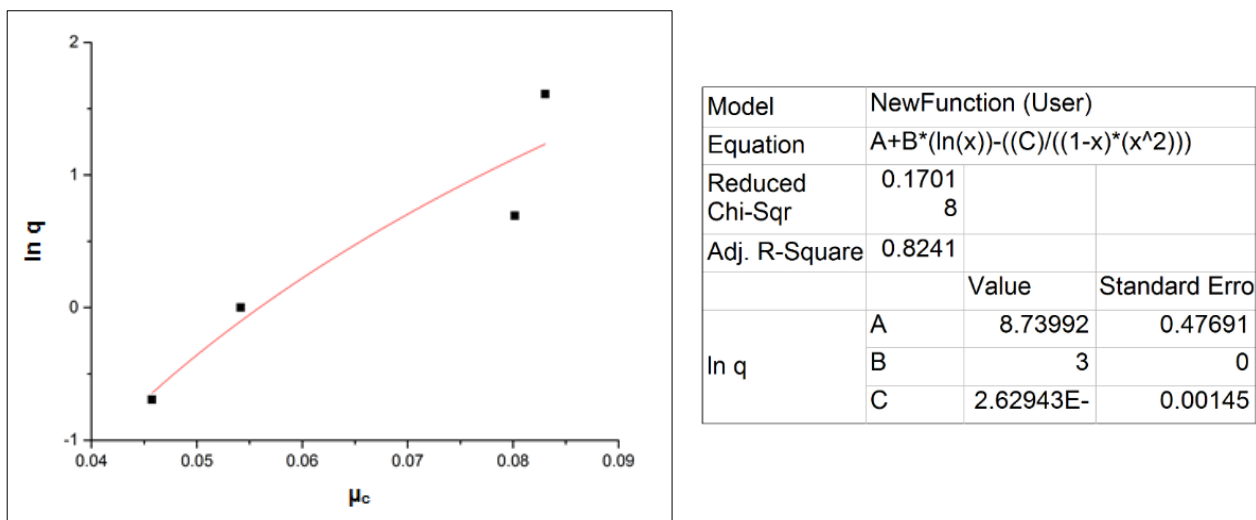


Figure 5.10: An example of curve fittings obtained from Origin Pro for progressive nucleation data for urea and 1% w/w biuret in ethanol.

An example of the non-linear curve fitting for urea and 1% w/w biuret in ethanol is shown in Figure 5.10, where A corresponds to $\ln q_0$, B corresponds to the free parameter a_1 , which was fixed at 3, and C corresponds to a_2 , which is used for the determination of interfacial tension.

v_0 , k_n , and λ were assumed to be the same as those used previously for urea in absolute ethanol. Table 5.10 presents values of effective interfacial tension (γ_{eff}), the critical nucleus radius (r^*), the number of molecules in the critical radius (i^*), and the nucleation rate (J).

Table 5.10: Calculated progressive nucleation kinetics for urea and 1% w/w biuret in ethanol.

Conc (g/mL)	q	μ_c	$\ln q_0$ [A]	a_1 [B]	a_2 [C]	V_{eff} (mJ/m ²)	r^* (nm)	i^*	J (1/nm ³ .s)
0.04	0.5	0.070	9.173	3	0.00918	5.862	0.562	9.854	9.25
	1	0.084					0.466	5.594	30.15
	2	0.094					0.416	3.979	55.77
	5	0.098					0.400	3.547	67.73

The results obtained for progressive nucleation kinetics for urea with 1%w/w biuret shows that the addition of biuret increased the effective interfacial tension. This increase in interfacial tension was also accompanied by a decrease in the critical nucleus radius and in the number of molecules in the critical nucleus radius. Additionally, at higher relative undercoolings, the addition of biuret results in a much higher nucleation rate in comparison with the pure urea system, by a factor of 3. At lower undercoolings, the rate at which the system is heated and cooled is sufficiently slow enough to allow the system to accommodate for changes in temperature and reach supersaturation much slower, however at higher undercoolings, supersaturation is reached rapidly, with a much smaller number of molecules in the critical nucleus radius, resulting in dramatic increase in nucleation rate.

5.4.2.2 Instantaneous Nucleation Kinetics for Urea and 1%w/w Biuret in Absolute Ethanol

Nucleation data obtained at higher concentrations for urea and 1%w/w biuret in absolute ethanol was analysed further, to determine instantaneous nucleation kinetics. These values were then compared to the values obtained for the system containing only urea, to establish the effect of the addition of biuret on kinetic parameters associated with the instantaneous nucleation mechanism.

Table 5.11: Calculated instantaneous nucleation kinetics for urea with biuret in ethanol.

Conc (g/mL)	K_G (m/s)	$\ln q_0$	n+1	n	$k_v (2A_0)$	d	m	C_0
0.046	3.42×10^{-8}	9.0555	3.1430	2.1430	3.85×10^{-9}	1	0.5	4.16×10^{14}
0.050	3.42×10^{-8}	9.5117	3.0037	2.0037	3.85×10^{-9}	1	0.5	7.45×10^{14}
0.058	3.42×10^{-8}	8.9046	2.3939	1.3939	3.85×10^{-9}	1	0.5	6.18×10^{14}
0.066	3.42×10^{-8}	6.1119	1.7530	0.7530	3.85×10^{-9}	1	0.5	1.32×10^{14}

The values of q_0 and $(n+1)$ were obtained from the plot of q vs μ_c in \ln - \ln coordinates. The concentration of nuclei (C_0), therefore, could be calculated through the following assumptions: $d = 1$, $m = 0.5$, $K_G = 3.42 \times 10^{-8}$, $k_v = 3.85 \times 10^{-9}$. The value of d is the dimensionality of crystal growth, and was assumed to be 1 as that corresponds to growth of needle-like crystals, m is a growth exponent for the system and was assumed to be 0.5 to indicate undisturbed diffusion of the solute to the crystal surface, K_G is the overall growth rate of the crystal, and was determined through single crystal experiments, where an average value of the growth rate was taken. Finally, k_v is the crystallite growth shape factor calculated through $k_v = 2A_0$, where A_0 is the fixed cross sectional area of a needle. The widths of urea crystals grown in the presence of biuret were measured, and an average value was taken as an approximation to calculate A_0 .

A comparison of the overall growth rate of the crystal for urea crystals grown with and without the presence of biuret in the system, shows that the presence of biuret hindered the growth of urea single crystals as the growth rate was much lower. Additionally, comparing the crystallite growth shape factor of both systems, it can be observed that the urea single crystals grown in the presence of biuret had a greater cross sectional area than those grown without the presence of an additive. Therefore, it can be concluded that the addition of biuret not only slowed the growth rate of urea single crystals, but the resultant crystals were also less needle-like.

Values of n are used to determine the rate limiting step of the growing crystallites, for example, if $n = 1$, this is indicative of a system where the growth of a crystallite is rate limited only by the diffusion of the growth unit to the growing crystallite. Also, if $n = 2$, this is indicative of a system where the growth of a crystallite is rate limited by the

rearrangement of the solute at the crystal/solution interface. The calculated values of n presented in Table 5.11 show that with increasing concentration, the rate limiting step changes from a system where the growth of a crystallite is rate limited by the rearrangement of the solute at the crystal/solution interface to a system where the growth is rate limited by the diffusion of a growth unit to the growing crystallite. Comparing these values with those obtained for the system without the presence of biuret shows that the addition of biuret changes the rate limiting step, by hindering the diffusion of urea to the growing crystallite.

The calculated concentration of nuclei (C_0) decreases with increasing concentration, as presented in Table 5.11, which was also found to occur in the system without the presence of biuret. However, at lower concentrations the concentration of nuclei in the presence of biuret was greater than that of the system containing only urea.

5.5 Growth Rate as a Function of Solution Environment, Predicted Growth Mechanism and Kinetics

Urea single crystals were grown in solution in a 0.5mL cuvette immersed in water in a cell. The growth rates of two faces, {110} and {111} were measured, and this data was used, along with intermolecular interactions to predict the growth mechanism and crystallisation kinetics.

5.5.1 Growth Rate of Urea Single Crystals as a Function of Solution Environment

Experimental growth rate data for urea in absolute ethanol and urea with 1% biuret in absolute ethanol has been provided in Appendix B1 and Appendix B2, respectively, which comprises of 60 single crystals spontaneously nucleated and grown over a supersaturation range from ~ 0.05 to 0.3. The crystals were grown in a stagnant solution under diffusion limited conditions in a 0.5mL cuvette immersed in water in a cell. The distance between the centre of the crystal and the face was then measured as a function of time. 30 of these single crystals have been grown in the presence of 1%w/w biuret, to determine the effect of an additive on the growth rate, mechanism and kinetics of a single crystal of urea.

The initial and final images of crystals grown spontaneously in the cuvette are shown in Table 5.12, where initial and final images on the left correspond to the single

crystals grown in absolute ethanol and initial and final images on the right correspond to the single crystals grown in the presence of 1%w/w biuret and absolute ethanol. Final images were taken when visible growth of the crystals could no longer be observed.

Table 5.12: An example of the experimental crystal images obtained at the initial and final time points for urea in ethanol and urea and 1% w/w biuret in ethanol at each supersaturation.

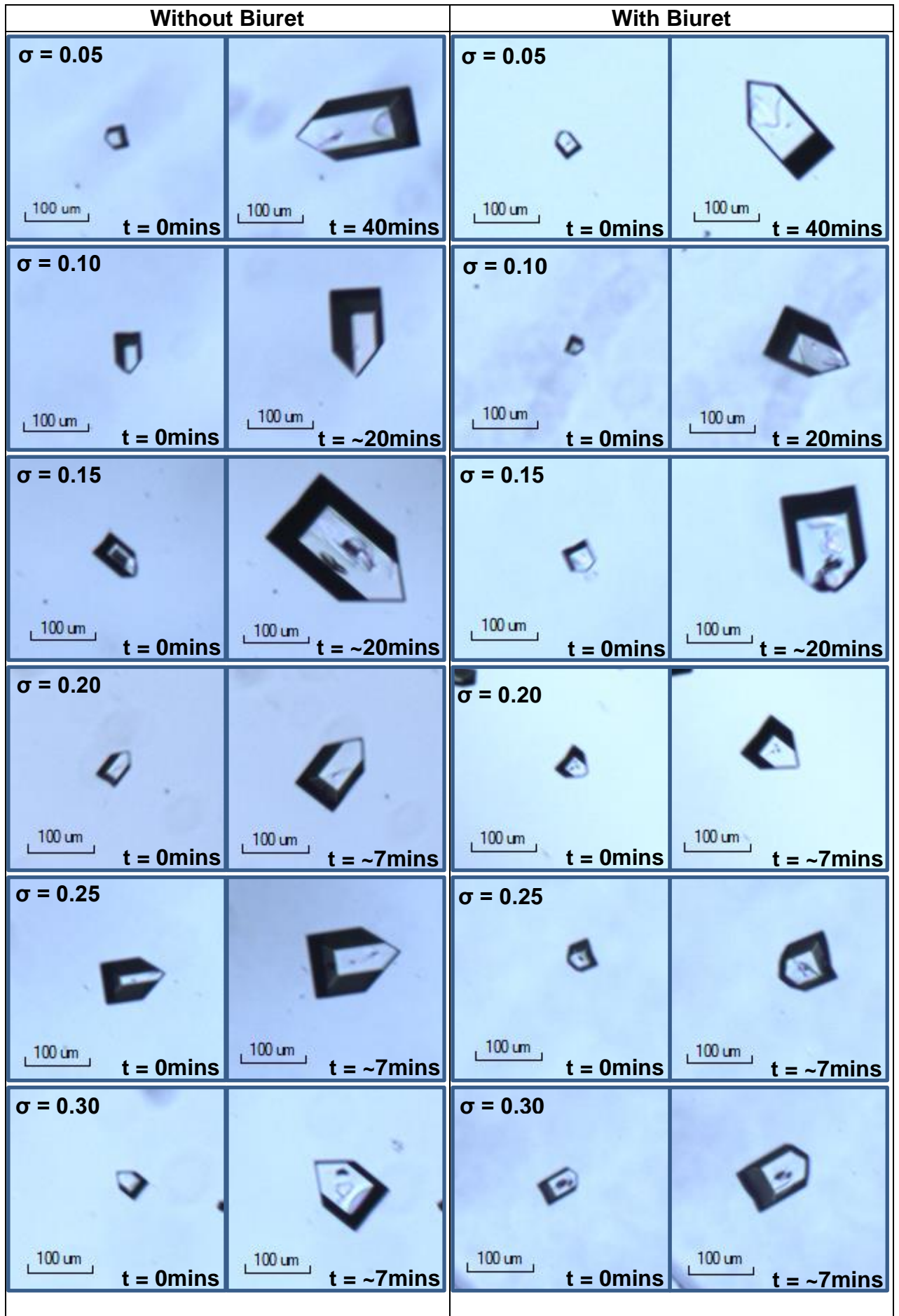


Table 5.13: Experimental mean growth rates and standard deviations obtained from crystal growth experiments of urea in ethanol and urea and 1% w/w biuret in ethanol.

	σ	Number of Crystals	Mean Growth Rate ($\mu\text{m/s}$)	
			{110}	{111}
Urea in Absolute Ethanol	0.05	5	0.009 ± 0.003	0.017 ± 0.007
	0.10	5	0.019 ± 0.008	0.030 ± 0.008
	0.15	5	0.039 ± 0.014	0.052 ± 0.014
	0.20	5	0.036 ± 0.018	0.059 ± 0.017
	0.25	5	0.047 ± 0.018	0.056 ± 0.018
	0.30	5	0.058 ± 0.012	0.072 ± 0.015
Urea and 1%w/w Biuret in Absolute Ethanol	0.05	5	0.009 ± 0.002	0.017 ± 0.003
	0.10	5	0.020 ± 0.004	0.027 ± 0.008
	0.15	5	0.029 ± 0.004	0.043 ± 0.005
	0.20	5	0.031 ± 0.009	0.047 ± 0.010
	0.25	5	0.036 ± 0.005	0.050 ± 0.009
	0.30	5	0.042 ± 0.004	0.058 ± 0.010

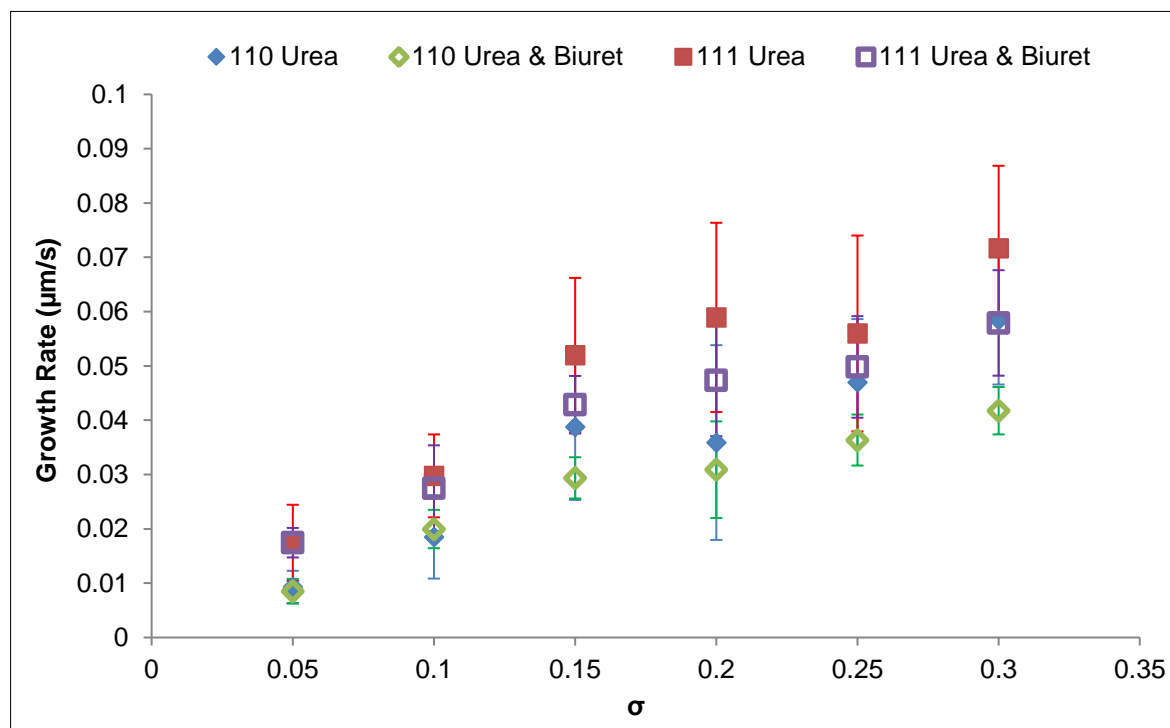


Figure 5.11: The relationship between growth rate and supersaturation for the {110} and {111} faces of urea in a pure system and with an additive in the system.

The growth rates of urea single crystals grown in ethanol, with and without 1%w/w biuret, at different levels of supersaturation show that the growth rate follows a first order dependence on supersaturation, and the addition of biuret does not affect this linear relationship. The mean growth rates of the {110} and {111} faces are both found to increase with increasing relative supersaturation, however the {111} face is found to have a more significant increase than the {110} face.

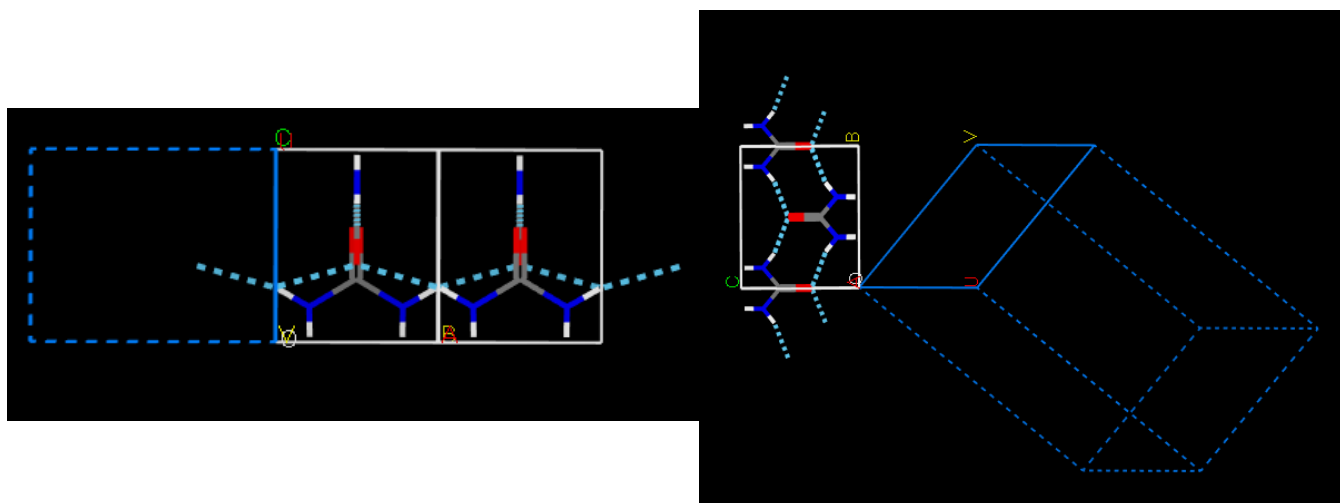


Figure 5.12: The unit cell of urea showing growth in the {110} direction and {111} direction, respectively.

The significant difference in growth rates for both faces of urea in ethanol can be attributed to the solvent environment, as ethanol is a polar protic solvent and as can be seen from Figure 5.12, growth in the {110} direction is hindered by the formation of hydrogen bonds with ethanol. This is reinforced by the experimental growth of urea in other polar solvents such as water and methanol which also form needle-like crystals, as the growth in the {110} direction is significantly decreased due to the interaction of the solvent with the crystal face. (Docherty, 1993).

Additionally, Salvalaglio et al. (2013) examined urea crystallisation from solutions of different compositions. Urea was crystallised in ethanol and acetonitrile to determine morphologies for different solvents, and it was theorised that in acetonitrile the growth of both the {110} and {111} faces were similar as it resulted in a prismatic-like crystal.

5.5.2 Predicted Growth Mechanism and Kinetics

The growth mechanism of a single crystal can be predicted through the calculation of attachment energies of morphologically important faces. These, in turn, can then be used to determine surface entropy α -factor values, which are dependent upon the nature of the interaction between solute and solvent. A lower α -factor implies the growth of a rough surface, and higher α -factor values are attributed to the growth of smoother faces through the BCF or B&S mechanisms. (Davey, 1982; Nguyen et al., 2017)

Table 5.14: α -factor ranges with their corresponding growth mechanism.

α-Factor Range	Predicted Growth Mechanism
$\alpha < 2$	The interface is rough; hence all growth units can be incorporated onto the growing surface (RIG).
$2 < \alpha < 5$	The interface is smoother, and the most probable mode of growth is B&S.
$\alpha > 5$	The surface becomes very smooth, and growth generally proceeds by screw dislocation (BCF).

For each of the morphologically important faces, the lattice energy was divided with respect to their contribution to the growth process of the crystal surface, through the calculation of slice and attachment energies.

The anisotropy factor ($\xi_{hkl} = E_{sl}^{hkl}/E_{cr}$) reflects the degree of saturation of a molecule when it is surface terminated and a fraction of the intermolecular interactions have been disconnected. Lattice, slice and attachment energies of the {110} and {111} faces were obtained from Yusop (2014).

Table 5.15: Calculated α -factors, anisotropy factor and predicted growth mechanism for the {110} and {111} faces of urea.

Face	Supersaturation (%)	Mole Fraction [Xseq]	T (K)	α -Factor	Predicted Mechanism	ξ
{110}	5	0.051	300	6.86	BCF	0.81
	10	0.053	298	6.85	BCF	
	15	0.056	296	6.85	BCF	
	20	0.058	294	6.84	BCF	
	25	0.061	293	6.82	BCF	
	30	0.063	291	6.82	BCF	
{111}	5	0.051	300	6.75	BCF	0.80
	10	0.053	298	6.74	BCF	
	15	0.056	296	6.73	BCF	
	20	0.058	294	6.73	BCF	
	25	0.061	293	6.71	BCF	
	30	0.063	291	6.71	BCF	

Table 5.15 shows the predicted mechanism for each face at different levels of supersaturation. The supersaturation of the solution did not increase enough to change the predicted growth mechanism, therefore the BCF mechanism was the predicted mechanism of growth for urea in absolute ethanol, meaning that the growth process for both faces was predicted to be very smooth and would take place through screw dislocation.

5.5.3 Calculated Growth Mechanism and Kinetics

As the experimental method used to determine the growth rates of single crystals did not incorporate agitation, the growth rates of the crystals have two influences – the first being the diffusion of growth units in the bulk solution towards the crystallite, and the second being the incorporation of the growth unit into the crystallite surface. As the two effects act simultaneously, the driving force of the growth of the crystal is shared between the two, allowing for the determination of a rate-limiting step. Camacho et al. (2017) derived growth models which combine these two effects on the growth of a single crystal acting in series, using an analogy of a circuit.

The power-law equation was first calculated which is a good approximation for the BCF growth mechanism, when $1 < r < 2$, and then BCF and B&S kinetic growth models were evaluated to determine the rate-limiting step during the growth process.

Table 5.16: Calculated growth mechanisms for the {110} and {111} surfaces of urea with and without the addition of biuret in the system.

Fitting Model		Urea in Ethanol		Urea and 1%w/w Biuret in Ethanol	
	Range of σ	0.04-0.32			
	Faces	{110}	{111}	{110}	{111}
Power Law	$\frac{1}{k'_{MT}}$	5.2x10⁶	3.9x10⁶	4.1x10⁶	2.0x10⁶
	k_{MT}	8.8x10 ⁻⁸ - 1.1x10 ⁻⁷	1.2x10 ⁻⁷ - 1.5x10 ⁻⁷	1.1E-07- 1.4E-07	2.4E-07- 3.0E-07
	$\frac{1}{k_G(\sigma)^{r-1}}$	2.0x10⁴	2.0x10⁴	4.5x10⁵- 3.4x10⁶	7.0x10⁵- 3.5x10⁶
	k_G (m/s)	5.0x10 ⁻⁵	5.0x10 ⁻⁵	9.3x10 ⁻⁸	1.1x10 ⁻⁷
	r	1.00	1.00	0.00	0.20
	R ²	96%	80%	99%	96%
B&S	$\frac{1}{k'_{MT}}$			5.2x10⁶	2.1x10 ⁵
	k_{MT}			8.8x10 ⁻⁸ - 1.1x10 ⁻⁷	2.2x10 ⁻⁶ - 2.7x10 ⁻⁶
	$\frac{1}{k_G(\sigma)^{-\frac{1}{6}}e^{\left(\frac{A_1}{\sigma}\right)}}$			2.0x10²- 2.4x10⁶	2.0x10⁶- 4.9x10⁶
	k_G (m/s)			8.5x10 ⁻⁸	1.5x10 ⁻⁷
	A ₁			0.438	0.027
	R ²			100%	94%
BCF	$\frac{1}{k'_{MT}}$	2.7x10⁶	1.4x10⁶	4.1x10⁶	1.9x10⁶
	k_{MT}	1.7x10 ⁻⁷ - 2.1x10 ⁻⁷	3.4x10 ⁻⁷ - 4.3x10 ⁻⁷	1.1x10 ⁻⁷ - 1.4x10 ⁻⁷	2.5x10 ⁻⁷ - 3.1x10 ⁻⁷
	$\frac{1}{k_G(\sigma) \tanh\left(\frac{A_2}{\sigma}\right)}$	2.5x10⁶- 2.5x10⁶	2.6x10⁶- 2.6x10⁶	2.6x10⁶- 2.6x10⁶	2.9x10⁶- 2.9x10⁶
	k_G (m/s)	4.8x10 ⁻⁵	5.0x10 ⁻⁵	5.0x10 ⁻⁵	5.0x10 ⁻⁵
	A ₂	0.008	0.008	0.008	0.007
	R ²	96%	80%	89%	74%
Rate Limiting Step		Balance between diffusion and surface integration	Surface integration	Diffusion of growth units	Surface integration

The best fittings to experimental data for urea grown from ethanol without the presence of an additive were obtained through the BCF model. In the evaluation of the power law model, a value of r obtained between 1 and 2 is considered a good approximation for the BCF growth mechanism. (Garside, 1985). Therefore, a value of $r=1$ which was obtained, was associated with the BCF mechanism. This shows that the rate limiting step for the $\{110\}$ face was between the diffusion of growth units in the solution and the surface integration of growth units into the crystal as the resistance values were found to be comparable. The rate limiting step for the $\{111\}$ face was found to be surface integration as the resistance value was much higher.

The rate limiting factors changed with the addition of 1%w/w biuret into the system, as values of r equal to 0 and 0.2 did not correspond with either model, therefore values were obtained from fitting both BCF and B&S model calculations, and compared to determine the rate-limiting step. BCF was found to have a better fit as B&S resulted in a wide range of values for the resistance to surface integration. Therefore, the rate limiting step for the $\{110\}$ face was found to change as the resistance to diffusion of the growth units significantly increased with little to no effect on the surface integration. This can be explained through experimental growth rate determination as the growth rate of the face did not change, as the surface integration value of growth units into the crystal was comparable between the pure and doped systems. The rate limiting step for the $\{111\}$ face however, did not change between the pure and the doped system and was due to surface integration. This was also observed experimentally, as an increase in resistance to surface integration in the doped system meant a larger barrier to overcome to incorporate the molecule into the crystal surface.

5.6 Surface Characterisation and Effect of Impurity

Molecular modelling using Mercury VisualHabit (Pickering et al., 2017) was carried out alongside experimental nucleation and growth studies in order to determine the molecular effect of biuret on each facet of urea studied.

Crystals of urea exhibit three dominant morphological faces – $\{110\}$, $\{111\}$ and $\{001\}$, which in turn affect the crystal habit of urea, depending on crystallisation conditions. Urea crystals mostly have a needle-like morphology dominated by the $\{110\}$ face,

with smaller {111} and {001} capped faces. The {001} face can also be morphologically insignificant when crystallised under certain conditions.

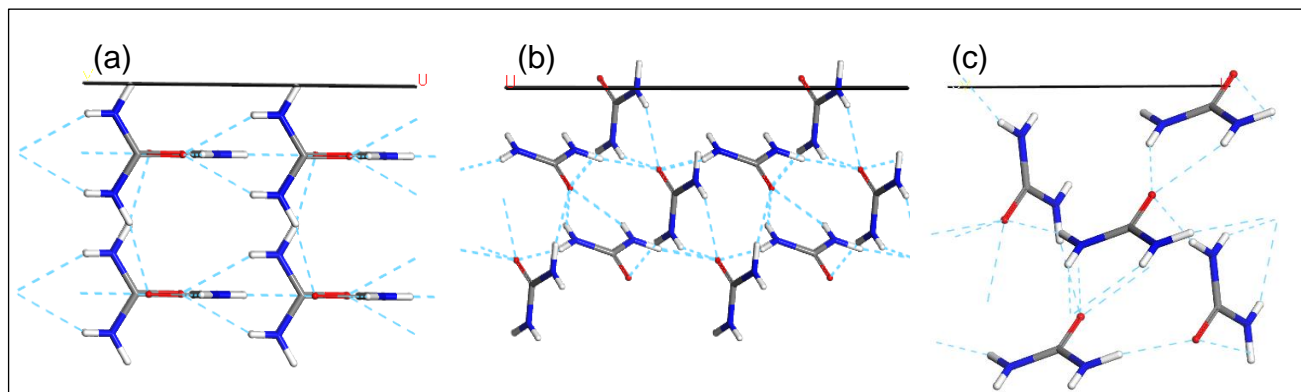


Figure 5.13: Molecular packing of the (a) {110}, (b) {111} and (c) {-1-1-1} surfaces of urea.

In the structure of urea, the two molecules in the unit cell are related through symmetry by the four-fold inversion axes of the space group. Both molecules have different orientations within the unit cell, where one is oriented parallel to the plane of projection and the other is oriented perpendicular to the plane of projection.

The {111} face has a polar opposite face, which in turn affects the surface chemistry at this face. At the {111} surface, the molecule oriented parallel to the plane of projection has a carbonyl group and a hydrogen from the amide group, whereas the molecule oriented perpendicular to the plane of projection has two hydrogens from the amide group. At the surface of the face which is polar opposite to the {111} however, the molecule oriented parallel to the plane of projection has two hydrogens from the amide group at the surface, whereas the molecule oriented perpendicular to the plane of projection has a carbonyl group. Therefore, it would be expected that there would be very little difference in surface chemistry of both polar faces, as there is only one additional hydrogen from the amide group at the {111} surface, hence it would be anticipated that the interactions of biuret with both faces would also be similar. (Docherty, 1993)

The morphology of urea has been predicted previously, alongside key molecular interactions, with two hydrogen bonding existing in a urea crystal (type a and b). Bond type 'a' is formed when the oxygen atom of a urea molecule forms hydrogen bonds with hydrogen atoms surrounding this molecule, and bond type 'b' is formed when the hydrogen atoms of the amide groups of the same urea molecule can form

hydrogen bonds with oxygen atoms from the surrounding molecules. (Docherty, 1993)

The interaction of biuret with the two faces under consideration for this study {110} and {111}, along with the polar opposite face {-1-1-1} were modelled through the systematic search function using Mercury VisualHabit.

5.6.1 {110}

The minimum interaction energy between a probe molecule of biuret and the {110} surface was found through the use of the systematic grid search function in VisualHabit. This minimum interaction energy is the strongest and most stable interaction between the probe and the surface. The grid search employed over one unit cell across the surface of the crystal is shown below. The surface, however, is built of multiple unit cells surrounding the cell in the middle, in order to ensure that edge effects do not interfere with the calculation of interaction energies.

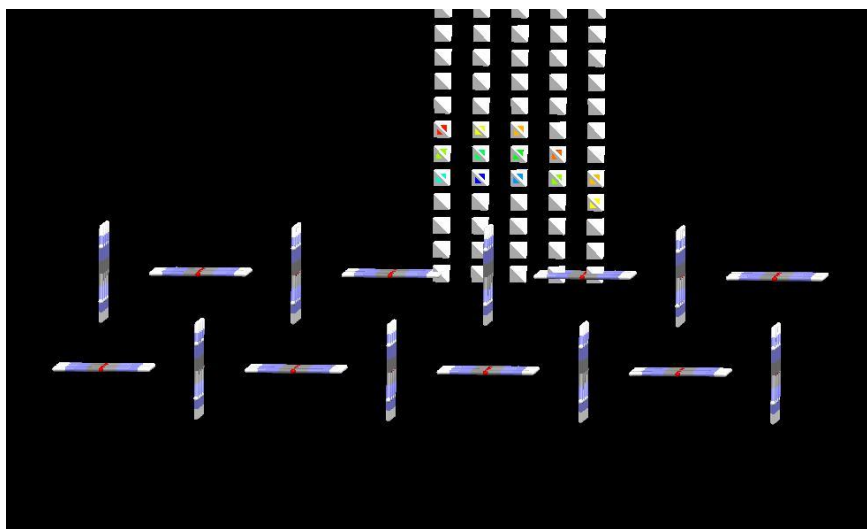


Figure 5.14: An example of the grid search applied to determine interactions of biuret with the {110} surface.

As the grid rows closest to the surface and furthest away from the surface contained only white tetrahedrons, meaning the interactions found in these spaces were small enough to be considered negligible, this placement of grid on the surface was deemed to provide accurate interaction results.

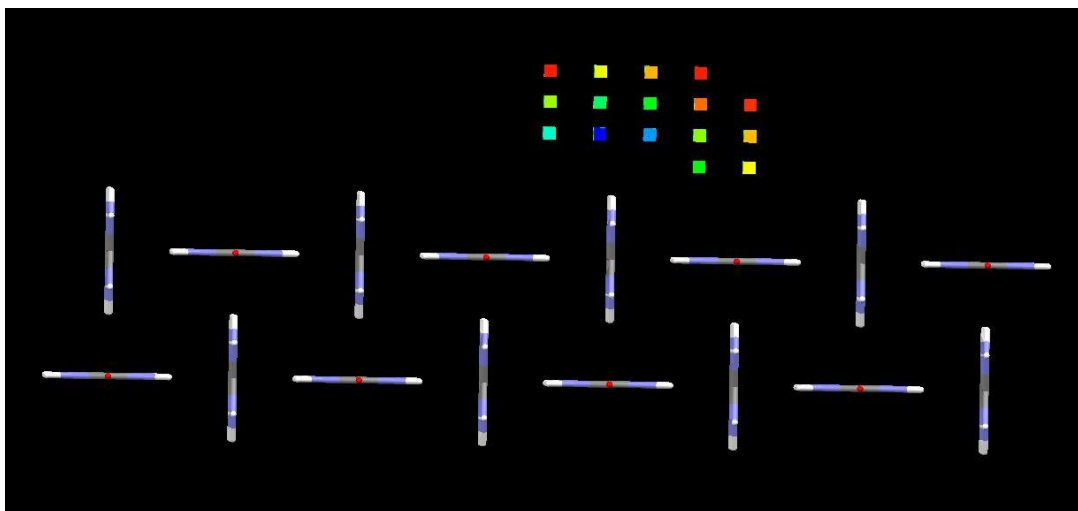


Figure 5.15: Removal of the grid applied to show the varying degrees of biuret interaction with the {110} surface.

Upon removing the grid, there were varying degrees of biuret interaction with the surface found, with the blue tetrahedrons depicting the strongest, and the red depicting the weakest. The highest energy interaction of biuret with the surface of the {110} face is shown in Figure 5.16.

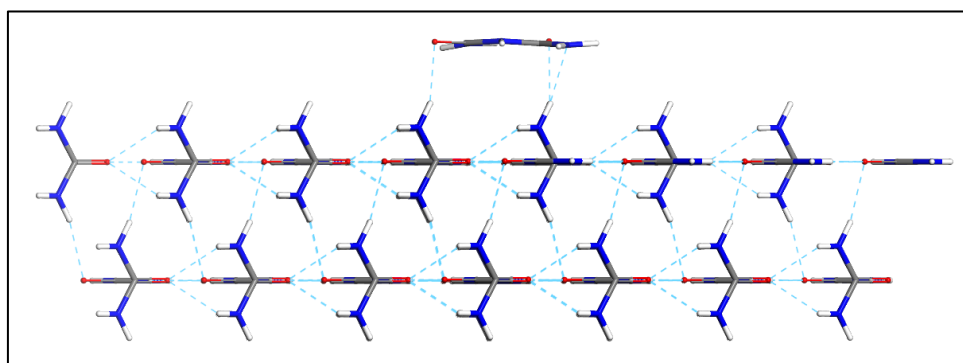


Figure 5.16: The strongest interaction of biuret with the {110} surface, with hydrogen bonding depicted.

Calculation of the interaction energy between the biuret probe molecule and the {110} surface through the SystSearch function allowed for the determination of the total energy interaction and also divided this total energy figure into van der Waals (dispersive), hydrogen bonding and electrostatic interactions. Thousands of interactions were calculated through the systsearch function, however, for the purposes of clarity, the 100 strongest interactions have been presented.

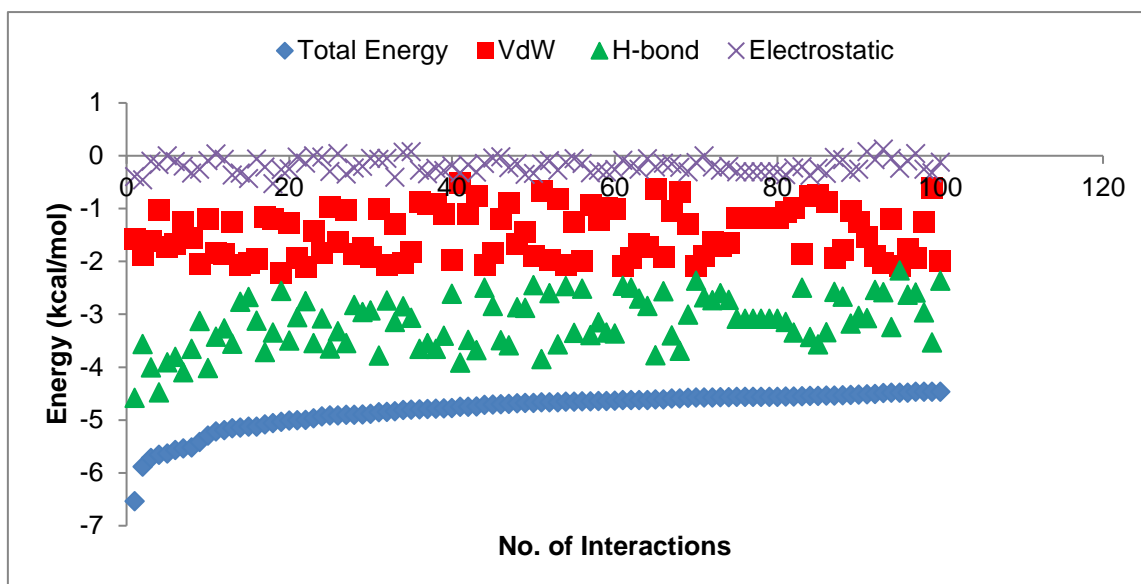


Figure 5.17: The top 100 interactions of biuret with the $\{110\}$ surface, broken down into hydrogen bonding, van der Waals and electrostatic interactions.

This suggests that the majority of the total interaction energy of the biuret probe with the $\{110\}$ surface is due to hydrogen bonding between the probe and surface, with Van der Waals and electrostatic interactions making up a minimal amount of the total interaction energy.

5.6.2 $\{111\}$ and $\{-1-1-1\}$

In order to compare the total interaction energies of biuret with the two faces that are under consideration, the interaction energy of biuret with the $\{111\}$ and its polar face $\{-1-1-1\}$ were also determined. This is because of the slight difference in surface chemistries as mentioned previously, therefore the biuret probe across the surface could have a slightly different interaction with the $\{-1-1-1\}$ face in comparison with the $\{111\}$ face.

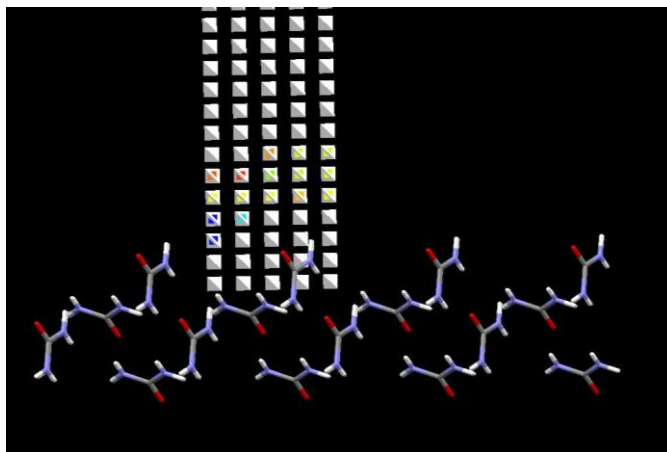


Figure 5.18: An example of the grid search applied to determine interactions of biuret with the {111} surface.

The grid rows closest to the {111} surface and furthest away from the surface contained only white tetrahedrons, meaning the interactions found in these spaces were small enough to be considered negligible, this placement of grid on the surface was deemed to provide accurate interaction results.

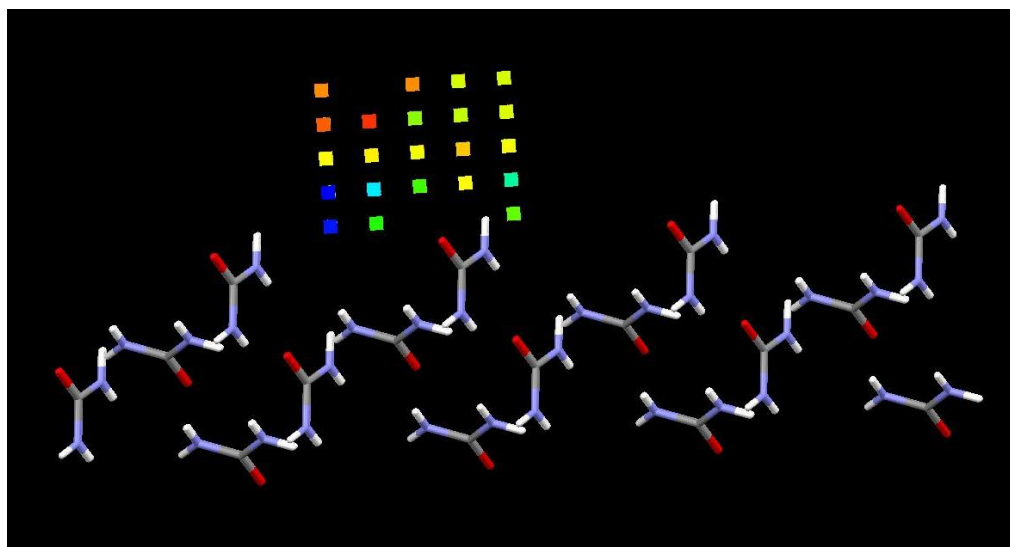


Figure 5.19: Removal of the grid applied to show the varying degrees of interaction of biuret with the {111} surface.

Upon removing the grid, there were varying degrees of biuret interaction with the {111} surface found, with the blue tetrahedrons depicting the strongest, and the red depicting the weakest. The highest energy interaction of biuret with the surface of the {111} face is shown in Figure 5.20.

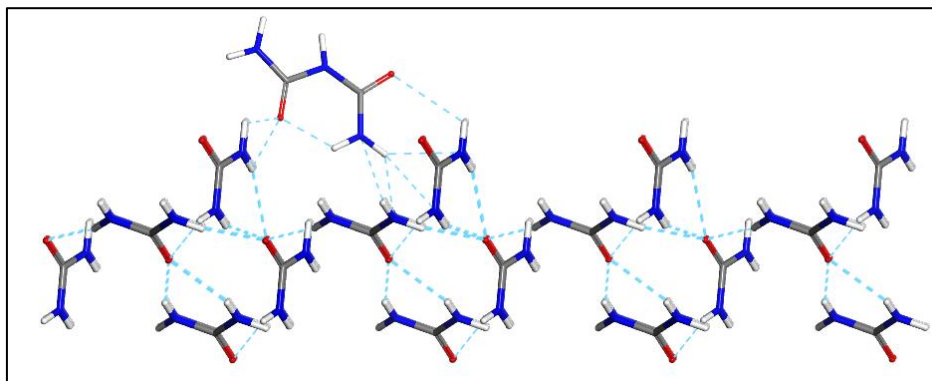


Figure 5.20: The strongest interaction of biuret with the {111} surface, with hydrogen bonding depicted.

The calculation of these energy interactions between the biuret probe molecule and the {111} surface, allowed for the determination of the type of interaction and the strength of these interactions.

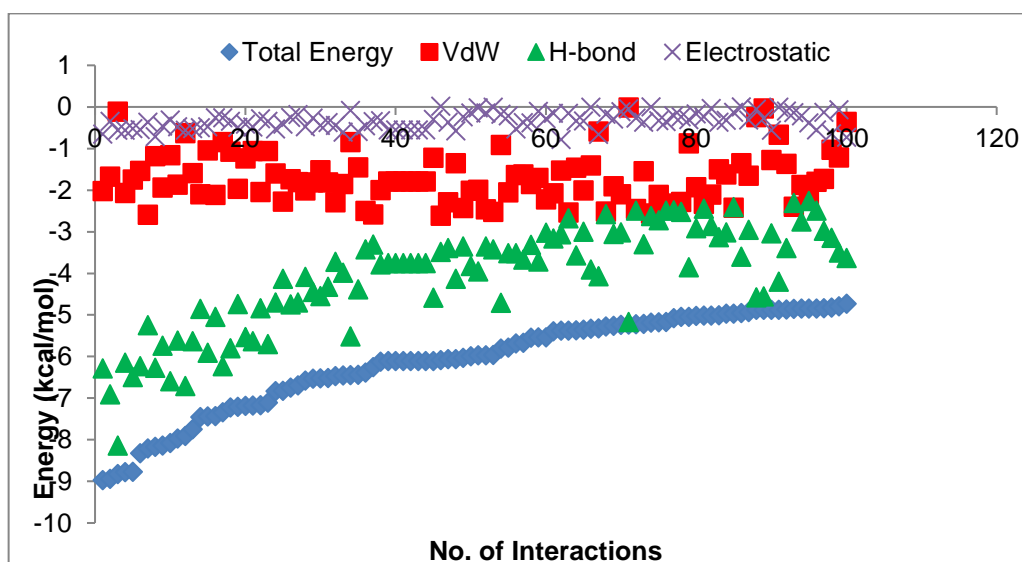


Figure 5.21: The top 100 interactions of biuret with the {111} surface, broken down into hydrogen bonding, van der Waals and electrostatic interactions.

The number of interactions calculated through the SystSearch function were in the thousands, however for the purposes of clarity the strongest 100 interactions have been presented. These top interactions suggest that the interaction of the biuret probe with the {111} surface was mostly due to hydrogen bonding between the two, with Van der Waals and electrostatic interactions making up a minimal amount of the interaction.

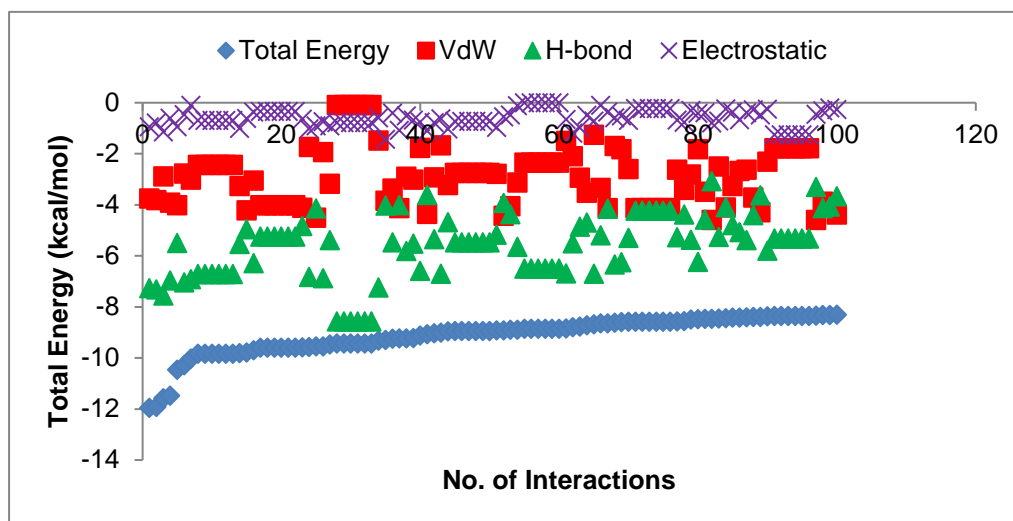


Figure 5.22: The top 100 interactions of biuret with the polar opposite $\{-1-1-1\}$ surface, broken down into hydrogen bonding, van der Waals and electrostatic interactions.

For the polar opposite $\{-1-1-1\}$ face, this same trend was observed, where the total interaction energy is mostly due to the hydrogen bonding between the probe and the surface.

5.6.3 Comparison of Surface Interactions

A comparison of the total interaction energy of the two faces under consideration and the polar $\{1-1-1\}$ face is shown in Figure 5.23.

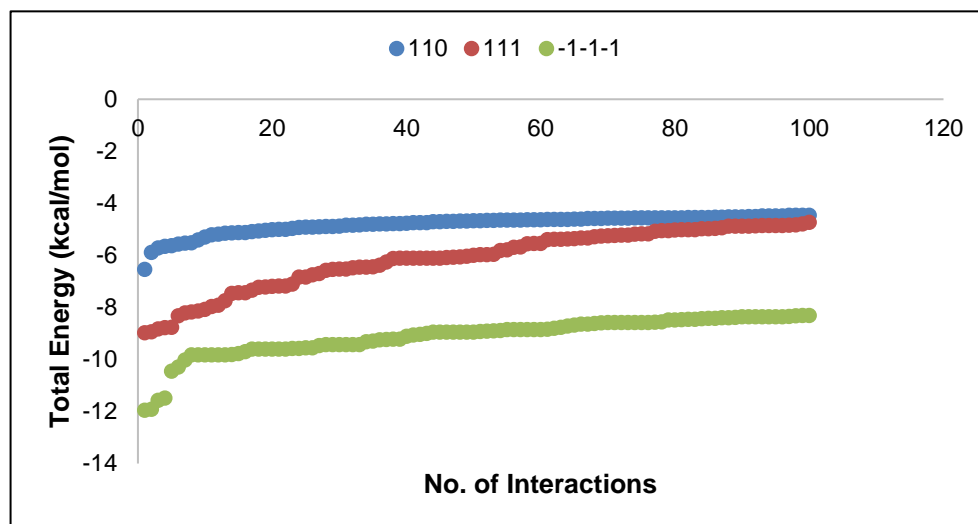


Figure 5.23: Comparison of the total energy interactions of both $\{110\}$ and $\{111\}$ surfaces under consideration, along with the $\{-1-1-1\}$ surface.

The biuret probe was found to have a stronger interaction with the $\{111\}$ and $\{-1-1-1\}$ surfaces in comparison with the $\{110\}$ surface. Additionally, the energies begin to converge to more similar interactions as the total energy interaction becomes lower,

suggesting that as the probe moves away from the surface, the interaction between the probe and all the surfaces become non-specific.

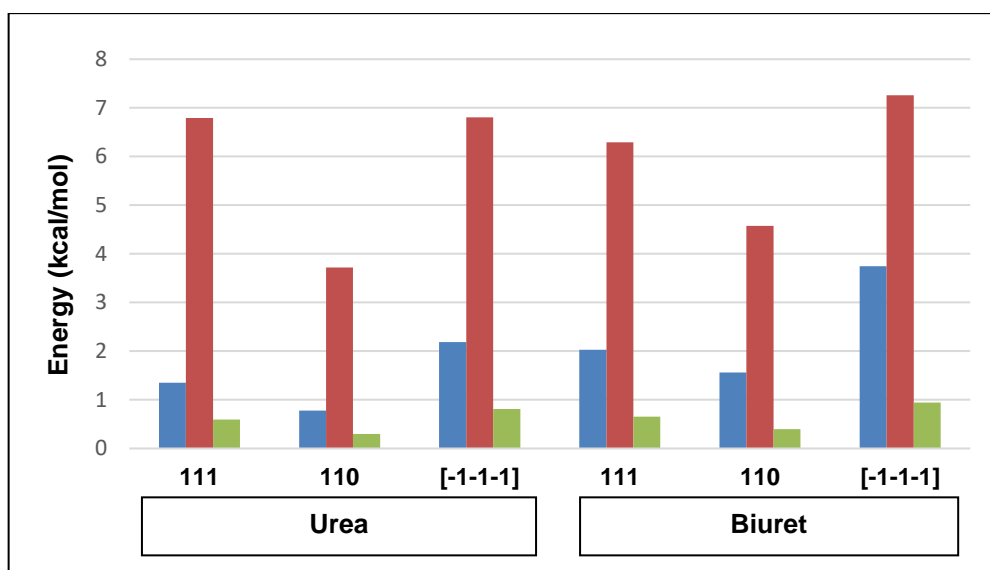


Figure 5.24: A breakdown of interaction energies into hydrogen bonding (■), dispersive van der Waals bonding (■) and electrostatic bonding (■) of urea and biuret with each surface under consideration.

Table 5.17: The total interaction energy of urea and biuret with each face under consideration.

	Total Interaction Energy (kcal/mol)	
	Urea	Biuret
{110}	4.791	6.536
{111}	8.743	8.973
{-1-1-1}	9.804	11.951

A comparison of the total interaction energy of urea and biuret as probes with each of the surfaces under consideration outlined in Figure 5.24 and Table 5.17, shows that the biuret probe was found to have a stronger interaction with all surfaces in comparison with urea. This reinforces the data obtained experimentally, as the addition of biuret in the solution slows down the growth of both faces in comparison with the system containing only urea, and also has a much greater effect on slowing down the growth of the {111} faces. Singh and Tiwari (2015) investigated the molecular scale interaction of urea with biuret to determine the adsorption energies of biuret associated with each face.

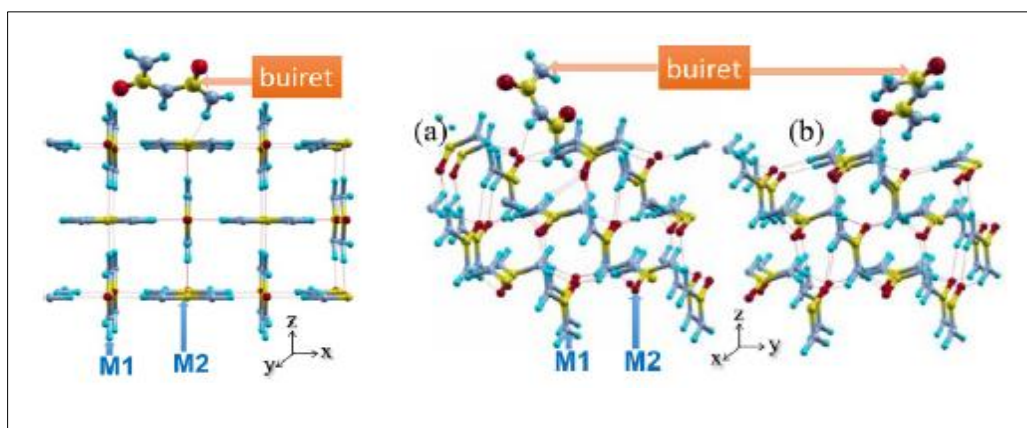


Figure 5.25: Interactions of biuret with the $\{110\}$ and $\{111\}$ surface, respectively, as determined by Singh and Tiwari (2015) through molecular dynamic simulations.

Optimised structures show that there are two distinct molecular orientations of biuret on the surface of the $\{111\}$ face, however there is only one orientation of biuret on the surface of the $\{110\}$ face. Therefore the expectation would be that experimentally, the addition of biuret would have a greater effect on slowing down the growth rate of the $\{111\}$ face than the $\{110\}$ face. This is further reinforced by the relaxed adsorption energies and surface coverage of strongly bonded biuret molecules on different faces relative to the $\{110\}$ face calculated by Singh and Tiwari (2015).

Table 5.18: The calculated adsorption energies and surface coverages of biuret on the $\{110\}$ and $\{111\}$ faces of urea.

Face	Orientation	Adsorption Energy (kJ/mol)	Surface Coverage Relative to $\{110\}$
$\{110\}$		-22.32	1
$\{111\}$	1	-30.05	22.7
	2	-21.95	

Table 5.18 shows that biuret has a stronger adsorption energy on the $\{111\}$ face than the $\{110\}$, and also has a significantly larger surface coverage relative to the $\{110\}$ face. All of these factors result in the expectation that biuret would have a greater effect in slowing down the growth of the $\{111\}$ face in comparison with the $\{110\}$ face, so the resultant crystals would be expected to be much shorter.

The increased resistance, the adsorption energy of biuret being much higher for the $\{111\}$ face, as well as biuret having more than one orientation with which to interact

with the {111} face are all contributing factors to biuret having more of an effect on slowing down the growth of the {111} face relative to the {110} face.

5.7 Conclusions

Solubility studies and the van't Hoff evaluation suggested that the solubility behaviour of urea in absolute ethanol is less than ideal; therefore solute-solute interactions are generally more favoured than solute-solvent interactions.

Determination of the MSZW using the slow cooling polythermal crystallisation method shows that the MSZW of urea in absolute ethanol decreases with increasing concentration due to the rapid onset of supersaturation. The addition of 1%w/w biuret widens the MSZW resulting in a more stable solution, thereby affecting solute-solvent interactions.

Determination of the MSZW using the slow cooling polythermal crystallisation method shows that the MSZW of urea in absolute ethanol decreases with increasing concentration due to the rapid onset of supersaturation, at lower concentrations $\Delta T = \sim 17^\circ\text{C}$, whereas at higher concentrations $\Delta T = 7^\circ\text{C}$. The addition of 1%w/w biuret widens the MSZW resulting in a more stable solution where $\Delta T = 5^\circ\text{C}-22^\circ\text{C}$, thereby affecting solute-solvent interactions.

The nucleation mechanism for urea in ethanol was found to be instantaneous at higher concentrations and progressive at lower concentrations. At lower concentrations, where progressive nucleation took place, the effective interfacial tension was found to decrease from 4.652 mJ/m^2 to 4.495 mJ/m^2 with an increase in concentration. This lower interfacial tension was also accompanied by a faster nucleation rate, with nucleation rates ranging from $9.22 \text{ nm}^{-3}\cdot\text{s}^{-1}$ - $20.48 \text{ nm}^{-3}\cdot\text{s}^{-1}$ for the lower concentration to $11.44 \text{ nm}^{-3}\cdot\text{s}^{-1}$ - $35.22 \text{ nm}^{-3}\cdot\text{s}^{-1}$ for the higher concentration at a progressive nucleation mechanism. The addition of 1%w/w biuret was found to alter the nucleation mechanism where, at a lower concentration, the nucleation mechanism changed from progressive to instantaneous. Additionally, it resulted in a significant increase in the nucleation rates with nucleation rates ranging from $9.25 \text{ nm}^{-3}\cdot\text{s}^{-1}$ - $67.73 \text{ nm}^{-3}\cdot\text{s}^{-1}$.

At higher concentrations, where instantaneous nucleation took place, the crystallite growth shape factor was determined to be larger for crystals grown in the presence of 1%w/w biuret, resulting in crystals with a greater cross-sectional area. Therefore,

biuret affects the morphology of crystallites grown, as they are less needle-like. Additionally, the values of the growth exponent 'n' suggests that the rate-limiting factor for urea in absolute ethanol was due to the rearrangement of the solute at the crystal-solution interface, however the addition of biuret into the system altered this process where at higher concentrations the rate-limiting factor was due to diffusion of a growth unit to the growing crystallite.

Solvent mediated growth rates of {110} and {111} faces of urea showed that the mean growth rates of both faces were found to have a linear dependence on supersaturation, where the growth rates of both faces increased with increasing supersaturation. The growth rate of the {111} face was found to increase greater than that of the {110} face, and this difference was attributed to the difference in surface chemistry at both faces and the interaction of both faces with solvent molecules.

A value of $r=1$ obtained through the power law model was associated with the BCF mechanism for growth in the pure system. As a result of this, the rate limiting step for growth of the {110} face was balanced between diffusion and surface integration of growth units, and for the {111} face was due to surface integration. However, values of $r=0$ and $r=0.2$ were obtained through the power law model for the system containing biuret which did not correspond to either the BCF or B&S model.

Therefore, values obtained from both models allowed for the conclusion that BCF mechanism was a better fit to the data, and the rate limiting step of the {110} face changed as the resistance to diffusion significantly increased with little effect on the resistance to surface integration. However, the rate limiting step for the {111} face stayed the same.

The addition of 1%w/w biuret was found to not have an effect on the linear relationship between growth rate and supersaturation, however biuret had a greater effect in slowing down the growth of the {111} face in comparison with the {110} face. This was found to be due to the interaction of biuret with both faces, as biuret has two distinct molecular interactions with the {111} face, a higher adsorption energy and a significantly larger surface coverage in comparison with the {110} face.

References

- Camacho, D. M.; Roberts, K. J.; Muller, F.; Thomas, D.; More, I.; Lewtas, K. Morphology and Growth of Methyl Stearate as a Function of Crystallisation Environment. *Cryst. Growth Des.* **2017**. 17 (2), 563-575.
- Capuci, A. P. S., N. D. de Carvalho, M. R. Franco Jr, R. A. Malagoni. Solubility of Urea in Ethanol-Water Mixtures and Pure Ethanol from 278.1K to 333.1K. *Revista Ion.* **2016**. 29(2), 125-133.
- Davey, R., S. J. Jancic (Ed), E. J. de Jong (Ed). The Role of Additives in Precipitation Processes. *Industrial Crystallisation 81*. **1982**. North-Holland Publishing Co.
- Docherty, R., K. J. Roberts, V. Saunders, S. Black, R. J. Davey. Theoretical Analysis of the Polar Morphology and Absolute Polarity of Crystalline Urea. *Faraday Discuss.* **1993**. 95, 11-25.
- Garside, J. Industrial Crystallisation from Solution. *Chem. Eng. Sci.* **1985**. 40(1), 3-26
- Kashchiev, D.; Borissov, A.; Hammond, R. B.; Roberts, K. J. Effect of Cooling Rate on the Critical Undercooling for Crystallisation. *J. Cryst. Growth.* **2010**. 312 (5), 698-704.
- Kashchiev, D.; Borissova, A.; Hammond, R. B.; Roberts, K. J. Dependence of the Critical Undercooling for Crystallisation on the Cooling Rate. *J. Phys. Chem.* **2010**. 114 (16), 5441-5446.
- Lee, F-M., L. E. Lahti. Solubility of Urea in Water-Alcohol Mixtures. *J. Chem. Eng. Data.* **1972**. 17(3), 304-306.
- Nguyen, T. T. H., I. Rosbottom, I. Marziano, R. B. Hammond, K. J. Roberts. Crystal Morphology and Interfacial Stability of RS-Ibuprofen in Relation to its Molecular and Synthonic Structure. *Cryst. Growth Des.* **2017**. 17(6), 3088-3099.
- Pencheva, K. Modelling the Solid-State and Surface Properties of Organic Nano-Sized Molecular Clusters. **2006**. PhD Thesis. University of Leeds.
- Pickering, J., R. B. Hammond, V. Ramachandran, M. Soufian, K. J. Roberts. Synthonic Engineering Modelling Tools for Product and Process Design. *Engineering Crystallography: From Molecule to Crystal to Functional Form.* **2017**. NATO: Springer.
- Salvalaglio, M., T. Vetter, M. Mazzotti, M. Parrinello. Controlling and Predicting Crystal Shapes: The Case of Urea. *Angew. Chem. Int. Ed.* **2013**. 52(50), 13369-13372.
- Singh, M. K.; Tiwari, V. S. Uncovering the Mode of Action of Solvent and Additive Controlled Crystallisation of Urea Crystal: A Molecular-Scale Study. *Cryst. Growth Des.* **2015**. 15 (7), 3220-3234.

Turner, T. D. Molecular Self-Assembly, Nucleation Kinetics and Cluster Formation Associated with Solution Crystallisation. **2015**. PhD Thesis. University of Leeds.

Yusop, S. N'A. Characterisation of the Morphological and Surface Properties of Organic Micro-Crystalline Particles. **2014**. PhD Thesis. University of Leeds.

Chapter 6: Dissolution of Urea Single Crystals

6.1 Introduction

Dissolution and crystallisation are opposing processes that occur when a solute is placed in undersaturated or supersaturated solution environments, respectively. Face-specific crystallisation, and the growth mechanism and kinetics of this process, have been widely studied, however dissolution has been assumed to be the direct opposite of this process, with no experimental data to verify this. (Wang et al., 2012) Additionally, computational models can be applied in order to predict the dissolution behaviour of a solute in a solvent based on theoretical equations.

This chapter aims to present the dissolution data of urea in absolute ethanol under the opposing undersaturation conditions as those presented in Chapter 5, allowing for a direct comparison between face specific crystallisation and dissolution. Also presented in this chapter is the dissolution data of urea in acetonitrile, allowing for a comparison in dissolution behaviour in different solution environments. Molecular modelling using Mercury VisualHabit (Pickering et al., 2017) has also been presented in order to determine face dependent molecular interactions between the solution environments.

Finally, following on from previous dissolution studies in ibuprofen (Pickering et al.), a number of dissolution models have been employed to determine the theoretical overall mass loss of a single crystal in differing solution environments, along with a comparison with the overall mass loss determined through experimentation. This chapter also presents an amendment to the dissolution model employed in order to obtain a more accurate prediction for mass loss of a single crystal under non-sink conditions.

6.2 Dissolution of Urea in Absolute Ethanol

Urea single crystals were dissolved in absolute ethanol under differing levels of undersaturation. The experimental dissolution rates of the two morphologically significant faces were determined. The dissolution rates of the faces were then compared to the intermolecular interactions of the two faces under consideration, and conclusions made were reinforced due to energy interactions obtained. Additionally, the collection of dissolution rate data allowed for a direct comparison between crystallisation and dissolution under the same supersaturation and undersaturation conditions, respectively.

6.2.1 Face Specific Dissolution Rate

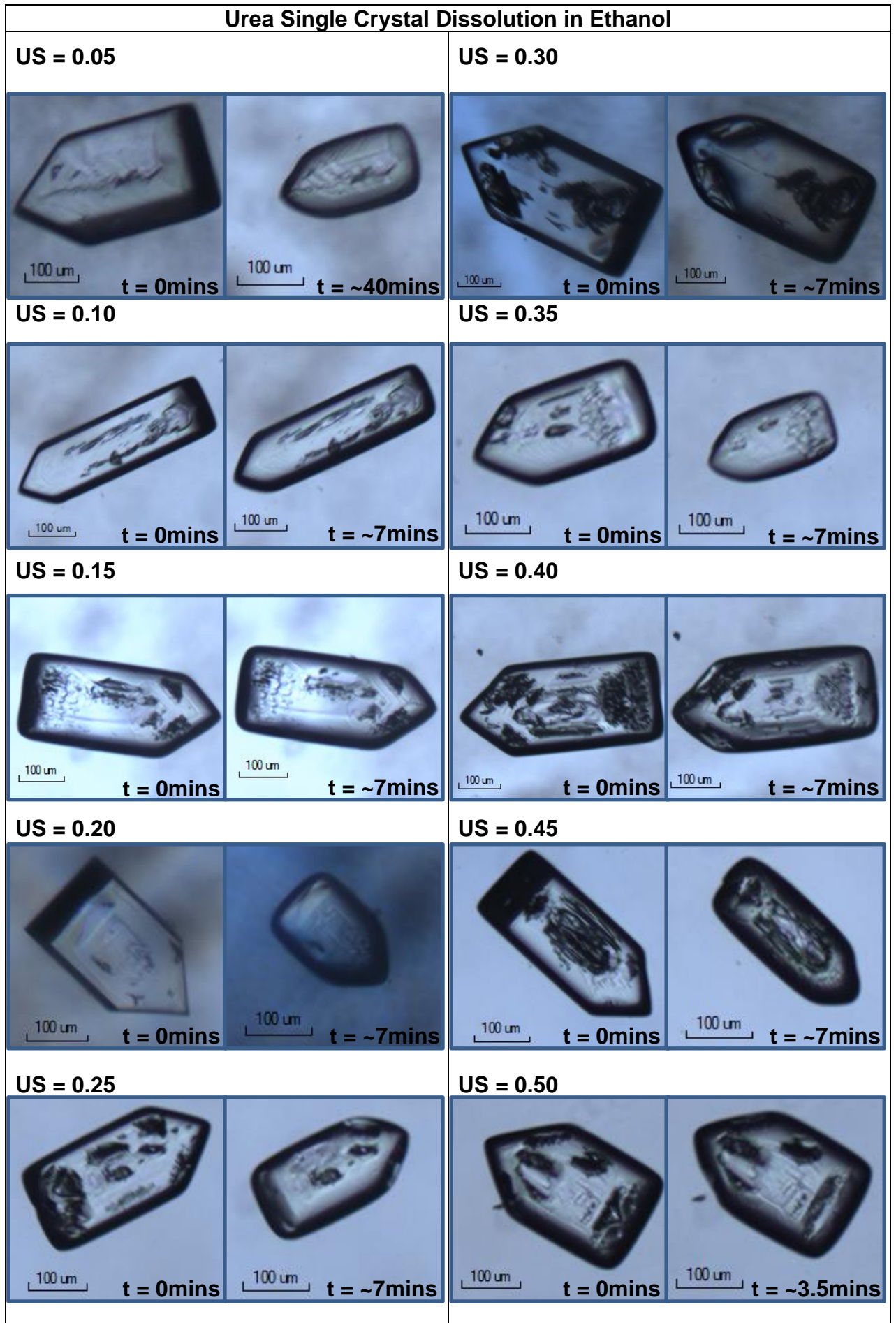
Experimental dissolution rate data has been provided in Appendix C1, which comprises of 50 single crystals spontaneously nucleated and grown in absolute ethanol over a period of three hours. These crystals have then been dissolved over an undersaturation range from ~0.05 to 0.5. The crystals were dissolved in a stagnant solution under diffusion limited conditions in a 0.5mL cuvette, immersed in a water cell. The distance between the centre of the crystal, and the face under consideration was then measured as a function of time.

Table 6.1: Experimental mean retreat rates and standard deviations obtained for urea in ethanol.

US	Number of Crystals	Mean Retreat Rate ($\mu\text{m/s}$)	
		{110}	{111}
0.05	5	0.010 \pm 0.003	0.017 \pm 0.003
0.10	5	0.016 \pm 0.007	0.024 \pm 0.009
0.15	5	0.017 \pm 0.004	0.030 \pm 0.014
0.20	5	0.040 \pm 0.017	0.074 \pm 0.028
0.25	5	0.046 \pm 0.036	0.098 \pm 0.047
0.30	5	0.041 \pm 0.001	0.065 \pm 0.012
0.35	5	0.053 \pm 0.043	0.098 \pm 0.045
0.40	5	0.035 \pm 0.008	0.069 \pm 0.010
0.45	5	0.049 \pm 0.014	0.080 \pm 0.035
0.50	5	0.069 \pm 0.059	0.130 \pm 0.091

The initial and final images of the retreat rate of crystals dissolved in the cuvette are shown in the figure below. Final images were taken when the dissolution of the crystals reached the point where further dissolution would result in rounding of the crystal faces.

Table 6.2: An example of the experimental crystal images obtained at the initial and final time points for urea in ethanol at each undersaturation.



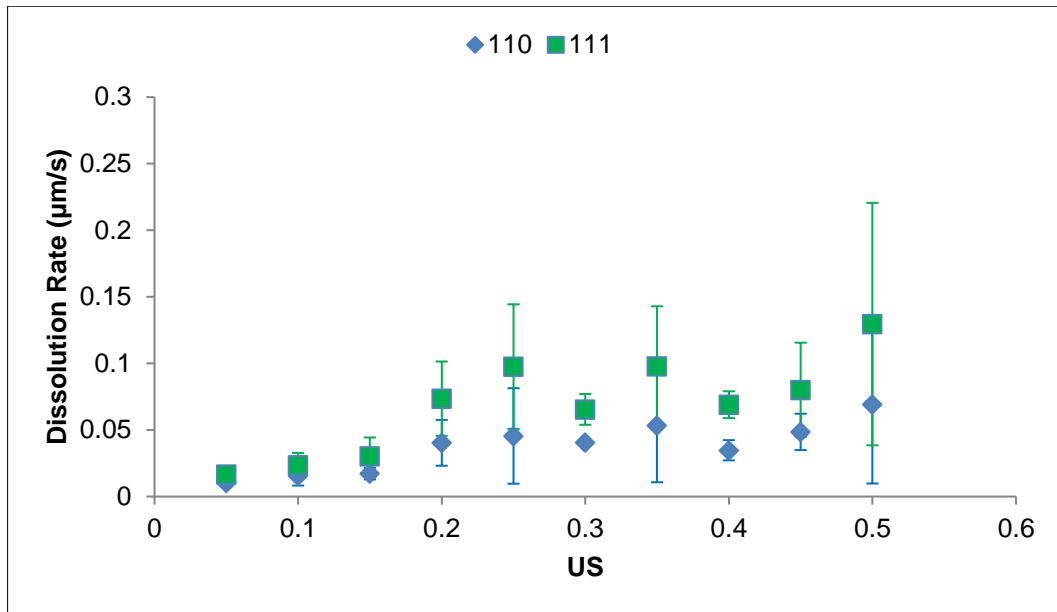


Figure 6.1: The relationship between dissolution rate and undersaturation for the {110} and {111} faces of urea in ethanol

The dissolution rates of the {110} and {111} show that the dissolution rates of both faces follows a first order dependence on undersaturation, with the mean dissolution rates increasing linearly with increasing relative undersaturation. The {111} face was found to have a more significant increase than the {110} face. A direct comparison of the growth rate data obtained in Chapter 5 with the dissolution rate data can be found in Figure 6.2.

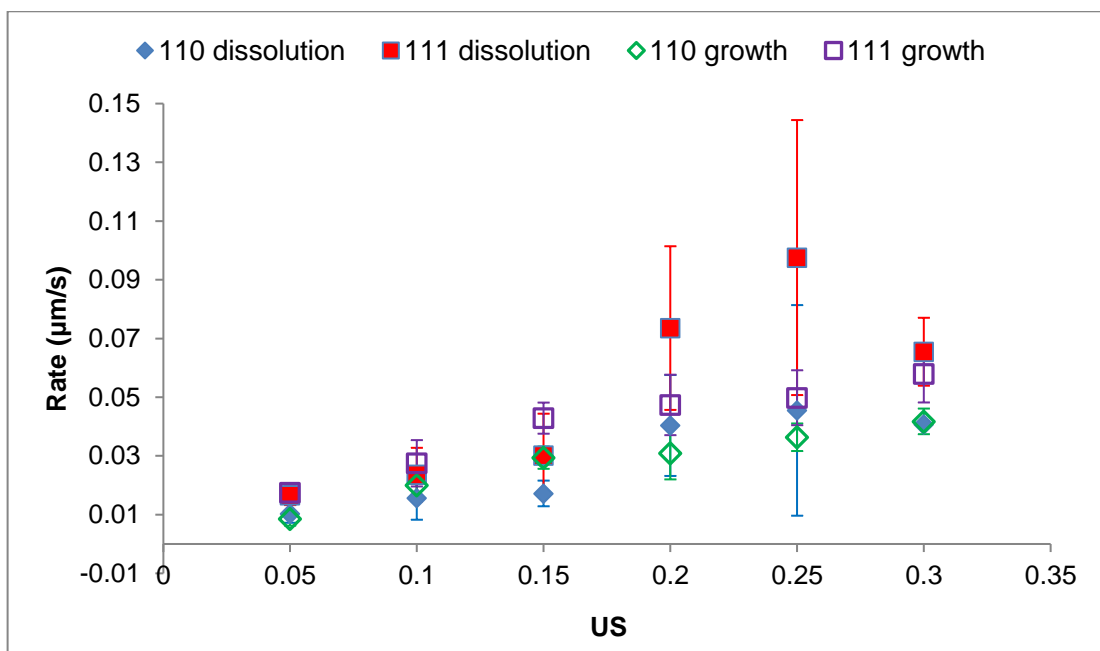


Figure 6.2: A comparison between growth and dissolution rates of the {110} and {111} faces of urea in ethanol.

The dissolution rates of both faces were found to be directly opposite to the growth rate data obtained in Chapter 5. Therefore, it can be concluded that different faces of a crystal can have different dissolution rates due to their interaction with the solution environment, however, in the same environment, the dissolution rate of a particular face of the crystal is the reverse process of crystal growth.

6.2.2 Intermolecular Interactions of Urea with Absolute Ethanol

Surface characterisation of urea has been carried out previously in Chapter 5, with the three main morphologically important faces being identified – {110}, {111} and its polar opposite {-1-1-1}. The interaction of ethanol with the faces under consideration were modelled through the systematic search function using Mercury VisualHabit.

6.2.1.1 {110}

The minimum interaction energy between a probe molecule of ethanol and the {110} surface was found. This minimum interaction energy is the strongest and most stable interaction between the solvent and the solute. The grid search was employed over one unit cell across the surface of the crystal. The surface was built of multiple unit cells surrounding the cell where calculations were carried out, in order to ensure that edge effects do not interfere with the calculation of interaction energies.

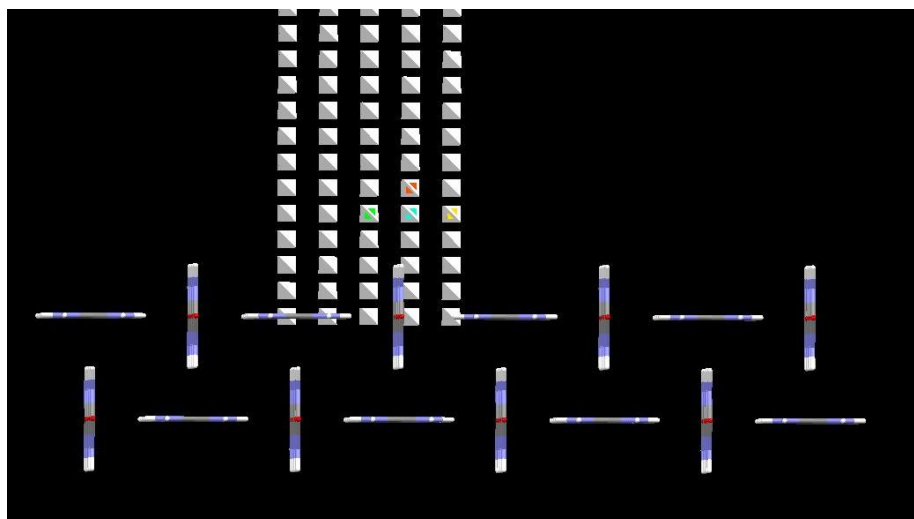


Figure 6.3: An example of the grid search applied to determine interactions of ethanol with the {110} surface.

The grid rows closest to the surface and furthest away from the surface contained only white tetrahedrons, therefore the interactions found in these spaces were small

enough to be considered negligible. Therefore, the placement of the grid on the surface was deemed to provide accurate interaction results.

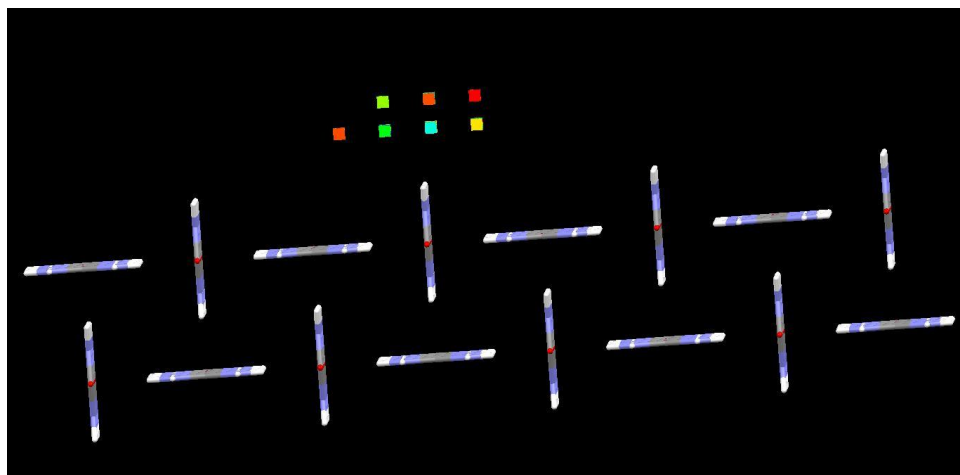


Figure 6.4: Removal of the grid applied to show the varying degrees of ethanol interaction with the {110} surface.

There were varying degrees of interaction found between ethanol and the {110} surface, with blue tetrahedrons depicting the strongest interactions, and the red tetrahedrons depicting the weakest. The highest energy interaction of the ethanol probe with the {110} surface is shown in Figure 6.5.

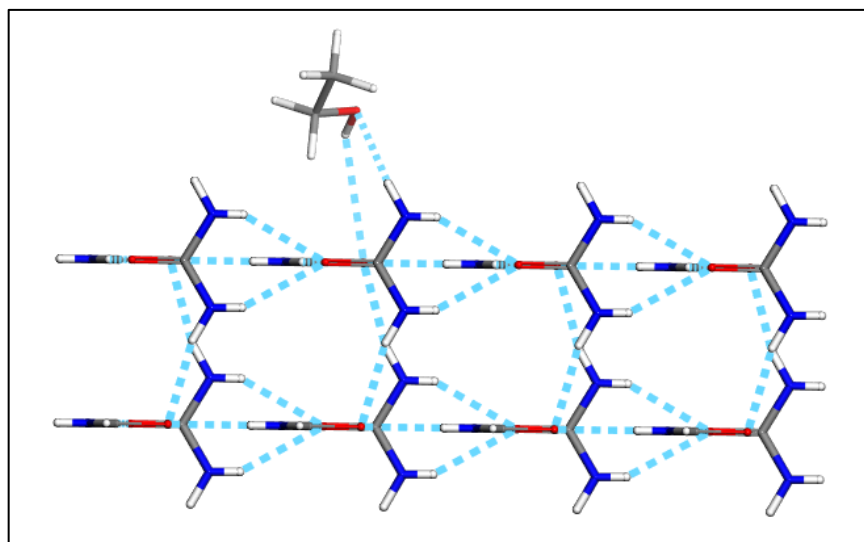


Figure 6.5: The strongest interaction of ethanol with the {110} surface, with hydrogen bonding depicted.

Calculation of the interaction energy between the ethanol probe molecule and the {110} surface through the SystSearch function allowed for the determination of the total interaction energy. Additionally, this total interaction energy was divided into

hydrogen bonding, Van der Waals (dispersive) and electrostatic interactions. Thousands of interaction were calculated, so for the purposes of clarity, the strongest 100 interactions have been presented in Figure 6.6.

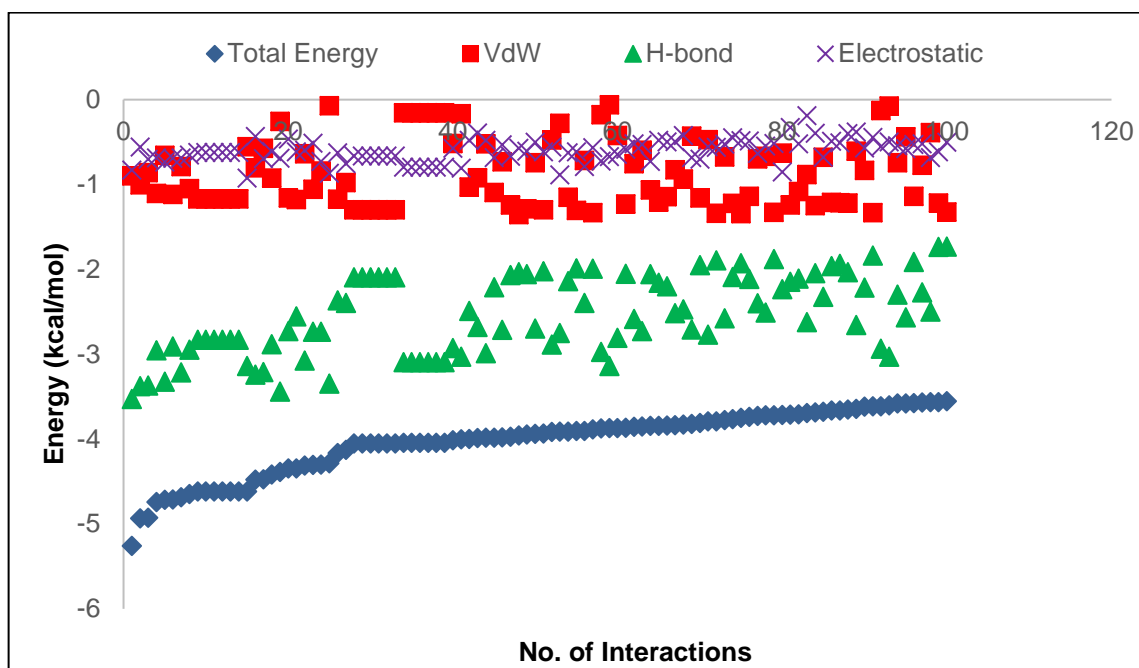


Figure 6.6: The top 100 interactions of ethanol with the $\{110\}$ surface, broken down into hydrogen bonding, van der Waals and electrostatic interactions.

This suggests that the majority of the total interaction energy of the ethanol probe molecule with the $\{110\}$ surface is due to hydrogen bonding between the probe and the surface, with dispersive and electrostatic energy interactions making up a minimal amount of the total interaction energy.

6.2.1.2 $\{111\}$ and $\{-1-1-1\}$

The interaction energies of ethanol with the $\{111\}$ and its polar face $\{-1-1-1\}$ were also determined, to allow for a comparison of the interaction energies between the two faces under consideration. The interaction energies of both faces were determined due to the slight difference in surface chemistries as mentioned in Chapter 5, therefore the ethanol probe could have a different level of interaction with the $\{-1-1-1\}$ face in comparison with $\{111\}$. The same process as was carried out for the $\{110\}$ surface was used for the $\{111\}$ and $\{-1-1-1\}$ surfaces.

Removal of the grid after grid search calculations were carried out showed that there were varying degrees of ethanol interaction with the $\{111\}$ surface calculated, with

the highest energy interaction of the ethanol probe with the surface of the {111} face being shown in Figure 6.7.

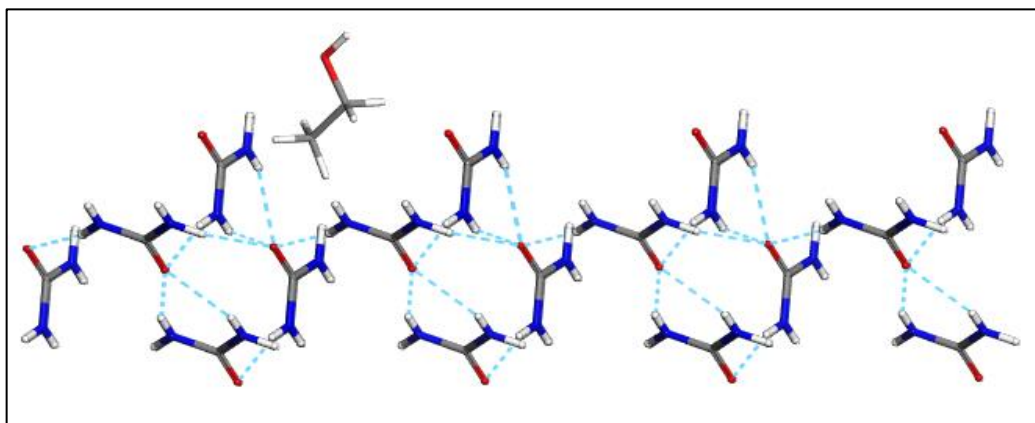


Figure 6.7: The strongest interaction of ethanol with the {111} surface, with hydrogen bonding depicted.

The calculation of these energy interactions between the ethanol probe molecule and the {111} surface allowed for the determination of the type of interaction and the strength of these interactions.

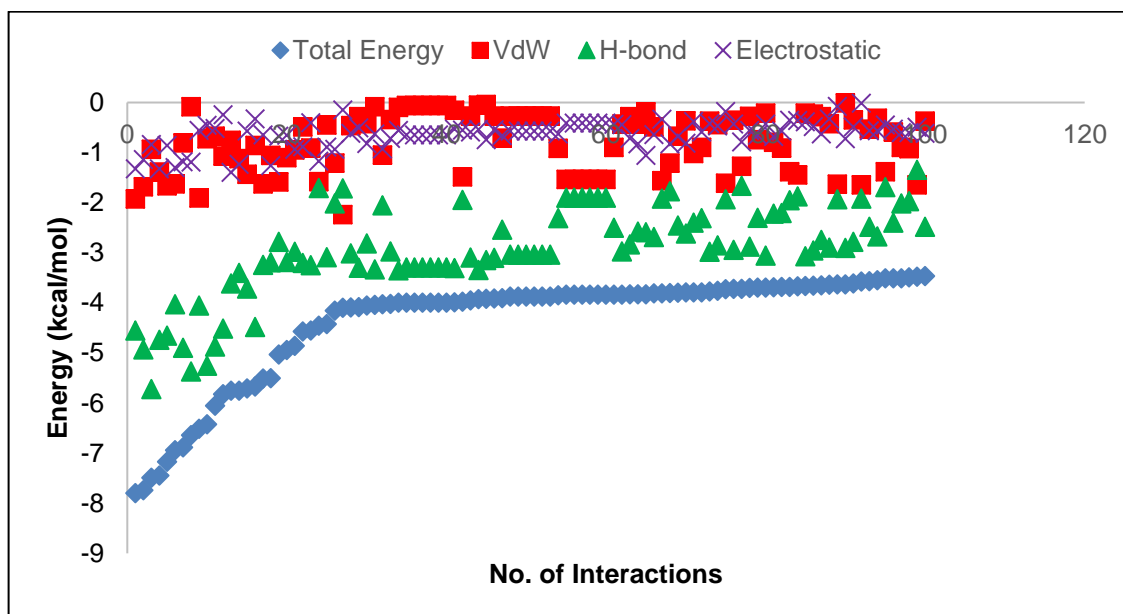


Figure 6.8: The top 100 interactions of ethanol with the {111} surface, broken down into hydrogen bonding, van der Waals and electrostatic interactions.

The number of interactions calculated through the SystSearch function were in the thousands, so for the purposes of clarity the 100 strongest interactions have been presented. These interactions suggest that the interaction of the ethanol probe molecule with the {111} surface was mostly due to hydrogen bonding between the

two, with dispersive and electrostatic energy interactions making up a minimal amount of the interaction.

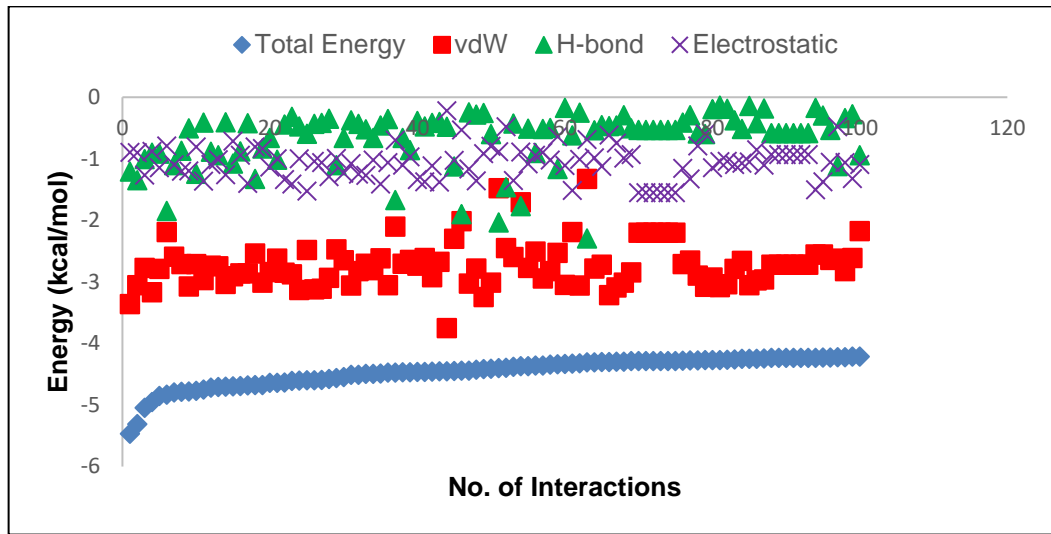


Figure 6.9: The top 100 interactions of ethanol with the $\{-1-1-1\}$ surface, broken down into hydrogen bonding, van der Waals and electrostatic interactions.

For the polar opposite $\{-1-1-1\}$ face, the total interaction energy was mostly due to dispersive interactions between the probe and the surface, with hydrogen bonding and electrostatic energy interactions making up a minimal amount of the interaction.

6.2.1.3 Comparison of Surface Interactions

A comparison of the total interaction energy of the two faces under consideration and the polar $\{1-1-1\}$ face is shown in Figure 6.10.

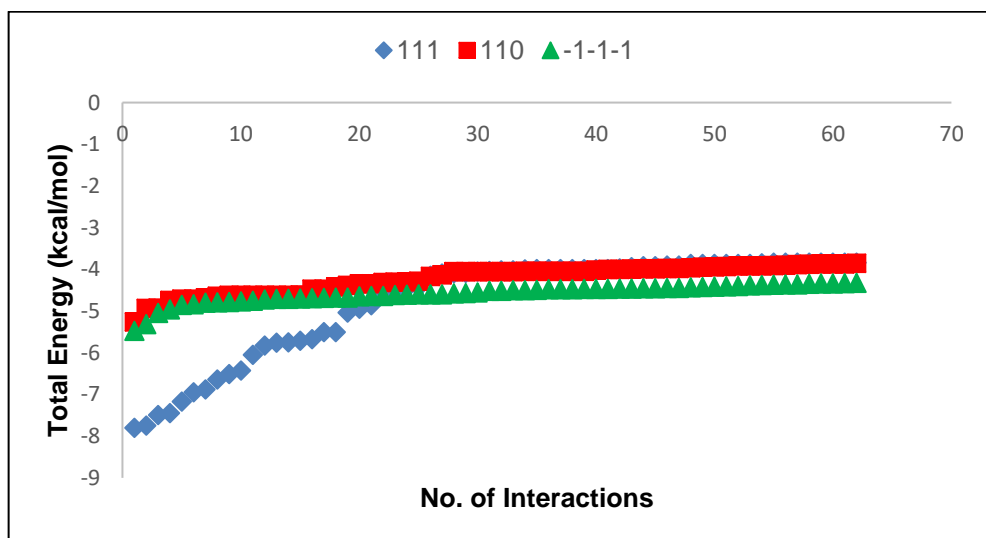


Figure 6.10: A comparison of the total energy interactions of $\{110\}$ and $\{111\}$ surfaces under consideration, along with the $\{-1-1-1\}$ surface.

The ethanol probe molecule was found to have a slightly stronger interaction with the {111} surface in comparison with the {110} and {-1-1-1} surfaces. However, the total energy of all three faces converges in the strongest 20-30 interactions as the total energy interaction decreases, suggesting that the ethanol probe does not have to move far from the surface for the interaction between the probe and all surfaces under consideration to become non-specific.

Wetting energies of the two faces under consideration were also determined through COSMOtherm (Cosmologic, 2019), which can be found in Table 6.3.

Table 6.3: The calculated wetting energies of the {110} and {111} faces of urea.

Face	Wetting Energy (kcal/mol)
{110}	-6.469
{111}	-18.531

As a result of this comparison, it is shown that ethanol has a stronger interaction with the {111} face in comparison with the {110} face, reinforcing the experimental results that {111} will have a faster dissolution rate. Comparing these energy interactions with those determined in Chapter 5, it is found that urea has a stronger interaction with {111} compared to ethanol, however has a weaker interaction with the {110} surface in comparison to ethanol. Additionally, the wetting energy of the {111} face is much larger than that of the {110}, and as the wetting energy is defined as the ability of a liquid to maintain contact with the solid surface, the experimental results showing that the dissolution rate of the {111} face will be faster than that of the {110} are validated.

6.3 Dissolution Model Predictions for Urea in Ethanol

The Noyes-Whitney (1897) and Hintz-Johnson (1989) dissolution models were calculated to determine the predicted mass loss of a crystal of urea in ethanol. As the Noyes-Whitney model states that boundary layer thickness is a function of particle size, a number of boundary layer thicknesses were used in order to determine the optimal thin-film thickness that corresponds best to the experimental data. Therefore, boundary layer thicknesses equal to 50%, 25%, 10% and 1% of the volume equivalent diameter of the particle were used.

6.3.1 Noyes-Whitney and Hintz-Johnson

An example of the Noyes-Whitney calculation of the mass loss as a function of time, with the boundary layer thickness equal to 50% of the volume equivalent diameter, at an undersaturation of 0.05 is shown in Table 6.4.

Table 6.4: An example of the Noyes-Whitney calculation, at an undersaturation of 0.05, with a boundary layer equal to 50% of the volume equivalent diameter.

Time (s)	Diffusion Coefficient [D] (m ² /s)	Surface Area (m ²)	Boundary Layer Thickness [h] (m)	C _s (kg/L)	C _t (kg/L)	dM/dt (kg/s)	mass lost (kg)	Density of Solute (kg/m ³)	Volume of Crystal (m ³)	Mass of Crystal (μg)	V.E.D	50% VED
0		6.51x10 ⁻⁸	6.39x10 ⁻⁵	0.0525	0.05			1320	1.09x10 ⁻¹²	1.44	127.70	63.85
	8.80x10 ⁻¹⁰					2.24x10 ⁻¹⁵	5.38x10 ⁻¹³					
240		6.51x10 ⁻⁸	6.38x10 ⁻⁵	0.0525	0.05			1320	1.09x10 ⁻¹²	1.44	127.68	63.84
	8.80x10 ⁻¹⁰					2.24x10 ⁻¹⁵	5.38x10 ⁻¹³					
480		6.51x10 ⁻⁸	6.38x10 ⁻⁵	0.0525	0.05			1320	1.09x10 ⁻¹²	1.44	127.67	63.83
	8.80x10 ⁻¹⁰					2.24x10 ⁻¹⁵	5.38x10 ⁻¹³					
720		6.50x10 ⁻⁸	6.38x10 ⁻⁵	0.0525	0.05			1320	1.09x10 ⁻¹²	1.44	127.65	63.83
	8.80x10 ⁻¹⁰					2.24x10 ⁻¹⁵	5.38x10 ⁻¹³					
960		6.50x10 ⁻⁸	6.38x10 ⁻⁵	0.0525	0.05			1320	1.09x10 ⁻¹²	1.44	127.64	63.82
	8.80x10 ⁻¹⁰					2.24x10 ⁻¹⁵	5.38x10 ⁻¹³					
1200		6.50x10 ⁻⁸	6.38x10 ⁻⁵	0.0525	0.05			1320	1.09x10 ⁻¹²	1.44	127.62	63.81
	8.80x10 ⁻¹⁰					2.24x10 ⁻¹⁵	5.38x10 ⁻¹³					
1440		6.50x10 ⁻⁸	6.38x10 ⁻⁵	0.0525	0.05			1320	1.09x10 ⁻¹²	1.44	127.61	63.80
	8.80x10 ⁻¹⁰					2.24x10 ⁻¹⁵	5.38x10 ⁻¹³					
1680		6.50x10 ⁻⁸	6.38x10 ⁻⁵	0.0525	0.05			1320	1.09x10 ⁻¹²	1.44	127.59	63.79
	8.80x10 ⁻¹⁰					2.24x10 ⁻¹⁵	5.38x10 ⁻¹³					
1920		6.50x10 ⁻⁸	6.38x10 ⁻⁵	0.0525	0.05			1320	1.09x10 ⁻¹²	1.44	127.57	63.79
	8.80x10 ⁻¹⁰					2.24x10 ⁻¹⁵	5.38x10 ⁻¹³					
2160		6.49x10 ⁻⁸	6.38x10 ⁻⁵	0.0525	0.05			1320	1.09x10 ⁻¹²	1.43	127.56	63.78
	8.80x10 ⁻¹⁰					2.24x10 ⁻¹⁵	4.03x10 ⁻¹³					
2340		6.49x10 ⁻⁸	6.38x10 ⁻⁵	0.0525	0.05			1320	1.09x10 ⁻¹²	1.43	127.55	63.77

Table 6.5: The calculated mass loss rate using the Noyes-Whitney equation, with a boundary layer equal to 50% of the volume equivalent diameter.

σ	Number of Crystals	Mass Loss Rate ($\mu\text{g/s}$)
0.05	5	$2.40 \times 10^{-6} \pm 5.48 \times 10^{-7}$
0.10	5	$4.40 \times 10^{-6} \pm 5.48 \times 10^{-7}$
0.15	5	$7.80 \times 10^{-6} \pm 1.48 \times 10^{-6}$
0.20	5	$1.16 \times 10^{-5} \pm 4.77 \times 10^{-6}$
0.25	5	$1.00 \times 10^{-5} \pm 0$
0.30	5	$2.00 \times 10^{-5} \pm 0$
0.35	5	$2.00 \times 10^{-5} \pm 8.16 \times 10^{-6}$
0.40	5	$3.20 \times 10^{-5} \pm 4.47 \times 10^{-6}$
0.45	5	$3.00 \times 10^{-5} \pm 1.73 \times 10^{-5}$
0.50	5	$3.60 \times 10^{-5} \pm 5.48 \times 10^{-6}$

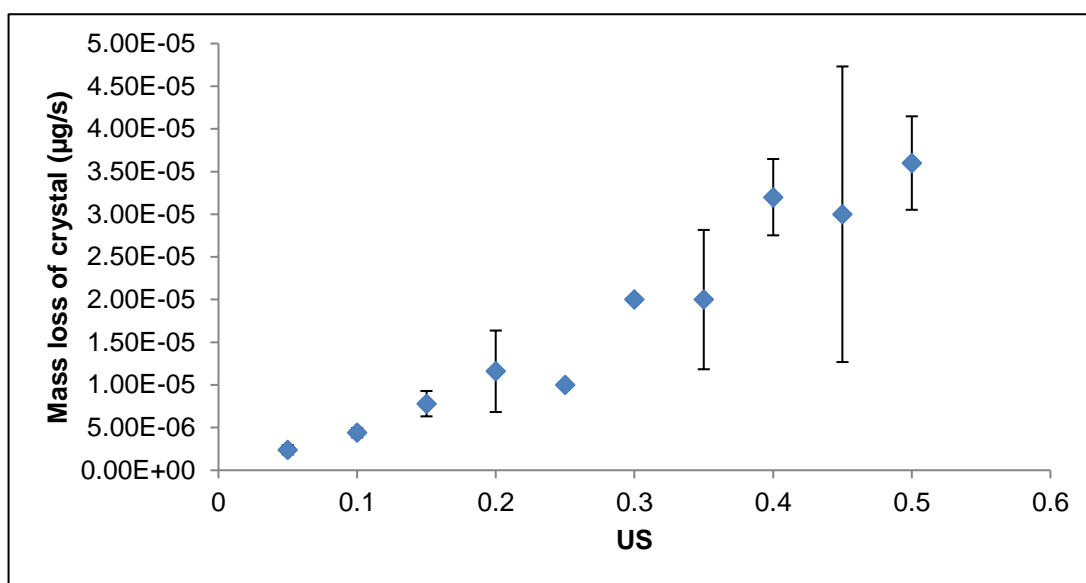


Figure 6.11: The relationship between the mass loss of a crystal of urea and the degree of undersaturation calculated using the Noyes-Whitney equation, with a boundary layer equal to 50% of the volume equivalent diameter.

The calculated mass loss using the Noyes-Whitney equation showed that the mass loss followed a linear trend with respect to undersaturation.

The mass loss rate calculated for the Noyes-Whitney model with the boundary layer thickness equal to 25% of the volume equivalent diameter over the range of experimental undersaturations is shown in Table 6.6.

Table 6.6: The calculated mass loss rate using the Noyes-Whitney equation, with a boundary layer equal to 25% of the volume equivalent diameter.

σ	Number of Crystals	Mass Loss Rate ($\mu\text{g/s}$)
0.05	5	$5.20 \times 10^{-6} \pm 1.64 \times 10^{-6}$
0.10	5	$9.20 \times 10^{-6} \pm 8.37 \times 10^{-7}$
0.15	5	$1.60 \times 10^{-5} \pm 5.48 \times 10^{-6}$
0.20	5	$2.60 \times 10^{-5} \pm 8.94 \times 10^{-6}$
0.25	5	$2.40 \times 10^{-5} \pm 5.48 \times 10^{-6}$
0.30	5	$3.40 \times 10^{-5} \pm 5.48 \times 10^{-6}$
0.35	5	$3.60 \times 10^{-5} \pm 1.34 \times 10^{-5}$
0.40	5	$6.60 \times 10^{-5} \pm 8.94 \times 10^{-6}$
0.45	5	$5.80 \times 10^{-5} \pm 2.49 \times 10^{-5}$
0.50	5	$7.20 \times 10^{-5} \pm 1.64 \times 10^{-5}$

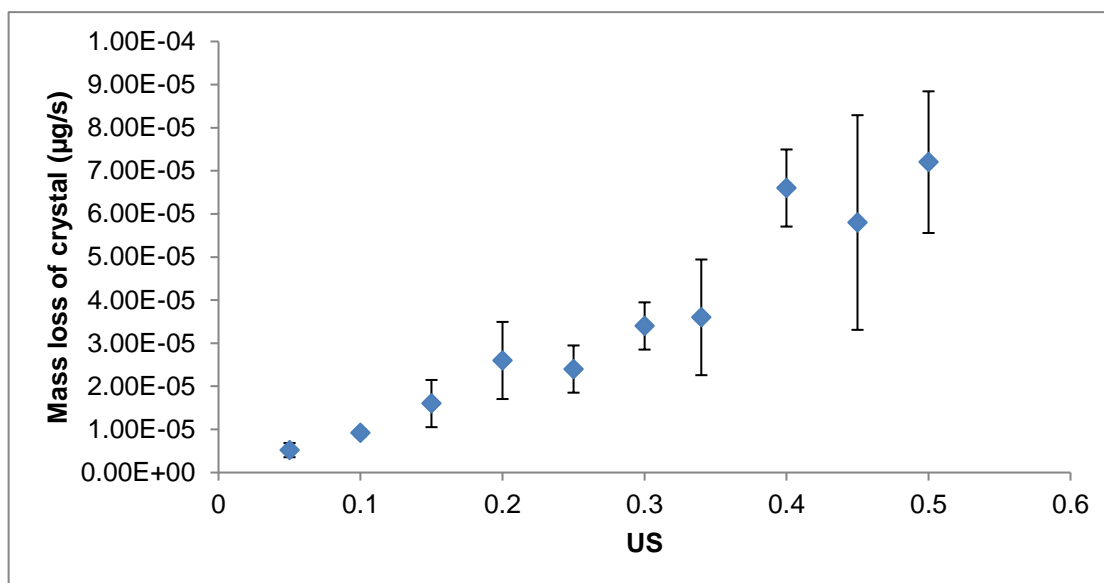


Figure 6.12: The relationship between the mass loss of a crystal of urea and the degree of undersaturation calculated using the Noyes-Whitney equation, with a boundary layer equal to 25% of the volume equivalent diameter.

The calculated mass loss using the Noyes-Whitney equation with a boundary layer thickness of 25% of the volume equivalent diameter also followed the same linear trend.

The mass loss rate calculated for the Noyes-Whitney model with the boundary layer thickness equal to 10% of the volume equivalent diameter, over the range of experimental undersaturations is shown in Table 6.7.

Table 6.7: The calculated mass loss rate using the Noyes-Whitney equation, with a boundary layer equal to 10% of the volume equivalent diameter.

σ	Number of Crystals	Mass Loss Rate ($\mu\text{g/s}$)
0.05	5	$1.38 \times 10^{-5} \pm 5.67 \times 10^{-6}$
0.10	5	$2.00 \times 10^{-5} \pm 0$
0.15	5	$3.80 \times 10^{-5} \pm 8.37 \times 10^{-6}$
0.20	5	$6.40 \times 10^{-5} \pm 2.30 \times 10^{-5}$
0.25	5	$6.00 \times 10^{-5} \pm 1.00 \times 10^{-5}$
0.30	5	$8.80 \times 10^{-5} \pm 1.10 \times 10^{-5}$
0.35	5	$1.10 \times 10^{-4} \pm 6.06 \times 10^{-5}$
0.40	5	$1.60 \times 10^{-4} \pm 5.48 \times 10^{-5}$
0.45	5	$1.60 \times 10^{-4} \pm 8.94 \times 10^{-5}$
0.50	5	$1.80 \times 10^{-4} \pm 4.47 \times 10^{-5}$

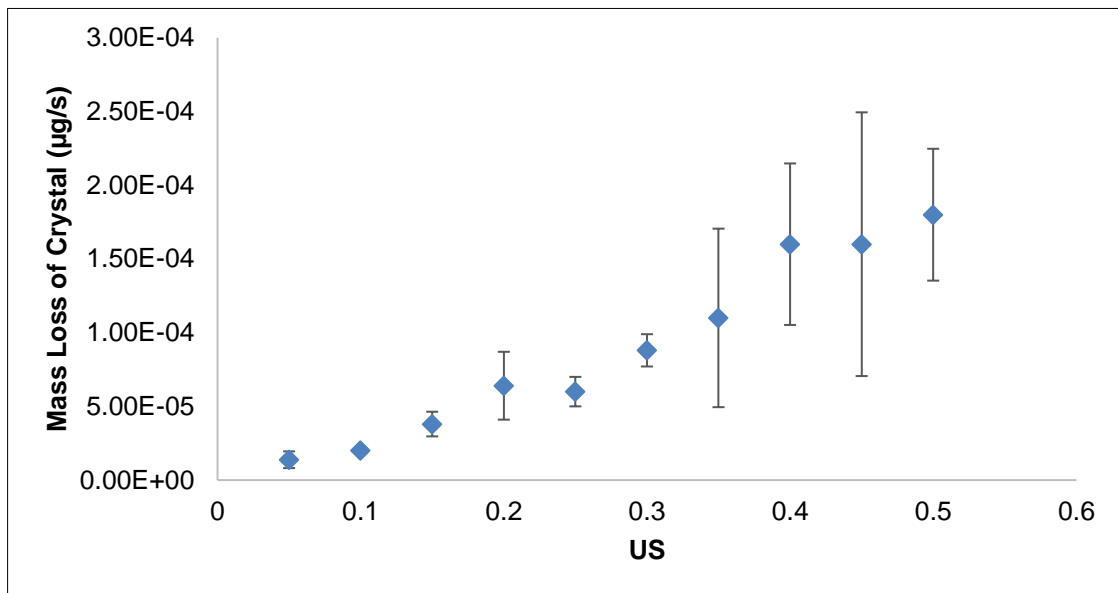


Figure 6.13: The relationship between the mass loss of a crystal of urea and the degree of undersaturation calculated using the Noyes-Whitney equation, with a boundary layer equal to 25% of the volume equivalent diameter.

The mass loss rate calculated for the Noyes-Whitney model with the boundary layer thickness equal to 1% of the volume equivalent diameter, over the range of experimental undersaturations is shown in Table 6.8.

Table 6.8: The calculated mass loss rate using the Noyes-Whitney equation, with a boundary layer equal to 1% of the volume equivalent diameter.

σ	Number of Crystals	Mass Loss Rate ($\mu\text{g/s}$)
0.05	5	$1.38 \times 10^{-4} \pm 5.67 \times 10^{-5}$
0.10	5	$2.00 \times 10^{-4} \pm 0$
0.15	5	$3.80 \times 10^{-4} \pm 8.37 \times 10^{-5}$
0.20	5	$6.60 \times 10^{-4} \pm 2.70 \times 10^{-4}$
0.25	5	$5.80 \times 10^{-4} \pm 1.10 \times 10^{-4}$
0.30	5	$8.60 \times 10^{-4} \pm 1.82 \times 10^{-4}$
0.35	5	$8.80 \times 10^{-4} \pm 3.56 \times 10^{-4}$
0.40	5	$1.58 \times 10^{-3} \pm 3.11 \times 10^{-4}$
0.45	5	$1.50 \times 10^{-3} \pm 8.28 \times 10^{-4}$
0.50	5	$1.78 \times 10^{-3} \pm 3.70 \times 10^{-4}$

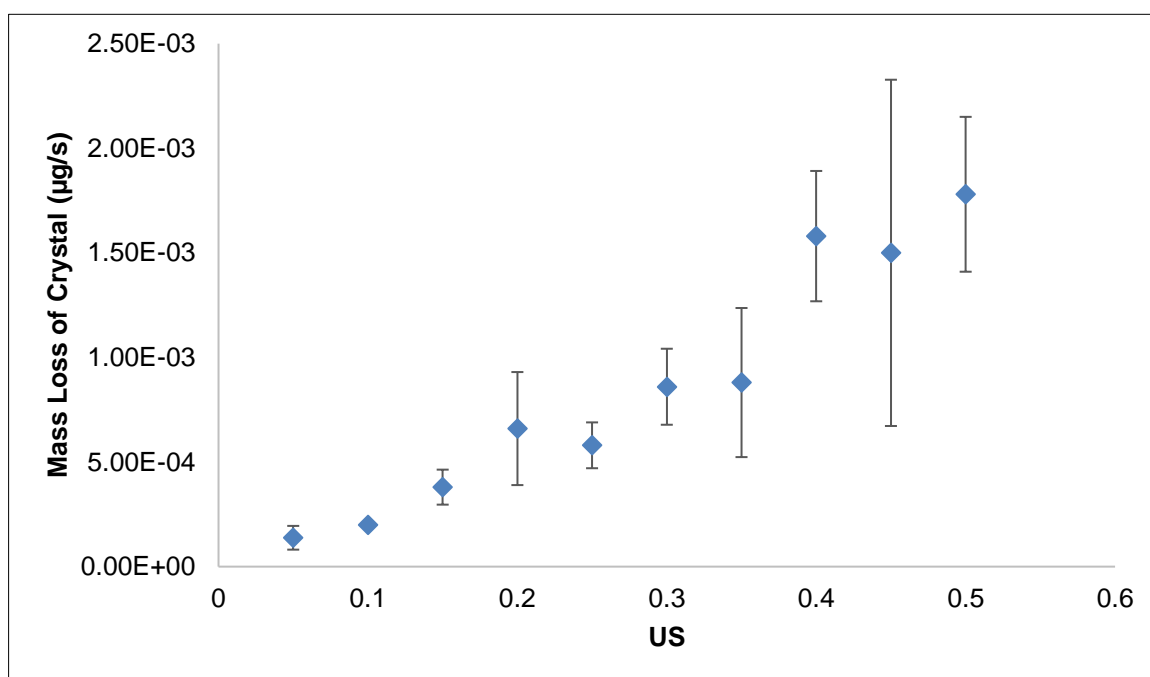


Figure 6.14: The relationship between the mass loss of a crystal of urea and the degree of undersaturation calculated using the Noyes-Whitney equation, with a boundary layer equal to 25% of the volume equivalent diameter.

The calculated mass loss using the Noyes-Whitney equation with a boundary layer thickness of 10% and 1% of the volume equivalent diameter also followed the same linear trend. Standard deviations of 0 were obtained for some calculations due to the rounding of mass loss rates. For example, taking the mass loss rate of the crystal, with the boundary layer being 1% of the volume equivalent diameter, at an undersaturation of 0.10, the standard deviation was actually found to be 0.000002, which is much smaller in comparison to other standard deviations obtained for this calculation.

Following on from this, the mass loss using the Hintz-Johnson dissolution model was also calculated. The Hintz-Johnson calculations followed the same methodology as the Noyes-Whitney, however there were 2 assumptions associated with this model:

1. The boundary layer thickness is 30 μ m for particles with radii larger than 30 μ m.
2. The boundary layer thickness is equal to the particle radius for particles with radii smaller than 30 μ m.

An example of the Hintz-Johnson calculation of the mass loss as a function of time, at an undersaturation of 0.05 is shown in Table 6.9.

Table 6.9: An example of the Hintz-Johnson calculation, at an undersaturation of 0.05.

Time (s)	Diffusion Coefficient [D] (m ² /s)	Surface Area (m ²)	Boundary Layer Thickness [h] (m)	C _s (kg/L)	C _t (kg/L)	dM/dt (kg/s)	mass lost (kg)	Density of Solute (kg/m ³)	Volume of Crystal (m ³)	Mass of Crystal (μg)	V.E.D	Particle Radius
0		6.51x10 ⁻⁸	3.00x10 ⁻⁵	0.0525	0.05			1320	1.09x10 ⁻¹²	1.44	127.70	63.85
	8.80x10 ⁻¹⁰					4.77x10 ⁻¹⁵	1.15x10 ⁻¹²					
240		6.51x10 ⁻⁸	3.00x10 ⁻⁵	0.0525	0.05			1320	1.09x10 ⁻¹²	1.44	127.67	63.83
	8.80x10 ⁻¹⁰					4.77x10 ⁻¹⁵	1.14x10 ⁻¹²					
480		6.50x10 ⁻⁸	3.00x10 ⁻⁵	0.0525	0.05			1320	1.09x10 ⁻¹²	1.44	127.63	63.82
	8.80x10 ⁻¹⁰					4.77x10 ⁻¹⁵	1.14x10 ⁻¹²					
720		6.50x10 ⁻⁸	3.00x10 ⁻⁵	0.0525	0.05			1320	1.09x10 ⁻¹²	1.44	127.60	63.80
	8.80x10 ⁻¹⁰					4.76x10 ⁻¹⁵	1.14x10 ⁻¹²					
960		6.50x10 ⁻⁸	3.00x10 ⁻⁵	0.0525	0.05			1320	1.09x10 ⁻¹²	1.43	127.57	63.78
	8.80x10 ⁻¹⁰					4.76x10 ⁻¹⁵	1.14x10 ⁻¹²					
1200		6.49x10 ⁻⁸	3.00x10 ⁻⁵	0.0525	0.05			1320	1.09x10 ⁻¹²	1.43	127.53	63.77
	8.80x10 ⁻¹⁰					4.76x10 ⁻¹⁵	1.14x10 ⁻¹²					
1440		6.49x10 ⁻⁸	3.00x10 ⁻⁵	0.0525	0.05			1320	1.09x10 ⁻¹²	1.43	127.50	63.75
	8.80x10 ⁻¹⁰					4.76x10 ⁻¹⁵	1.14x10 ⁻¹²					
1680		6.48x10 ⁻⁸	3.00x10 ⁻⁵	0.0525	0.05			1320	1.08x10 ⁻¹²	1.43	127.46	63.73
	8.80x10 ⁻¹⁰					4.75x10 ⁻¹⁵	1.14x10 ⁻¹²					
1920		6.48x10 ⁻⁸	3.00x10 ⁻⁵	0.0525	0.05			1320	1.08x10 ⁻¹²	1.43	127.43	63.71
	8.80x10 ⁻¹⁰					4.75x10 ⁻¹⁵	1.14x10 ⁻¹²					
2160		6.48x10 ⁻⁸	3.00x10 ⁻⁵	0.0525	0.05			1320	1.08x10 ⁻¹²	1.43	127.40	63.70
	8.80x10 ⁻¹⁰					4.75x10 ⁻¹⁵	8.55x10 ⁻¹³					
2340		6.48x10 ⁻⁸	3.00x10 ⁻⁵	0.0525	0.05			1320	1.08x10 ⁻¹²	1.43	127.37	63.69

Table 6.10: The calculated mass loss rate using the Hintz-Johnson equation.

σ	Number of Crystals	Mass Loss Rate ($\mu\text{g/s}$)
0.05	5	$6.00 \times 10^{-6} \pm 2.92 \times 10^{-6}$
0.10	5	$8.75 \times 10^{-6} \pm 1.50 \times 10^{-6}$
0.15	5	$1.60 \times 10^{-5} \pm 5.48 \times 10^{-6}$
0.20	5	$4.00 \times 10^{-5} \pm 3.54 \times 10^{-5}$
0.25	5	$2.40 \times 10^{-5} \pm 5.48 \times 10^{-6}$
0.30	5	$4.00 \times 10^{-5} \pm 3.27 \times 10^{-5}$
0.35	5	$4.20 \times 10^{-5} \pm 3.27 \times 10^{-5}$
0.40	5	$1.08 \times 10^{-4} \pm 5.26 \times 10^{-5}$
0.45	5	$9.80 \times 10^{-5} \pm 1.15 \times 10^{-4}$
0.50	5	$8.20 \times 10^{-5} \pm 2.49 \times 10^{-5}$

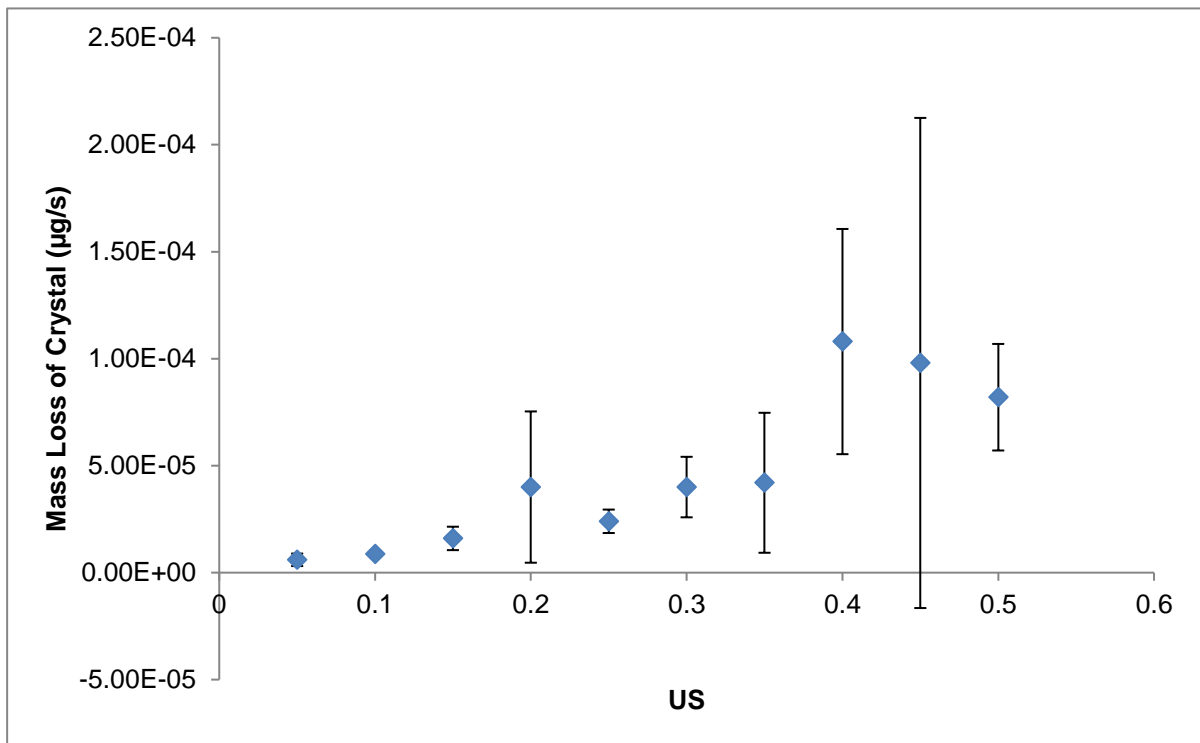


Figure 6.15: The relationship between the mass loss of a crystal of urea and the degree of undersaturation calculated using the Hintz-Johnson model.

6.3.2 Comparison of Models with Experimental Data

The predictions calculated using the Noyes-Whitney and Hintz-Johnson models were compared to the actual mass loss determined through dissolution experiments. The actual mass loss was calculated through the use of Heron's formula (Hammond,

2006) as outlined in Chapter 4 to determine the surface area, and the shape factor to determine the volume and hence the mass for each crystal.

Table 6.11: An example of the calculation of actual mass loss as a function of time, at an undersaturation of 0.05.

Time (s)	Surface Area (m ²)	Volume (m ³)	Density (kg/m ³)	Mass (µg)
0	6.51x10 ⁻⁸	1.09x10 ⁻¹²	1320	1.44
240	3.78x10 ⁻⁸	4.82x10 ⁻¹³	1320	0.64
480	3.46x10 ⁻⁸	4.23x10 ⁻¹³	1320	0.56
720	3.12x10 ⁻⁸	3.62x10 ⁻¹³	1320	0.48
960	2.95x10 ⁻⁸	3.32x10 ⁻¹³	1320	0.44
1200	2.74x10 ⁻⁸	2.97x10 ⁻¹³	1320	0.39
1440	2.51x10 ⁻⁸	2.60x10 ⁻¹³	1320	0.34
1680	2.27x10 ⁻⁸	2.24x10 ⁻¹³	1320	0.30
1920	2.14x10 ⁻⁸	2.05x10 ⁻¹³	1320	0.27
2160	2.02x10 ⁻⁸	1.89x10 ⁻¹³	1320	0.25
2340	1.87x10 ⁻⁸	1.67x10 ⁻¹³	1320	0.22

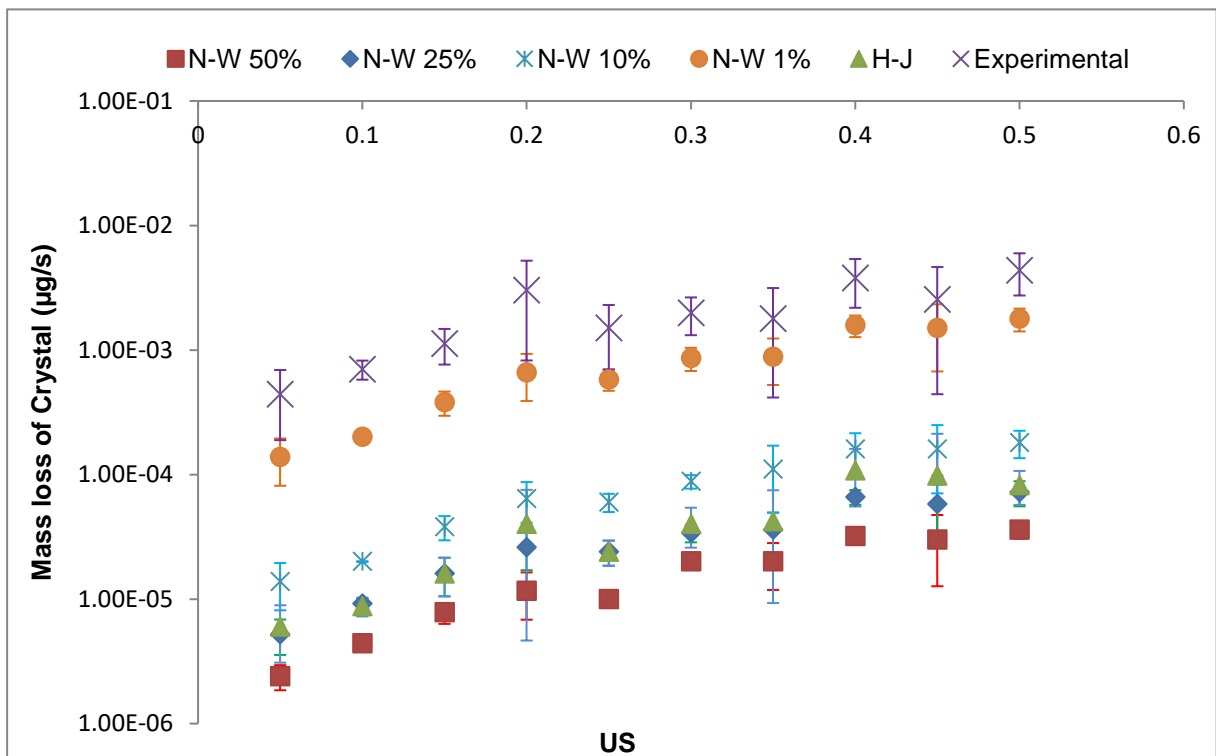


Figure 6.16: A comparison between the experimental mass loss and calculated mass losses using Noyes-Whitney and Hintz-Johnson.

The predicted mass loss of the crystal for all models shows an inconsistency between the predicted values of mass loss in comparison with the experimental mass

loss. The percentage difference between the actual mass loss and predicted mass loss is shown in Table 6.12.

Table 6.12: The percentage difference between values of experimental mass loss and calculated mass loss.

US	% difference				
	N-W (50%)	N-W (25%)	N-W (10%)	N-W (1%)	H-J
0.05	99.45	98.82	96.86	68.64	98.64
0.10	99.37	98.69	97.14	71.43	98.75
0.15	99.30	98.57	96.61	66.07	98.57
0.20	99.62	99.14	97.88	78.15	98.68
0.25	99.33	98.40	96.00	61.33	98.40
0.30	98.99	98.28	95.56	56.57	97.98
0.35	98.88	97.98	93.82	50.56	97.64
0.40	99.15	98.25	95.77	58.20	97.14
0.45	98.82	97.72	93.70	40.94	96.14
0.50	99.17	98.35	95.87	59.17	98.12

The percentage difference further reinforces that the predicted model values for mass loss in comparison with the actual experimental mass loss are inconsistent. Therefore, current dissolution models could not be used in the pharmaceutical industry and would need to be modified.

6.3.3 Modification of Dissolution Models

To modify dissolution models in order to obtain a better prediction, the main equation used was the Noyes-Whitney (equation 4.6) as the Hintz-Johnson equation is a modification of the Noyes-Whitney.

The boundary layer thickness, being the parameter that was estimated, was changed. This is because both the Noyes-Whitney and Hintz-Johnson models treat the boundary layer thickness in different ways. The Noyes-Whitney model assumes that the boundary layer thickness is a thin-film that is a function of the particle size, however the Hintz-Johnson model only assumes this is the case up to a certain critical size of the particle. Beyond this size the Hintz-Johnson model assumes that the boundary layer thickness is fixed.

Therefore, in order to further modify the models, a fixed boundary layer was assumed, and the models re-calculated. A fixed boundary layer of $0.5\mu\text{m}$ was used, an example of this calculation for an undersaturation of 0.05 is shown in Table 6.13.

Table 6.13: An example of the Noyes-Whitney calculation with a fixed boundary layer parameter of 0.5 μm .

Time (s)	Diffusion Coefficient [D] (m ² /s)	Surface Area (m ²)	Boundary Layer Thickness [h] (m)	C _s (kg/L)	C _t (kg/L)	dM/dt (kg/s)	mass lost (kg)	Density of Solute (kg/m ³)	Volume of Crystal (m ³)	Mass of Crystal (μg)
0		6.51x10 ⁻⁸	5.00x10 ⁻⁷	0.0525	0.05			1320	1.09 x10 ⁻¹²	1.44
	8.80x10 ⁻¹⁰					2.86 x10 ⁻¹³	6.87 x10 ⁻¹¹			
240		6.30x10 ⁻⁸	5.00x10 ⁻⁷	0.0525	0.05			1320	1.04 x10 ⁻¹²	1.37
	8.80x10 ⁻¹⁰					2.77 x10 ⁻¹³	6.65 x10 ⁻¹¹			
480		6.09x10 ⁻⁸	5.00x10 ⁻⁷	0.0525	0.05			1320	9.88 x10 ⁻¹³	1.30
	8.80x10 ⁻¹⁰					2.68 x10 ⁻¹³	6.43 x10 ⁻¹¹			
720		5.89x10 ⁻⁸	5.00x10 ⁻⁷	0.0525	0.05			1320	9.39 x10 ⁻¹³	1.24
	8.80x10 ⁻¹⁰					2.59 x10 ⁻¹³	6.22 x10 ⁻¹¹			
960		5.69x10 ⁻⁸	5.00x10 ⁻⁷	0.0525	0.05			1320	8.92 x10 ⁻¹³	1.18
	8.80x10 ⁻¹⁰					2.50 x10 ⁻¹³	6.01 x10 ⁻¹¹			
1200		5.50x10 ⁻⁸	5.00x10 ⁻⁷	0.0525	0.05			1320	8.47 x10 ⁻¹³	1.12
	8.80x10 ⁻¹⁰					2.42 x10 ⁻¹³	5.80 x10 ⁻¹¹			
1440		5.31x10 ⁻⁸	5.00x10 ⁻⁷	0.0525	0.05			1320	8.03 x10 ⁻¹³	1.06
	8.80x10 ⁻¹⁰					2.33 x10 ⁻¹³	5.60 x10 ⁻¹¹			
1680		5.12x10 ⁻⁸	5.00x10 ⁻⁷	0.0525	0.05			1320	7.60 x10 ⁻¹³	1.00
	8.80x10 ⁻¹⁰					2.25 x10 ⁻¹³	5.40 x10 ⁻¹¹			
1920		4.93x10 ⁻⁸	5.00x10 ⁻⁷	0.0525	0.05			1320	7.19 x10 ⁻¹³	0.95
	8.80x10 ⁻¹⁰					2.17 x10 ⁻¹³	5.21 x10 ⁻¹¹			
2160		4.75x10 ⁻⁸	5.00x10 ⁻⁷	0.0525	0.05			1320	6.80 x10 ⁻¹³	0.90
	8.80x10 ⁻¹⁰					2.09 x10 ⁻¹³	3.76 x10 ⁻¹¹			
2340		4.62x10 ⁻⁸	5.00x10 ⁻⁷	0.0525	0.05			1320	6.51 x10 ⁻¹³	0.86

A comparison of the mass loss values with a fixed boundary layer thickness with the experimental values obtained is shown in Figure 6.17.

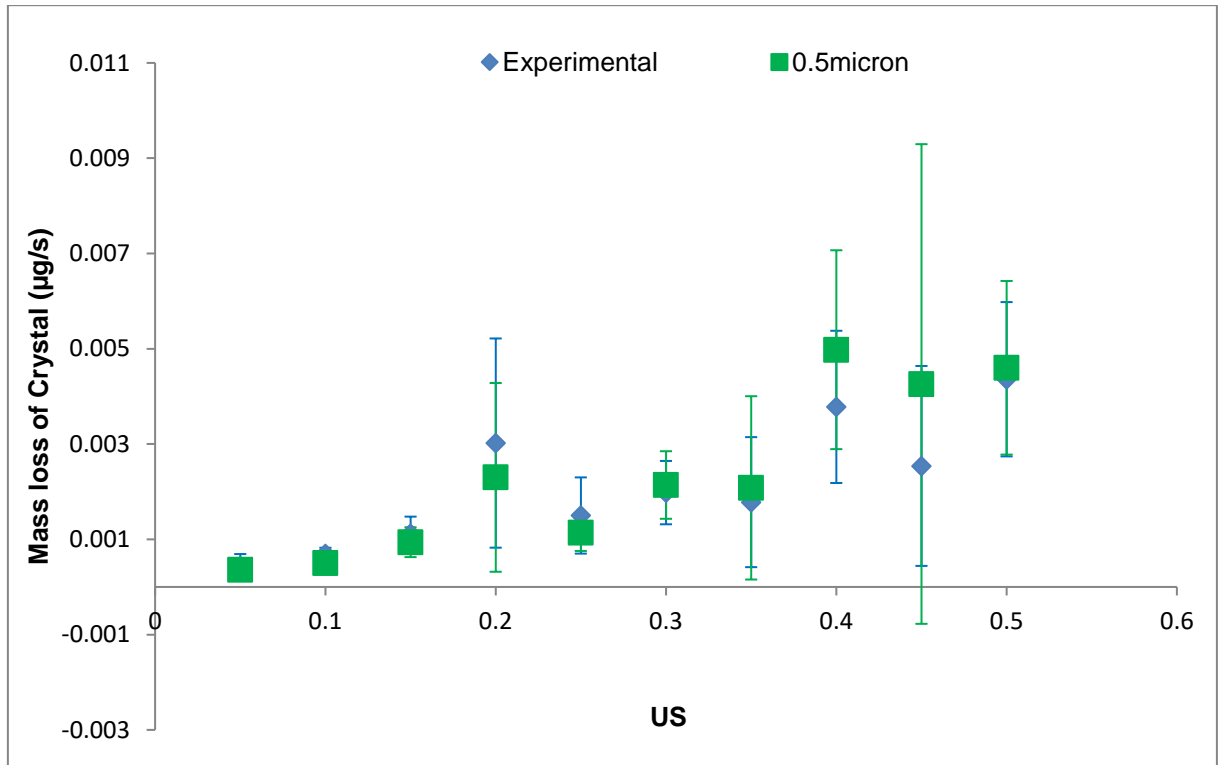


Figure 6.17: Comparison between the experimental mass loss and calculated values with a fixed boundary layer.

Table 6.14: The percentage difference between values of experimental mass loss and calculated mass loss with a fixed boundary layer.

Undersaturation	% difference
0.05	18.18
0.10	28.57
0.15	16.07
0.20	23.84
0.25	24.00
0.30	7.48
0.35	14.42
0.40	24.10
0.45	40.38
0.50	5.22

This modification showed more consistent values between the predicted values for mass loss and experimental values obtained. These values are reinforced by Bunn and Emmett (1949) who measured the average thickness of layers, and after correcting for the refractive index of the solution, found layer thicknesses to be between $0.17\mu\text{m} - 0.41\mu\text{m}$ for sodium chloride and in cadmium iodide found to be between $0.3\mu\text{m} - 0.5\mu\text{m}$.

6.4 Dissolution of Urea in Acetonitrile

Urea single crystals were dissolved in acetonitrile under differing levels of undersaturation. The experimental dissolution rates of the two faces under consideration were determined. The dissolution rates were then compared to the intermolecular interactions of the two faces and the experimental conclusions made were reinforced due to energy interactions obtained. Additionally, the dissolution of urea in different solution environments was compared.

6.4.1 Face Specific Dissolution Rate

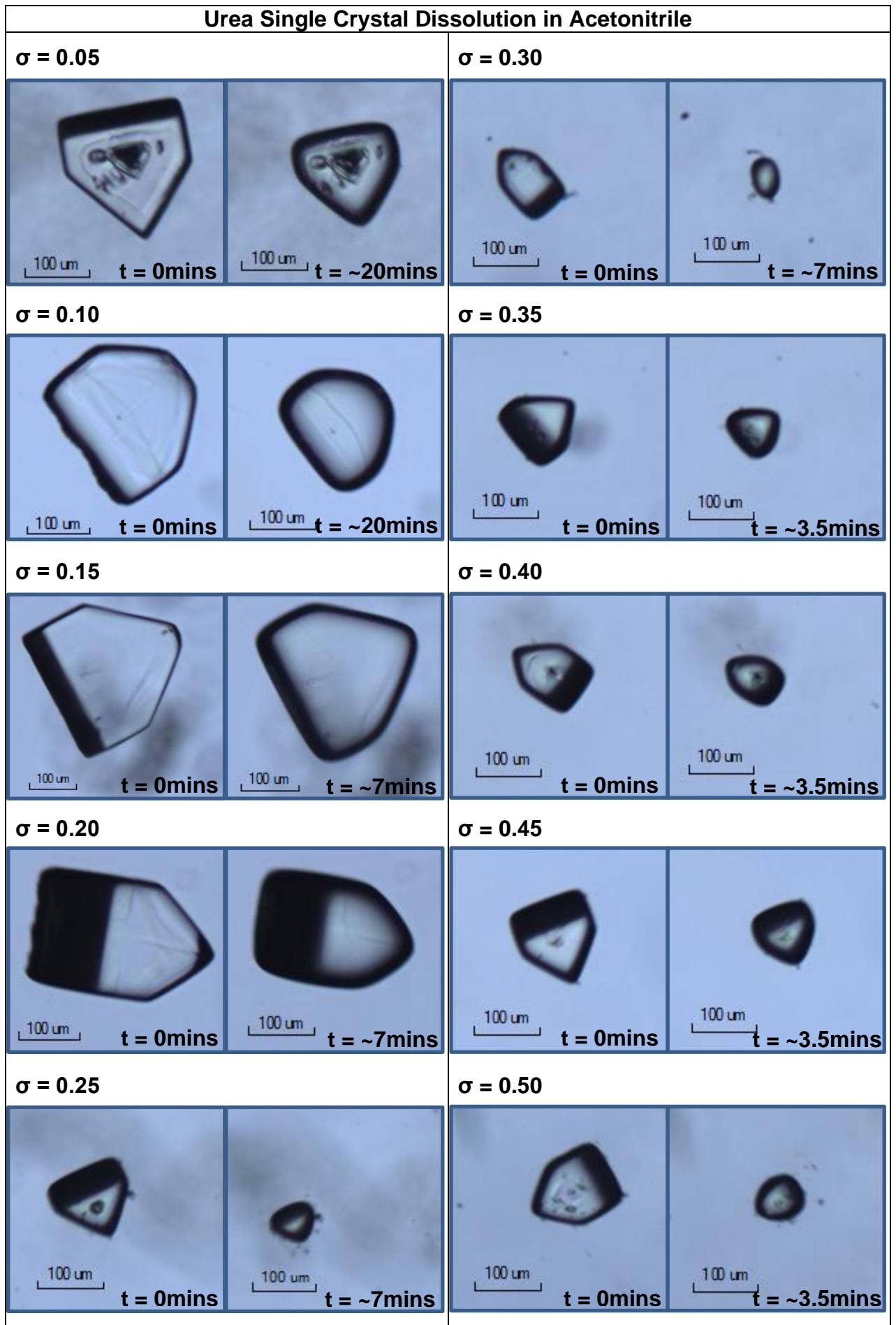
Experimental dissolution rate data has been provided in Appendix C2, which comprises of 50 single crystals spontaneously nucleated and grown in acetonitrile over a period of three hours. These crystals have then been dissolved over an undersaturation range from ~ 0.05 to 0.5 . The crystals were dissolved in a stagnant solution under diffusion limited conditions in a 0.5mL cuvette, immersed in a water cell. The distance between the centre of the crystal, and the face under consideration was then measured as a function of time.

Table 6.15: Experimental mean retreat rates and standard deviations obtained for urea in acetonitrile.

σ	Number of Crystals	Mean Retreat Rate ($\mu\text{m/s}$)	
		{110}	{111}
0.05	5	0.017 ± 0.005	0.011 ± 0.006
0.10	5	0.027 ± 0.018	0.026 ± 0.019
0.15	5	0.033 ± 0.011	0.031 ± 0.015
0.20	5	0.029 ± 0.015	0.028 ± 0.007
0.25	5	0.060 ± 0.024	0.050 ± 0.023
0.30	5	0.093 ± 0.054	0.090 ± 0.056
0.35	5	0.076 ± 0.017	0.044 ± 0.024
0.40	5	0.100 ± 0.058	0.074 ± 0.037
0.45	5	0.091 ± 0.040	0.066 ± 0.037
0.50	5	0.083 ± 0.057	0.113 ± 0.068

The initial and final images of the retreat rate of crystals dissolved in the cuvette are shown in Table 6.16. Final images were taken when the dissolution of the crystals reached the point where further dissolution would result in rounding of the crystal faces.

Table 6.16: An example of the experimental crystal images obtained at the initial and final time points for urea in ethanol at each undersaturation



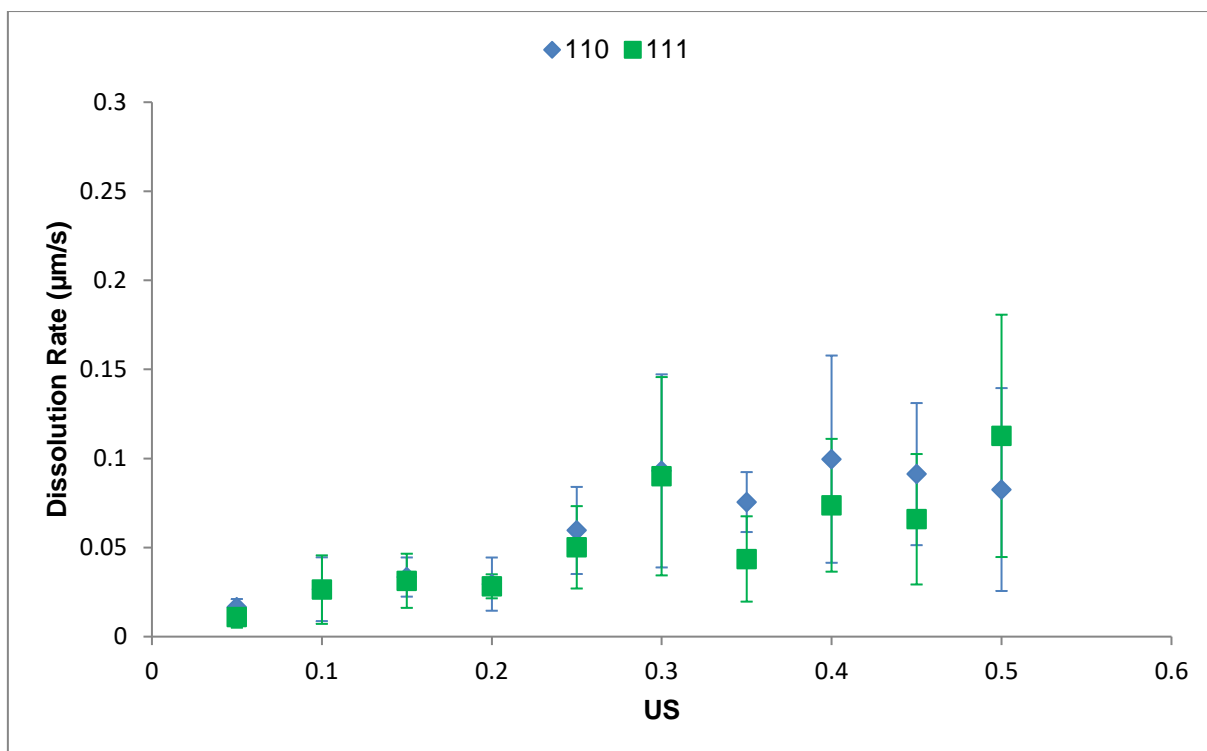


Figure 6.18: The relationship between dissolution rate and undersaturation of the {110} and {111} face of urea in acetonitrile.

The dissolution rates of the {110} and {111} show that the dissolution rates of both faces in acetonitrile follow a first order dependence on undersaturation, with the mean dissolution rates increasing linearly with increasing relative undersaturation. Both faces were found to have similar dissolution rates in acetonitrile with respect to undersaturation.

6.4.2 Intermolecular Interactions of Urea with Acetonitrile

Surface characterisation of urea has been carried out previously in Chapter 5, with the three main morphologically important faces being identified – {110}, {111} and its polar opposite {-1-1-1}. The interaction of acetonitrile with the faces under consideration were modelled through the systematic search function using Mercury VisualHabit.

6.3.1.1 {110}

The minimum interaction energy between a probe molecule of acetonitrile and the {110} surface was found using the systematic grid search function in VisualHabit. This minimum interaction energy is the strongest and most stable interaction between the probe and the surface.

The {110} surface was built of multiple unit cells surrounding the unit cell used for the grid search function in order to ensure that edge effects do not interfere with the calculation of interaction energies. As the grid rows closest to and furthest away from the surface contained white tetrahedrons only, the interactions found in these spaces were found to be smaller than the defined minimum value, therefore were considered negligible.

Removal of the grid showed that there were varying degrees of acetonitrile interaction with the {110} surface. The strongest interaction of acetonitrile with the surface is shown in Figure 6.19.

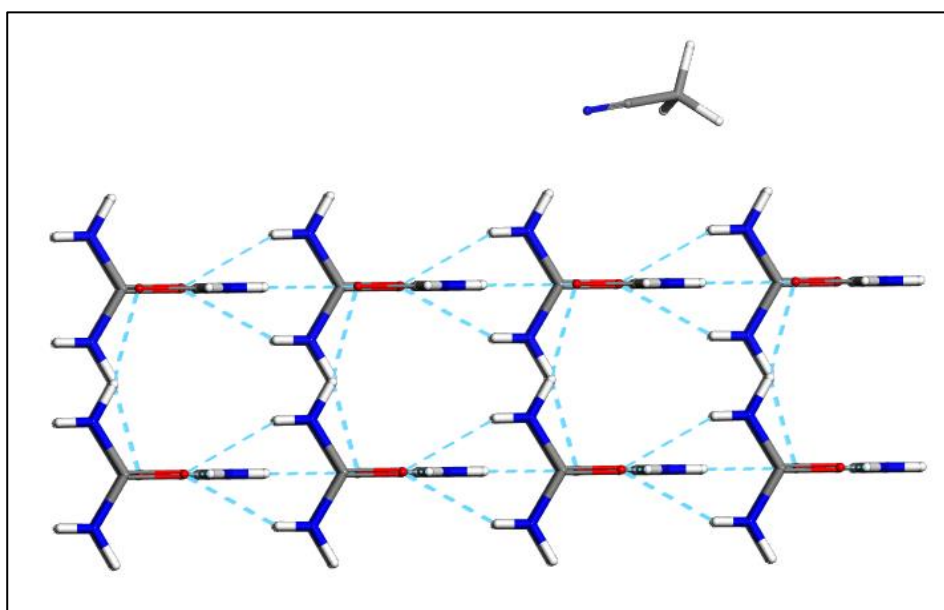


Figure 6.19: The strongest interaction of acetonitrile with the {110} surface, with hydrogen bonding depicted.

Calculation of the interaction energy between the acetonitrile probe molecule and the {110} surface through the SystSearch function allowed for the determination of the total energy interaction and also divided this total energy figure into van der Waals (dispersive), hydrogen bonding and electrostatic interactions. Thousands of interactions were calculated through the SystSearch function, however, for the purposes of clarity, the 100 strongest interactions have been presented.

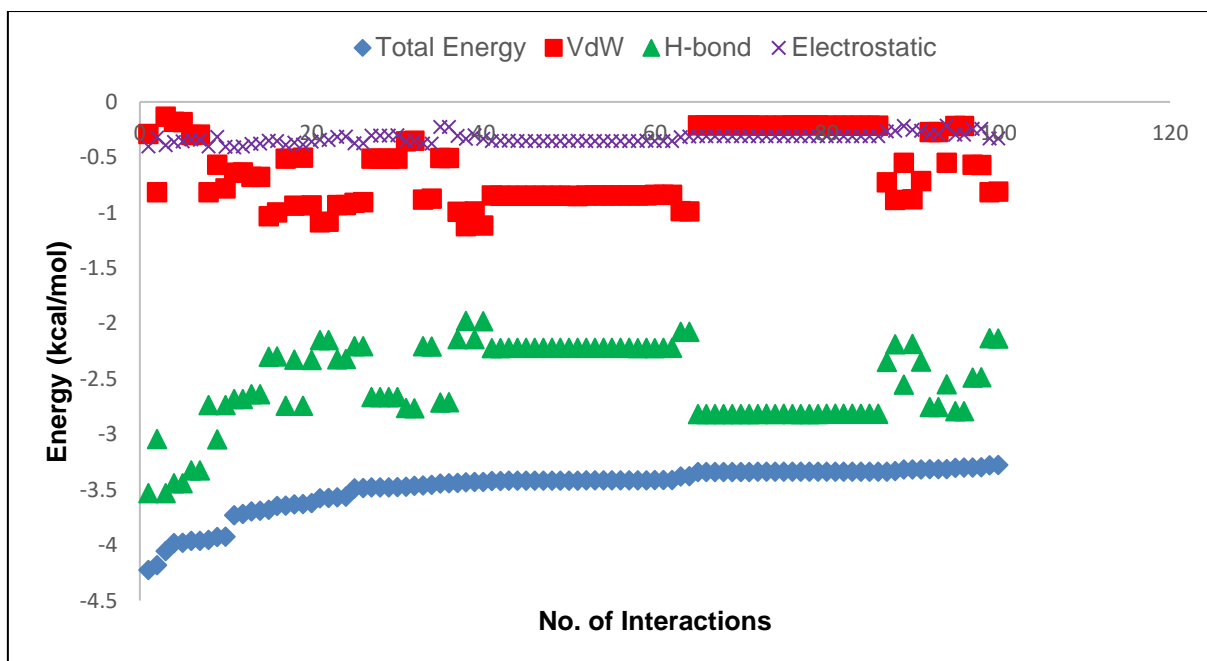


Figure 6.20: The top 100 interactions of acetonitrile with the {110} surface, broken down into hydrogen bonding, van der Waals and electrostatic interactions.

This suggests that the majority of the total interaction energy of the acetonitrile probe molecule with the {110} surface is due to hydrogen bonding between the probe and surface, with Van der Waals and electrostatic interactions making up a minimal amount of the total interaction energy.

6.3.1.2 {111} and {-1-1-1}

In order to compare the total interaction energies of acetonitrile with the two faces that are under consideration, the interaction energy of acetonitrile with the {111} and its polar face {-1-1-1} were also determined. This is because of the slight difference in surface chemistries as mentioned previously in Chapter 5, therefore the acetonitrile probe molecule across the surface could have a slightly different interaction with the {-1-1-1} face in comparison with the {111} face.

The same process was used for the {111} and {-1-1-1} surface calculations as for the {110} surface grid search calculations. Upon removing the grid, there were varying degrees of acetonitrile interaction with the {111} surface found, with the highest energy interaction of acetonitrile with the surface of the {111} face being shown in Figure 6.21.

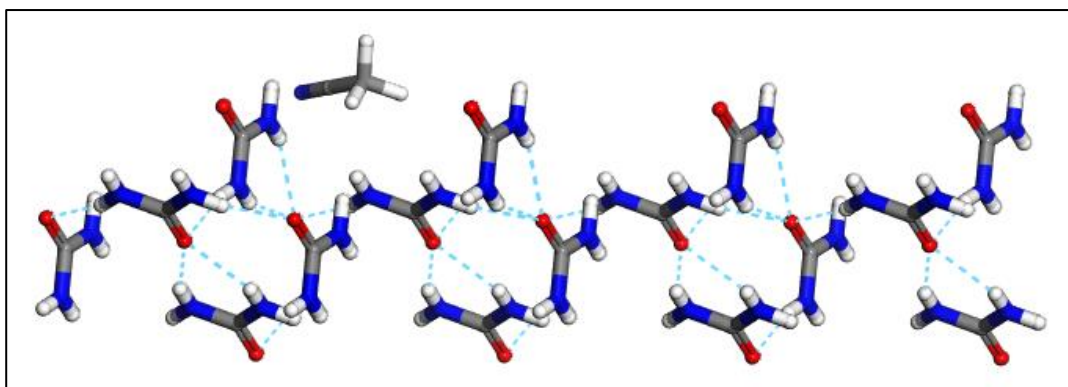


Figure 6.21: The strongest interaction of acetonitrile with the {111} surface, with hydrogen bonding depicted.

The calculation of these energy interactions between the acetonitrile probe molecule and the {111} surface, allowed for the determination of the type of interaction and the strength of these interactions.

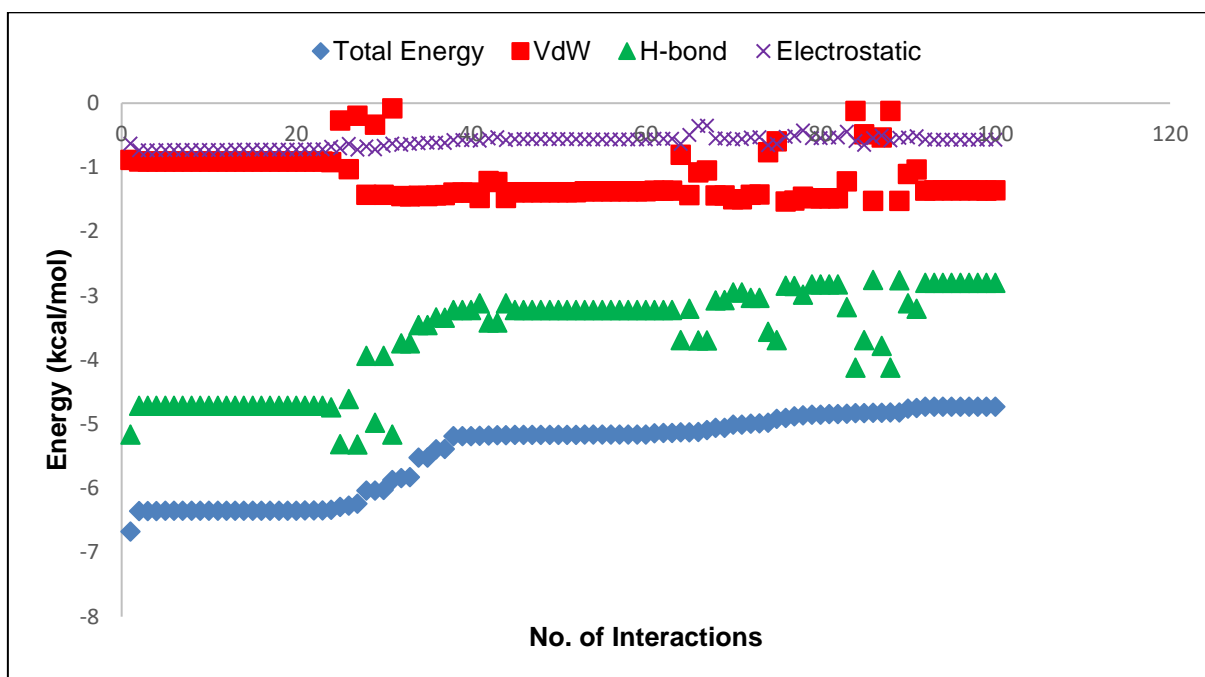


Figure 6.22: The top 100 interactions of acetonitrile with the {111} surface, broken down into hydrogen bonding, van der Waals and electrostatic interactions.

The number of interactions calculated through the SystSearch function were in the thousands, however for the purposes of clarity the strongest 100 interactions have been presented. These top interactions suggest that the interaction of the acetonitrile probe with the {111} surface was mostly due to hydrogen bonding between the two, with van der Waals and electrostatic interactions making up a minimal amount of the interaction.

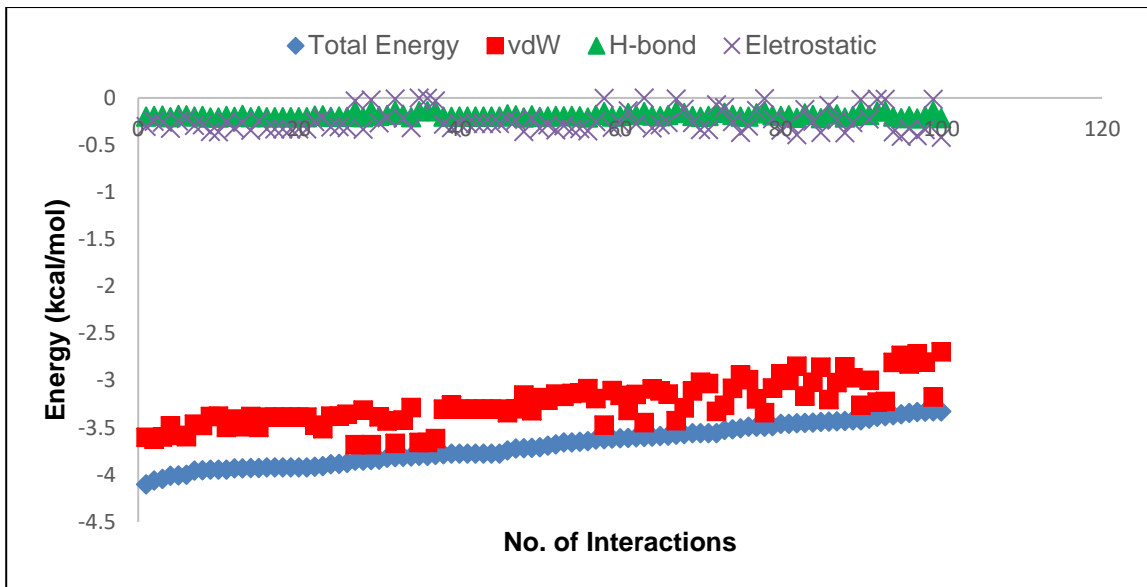


Figure 6.23: The top 100 interactions of acetonitrile with the $\{-1-1-1\}$ surface, broken down into hydrogen bonding, van der Waals and electrostatic interactions.

For the polar opposite $\{-1-1-1\}$ face, the total interaction energy is mostly due to the dispersive interactions between the probe and the surface, with hydrogen bonding and electrostatic interactions making up a minimal amount of the interaction.

6.3.1.3 Comparison of Surface Interactions

A comparison of the total interaction energy of the two faces under consideration and the polar $\{-1-1-1\}$ face is shown in Figure 6.24.

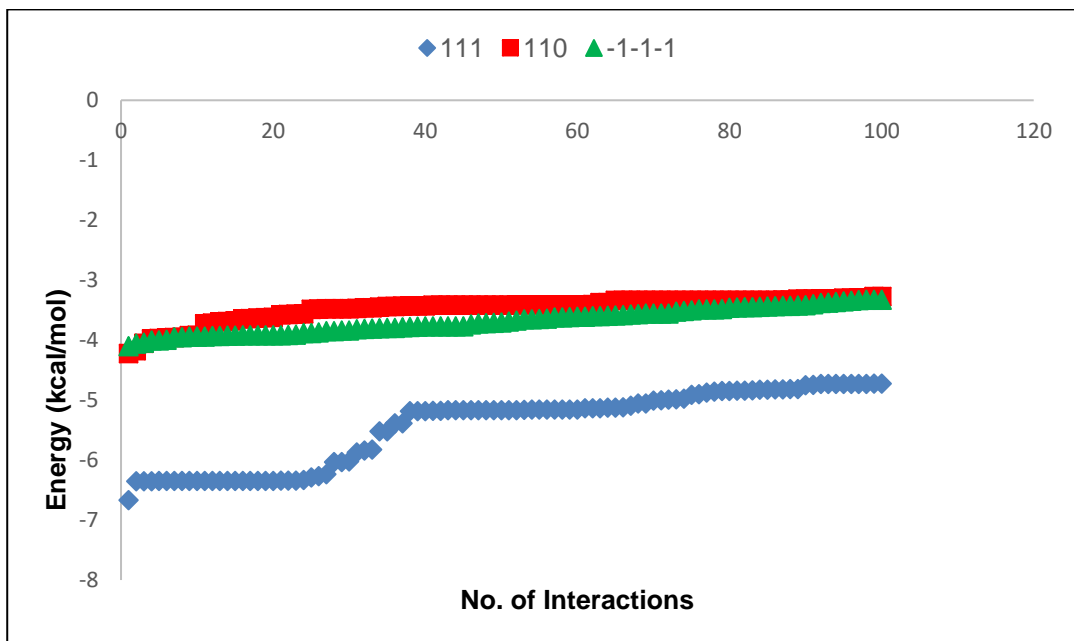


Figure 6.24: Comparison of the total energy interactions of both $\{110\}$ and $\{111\}$ surfaces, along with the $\{-1-1-1\}$ surface.

The acetonitrile probe molecule was found to have a slightly stronger interactions with the {111} surface in comparison with the {110} and {-1-1-1} surfaces. This was also determined to be the case for the ethanol probe. Perhaps the weaker interaction of {-1-1-1} compared to {111} with both probes could be the reason why the {-1-1-1} facet is not obtained experimentally. Additionally, wetting energies of the two faces under consideration were determined through COSMOtherm.

Table 6.17: The calculated wetting energies of the {110} and {111} faces of urea.

Face	Wetting Energy (kcal/mol)
{110}	-4.368
{111}	-6.846

As a result of this comparison, with both faces having similar interactions with the acetonitrile probe molecule, and also having similar wetting energies, meaning that acetonitrile has a similar ability to maintain contact with both faces, the experimental results were validated in that the dissolution rates of the {110} and {111} faces are comparable.

6.5 Dissolution Model Predictions for Urea in Acetonitrile

In order to validate the amendment to the Noyes-Whitney model outlined in section 6.3, further calculations were carried out for urea in acetonitrile.

6.5.1 Noyes-Whitney and Hintz-Johnson

The same process was followed as that for urea in ethanol, where the Noyes-Whitney and Hintz-Johnson dissolution models were first calculated to determine a predicted mass loss and compared to the experimental mass loss data obtained from single crystal data.

An example of the Noyes-Whitney calculation of the mass loss as a function of time, with the boundary layer thickness equal to 50% of the volume equivalent diameter, at an undersaturation of 0.05 is shown in Table 6.18.

Table 6.18: An example of the Noyes-Whitney calculation, at an undersaturation of 0.05, with a boundary layer equal to 50% of the volume equivalent diameter.

Time (s)	Diffusion Coefficient [D] (m ² /s)	Surface Area (m ²)	Boundary Layer Thickness [h] (m)	Cs (kg/L)	Ct (kg/L)	dM/dt (kg/s)	mass lost (kg)	Density of Solute (kg/m ³)	Volume of Crystal (m ³)	Mass of Crystal (μg)	V.E.D	50% V.E.D
0		1.52x10 ⁻⁸	3.12x10 ⁻⁵	0.0061	0.0058			1320	1.28x10 ⁻¹³	0.17	62.46	31.23
	2.58x10 ⁻⁹					3.76x10 ⁻¹⁶	4.52x10 ⁻¹⁴					
120		1.52x10 ⁻⁸	3.12x10 ⁻⁵	0.0061	0.0058			1320	1.28x10 ⁻¹³	0.17	62.45	31.23
	2.58x10 ⁻⁹					3.76x10 ⁻¹⁶	4.52x10 ⁻¹⁴					
240		1.52x10 ⁻⁸	3.12x10 ⁻⁵	0.0061	0.0058			1320	1.27x10 ⁻¹³	0.17	62.45	31.22
	2.58x10 ⁻⁹					3.76x10 ⁻¹⁶	4.52x10 ⁻¹⁴					
360		1.52x10 ⁻⁸	3.12x10 ⁻⁵	0.0061	0.0058			1320	1.27x10 ⁻¹³	0.17	62.44	31.22
	2.58x10 ⁻⁹					3.76x10 ⁻¹⁶	4.52x10 ⁻¹⁴					
480		1.52x10 ⁻⁸	3.12x10 ⁻⁵	0.0061	0.0058			1320	1.27x10 ⁻¹³	0.17	62.43	31.22
	2.58x10 ⁻⁹					3.76x10 ⁻¹⁶	4.52x10 ⁻¹⁴					
600		1.52x10 ⁻⁸	3.12x10 ⁻⁵	0.0061	0.0058			1320	1.27x10 ⁻¹³	0.17	62.43	31.21
	2.58x10 ⁻⁹					3.76x10 ⁻¹⁶	4.51x10 ⁻¹⁴					
720		1.51x10 ⁻⁸	3.12x10 ⁻⁵	0.0061	0.0058			1320	1.27x10 ⁻¹³	0.17	62.42	31.21
	2.58x10 ⁻⁹					3.76x10 ⁻¹⁶	4.51x10 ⁻¹⁴					
840		1.51x10 ⁻⁸	3.12x10 ⁻⁵	0.0061	0.0058			1320	1.27x10 ⁻¹³	0.17	62.42	31.21
	2.58x10 ⁻⁹					3.76x10 ⁻¹⁶	4.51x10 ⁻¹⁴					
960		1.51x10 ⁻⁸	3.12x10 ⁻⁵	0.0061	0.0058			1320	1.27x10 ⁻¹³	0.17	62.41	31.21
	2.58x10 ⁻⁹					3.76x10 ⁻¹⁶	4.51x10 ⁻¹⁴					
1080		1.51x10 ⁻⁸	3.12x10 ⁻⁵	0.0061	0.0058			1320	1.27x10 ⁻¹³	0.17	62.41	31.20
	2.58x10 ⁻⁹					3.76x10 ⁻¹⁶	3.38x10 ⁻¹⁴					
1170		1.51x10 ⁻⁸	3.12x10 ⁻⁵	0.0061	0.0058			1320	1.27x10 ⁻¹³	0.17	62.40	31.20

Table 6.19: The calculated mass loss rate using the Noyes-Whitney equation, with a boundary layer equal to 50% of the volume equivalent diameter.

US	Number of Crystals	Mass Loss Rate ($\mu\text{g/s}$)
0.05	5	$3.60 \times 10^{-7} \pm 1.14 \times 10^{-7}$
0.10	5	$1.00 \times 10^{-6} \pm 0$
0.15	5	$1.80 \times 10^{-6} \pm 4.47 \times 10^{-7}$
0.20	5	$2.80 \times 10^{-6} \pm 8.37 \times 10^{-7}$
0.25	5	$1.00 \times 10^{-6} \pm 0$
0.30	5	$1.60 \times 10^{-6} \pm 5.48 \times 10^{-7}$
0.35	5	$2.00 \times 10^{-6} \pm 0$
0.40	5	$1.80 \times 10^{-6} \pm 8.37 \times 10^{-7}$
0.45	5	$2.20 \times 10^{-6} \pm 4.47 \times 10^{-7}$
0.50	5	$2.60 \times 10^{-6} \pm 5.48 \times 10^{-7}$

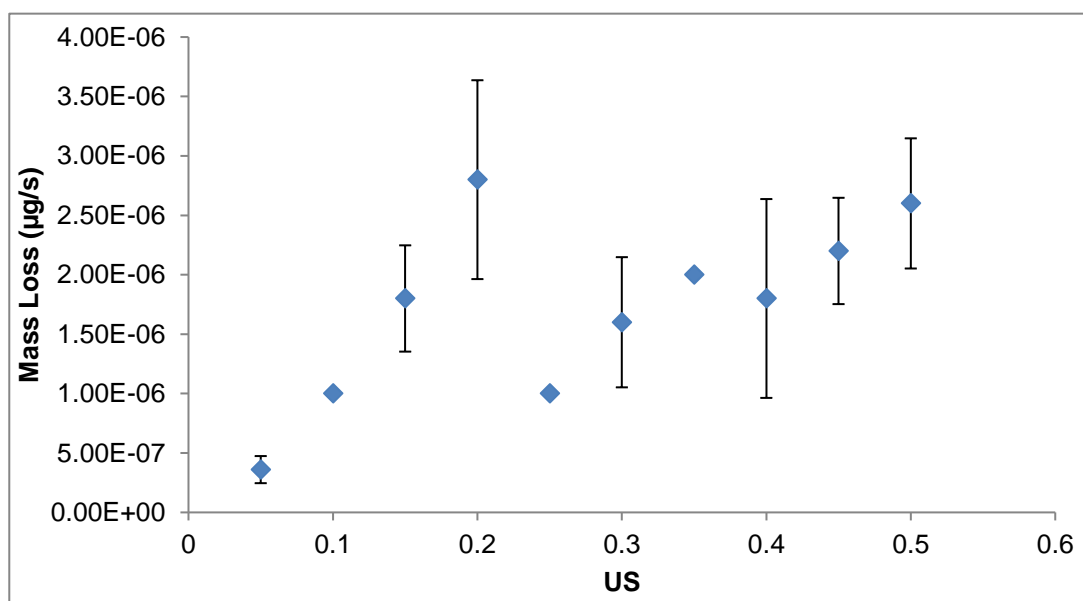


Figure 6.25: The relationship between the mass loss of a crystal of urea and the degree of undersaturation calculated using the Noyes-Whitney equation, with a boundary layer equal to 50% of the volume equivalent diameter.

The calculated mass loss using the Noyes-Whitney equation showed that the mass loss followed a linear trend with respect to undersaturation.

The mass loss rate calculated for the Noyes-Whitney model with the boundary layer thickness equal to 25% of the volume equivalent diameter over the range of experimental undersaturations is shown in Table 6.20.

Table 6.20: The calculated mass loss rate using the Noyes-Whitney equation, with a boundary layer equal to 25% of the volume equivalent diameter.

US	Number of Crystals	Mass Loss Rate ($\mu\text{g/s}$)
0.05	5	$6.80 \times 10^{-7} \pm 1.79 \times 10^{-7}$
0.10	5	$2.20 \times 10^{-6} \pm 4.47 \times 10^{-7}$
0.15	5	$4.20 \times 10^{-6} \pm 8.37 \times 10^{-7}$
0.20	5	$5.80 \times 10^{-6} \pm 1.48 \times 10^{-6}$
0.25	5	$2.20 \times 10^{-6} \pm 4.47 \times 10^{-7}$
0.30	5	$3.00 \times 10^{-6} \pm 1.00 \times 10^{-6}$
0.35	5	$3.20 \times 10^{-6} \pm 4.47 \times 10^{-7}$
0.40	5	$3.80 \times 10^{-6} \pm 8.37 \times 10^{-7}$
0.45	5	$4.40 \times 10^{-6} \pm 8.94 \times 10^{-7}$
0.50	5	$5.80 \times 10^{-6} \pm 8.37 \times 10^{-7}$

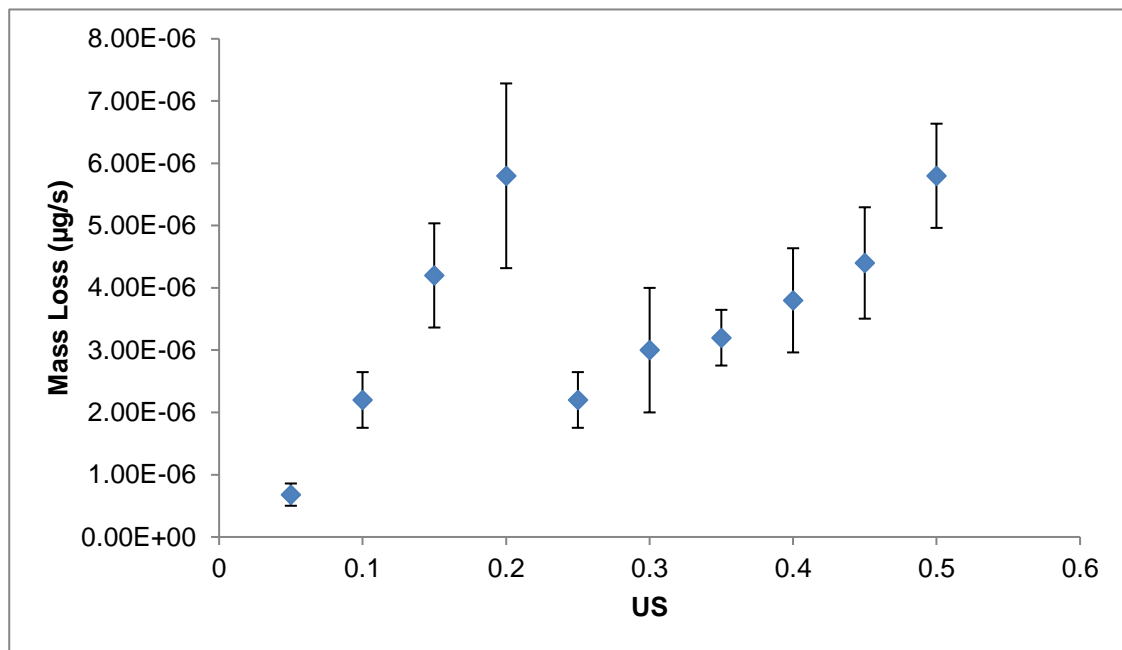


Figure 6.26: The relationship between the mass loss of a crystal of urea and the degree of undersaturation calculated using the Noyes-Whitney equation, with a boundary layer equal to 25% of the volume equivalent diameter.

The calculated mass loss using the Noyes-Whitney equation with a boundary layer thickness of 25% of the volume equivalent diameter also followed the same linear trend.

The mass loss rate calculated for the Noyes-Whitney model with the boundary layer thickness equal to 10% of the volume equivalent diameter, over the range of experimental undersaturations is shown in Table 6.21.

Table 6.21: The calculated mass loss rate using the Noyes-Whitney equation, with a boundary layer equal to 10% of the volume equivalent diameter.

US	Number of Crystals	Mass Loss Rate ($\mu\text{g/s}$)
0.05	5	$1.60 \times 10^{-6} \pm 5.48 \times 10^{-7}$
0.10	5	$5.60 \times 10^{-6} \pm 8.94 \times 10^{-7}$
0.15	5	$9.40 \times 10^{-6} \pm 1.34 \times 10^{-6}$
0.20	5	$1.20 \times 10^{-5} \pm 4.47 \times 10^{-6}$
0.25	5	$5.40 \times 10^{-6} \pm 5.48 \times 10^{-7}$
0.30	5	$7.60 \times 10^{-6} \pm 1.82 \times 10^{-6}$
0.35	5	$8.40 \times 10^{-6} \pm 5.48 \times 10^{-7}$
0.40	5	$8.60 \times 10^{-6} \pm 1.52 \times 10^{-6}$
0.45	5	$9.60 \times 10^{-6} \pm 5.48 \times 10^{-7}$
0.50	5	$1.40 \times 10^{-5} \pm 5.48 \times 10^{-6}$

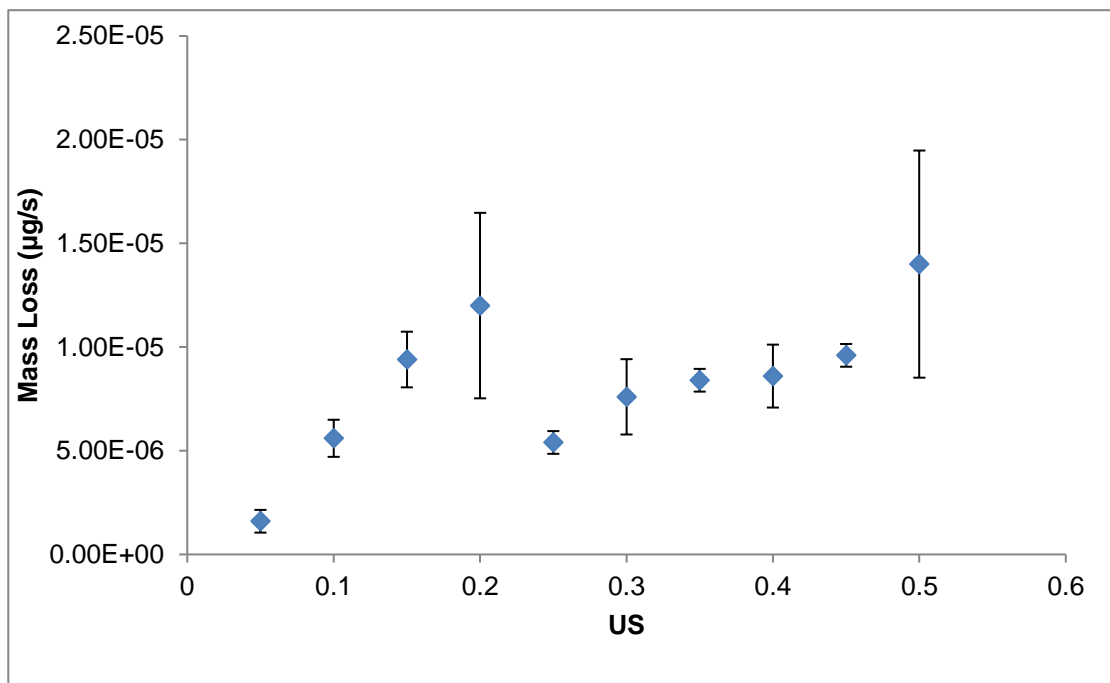


Figure 6.27: The relationship between the mass loss of a crystal of urea and the degree of undersaturation calculated using the Noyes-Whitney equation, with a boundary layer equal to 10% of the volume equivalent diameter.

The mass loss rate calculated for the Noyes-Whitney model with the boundary layer thickness equal to 1% of the volume equivalent diameter, over the range of experimental undersaturations is shown in Table 6.22.

Table 6.22: The calculated mass loss rate using the Noyes-Whitney equation, with a boundary layer equal to 1% of the volume equivalent diameter.

US	Number of Crystals	Mass Loss Rate ($\mu\text{g/s}$)
0.05	5	$1.60 \times 10^{-5} \pm 5.48 \times 10^{-6}$
0.10	5	$5.40 \times 10^{-5} \pm 5.48 \times 10^{-6}$
0.15	5	$9.40 \times 10^{-5} \pm 1.34 \times 10^{-5}$
0.20	5	$1.20 \times 10^{-4} \pm 4.47 \times 10^{-5}$
0.25	5	$4.80 \times 10^{-5} \pm 8.37 \times 10^{-6}$
0.30	5	$7.00 \times 10^{-5} \pm 1.58 \times 10^{-5}$
0.35	5	$7.80 \times 10^{-5} \pm 4.47 \times 10^{-6}$
0.40	5	$7.80 \times 10^{-5} \pm 1.79 \times 10^{-5}$
0.45	5	$9.00 \times 10^{-5} \pm 1.41 \times 10^{-5}$
0.50	5	$1.20 \times 10^{-4} \pm 4.47 \times 10^{-5}$

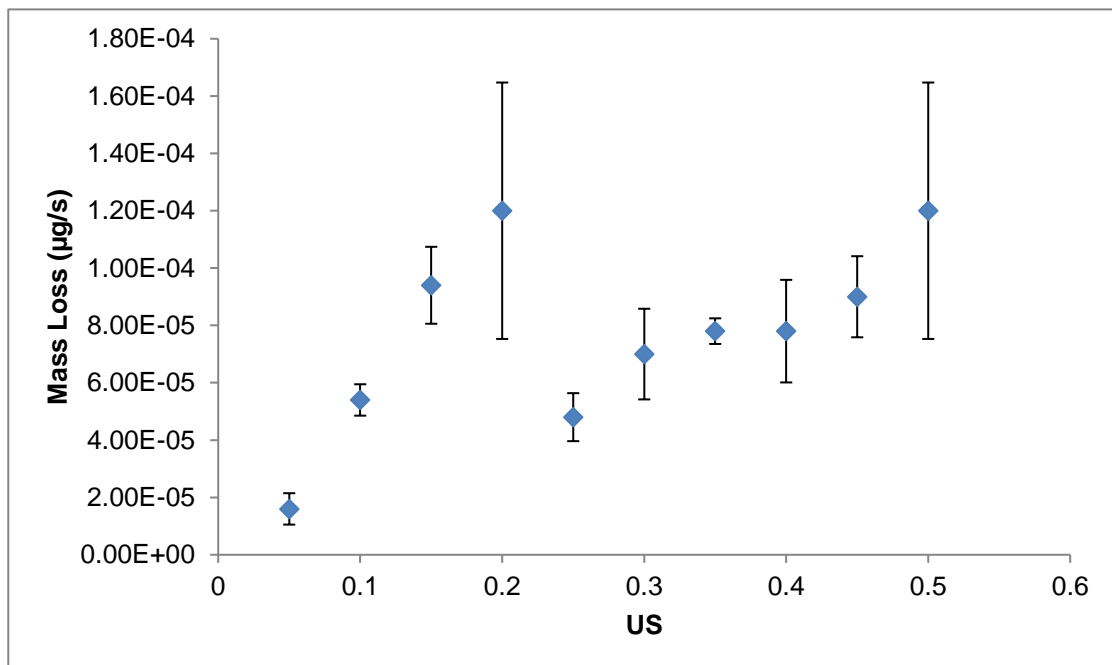


Figure 6.28: The relationship between the mass loss of a crystal of urea and the degree of undersaturation calculated using the Noyes-Whitney equation, with a boundary layer equal to 1% of the volume equivalent diameter.

Following on from this, the mass loss using the Hintz-Johnson dissolution model was also calculated. An example of the Hintz-Johnson calculation of the mass loss as a function of time, at an undersaturation of 0.05 is shown in Table 6.23.

Table 6.23: An example of the Hintz-Johnson calculation, at an undersaturation of 0.05.

Time (s)	Diffusion Coefficient [D] (m ² /s)	Surface Area (m ²)	Boundary Layer Thickness [h] (m)	Cs (kg/L)	Ct (kg/L)	dM/dt (kg/s)	mass lost (kg)	Density of Solute (kg/m ³)	Volume of Crystal (m ³)	Mass of Crystal (μg)	V.E.D	Particle Radius
0		1.52x10 ⁻⁸	3.00x10 ⁻⁵	0.0061	0.0058			1320	1.28x10 ⁻¹³	0.17	62.46	31.23
	2.58x10 ⁻⁹					3.92x10 ⁻¹⁶	4.70x10 ⁻¹⁴					
120		1.52x10 ⁻⁸	3.00x10 ⁻⁵	0.0061	0.0058			1320	1.28x10 ⁻¹³	0.17	62.45	31.23
	2.58x10 ⁻⁹					3.92x10 ⁻¹⁶	4.70x10 ⁻¹⁴					
240		1.52x10 ⁻⁸	3.00x10 ⁻⁵	0.0061	0.0058			1320	1.27x10 ⁻¹³	0.17	62.45	31.22
	2.58x10 ⁻⁹					3.92x10 ⁻¹⁶	4.70x10 ⁻¹⁴					
360		1.52x10 ⁻⁸	3.00x10 ⁻⁵	0.0061	0.0058			1320	1.27x10 ⁻¹³	0.17	62.44	31.22
	2.58x10 ⁻⁹					3.92x10 ⁻¹⁶	4.70x10 ⁻¹⁴					
480		1.52x10 ⁻⁸	3.00x10 ⁻⁵	0.0061	0.0058			1320	1.27x10 ⁻¹³	0.17	62.43	31.22
	2.58x10 ⁻⁹					3.92x10 ⁻¹⁶	4.70x10 ⁻¹⁴					
600		1.52x10 ⁻⁸	3.00x10 ⁻⁵	0.0061	0.0058			1320	1.27x10 ⁻¹³	0.17	62.43	31.21
	2.58x10 ⁻⁹					3.91x10 ⁻¹⁶	4.70x10 ⁻¹⁴					
720		1.51x10 ⁻⁸	3.00x10 ⁻⁵	0.0061	0.0058			1320	1.27x10 ⁻¹³	0.17	62.42	31.21
	2.58x10 ⁻⁹					3.91x10 ⁻¹⁶	4.70x10 ⁻¹⁴					
840		1.51x10 ⁻⁸	3.00x10 ⁻⁵	0.0061	0.0058			1320	1.27x10 ⁻¹³	0.17	62.42	31.21
	2.58x10 ⁻⁹					3.91x10 ⁻¹⁶	4.70x10 ⁻¹⁴					
960		1.51x10 ⁻⁸	3.00x10 ⁻⁵	0.0061	0.0058			1320	1.27x10 ⁻¹³	0.17	62.41	31.21
	2.58x10 ⁻⁹					3.91x10 ⁻¹⁶	4.69x10 ⁻¹⁴					
1080		1.51x10 ⁻⁸	3.00x10 ⁻⁵	0.0061	0.0058			1320	1.27x10 ⁻¹³	0.17	62.40	31.20
	2.58x10 ⁻⁹					3.91x10 ⁻¹⁶	3.52x10 ⁻¹⁴					
1170		1.51x10 ⁻⁸	3.00x10 ⁻⁵	0.0061	0.0058			1320	1.27x10 ⁻¹³	0.17	62.40	31.20

Table 6.24: The calculated mass loss rate using the Hintz-Johnson model.

US	Number of Crystals	Mass Loss Rate ($\mu\text{g/s}$)
0.05	5	$3.80 \times 10^{-7} \pm 1.48 \times 10^{-7}$
0.10	5	$1.40 \times 10^{-6} \pm 5.48 \times 10^{-7}$
0.15	5	$4.00 \times 10^{-6} \pm 1.22 \times 10^{-6}$
0.20	5	$5.60 \times 10^{-6} \pm 2.70 \times 10^{-6}$
0.25	5	$1.00 \times 10^{-6} \pm 0$
0.30	5	$1.60 \times 10^{-6} \pm 5.48 \times 10^{-7}$
0.35	5	$2.00 \times 10^{-6} \pm 0$
0.40	5	$1.80 \times 10^{-6} \pm 8.37 \times 10^{-7}$
0.45	5	$2.20 \times 10^{-6} \pm 4.47 \times 10^{-7}$
0.50	5	$2.60 \times 10^{-6} \pm 5.48 \times 10^{-7}$

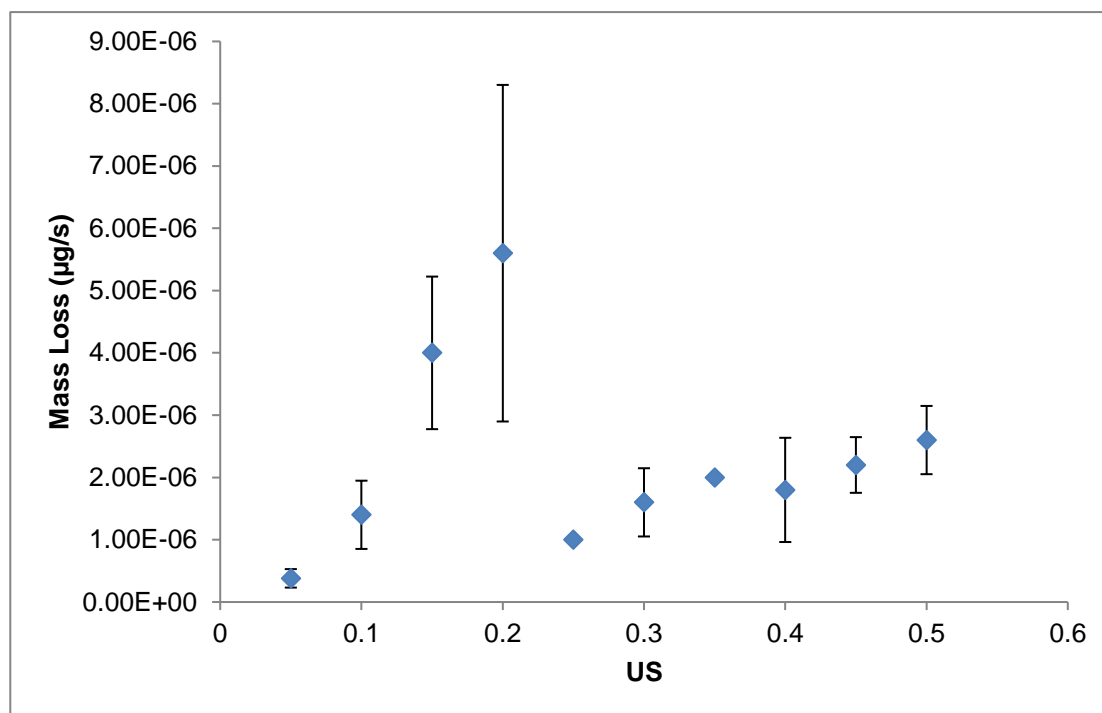


Figure 6.29: The relationship between the mass loss of a crystal of urea and the degree of undersaturation calculated using the Hintz-Johnson model.

6.5.2 Comparison of Models with Experimental Data

The predictions calculated for urea in acetonitrile using the Noyes-Whitney and Hintz-Johnson models were compared to the actual mass loss determined through dissolution experiments. The actual mass loss was calculated through the use of

Heron's formula to determine the surface area, and the shape factor to determine the volume and hence the mass for each crystal.

Table 6.25: An example of the calculation of actual mass loss as a function of time, at an undersaturation of 0.05

Time (s)	Surface Area (m ²)	Volume (m ³)	Density (kg/m ³)	Mass (µg)
0	1.52x10 ⁻⁸	1.28x10 ⁻¹³	1320	0.17
120	1.38x10 ⁻⁸	1.11x10 ⁻¹³	1320	0.15
240	1.42x10 ⁻⁸	1.15x10 ⁻¹³	1320	0.15
360	1.32x10 ⁻⁸	1.04x10 ⁻¹³	1320	0.14
480	1.23x10 ⁻⁸	9.29x10 ⁻¹⁴	1320	0.12
600	1.33x10 ⁻⁸	1.05x10 ⁻¹⁴	1320	0.14
720	1.19x10 ⁻⁸	8.89x10 ⁻¹⁴	1320	0.12
840	1.03x10 ⁻⁸	7.15x10 ⁻¹⁴	1320	0.09
960	1.10x10 ⁻⁸	7.86x10 ⁻¹⁴	1320	0.10
1080	1.07x10 ⁻⁸	7.55x10 ⁻¹⁴	1320	0.10
1170	1.00x10 ⁻⁸	6.86x10 ⁻¹⁴	1320	0.09

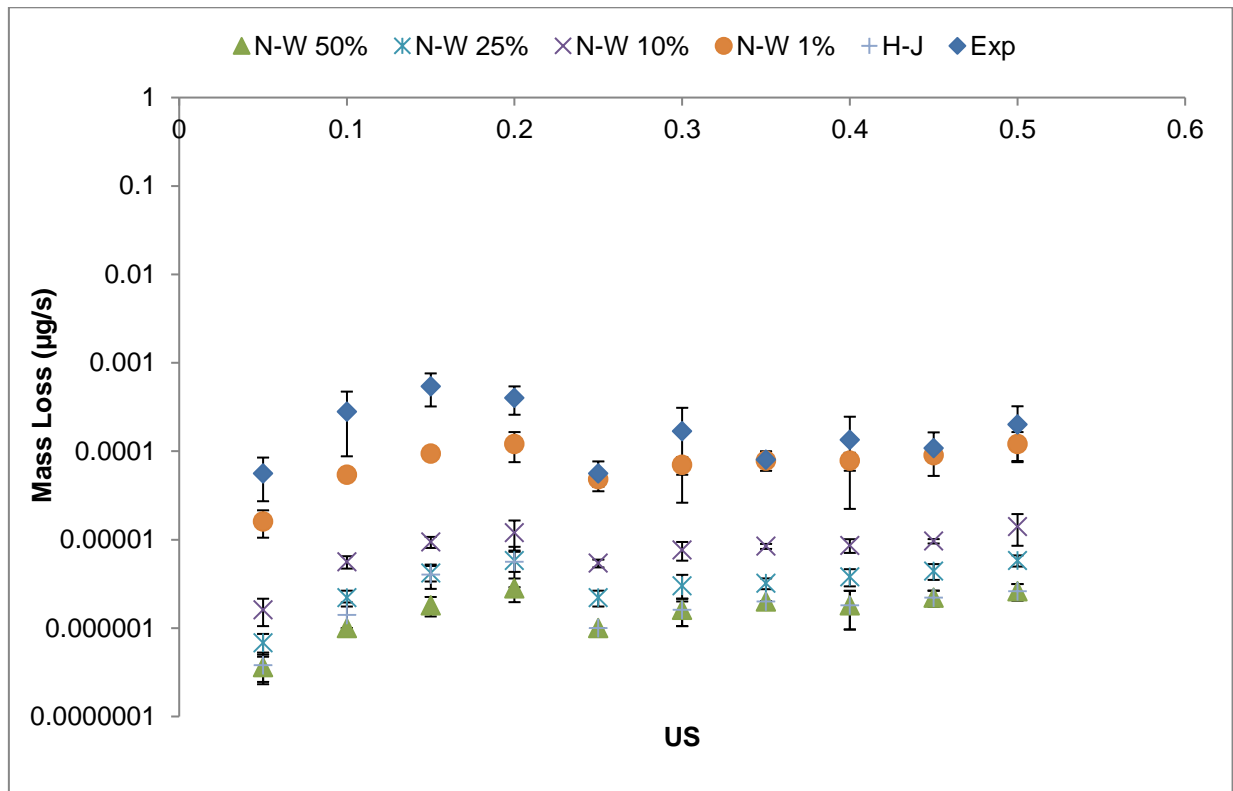


Figure 6.30: A comparison between the experimental mass loss and calculated mass losses using Noyes-Whitney and Hintz-Johnson.

The predicted mass loss of the crystal for all models is not an accurate prediction in comparison with the experimental mass loss. The percentage difference between the actual mass loss and predicted mass loss is shown in Table 6.26.

Table 6.26: The percentage difference between values of experimental mass loss and calculated mass loss.

US	% difference				
	N-W (50%)	N-W (25%)	N-W (10%)	N-W (1%)	H-J
0.05	99.36	98.79	97.14	71.43	99.32
0.10	99.64	99.21	98.00	80.71	99.50
0.15	99.67	99.22	98.26	82.59	99.26
0.20	99.30	98.55	97.00	70.00	98.60
0.25	98.21	96.07	90.36	14.29	98.21
0.30	99.05	98.21	95.48	58.33	99.05
0.35	97.50	96.00	89.50	2.50	97.50
0.40	98.66	97.16	93.58	41.79	98.66
0.45	97.96	95.93	91.11	16.67	97.96
0.50	98.70	97.10	93.00	40.00	98.70

The percentage difference shows that the predicted values are inaccurate and in the same range of inaccuracy as that of urea in ethanol, in comparison with the actual experimental mass loss.

6.5.3 Modification of Dissolution Models

The modification to the dissolution model was carried out for the data obtained for urea in acetonitrile, in order to validate the results obtained for urea in ethanol. Therefore, in order to further modify the models, a fixed boundary layer was assumed, and the models re-calculated. A fixed boundary layer of $0.3\mu\text{m}$ was used, an example of this calculation for an undersaturation of 0.05 is shown in Table 6.27.

Table 6.27: An example of the Noyes-Whitney calculation with a fixed boundary layer parameter of 0.3 μm .

Time (s)	Diffusion Coefficient [D] (m ² /s)	Surface Area (m ²)	Boundary Layer Thickness [h] (m)	C _s (kg/L)	C _t (kg/L)	dM/dt (kg/s)	mass lost (kg)	Density of Solute (kg/m ³)	Volume of Crystal (m ³)	Mass of Crystal (μg)
0		1.52 x10 ⁻⁸	3.00 x10 ⁻⁷	0.0061	0.0058			1320	1.28 x10 ⁻¹³	0.17
	2.58x10 ⁻⁹					3.92 x10 ⁻¹⁴	4.70 x10 ⁻¹²			
120		1.49 x10 ⁻⁸	3.00 x10 ⁻⁷	0.0061	0.0058			1320	1.24 x10 ⁻¹³	0.16
	2.58x10 ⁻⁹					3.84 x10 ⁻¹⁴	4.61 x10 ⁻¹²			
240		1.46 x10 ⁻⁸	3.00 x10 ⁻⁷	0.0061	0.0058			1320	1.21 x10 ⁻¹³	0.16
	2.58x10 ⁻⁹					3.77 x10 ⁻¹⁴	4.53 x10 ⁻¹²			
360		1.43 x10 ⁻⁸	3.00 x10 ⁻⁷	0.0061	0.0058			1320	1.17 x10 ⁻¹³	0.15
	2.58x10 ⁻⁹					3.70 x10 ⁻¹⁴	4.44 x10 ⁻¹²			
480		1.40 x10 ⁻⁸	3.00 x10 ⁻⁷	0.0061	0.0058			1320	1.14 x10 ⁻¹³	0.15
	2.58x10 ⁻⁹					3.63 x10 ⁻¹⁴	4.35 x10 ⁻¹²			
600		1.38 x10 ⁻⁸	3.00 x10 ⁻⁷	0.0061	0.0058			1320	1.10 x10 ⁻¹³	0.15
	2.58x10 ⁻⁹					3.56 x10 ⁻¹⁴	4.27 x10 ⁻¹²			
720		1.35 x10 ⁻⁸	3.00 x10 ⁻⁷	0.0061	0.0058			1320	1.07 x10 ⁻¹³	0.14
	2.58x10 ⁻⁹					3.49 x10 ⁻¹⁴	4.19 x10 ⁻¹²			
840		1.32 x10 ⁻⁸	3.00 x10 ⁻⁷	0.0061	0.0058			1320	1.04 x10 ⁻¹³	0.14
	2.58x10 ⁻⁹					3.42 x10 ⁻¹⁴	4.10 x10 ⁻¹²			
960		1.30 x10 ⁻⁸	3.00 x10 ⁻⁷	0.0061	0.0058			1320	1.01 x10 ⁻¹³	0.13
	2.58x10 ⁻⁹					3.35 x10 ⁻¹⁴	4.02 x10 ⁻¹²			
1080		1.27 x10 ⁻⁸	3.00 x10 ⁻⁷	0.0061	0.0058			1320	9.79 x10 ⁻¹⁴	0.13
	2.58x10 ⁻⁹					3.28 x10 ⁻¹⁴	2.95 x10 ⁻¹²			
1170		1.25 x10 ⁻⁸	3.00 x10 ⁻⁷	0.0061	0.0058			1320	9.56 x10 ⁻¹⁴	0.13

A comparison of the mass loss values with a fixed boundary layer thickness with the experimental values obtained is shown below.

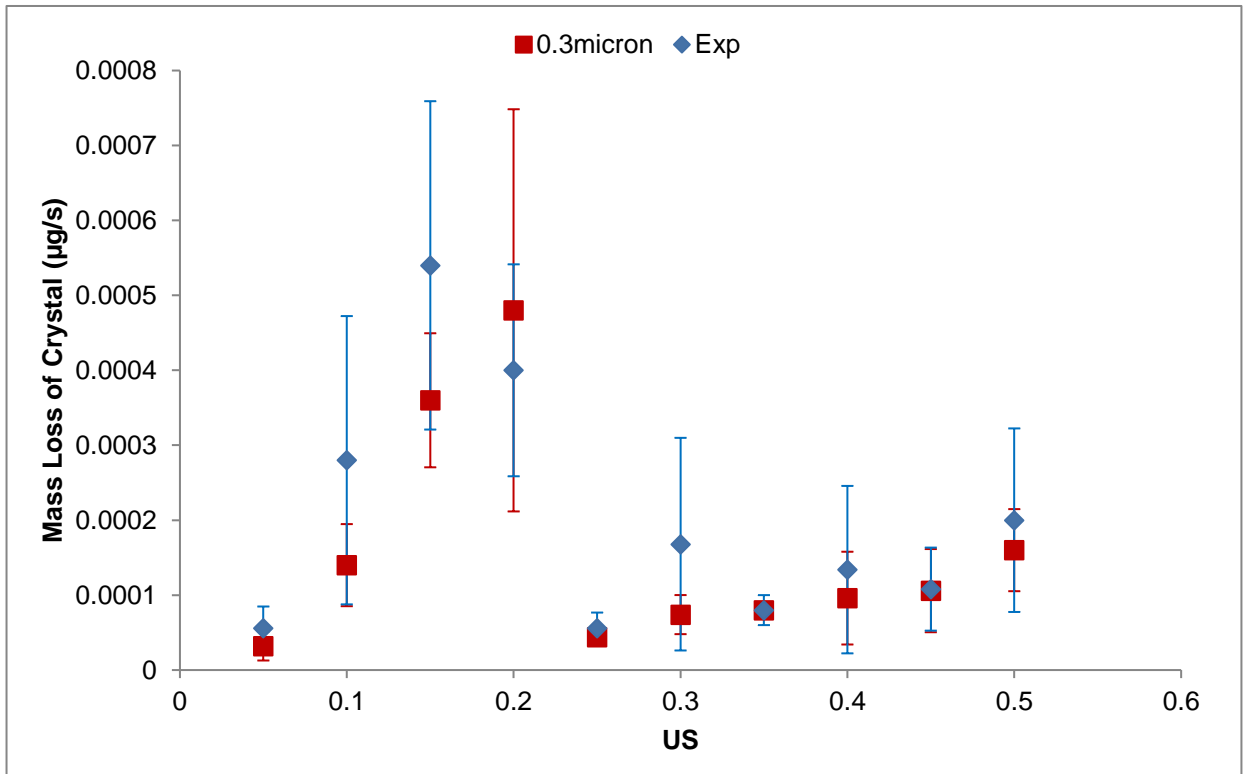


Figure 6.31: Comparison between the experimental mass loss and calculated values with a fixed boundary layer.

Table 6.28: The percentage difference between values of experimental mass loss and calculated mass loss with a fixed boundary layer.

Undersaturation	% difference
0.05	42.86
0.10	50.00
0.15	33.33
0.20	16.67
0.25	21.43
0.30	55.95
0.35	0.00
0.40	28.36
0.45	1.85
0.50	20.00

This modification resulted in a much more consistent prediction for the mass loss in comparison with the experimental mass loss, and the fixed boundary layer thickness values are consistent with the values determined by Bunn and Emmett (1949).

Upon comparison of the fixed boundary layers of urea in ethanol and acetonitrile, the prediction of the modified model shows that for ethanol the boundary layer thickness should be $0.5\mu\text{m}$ for a consistent dissolution prediction, whereas for acetonitrile, the prediction of the modified model shows that the boundary layer thickness should be $0.3\mu\text{m}$.

This can be explained through the interaction energies calculated, as ethanol has a stronger interaction on average with the surfaces of urea. Additionally, as ethanol is a polar protic solvent, therefore can accept and donate hydrogen bonds with urea, which are longer range bonds than van der Waals dispersive interactions, the boundary layer thickness does not need to be as small in order for the dissolving urea molecules to move across the boundary layer and interact with the bulk of the solution. As acetonitrile is a polar aprotic solvent, therefore can only accept hydrogen bonds with urea, a majority of interactions are due to van der Waals dispersive interactions mean the boundary layer thickness has to be much closer to the dissolving particle, in order for the dissolving molecules of urea to interact with the bulk of the solution.

6.6 Comparison of Urea Dissolution in Ethanol and Acetonitrile

The data obtained from molecular modelling and wetting energy calculations allows for predictions to be made regarding the dissolution of faces of a compound in different solvents. A comparison of the total interaction energy data obtained from VisualHabit systsearch, and wetting energies obtained from COSMOtherm, for both faces of urea in ethanol and acetonitrile has been presented in Figure 6.32.

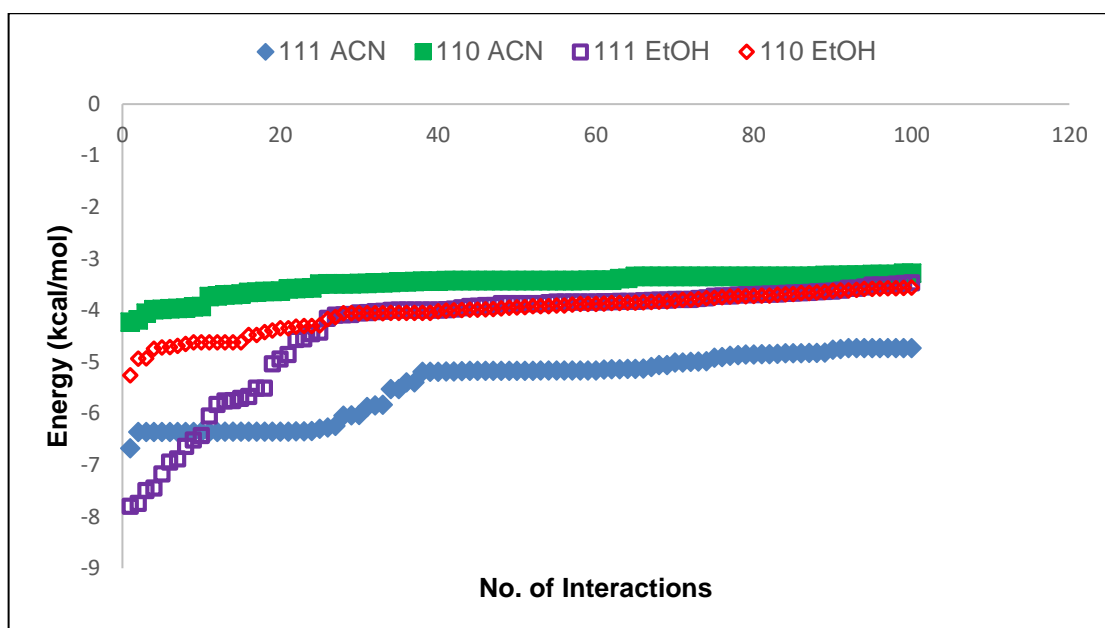


Figure 6.32: A comparison of the total interaction energies of {110} and {111} surfaces with ethanol and acetonitrile.

Table 6.29: A comparison of the wetting energies of {110} and {111} surfaces of urea with ethanol and acetonitrile.

Face	Wetting Energy (kcal/mol)	
	Ethanol	Acetonitrile
{110}	-6.469	-4.368
{111}	-18.531	-6.846

This data shows that the total interaction energies are similar for both faces in ethanol and acetonitrile. The wetting energies for both faces in acetonitrile and for the {110} face in ethanol are also similar, however the wetting energy for the {111} face in ethanol is much larger than the other energy values. As a result of this, the expectation would be that the dissolution of both faces in acetonitrile and the {110} face in ethanol would have similar rates, and the dissolution rate of the {111} face in ethanol would be faster than that of the other faces. The experimental dissolution rates of both faces obtained in ethanol and acetonitrile are presented in Figure 6.33.

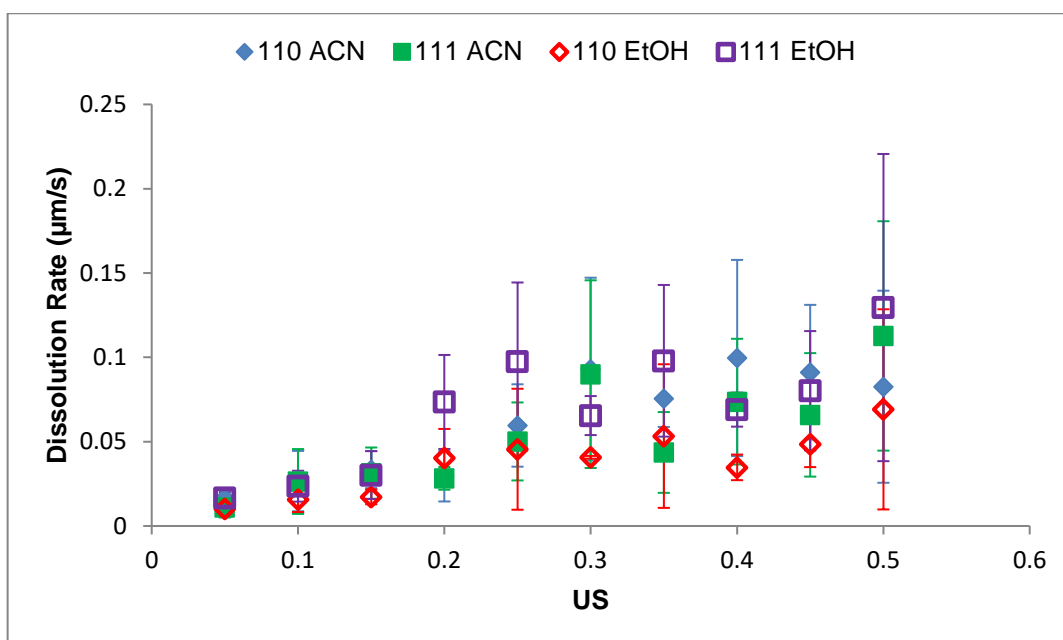


Figure 6.33: A comparison of the dissolution rates of {110} and {111} surfaces of urea in ethanol and acetonitrile.

This experimental data shows that the {110} face in ethanol, and the {110} and {111} face of urea in acetonitrile have similar dissolution rates, whereas the dissolution of the {111} face of urea in ethanol is faster than that of the other faces. This reinforces conclusions made through the determination of intermolecular interactions and wetting energies of the faces.

6.7 Conclusions

This chapter aimed to present the dissolution rate data of urea in absolute ethanol under opposing undersaturation conditions as Chapter 5. It was found that both the {110} and {111} faces follow a first-order linear dependence with respect to undersaturation, with the {111} face dissolving faster than {110} with increasing levels of undersaturation. In direct comparison with growth rate data, the growth and dissolution rates of both faces were found to be the same, allowing for the conclusion to be made that in the case of urea in absolute ethanol, the dissolution rates of both faces under consideration are the reverse process of the growth rates. The determination of interaction energies of both {110} and {111} surfaces with an ethanol probe reinforced the experimental data obtained as ethanol was found to have a stronger interaction with the {111} face and a much higher wetting energy.

This chapter also aimed to compare the dissolution behaviour of urea in different solution environments. It was found that the dissolution rates of {110} and {111} of

urea also followed a first-order linear dependence, however in acetonitrile both faces were found to have comparable dissolution rates with respect to undersaturation, although the dissolution rate of the {111} face was slightly higher. The determination of interaction energies of both surfaces with an acetonitrile probe reinforced the experimental data obtained as acetonitrile was found to have similar interactions with both faces, although the interaction with the {111} surface was slightly higher, and also similar wetting energies. The difference between the interaction energies of {110} and {111} and the standard deviations of the experimental results were not significant enough to conclude that {111} would have a stronger interaction with acetonitrile.

A comparison of the dissolution rates of urea in both solvent environments showed that the interaction of ethanol with the {111} surface was stronger and the wetting energy was significantly higher, whereas the interaction of ethanol with the {110} surface and interactions of acetonitrile with both surfaces were comparable. This validated the experimental results obtained as the dissolution rates of both faces in acetonitrile and the {110} face in ethanol were comparable, whereas the dissolution rate of {111} in ethanol was higher. Finally, calculation of the dissolution models to obtain theoretical overall mass loss data during dissolution experiments and comparing them to the experimental mass loss showed that the predicted values of the models were inconsistent, therefore current dissolution models could not be used to calculate mass loss in non-sink conditions. This was found to be the case for both solution systems.

Therefore, the dissolution models were modified, altering the boundary layer thickness as of the two models used for prediction calculations, both treated this parameter in different ways. A fixed boundary layer thickness was used for both solution systems, and a more consistent prediction was found for both systems, with boundary layer thicknesses of 0.5 μm and 0.3 μm for ethanol and acetonitrile, respectively. This difference in thicknesses was explained through interaction energies calculated as, on average, ethanol had a stronger interaction with the urea surfaces. This was due to ethanol being a polar protic solvent and being able to both accept and donate hydrogen bonds with urea, therefore urea could interact with the bulk of solution over a larger boundary layer. Acetonitrile, however, being a polar aprotic solvent, meant that a smaller boundary layer would be needed in order for urea to interact with the bulk of solution.

References

Bunn, C. W., H. Emmett. Crystal Growth from Solution: 1. Layer Formation on Crystal Faces. *Discuss. Faraday Soc.* **1949**. 5, 119-132.

Cosmologic. **2019**. <http://www.cosmologic.de/products/cosmotherm.html>

Hammond, R. B., K. Pencheva, K. J. Roberts. A Structural-Kinetic Approach to Model Face Specific Solution/Crystal Surface Energy Associated with the Crystallisation of Acetyl Salicylic Acid from Supersaturated Aqueous/Ethanol Solution. *Cryst. Growth. Des.* **2006**. 6(6), 1324-1334.

Hintz, R. J., K. C. Johnson. The Effect of Particle Size Distribution on Dissolution Rate and Oral Absorption. . *Int. J. Pharm.* **1989**. 51(1), 9-17.

Noyes, A. A., W. R. Whitney. The Rate of Solution of Solid Substances in their Own Solutions. *J. Am. Chem. Soc.* **1897**. 19(12), 930-934.

Pickering, J., Kathyola, T., Nguyen, T. H., Ramachandran, V., Soufian, M., Hammond, R. B., Roberts, K. J., Pencheva, K., Ticehurst, M. A Comparative Study of the Experimental and Theoretical Dissolution Kinetics of Ibuprofen in Ethanol. (*Submitted J. Pharm. Sci.*)

Pickering, J., R. B. Hammond, V. Ramachandran, M. Soufian, K. J. Roberts. Synthonic Engineering Modelling Tools for Product and Process Design. *Engineering Crystallography: From Molecule to Crystal to Functional Form*. **2017**. NATO: Springer.

Wang, Y. Abrahamsson, B., Lindfors, L., Brasseur, J. G. Comparison and Analysis of Theoretical Models for Diffusion Controlled Dissolution. *Mol. Pharmaceutics*. **2012**. 9(5), 1052-1066.

Chapter 7: Dissolution of Paracetamol Single Crystals

7.1 Introduction

Dissolution of pharmaceutical single crystals or powders is crucial in establishing an in-vitro in-vivo relationship of an API which results in a more in-depth characterisation. As a result, this can be used to request a waiver from regulatory authorities, decreasing the time needed for development. (Khadka et al., 2014) Face-specific dissolution of pharmaceutical materials has not widely been studied, although there has been increasing interest in the development of a reliable in-vitro process that can accurately predict the rate of dissolution. (McAllister, 2010)

This chapter aims to present the dissolution data of paracetamol in acetonitrile and fed-state simulated intestinal fluid (FeSSIF), which firstly, allows for a comparison of the dissolution of paracetamol in different solution environments, and secondly, allows for the determination of the dissolution of a pharmaceutical single crystal in non-sink conditions in intestinal fluid. In addition, molecular modelling using Mercury VisualHabit (Pickering et al., 2017) has also been presented in order to determine face dependent molecular interactions between the solution environments in order to rationalise experimental data obtained.

Finally, a number of dissolution models have been employed to determine the theoretical overall mass loss of a single crystal in differing solution environments, along with a comparison with the overall mass loss determined through experimentation. The amendments made to the dissolution models in Chapter 6 have also been employed in order to obtain a more consistent prediction to facilitate the development of a reliable in-vitro process to determine in-vivo dissolution.

7.2 Solubility of Paracetamol

The solubility of Paracetamol in acetonitrile, water and FeSSIF was obtained experimentally using Crystal 16 and from literature. (Granberg et al., 1999)

Table 7.1: Solubilities of paracetamol in acetonitrile, water and FeSSIF.

Temperature (°C)	Solubility (mg/mL)		
	Acetonitrile	Water	FeSSIF
-5	7		
0	9	7.21	
5	11	8.21	
10	13	9.44	
15	15	10.97	
20	18	12.78	
25	22	14.90	10
27			10.5
30	26	17.39	11
32			12
35	29	19.20	13
37			14
40	34	21.80	15
42			18

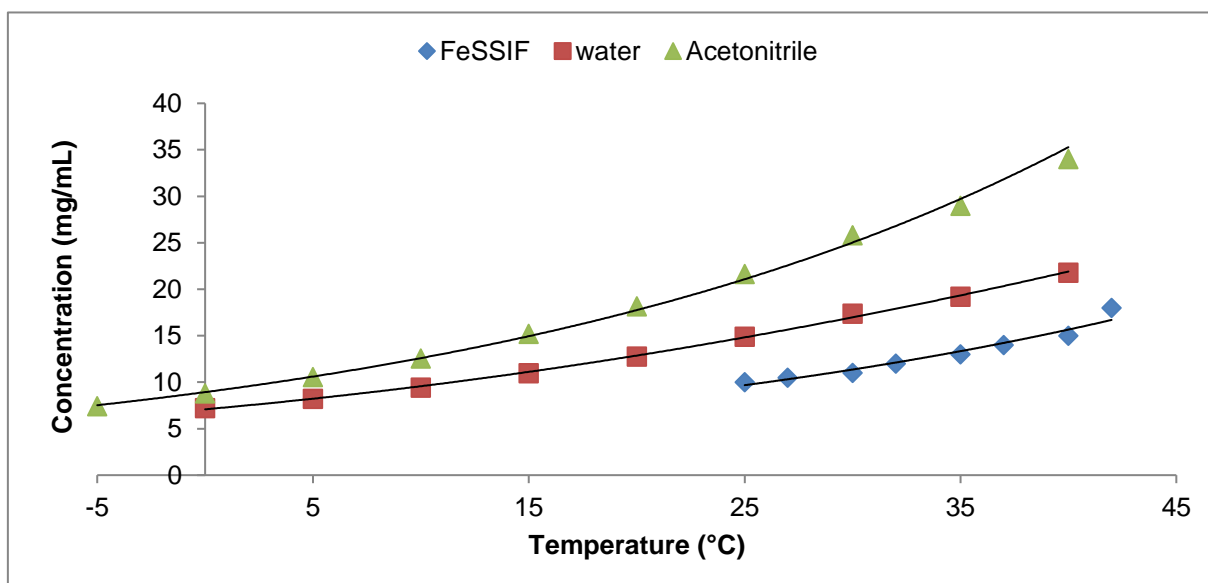


Figure 7.1: A comparison of the solubilities of paracetamol in acetonitrile, water and FeSSIF.

The theoretical solubility of Paracetamol in the three solvents were determined through the van't Hoff equation, assuming ideal solution behaviour, and this was compared to the solubility data obtained.

Table 7.2: Calculated activity coefficients of paracetamol in acetonitrile, water and FeSSIF.

	Temperature (°C)	1/T	X _{ideal}	X _{solubility}	Activity coefficient
Acetonitrile	-5	0.0037	0.0085	0.0026	3.31
	0	0.0037	0.0106	0.0030	3.49
	5	0.0036	0.0131	0.0037	3.59
	10	0.0035	0.0161	0.0043	3.71
	15	0.0035	0.0197	0.0053	3.74
	20	0.0034	0.0238	0.0063	3.80
	25	0.0034	0.0287	0.0075	3.84
	30	0.0033	0.0344	0.0089	3.85
	35	0.0032	0.0409	0.0100	4.08
	40	0.0032	0.0484	0.0117	4.12
Water	0	0.0037	0.0106	0.0009	12.32
	5	0.0036	0.0131	0.0010	13.40
	10	0.0035	0.0161	0.0011	14.33
	15	0.0035	0.0197	0.0013	15.05
	20	0.0034	0.0238	0.0015	15.66
	25	0.0034	0.0287	0.0018	16.17
	30	0.0033	0.0344	0.0021	16.59
	35	0.0032	0.0409	0.0023	17.88
	40	0.0032	0.0484	0.0026	18.63
FeSSIF	25	0.0034	0.0287	0.0012	24.10
	27	0.0033	0.0309	0.0013	24.68
	30	0.0033	0.0344	0.0013	26.22
	32	0.0033	0.0369	0.0014	25.79
	35	0.0032	0.0409	0.0015	26.40
	37	0.0032	0.0438	0.0017	26.24
	40	0.0032	0.0484	0.0018	27.08
	42	0.0032	0.0517	0.0021	24.10

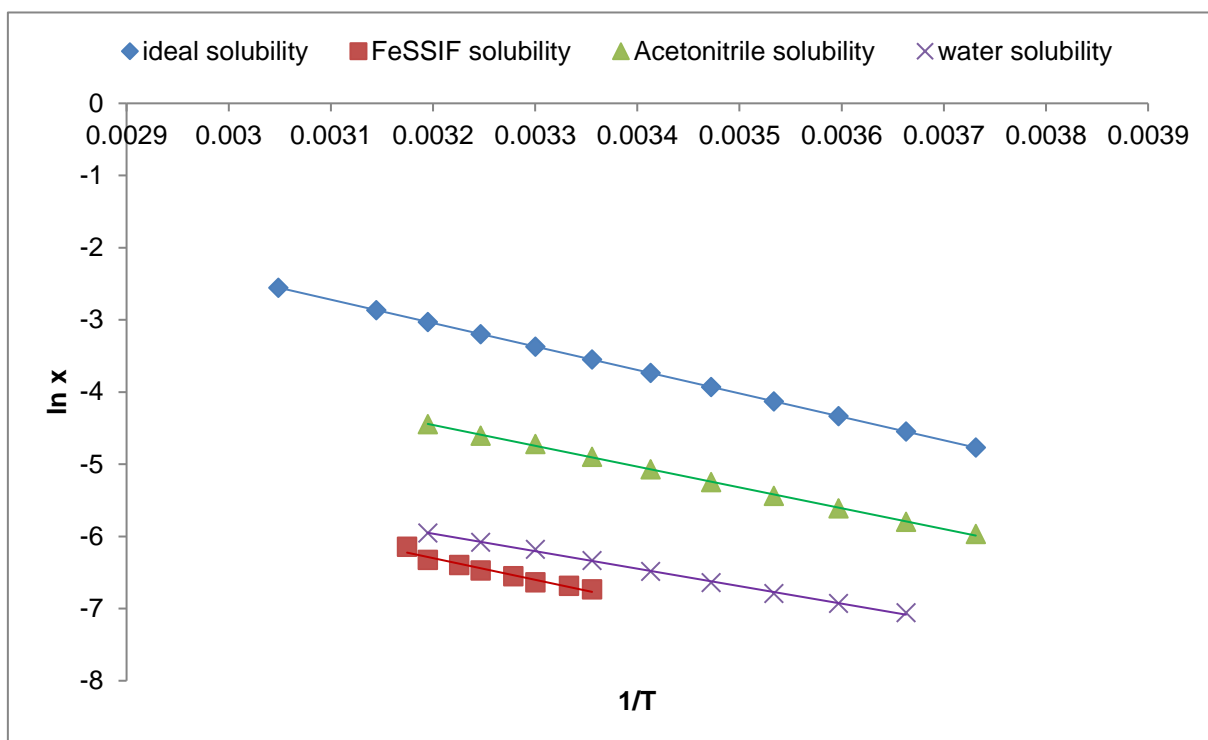


Figure 7.2: A comparison of the ideal solubility of paracetamol, calculated using van't Hoff equation, with solubilities in the three solvents.

In an ideal solution, the amount of energy required to break solute-solute interactions in addition to the amount of energy required to break solvent-solvent interactions is equal to the amount of energy required to make solute-solvent interactions. The solubility of Paracetamol in all three solvents is less than ideal, therefore solute-solute interactions are favoured. This is reinforced by the calculation of activity coefficient, as the activity coefficient is greater than 1, so the forces of attraction between solute-solute molecules would be favoured over forces of attraction between solute-solvent molecules. Comparison of the three solvents shows that acetonitrile has greater ideality than water and FeSSIF, and has an activity coefficient greater than one, whereas FeSSIF has a much higher activity coefficient, therefore Paracetamol solubility in the three solvents is acetonitrile > water > FeSSIF.

A solution can exhibit behaviour different to that of an ideal solution due to either enthalpic or entropic factors, or both. This can be determined through the Van't Hoff plots, i.e. if the gradients of the lines differ, the deviation from ideal solution would be due to both enthalpic and entropic factors. However, if the lines are parallel, the deviation from ideal behaviour is only due to entropic factors. As the gradient of solubility of acetonitrile is similar to that of the ideal, it can be concluded that

deviation from ideal behaviour is only due to entropic factors. However, in water and FeSSIF, deviation from ideal behaviour is both enthalpically and entropically driven.

7.3 Surface Characterisation of Paracetamol

Crystals of Paracetamol exhibit five approximately equivalent morphologically important faces – {011}, {100}, {110}, {201} and {001} giving rise to a prismatic crystal habit. (Sudha et al., 2014; Prasad et al., 2002) These faces can affect the crystal habit of Paracetamol depending on supersaturation or crystallisation conditions, with a dominant {110} face grown in water giving rise to a more columnar morphology and a dominant {001} face grown in organic solvents giving rise to a more plate-like morphology. (Finnie et al., 2001)

This approximately equivalent morphological importance of the faces can be explained through their surface chemistry's. This is because Paracetamol is formed of a phenol, with a methylamide group, and a carbonyl group. The amide group acts as a hydrogen bond donor and the carbonyl group acts as a hydrogen bond acceptor, along with the hydroxyl group which can act as either donor or acceptor.

The {201}, {001} and {011} surfaces have similar functional group contributions, with the slight differences between the faces being attributed to the difference in the orientation of functional groups at the surface. Heng et al. (2006) found that the relative surface polarity of the facets in decreasing order was (001) > (011) > (201) > (110). The polarity of the {110} surface was lower than all the other external surfaces studied because although the hydroxyl, amine and carbonyl groups were present at the surface they were not free to interact with external molecules.

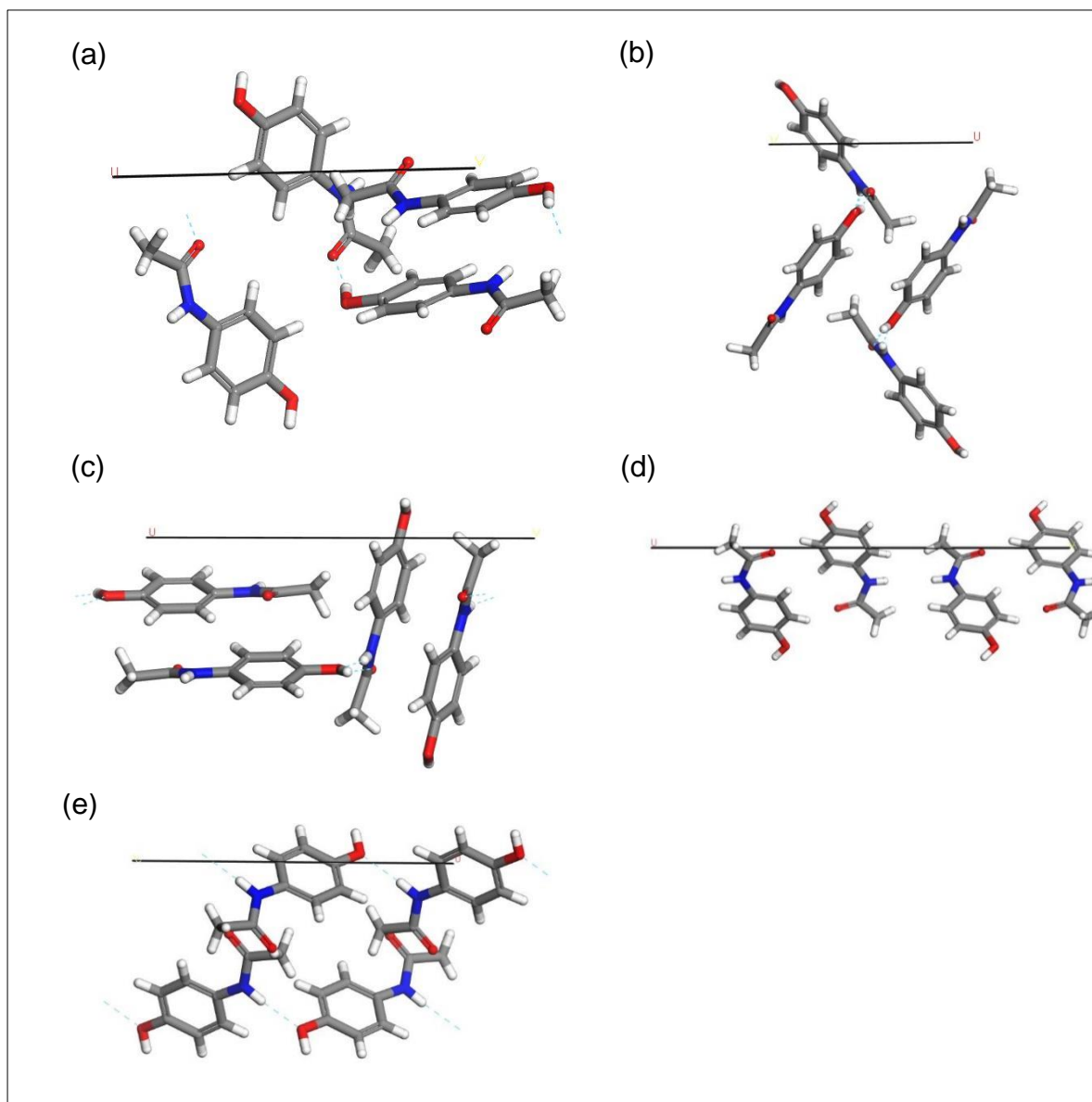


Figure 7.3: The (a) $\{011\}$, (b) $\{100\}$, (c) $\{110\}$, (d) $\{201\}$ and (e) $\{001\}$ surfaces of paracetamol.

7.4 Dissolution of Paracetamol in Acetonitrile

Paracetamol single crystals were dissolved in acetonitrile under differing levels of undersaturation. The experimental dissolution rates of the five faces mentioned in Chapter 3 which have been shown to have equivalent morphological importance were determined. The dissolution rates of the five faces were then compared to the intermolecular interactions of the faces under consideration, and conclusions made were reinforced due to energy interactions obtained.

7.4.1 Face Specific Dissolution Rate

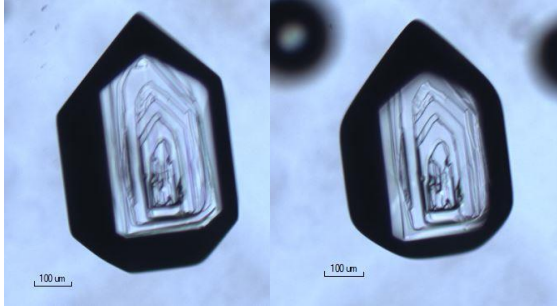
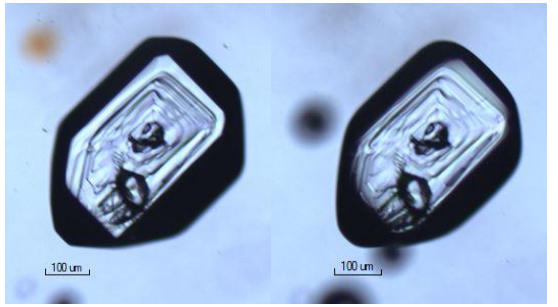
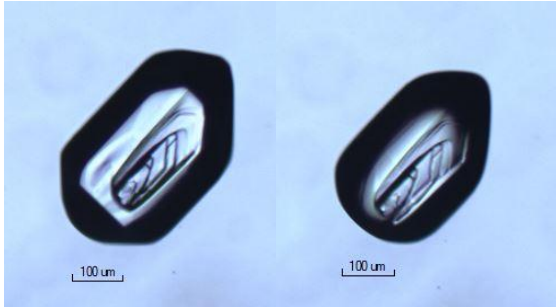
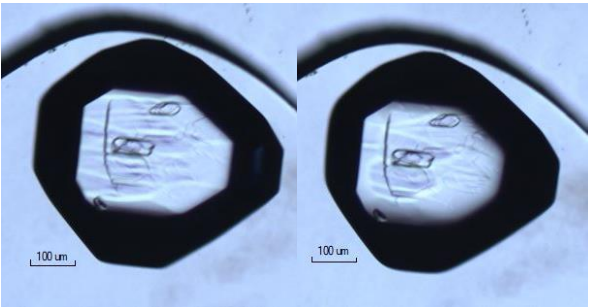
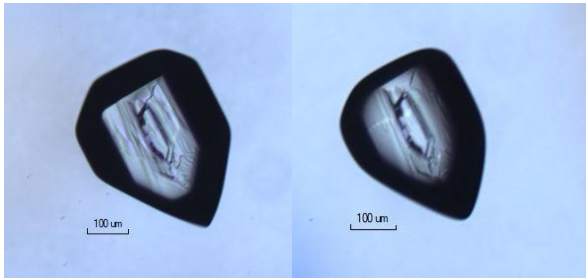
Experimental dissolution rate data has been provided in Appendix C3, which comprises of 25 single crystals spontaneously nucleated and grown in acetonitrile over a period of three hours. These crystals were then dissolved over an undersaturation range from ~0.05 to 0.25. The crystals were dissolved in a stagnant solution under diffusion limited conditions in a 0.5mL cuvette, immersed in a water cell. The distance between the centre of the crystal, and the face under consideration was then measured as a function of time.

Table 7.3: Experimental mean retreat rates and standard deviations obtained for paracetamol in acetonitrile.

US	No. of Crystals	Mean Retreat Rate ($\mu\text{m/s}$)			
		{110}	{011}	{201}	{100}
0.05	5	$7.18 \times 10^{-2} \pm 2.12 \times 10^{-2}$	$3.67 \times 10^{-2} \pm 1.80 \times 10^{-2}$	$2.20 \times 10^{-2} \pm 1.34 \times 10^{-2}$	$6.19 \times 10^{-2} \pm 0$
0.10	5	$4.49 \times 10^{-2} \pm 2.08 \times 10^{-2}$	$3.16 \times 10^{-2} \pm 1.06 \times 10^{-2}$	$2.50 \times 10^{-2} \pm 1.22 \times 10^{-2}$	$2.75 \times 10^{-2} \pm 2.72 \times 10^{-2}$
0.15	5	$5.23 \times 10^{-2} \pm 2.58 \times 10^{-2}$	$5.05 \times 10^{-2} \pm 3.49 \times 10^{-2}$	$6.38 \times 10^{-2} \pm 3.36 \times 10^{-2}$	$7.36 \times 10^{-2} \pm 4.94 \times 10^{-2}$
0.20	5	$2.96 \times 10^{-2} \pm 4.78 \times 10^{-2}$	$6.36 \times 10^{-2} \pm 3.02 \times 10^{-2}$	$6.75 \times 10^{-2} \pm 6.77 \times 10^{-2}$	$6.02 \times 10^{-2} \pm 3.67 \times 10^{-2}$
0.25	5	$7.25 \times 10^{-2} \pm 6.46 \times 10^{-2}$	$3.65 \times 10^{-2} \pm 1.65 \times 10^{-2}$	$2.70 \times 10^{-2} \pm 5.64 \times 10^{-2}$	$5.85 \times 10^{-2} \pm 3.60 \times 10^{-2}$

The initial and final images of the retreat rate of crystals dissolved in the cuvette are shown in Table 7.4. Final images were taken when the dissolution of the crystals reached the point where further dissolution would result in rounding of the crystal faces.

Table 7.4: An example of the experimental crystal images obtained at the initial and final time points for paracetamol in acetonitrile at each undersaturation.

Paracetamol Single Crystal Dissolution in Acetonitrile	
<p>US = 0.05</p> <p>t = 0mins t = ~10mins</p> 	<p>US = 0.10</p> <p>t = 0mins t = ~7mins</p> 
<p>US = 0.15</p> <p>t = 0 mins t = ~7mins</p> 	<p>US = 0.20</p> <p>t = 0mins t = ~3mins</p> 
<p>US = 0.25</p> <p>t = 0mins t = ~3mins</p> 	

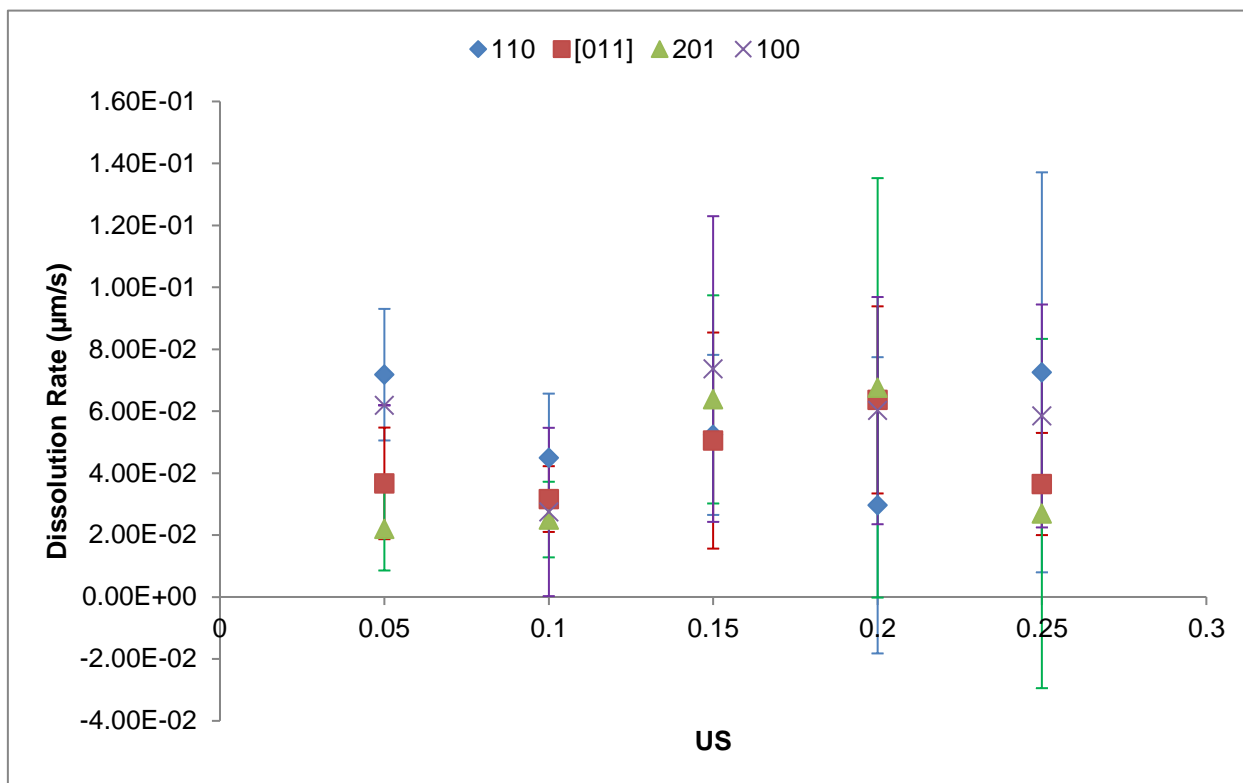


Figure 7.4: The relationship between dissolution rate and undersaturation for the faces of paracetamol in acetonitrile.

The dissolution rates of the faces under consideration showed that it is difficult to make a definitive conclusion regarding a trend between the undersaturation and the dissolution rate due to the errors obtained. However, there was found to be no significant solvent effect on any of the faces, and all of the faces were found to have similar dissolution rates.

7.4.2 Intermolecular Interactions of Paracetamol with Acetonitrile

Surface characterisation of Paracetamol has been carried out in Section 7.3, with the five main morphologically important faces being identified – {011}, {100}, {110}, {201}, and {001}. The interaction of acetonitrile with the crystal faces under consideration after having been grown from acetonitrile were modelled through the systematic search function using Mercury VisualHabit.

7.4.2.1 {011}

The minimum interaction energy between a probe molecule of acetonitrile and the {011} surface was found. This minimum interaction energy is the strongest and most stable interaction between the solvent and the solute.

The {011} surface was built of multiple unit cells surrounding the unit cell used for the grid search function in order to ensure that edge effects do not interfere with the calculation of interaction energies. It was ensured that grid rows closest to and furthest away from the surface contained white tetrahedrons only, as the interactions were found to be smaller than the defined minimum value, therefore were considered negligible.

Removal of the grid showed that there were varying degrees of acetonitrile interaction with the {011} surface with the strongest of these interactions being shown in Figure 7.5.

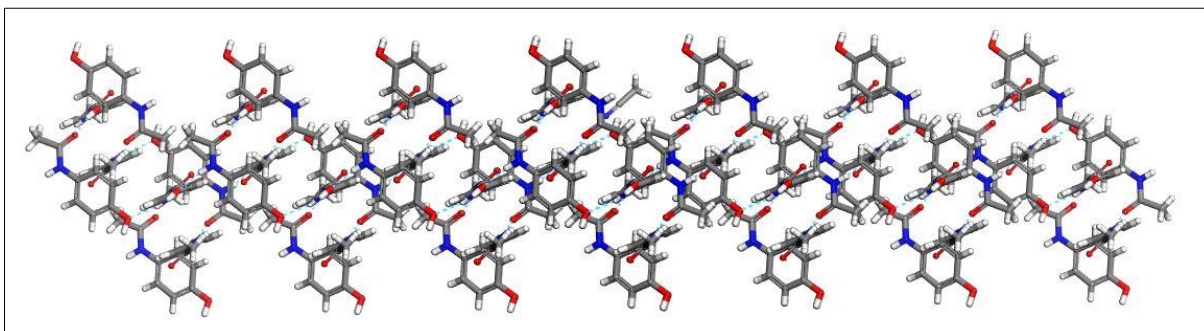


Figure 7.5: The strongest interaction of acetonitrile with the {011} surface, with hydrogen bonding depicted.

Calculation of the interaction energy between the acetonitrile probe molecule and the {011} surface allowed for the determination of the total interaction energy, and also divided this total interaction energy figure into van der Waals (dispersive), hydrogen bonding, and electrostatic interactions. Thousands of interactions were calculated through the SystSearch function, however, for the purposes of clarity, the 100 strongest interactions have been presented.

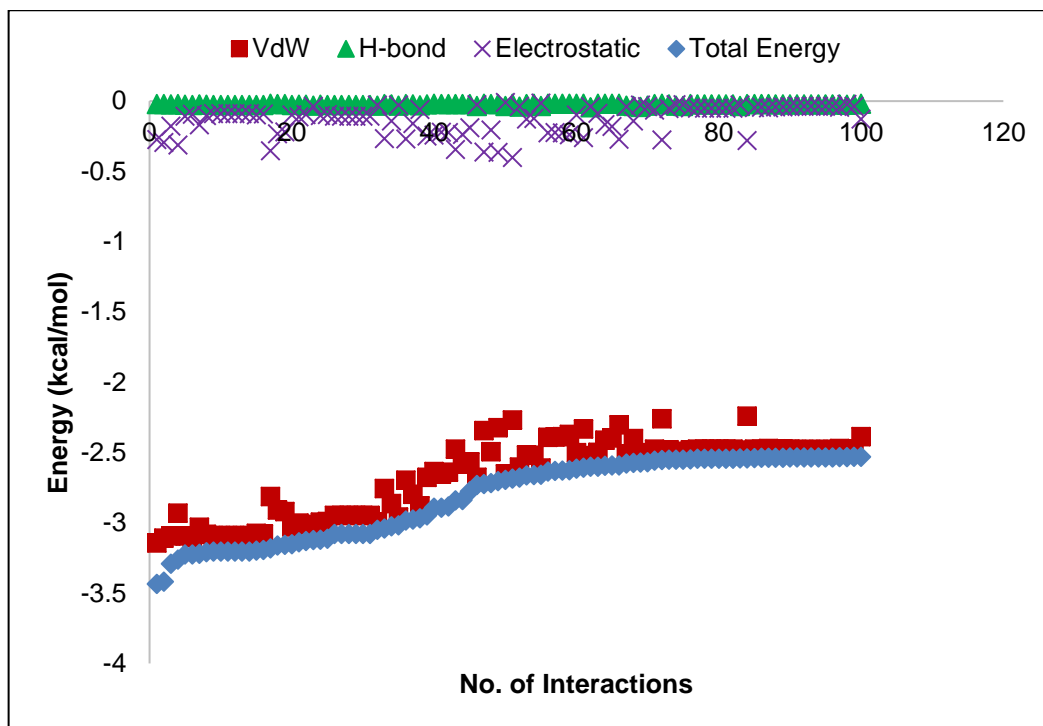


Figure 7.6: The top 100 interactions of acetonitrile with the {011} surface, broken down into hydrogen bonding, van der Waals and electrostatic interactions.

This suggests that the majority of the total interaction energy of the acetonitrile probe molecule with the {011} surface is due to van der Waals dispersive interactions, with hydrogen bonding and electrostatic interactions making up a minimal amount of the total interaction energy.

7.4.2.2 {100}, {110}, and {201}

The interaction energies of acetonitrile with the {100}, {110} and {201} faces were also determined, to allow for a comparison of the interaction energies between the faces under consideration. The same process as was carried out for the {011} surface was also used for the other surface calculations.

Removal of the grid after grid search calculations were carried out showed that there were varying degrees of acetonitrile interaction with each of the faces, with the highest energy interactions of the {100}, {110} and {201} surfaces with the acetonitrile probe being shown in Figure 7.7, respectively.

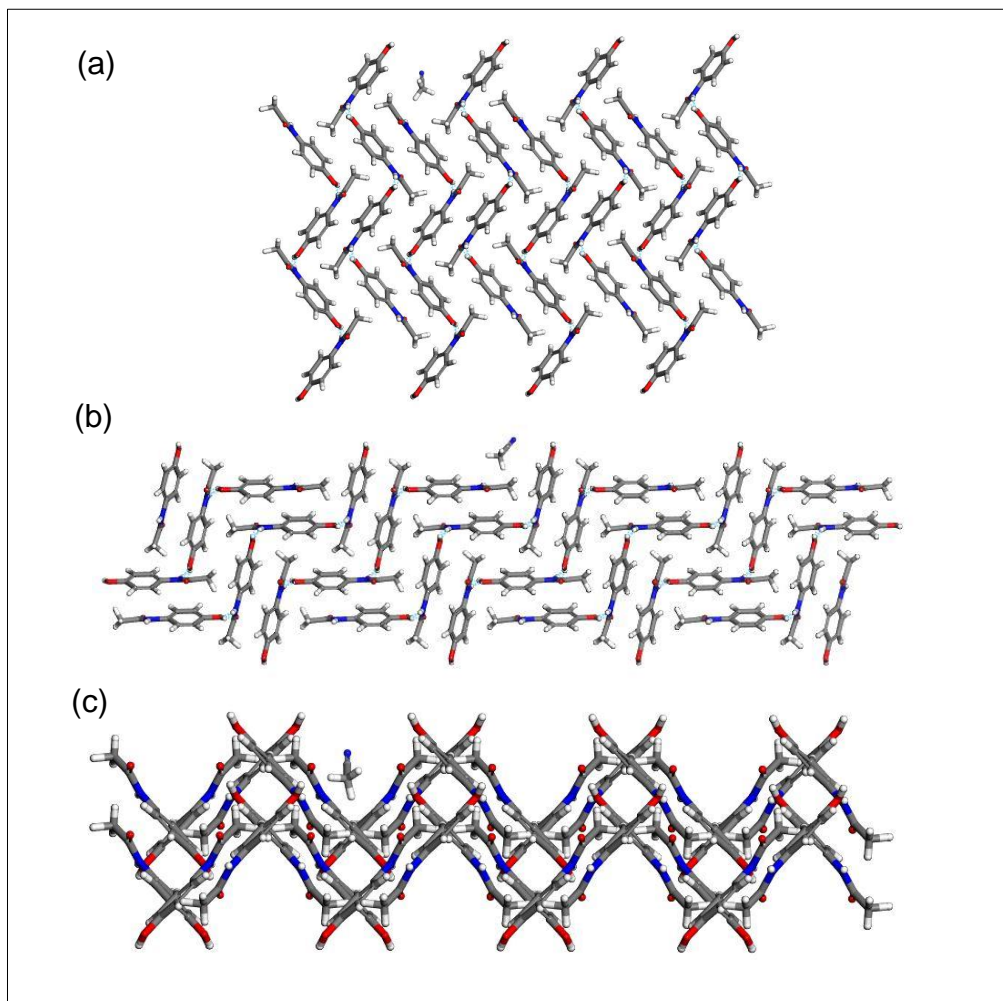


Figure 7.7: The strongest interaction of acetonitrile with the (a) {100}, (b) {110} and (c) {201} surfaces of paracetamol, with hydrogen bonding depicted.

The calculation of these energy interactions between the acetonitrile probe molecule and the surfaces under consideration allowed for the determination of the type of interaction and the strength of these interactions. The number of interactions calculated through the SystSearch function were in the thousands, therefore for the purposes of clarity, the 100 strongest interactions have been presented.

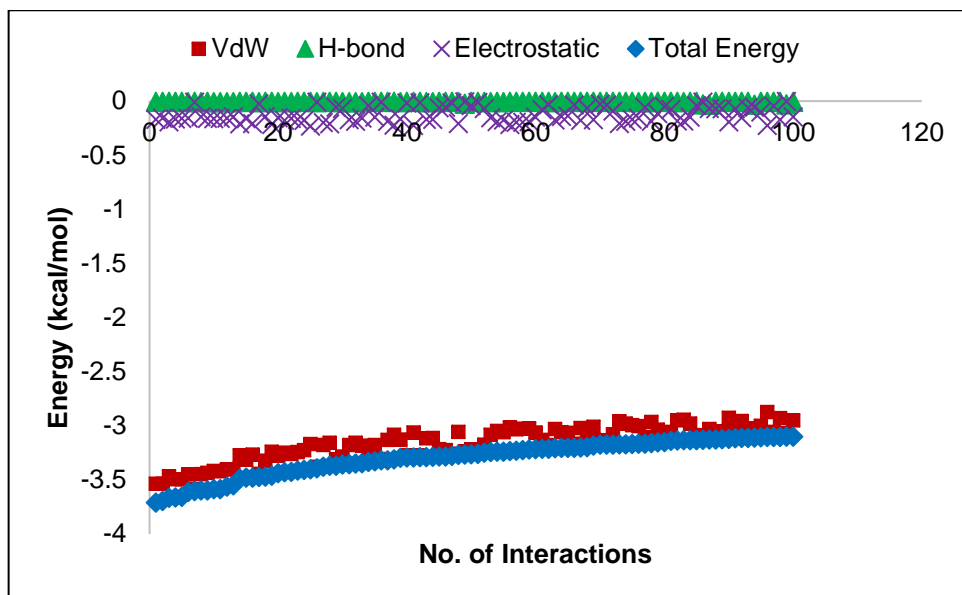


Figure 7.8: The top 100 interactions of acetonitrile with the {100} surface, broken down into hydrogen bonding, van der Waals and electrostatic interactions.

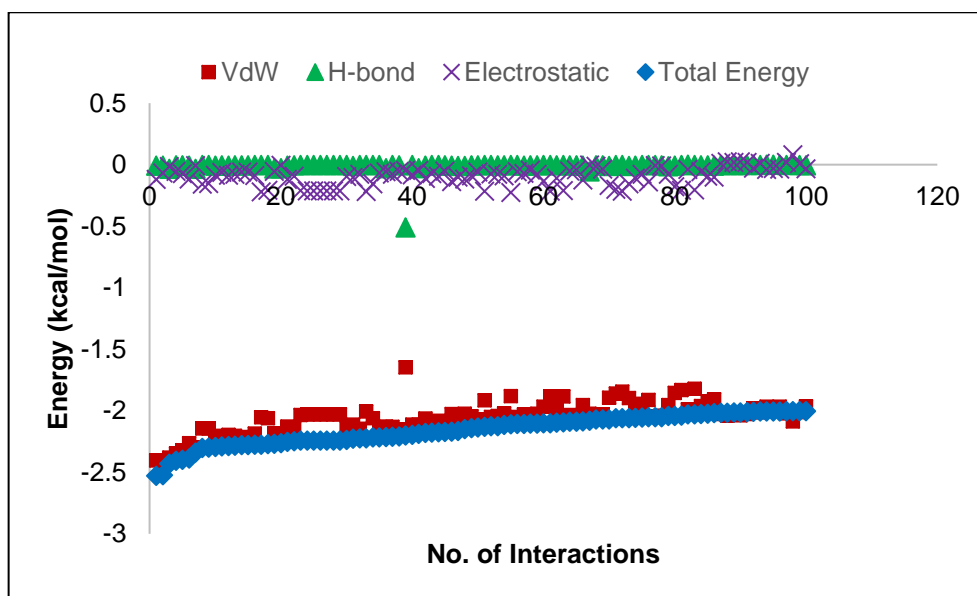


Figure 7.9: The top 100 interactions of acetonitrile with the {110} surface, broken down into hydrogen bonding, van der Waals and electrostatic interactions.

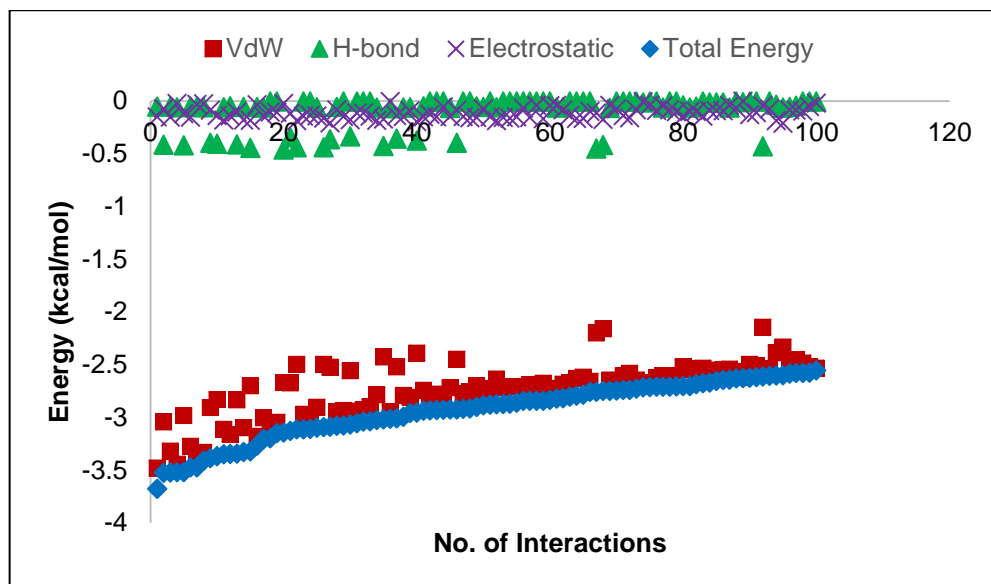


Figure 7.10: The top 100 interactions of acetonitrile with the {201} surface, broken down into hydrogen bonding, van der Waals and electrostatic interactions.

These interactions suggest that the interaction of the acetonitrile probe with the other surfaces under consideration are mostly van der Waals dispersive interactions, with hydrogen bonding and electrostatic interactions making up a minimal amount of the interaction.

7.4.2.3 Comparison of Surface Interactions

A comparison of the total interaction energies of the four surfaces under consideration are shown below.

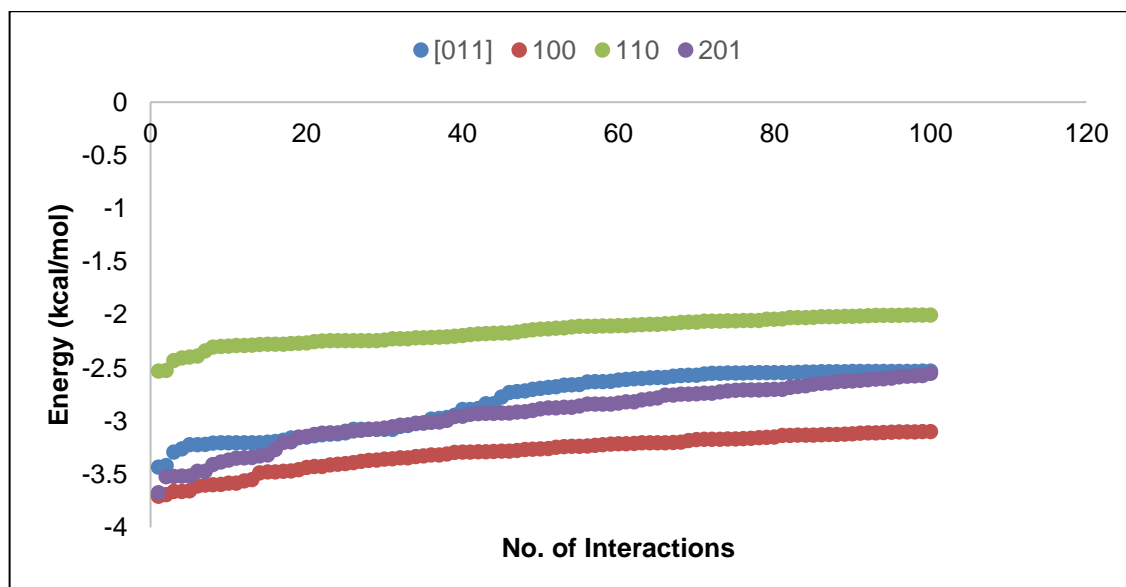


Figure 7.11: A comparison of the total energy interactions of acetonitrile with all surfaces of paracetamol.

The acetonitrile probe was found to have a similar energy interaction with all of the faces under consideration. As a result of this comparison, the experimental results were validated in that the dissolution rates of all four faces in acetonitrile are comparable. These results were in good agreement with work carried out previously (Heng et al., 2006) as the {110} surface was found to have a lower polarity than the other surfaces, Therefore as acetonitrile is a polar solvent, it would be expected that the {110} surface would have a slightly weaker interaction with this surface in comparison with the other surfaces under consideration.

7.5 Dissolution Model Predictions for Paracetamol in Acetonitrile

The Noyes-Whitney (1897) and Hintz-Johnson (1989) dissolution models were calculated to determine the predicted mass loss of a crystal of paracetamol in acetonitrile. Additionally, these calculations were carried out in order to further validate the conclusions made in Chapter 6. As the Noyes-Whitney model states that boundary layer thickness is a function of particle size, a number of boundary layer thicknesses were used in order to determine the optimal thin-film thickness that corresponds best to the experimental data. Therefore, boundary layer thicknesses equal to 50%, 25%, 10% and 1% of the volume equivalent diameter of the particle were used.

7.5.1 Noyes-Whitney and Hintz-Johnson

An example of the Noyes-Whitney calculation of the mass loss as a function of time, with the boundary layer thickness equal to 50% of the volume equivalent diameter, at an undersaturation of 0.05 is shown in Table 7.5.

Table 7.5: An example of the Noyes-Whitney calculation, at an undersaturation of 0.05, with a boundary layer equal to 50% of the volume equivalent diameter.

Time (s)	Diffusion Coefficient [D] (m ² /s)	Surface Area (m ²)	Boundary Layer Thickness [h] (m)	Cs (kg/L)	Ct (kg/L)	dM/dt (kg/s)	mass lost (kg)	Density of Solute (kg/m ³)	Volume of Crystal (m ³)	Mass of Crystal (μg)	V.E.D	Radius (50% VED)
0		1.22x10 ⁻⁷	8.80x10 ⁻⁵	0.027	0.026			1290	2.86x10 ⁻¹²	3.68	176.01	88.01
	1.83x10 ⁻⁹					2.53x10 ⁻¹⁵	1.52x10 ⁻¹³					
60		1.22x10 ⁻⁷	8.80x10 ⁻⁵	0.027	0.026			1290	2.86x10 ⁻¹²	3.68	176.01	88.00
	1.83x10 ⁻⁹					2.53x10 ⁻¹⁵	1.52x10 ⁻¹³					
120		1.22x10 ⁻⁷	8.80x10 ⁻⁵	0.027	0.026			1290	2.85x10 ⁻¹²	3.68	176.01	88.00
	1.83x10 ⁻⁹					2.53x10 ⁻¹⁵	1.52x10 ⁻¹³					
180		1.22x10 ⁻⁷	8.80x10 ⁻⁵	0.027	0.026			1290	2.85x10 ⁻¹²	3.68	176.00	88.00
	1.83x10 ⁻⁹					2.53x10 ⁻¹⁵	1.52x10 ⁻¹³					
240		1.22x10 ⁻⁷	8.80x10 ⁻⁵	0.027	0.026			1290	2.85x10 ⁻¹²	3.68	176.00	88.00
	1.83x10 ⁻⁹					2.53x10 ⁻¹⁵	1.52x10 ⁻¹³					
300		1.22x10 ⁻⁷	8.80x10 ⁻⁵	0.027	0.026			1290	2.85x10 ⁻¹²	3.68	176.00	88.00
	1.83x10 ⁻⁹					2.53x10 ⁻¹⁵	1.52x10 ⁻¹³					
360		1.22x10 ⁻⁷	8.80x10 ⁻⁵	0.027	0.026			1290	2.85x10 ⁻¹²	3.68	176.00	88.00
	1.83x10 ⁻⁹					2.53x10 ⁻¹⁵	1.52x10 ⁻¹³					
420		1.22x10 ⁻⁷	8.80x10 ⁻⁵	0.027	0.026			1290	2.85x10 ⁻¹²	3.68	175.99	88.00
	1.83x10 ⁻⁹					2.53x10 ⁻¹⁵	1.52x10 ⁻¹³					
480		1.22x10 ⁻⁷	8.80x10 ⁻⁵	0.027	0.026			1290	2.85x10 ⁻¹²	3.68	175.99	88.00
	1.83x10 ⁻⁹					2.53x10 ⁻¹⁵	1.52x10 ⁻¹³					
540		1.22x10 ⁻⁷	8.80x10 ⁻⁵	0.027	0.026			1290	2.85x10 ⁻¹²	3.68	175.99	87.99
	1.83x10 ⁻⁹					2.53x10 ⁻¹⁵	7.59x10 ⁻¹⁴					
570		1.22x10 ⁻⁷	8.80x10 ⁻⁵	0.027	0.026			1290	2.85x10 ⁻¹²	3.68	175.98	87.99

Table 7.6: The calculated mass loss rate using the Noyes-Whitney equation, with a boundary layer equal to 50% of the volume equivalent diameter.

US	Number of Crystals	Mass Loss Rate ($\mu\text{g/s}$)
0.05	5	$2.00 \times 10^{-6} \pm 7.07 \times 10^{-7}$
0.10	5	$5.80 \times 10^{-6} \pm 1.40 \times 10^{-6}$
0.15	5	$7.00 \times 10^{-6} \pm 1.87 \times 10^{-6}$
0.20	5	$7.20 \times 10^{-6} \pm 1.92 \times 10^{-6}$
0.25	5	$9.00 \times 10^{-6} \pm 1.22 \times 10^{-6}$

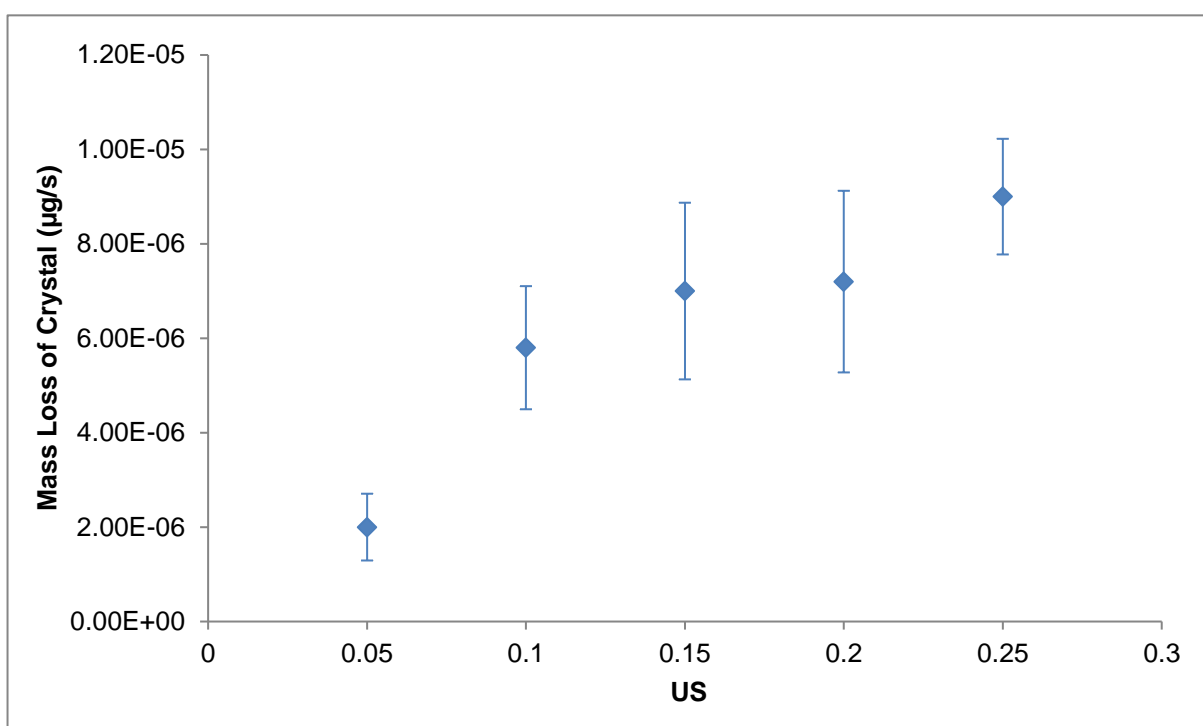


Figure 7.12: The relationship between the mass loss of a crystal of paracetamol and the degree of undersaturation calculated using the Noyes-Whitney equation, with a boundary layer equal to 50% of the volume equivalent diameter.

The calculated mass loss using the Noyes-Whitney equation showed that the mass loss followed a linear trend with respect to undersaturation.

The mass loss rate calculated for the Noyes-Whitney model with the boundary layer thickness equal to 25% of the volume equivalent diameter over the range of experimental undersaturations is shown in Table 7.7.

Table 7.7: The calculated mass loss rate using the Noyes-Whitney equation, with a boundary layer equal to 25% of the volume equivalent diameter.

US	Number of Crystals	Mass Loss Rate ($\mu\text{g/s}$)
0.05	5	$3.80 \times 10^{-6} \pm 8.37 \times 10^{-7}$
0.10	5	$9.60 \times 10^{-6} \pm 8.94 \times 10^{-7}$
0.15	5	$1.40 \times 10^{-5} \pm 8.94 \times 10^{-6}$
0.20	5	$1.40 \times 10^{-5} \pm 5.48 \times 10^{-6}$
0.25	5	$1.80 \times 10^{-5} \pm 4.47 \times 10^{-6}$

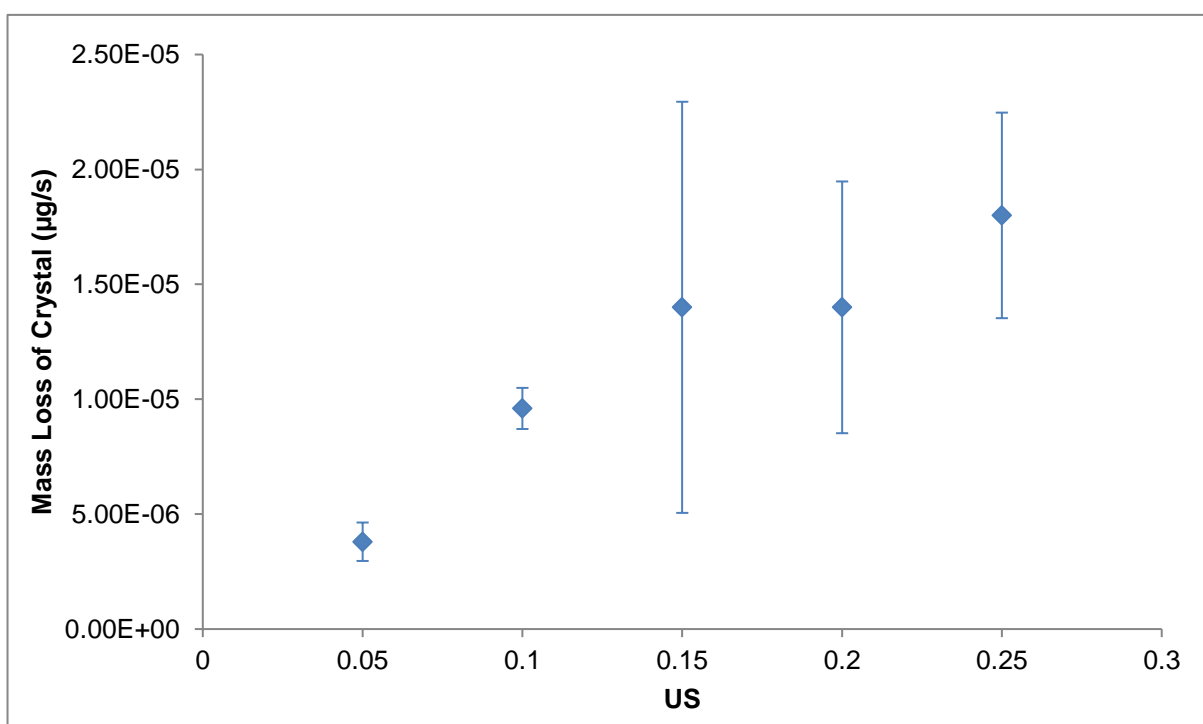


Figure 7.13: The relationship between the mass loss of a crystal of paracetamol and the degree of undersaturation calculated using the Noyes-Whitney equation, with a boundary layer equal to 25% of the volume equivalent diameter.

The calculated mass loss using the Noyes-Whitney equation with a boundary layer thickness of 25% of the volume equivalent diameter also followed the same linear trend.

The mass loss rate calculated for the Noyes-Whitney model with the boundary layer thickness equal to 10% of the volume equivalent diameter, over the range of experimental undersaturations is shown in Table 7.8.

Table 7.8: The calculated mass loss rate using the Noyes-Whitney equation, with a boundary layer equal to 10% of the volume equivalent diameter.

US	Number of Crystals	Mass Loss Rate ($\mu\text{g/s}$)
0.05	5	$8.60 \times 10^{-6} \pm 1.14 \times 10^{-6}$
0.10	5	$3.00 \times 10^{-5} \pm 1.00 \times 10^{-5}$
0.15	5	$3.60 \times 10^{-5} \pm 1.95 \times 10^{-5}$
0.20	5	$3.80 \times 10^{-5} \pm 8.37 \times 10^{-6}$
0.25	5	$4.80 \times 10^{-5} \pm 8.37 \times 10^{-6}$

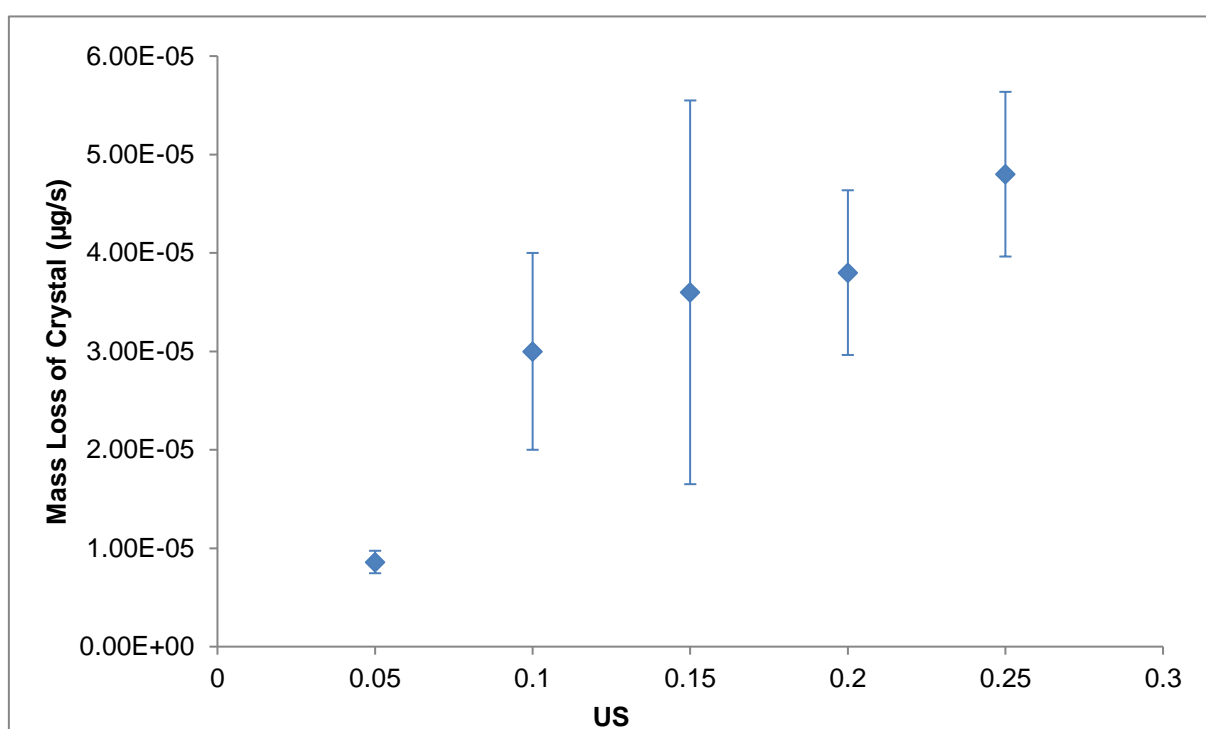


Figure 7.14: The relationship between the mass loss of a crystal of paracetamol and the degree of undersaturation calculated using the Noyes-Whitney equation, with a boundary layer equal to 10% of the volume equivalent diameter.

The mass loss rate calculated for the Noyes-Whitney model with the boundary layer thickness equal to 1% of the volume equivalent diameter, over the range of experimental undersaturations is shown in Table 7.9.

Table 7.9: The calculated mass loss rate using the Noyes-Whitney equation, with a boundary layer equal to 1% of the volume equivalent diameter.

US	Number of Crystals	Mass Loss Rate ($\mu\text{g/s}$)
0.05	5	$8.60 \times 10^{-5} \pm 1.14 \times 10^{-5}$
0.10	5	$3.00 \times 10^{-4} \pm 1.00 \times 10^{-4}$
0.15	5	$3.60 \times 10^{-4} \pm 1.95 \times 10^{-4}$
0.20	5	$3.80 \times 10^{-4} \pm 8.37 \times 10^{-5}$
0.25	5	$4.40 \times 10^{-4} \pm 1.14 \times 10^{-4}$

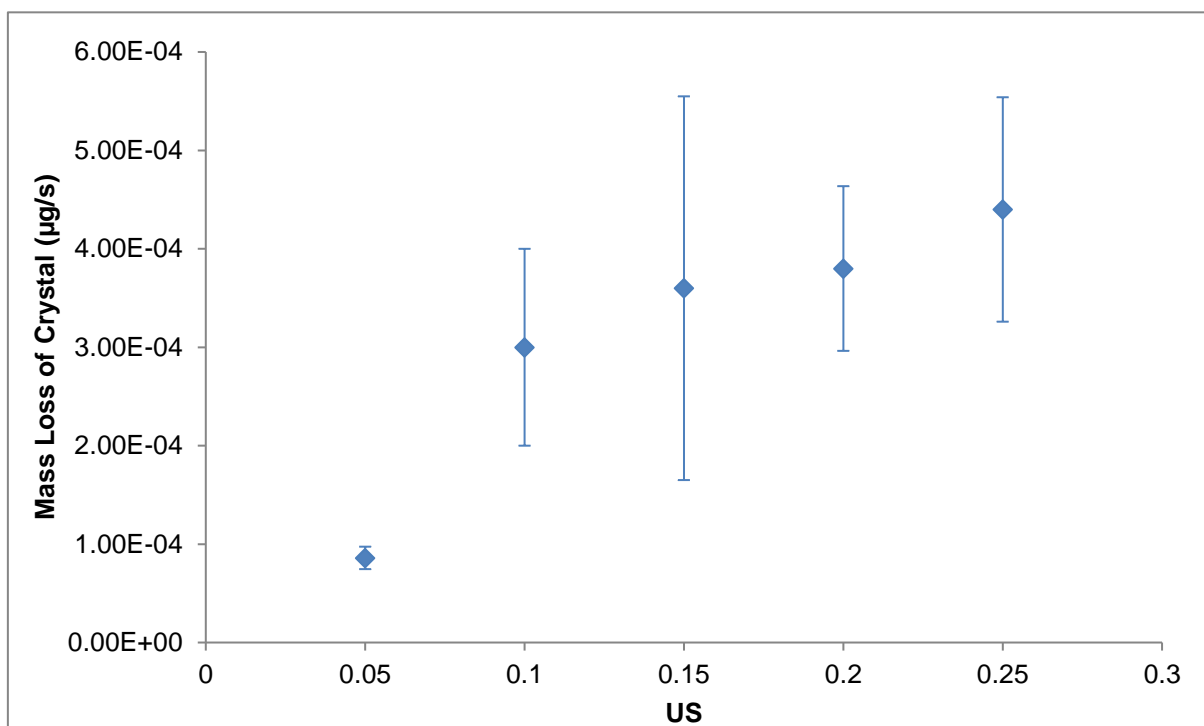


Figure 7.15: The relationship between the mass loss of a crystal of paracetamol and the degree of undersaturation calculated using the Noyes-Whitney equation, with a boundary layer equal to 1% of the volume equivalent diameter.

The calculated mass loss using the Noyes-Whitney equation with a boundary layer thickness of 10% and 1% of the volume equivalent diameter also followed the same linear trend.

Following on from this, the mass loss using the Hintz-Johnson dissolution model was also calculated. The Hintz-Johnson calculations followed the same methodology as the Noyes-Whitney, however there were 2 assumptions associated with this model:

1. The boundary layer thickness is $30\mu\text{m}$ for particles with radii larger than $30\mu\text{m}$.
2. The boundary layer thickness is equal to the particle radius for particles with radii smaller than $30\mu\text{m}$.

An example of the Hintz-Johnson calculation of the mass loss as a function of time, at an undersaturation of 0.05 is shown in Table 7.10.

Table 7.10: An example of the Hintz-Johnson calculation, at an undersaturation of 0.05.

Time (s)	Diffusion Coefficient [D] (m ² /s)	Surface Area (m ²)	Boundary Layer Thickness [h] (m)	Cs (kg/L)	Ct (kg/L)	dM/dt (kg/s)	mass lost (kg)	Density of Solute (kg/m ³)	Volume of Crystal (m ³)	Mass of Crystal (μg)	V.E.D	Radius
0		1.22x10 ⁻⁷	0.00003	0.027	0.026			1290	2.86x10 ⁻¹²	3.68	176.01	88.01
	1.83x10 ⁻⁹					7.42x10 ⁻¹⁵	4.45x10 ⁻¹³					
60		1.22x10 ⁻⁷	0.00003	0.027	0.026			1290	2.85x10 ⁻¹²	3.68	176.00	88.00
	1.83x10 ⁻⁹					7.42x10 ⁻¹⁵	4.45x10 ⁻¹³					
120		1.22x10 ⁻⁷	0.00003	0.027	0.026			1290	2.85x10 ⁻¹²	3.68	176.00	88.00
	1.83x10 ⁻⁹					7.42x10 ⁻¹⁵	4.45x10 ⁻¹³					
180		1.22x10 ⁻⁷	0.00003	0.027	0.026			1290	2.85x10 ⁻¹²	3.68	175.99	88.00
	1.83x10 ⁻⁹					7.42x10 ⁻¹⁵	4.45x10 ⁻¹³					
240		1.22x10 ⁻⁷	0.00003	0.027	0.026			1290	2.85x10 ⁻¹²	3.68	175.98	87.99
	1.83x10 ⁻⁹					7.42x10 ⁻¹⁵	4.452x10 ⁻¹³					
300		1.22x10 ⁻⁷	0.00003	0.027	0.026			1290	2.85x10 ⁻¹²	3.68	175.98	87.99
	1.83x10 ⁻⁹					7.42x10 ⁻¹⁵	4.45x10 ⁻¹³					
360		1.22x10 ⁻⁷	0.00003	0.027	0.026			1290	2.85x10 ⁻¹²	3.68	175.97	87.98
	1.83x10 ⁻⁹					7.42x10 ⁻¹⁵	4.45x10 ⁻¹³					
420		1.22x10 ⁻⁷	0.00003	0.027	0.026			1290	2.85x10 ⁻¹²	3.68	175.96	87.98
	1.83x10 ⁻⁹					7.42x10 ⁻¹⁵	4.45x10 ⁻¹³					
480		1.22x10 ⁻⁷	0.00003	0.027	0.026			1290	2.85x10 ⁻¹²	3.68	175.95	87.98
	1.83x10 ⁻⁹					7.42x10 ⁻¹⁵	4.45x10 ⁻¹³					
540		1.22x10 ⁻⁷	0.00003	0.027	0.026			1290	2.85x10 ⁻¹²	3.68	175.95	87.97
	1.83x10 ⁻⁹					7.42x10 ⁻¹⁵	2.23x10 ⁻¹³					
570		1.22x10 ⁻⁷	0.00003	0.027	0.026			1290	2.85x10 ⁻¹²	3.68	175.94	87.97

Table 7.11: The calculated mass loss rate using the Hintz-Johnson model.

US	Number of Crystals	Mass Loss Rate ($\mu\text{g/s}$)
0.05	5	$4.00 \times 10^{-6} \pm 1.87 \times 10^{-6}$
0.10	5	$1.48 \times 10^{-5} \pm 7.16 \times 10^{-6}$
0.15	5	$1.92 \times 10^{-5} \pm 2.29 \times 10^{-5}$
0.20	5	$1.08 \times 10^{-5} \pm 5.36 \times 10^{-6}$
0.25	5	$1.16 \times 10^{-5} \pm 4.77 \times 10^{-6}$

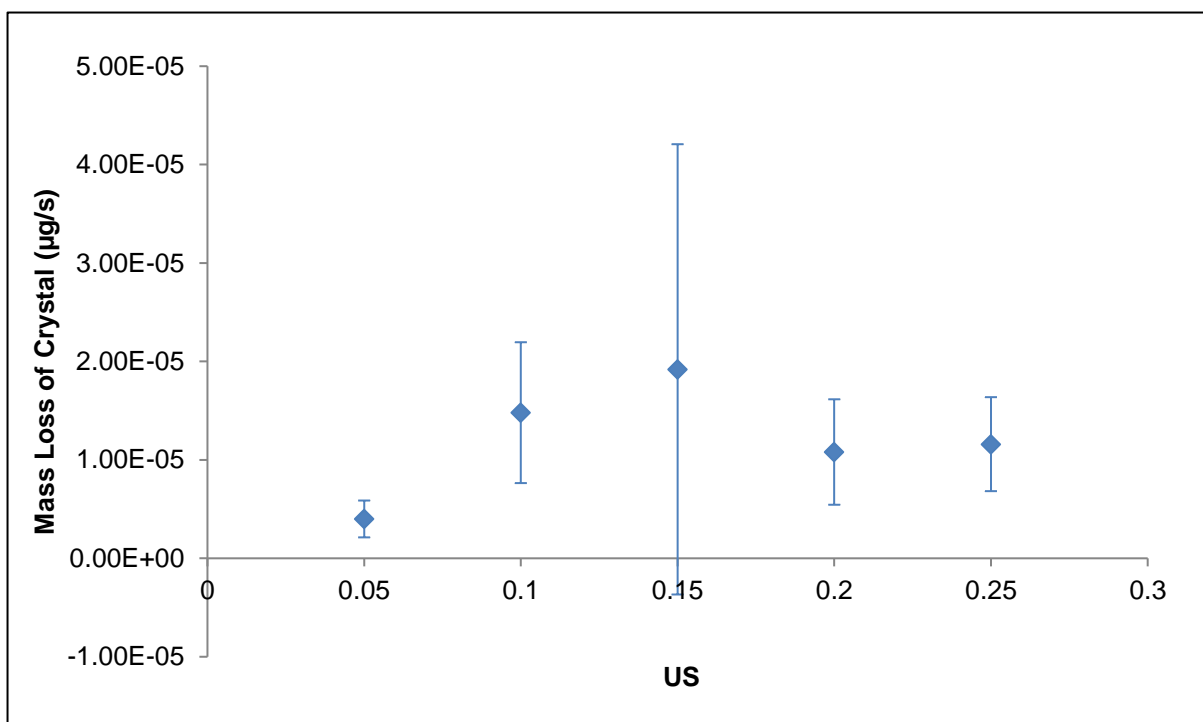


Figure 7.16: The relationship between the mass loss of a crystal of paracetamol and the degree of undersaturation calculated using the Hintz-Johnson model.

7.5.2 Comparison of Models with Experimental Data

The predictions calculated using the Noyes-Whitney and Hintz-Johnson models were compared to the actual mass loss determined through dissolution experiments. The actual mass loss was calculated through the use of Heron's formula (Hammond, 2006) as outlined in Chapter 4 to determine the surface area, and the shape factor to determine the volume and hence the mass for each crystal.

An example of the calculation of actual mass loss as a function of time, at an undersaturation of 0.05 is shown in Table 7.12.

Table 7.12: An example of the calculation of actual mass loss as a function of time, at an undersaturation of 0.05.

Time (s)	Surface Area (m ²)	Volume (m ³)	Density (kg/m ³)	Mass (µg)
0	1.22x10 ⁻⁷	2.65x10 ⁻¹²	1290	3.41
60	1.17x10 ⁻⁷	2.51x10 ⁻¹²	1290	3.23
120	1.14x10 ⁻⁷	2.41x10 ⁻¹²	1290	3.11
180	1.13x10 ⁻⁷	2.37x10 ⁻¹²	1290	3.05
240	1.09x10 ⁻⁷	2.24x10 ⁻¹²	1290	2.89
300	1.05x10 ⁻⁷	2.13x10 ⁻¹²	1290	2.75
360	1.04x10 ⁻⁷	2.10x10 ⁻¹²	1290	2.71
420	1.01x10 ⁻⁷	2.01x10 ⁻¹²	1290	2.59
480	9.79x10 ⁻⁸	1.91x10 ⁻¹²	1290	2.46
540	9.69x10 ⁻⁸	1.88x10 ⁻¹²	1290	2.42
570	9.86x10 ⁻⁸	1.93x10 ⁻¹²	1290	2.49

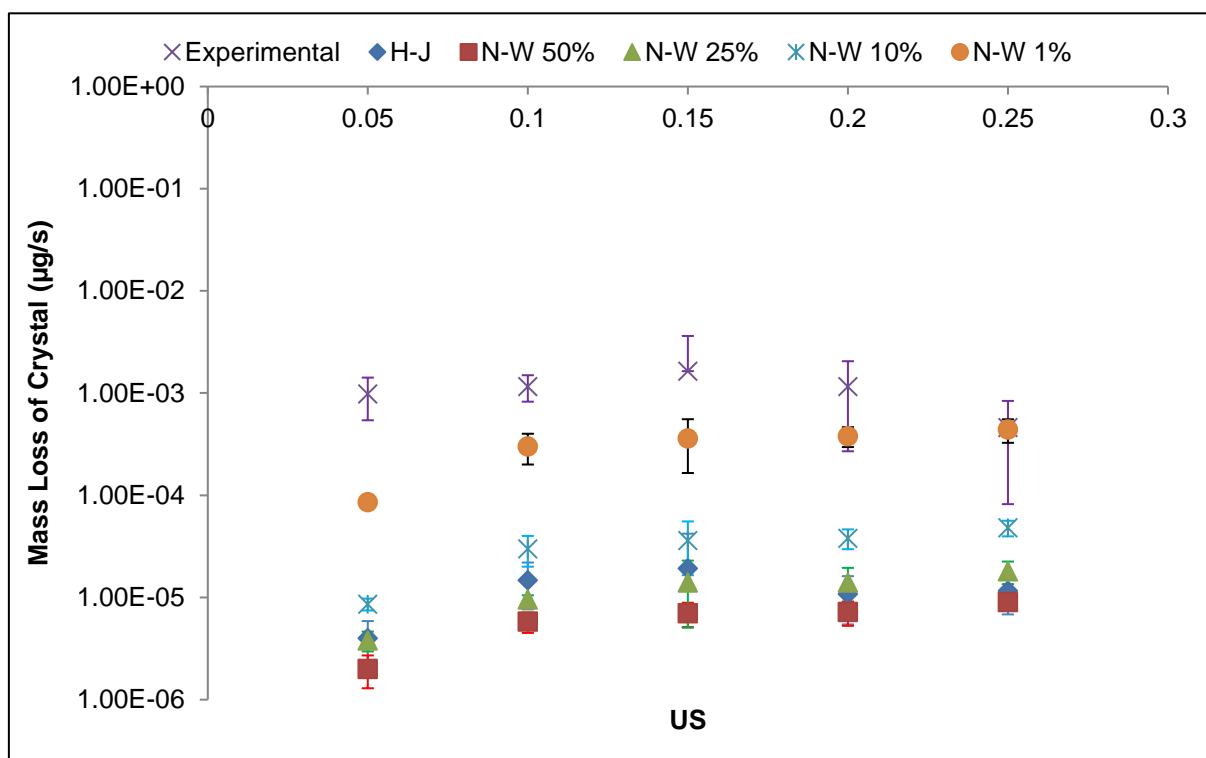


Figure 7.17: A comparison between the experimental mass loss and calculated mass losses using Noyes-Whitney and Hinz-Johnson.

The predicted mass loss of the paracetamol crystal for all models was not a consistent prediction in comparison with the experimental mass loss. The percentage difference between the actual mass loss and the predicted mass loss is shown in Table 7.13.

Table 7.13: The percentage difference between values of experimental mass loss and calculated mass loss.

US	% difference				
	N-W (50%)	N-W (25%)	N-W (10%)	N-W (1%)	H-J
0.05	99.80	99.61	99.12	91.22	99.59
0.10	99.50	99.17	97.41	74.14	98.72
0.15	99.57	99.15	97.80	78.05	98.83
0.20	99.38	98.79	96.72	67.24	99.07
0.25	98.04	96.09	89.57	4.35	97.48

The percentage difference shows that the predicted values are inaccurate in comparison with the actual experimental mass loss. Therefore, current dissolution models could not be used in the pharmaceutical industry and would need to be modified.

The modification to the dissolution models carried out in Chapter 6, where a fixed boundary layer thickness was used, was also carried out for the mass loss data for Paracetamol in acetonitrile. Therefore, the models were re-calculated using a fixed boundary layer of 0.3 μ m. An example of this calculation for an undersaturation of 0.05 is shown in Table 7.14.

Table 7.14: An example of the Noyes-Whitney calculation with a fixed boundary layer parameter of 0.3 μm

Time (s)	Diffusion Coefficient [D] (m^2/s)	Surface Area (m^2)	Boundary Layer Thickness [h] (m)	Cs (kg/L)	Ct (kg/L)	dM/dt (kg/s)	mass lost (kg)	Density of Solute (kg/m^3)	Volume of Crystal (m^3)	Mass of Crystal (μg)
0		1.22×10^{-7}	0.0000003	0.027	0.026			1290	2.86×10^{-12}	3.68
	1.83×10^{-9}					7.42×10^{-13}	4.45×10^{-11}			
60		1.21×10^{-7}	0.0000003	0.027	0.026			1290	2.82×10^{-12}	3.64
	1.83×10^{-9}					7.36×10^{-13}	4.42×10^{-11}			
120		1.20×10^{-7}	0.0000003	0.027	0.026			1290	2.79×10^{-12}	3.59
	1.83×10^{-9}					7.30×10^{-13}	4.38×10^{-11}			
180		1.19×10^{-7}	0.0000003	0.027	0.026			1290	2.75×10^{-12}	3.55
	1.83×10^{-9}					7.24×10^{-13}	4.35×10^{-11}			
240		1.18×10^{-7}	0.0000003	0.027	0.026			1290	2.72×10^{-12}	3.51
	1.83×10^{-9}					7.18×10^{-13}	4.31×10^{-11}			
300		1.17×10^{-7}	0.0000003	0.027	0.026			1290	2.69×10^{-12}	3.46
	1.83×10^{-9}					7.13×10^{-13}	4.28×10^{-11}			
360		1.16×10^{-7}	0.0000003	0.027	0.026			1290	2.65×10^{-12}	3.42
	1.83×10^{-9}					7.07×10^{-13}	4.24×10^{-11}			
420		1.15×10^{-7}	0.0000003	0.027	0.026			1290	2.62×10^{-12}	3.38
	1.83×10^{-9}					7.01×10^{-13}	4.21×10^{-11}			
480		1.14×10^{-7}	0.0000003	0.027	0.026			1290	2.59×10^{-12}	3.34
	1.83×10^{-9}					6.95×10^{-13}	4.17×10^{-11}			
540		1.13×10^{-7}	0.0000003	0.027	0.026			1290	2.55×10^{-12}	3.30
	1.83×10^{-9}					6.89×10^{-13}	2.07×10^{-11}			
570		1.13×10^{-7}	0.0000003	0.027	0.026			1290	2.54×10^{-12}	3.27

A comparison of the mass loss values with a fixed boundary layer thickness with the experimental values obtained is shown in Figure 7.18.

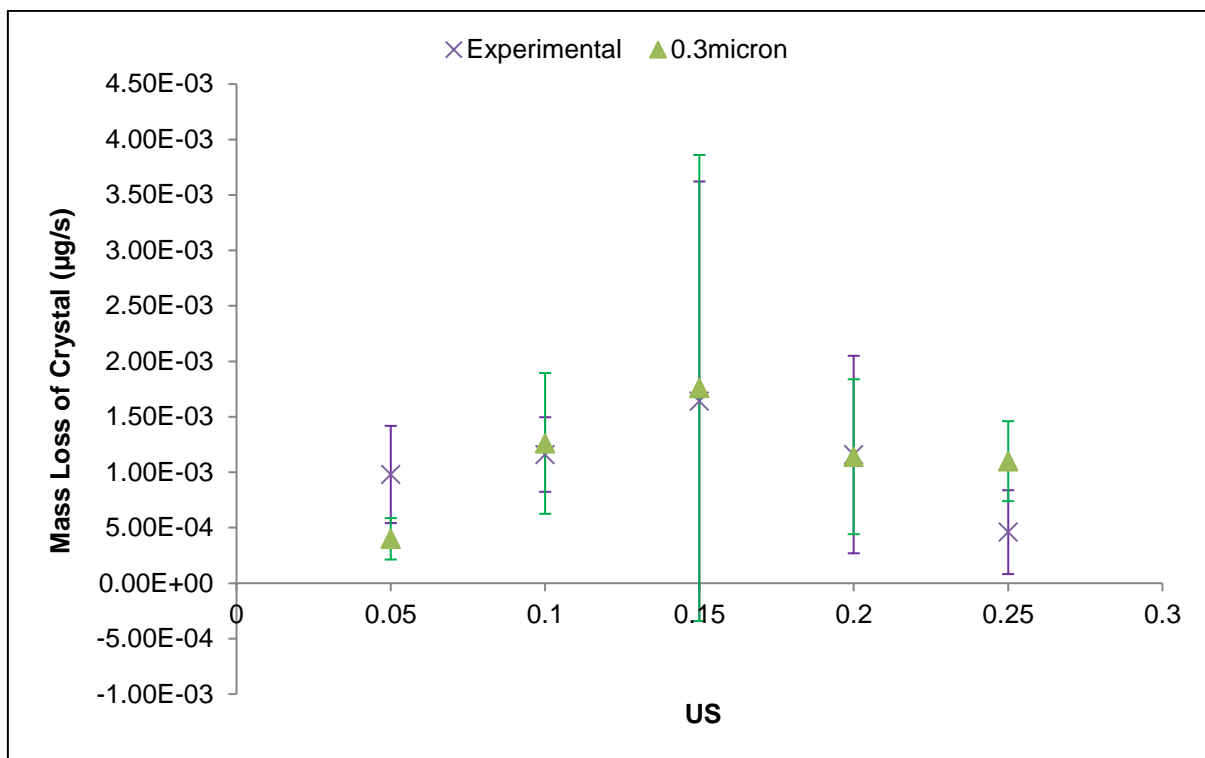


Figure 7.18: Comparison between the experimental mass loss and calculated values with a fixed boundary layer.

Table 7.15: The percentage difference between values of experimental mass loss and calculated mass loss with a fixed boundary layer.

Undersaturation	% difference
0.05	59.18
0.10	7.94
0.15	6.82
0.20	1.72
0.25	58.18

This modification resulted in a much more consistent prediction for the mass loss in comparison with the experimental mass loss, and the values for the boundary layer thickness remained consistent with previous values stated by Bunn and Emmett (1949).

7.6 Dissolution of Paracetamol in FeSSIF

Paracetamol single crystals were dissolved in FeSSIF at a temperature range where FeSSIF is viable. The experimental dissolution rates of the five faces under consideration were determined. The experimental dissolution rates were then compared to the intermolecular interactions of the faces with FeSSIF, and experimental conclusions were reinforced due to energy interactions obtained.

7.6.1 Face Specific Dissolution Rate

Experimental dissolution rate data has been provided in Appendix C4, which comprises of 20 single crystals spontaneously nucleated and grown in water overnight. The solvent has then been removed and replaced with FeSSIF, and dissolved over the temperature range 30°C-40°C, i.e. the temperatures where FeSSIF is viable. The crystals were dissolved in a stagnant solution under diffusion limited conditions in a 0.5mL cuvette, immersed in a water cell. The distance between the centre of the crystal, and the face under consideration was then measured as a function of time.

Table 7.16: Experimental mean retreat rates and standard deviations obtained for paracetamol in FeSSIF.

°C	No. of Crystals	Mean Retreat Rate ($\mu\text{m/s}$)			
		{201}	{100}	{001}	{011}
30	5	$3.27 \times 10^{-2} \pm$	$1.72 \times 10^{-2} \pm$	$2.64 \times 10^{-2} \pm$	$2.63 \times 10^{-2} \pm$
		1.10×10^{-2}	1.11×10^{-2}	1.69×10^{-2}	1.55×10^{-2}
33	5	$3.91 \times 10^{-2} \pm$	$1.69 \times 10^{-2} \pm$	$2.55 \times 10^{-2} \pm$	$2.42 \times 10^{-2} \pm$
		2.99×10^{-2}	1.01×10^{-2}	2.77×10^{-2}	1.07×10^{-2}
37	5	$8.15 \times 10^{-2} \pm$	$4.12 \times 10^{-2} \pm$	$3.15 \times 10^{-2} \pm$	$5.30 \times 10^{-2} \pm$
		3.22×10^{-2}	1.70×10^{-2}	4.00×10^{-2}	1.77×10^{-2}
40	5	$8.20 \times 10^{-2} \pm$	$5.50 \times 10^{-2} \pm$	$6.21 \times 10^{-2} \pm$	$3.30 \times 10^{-2} \pm$
		4.03×10^{-2}	3.70×10^{-2}	6.86×10^{-2}	3.80×10^{-2}

The initial and final images of the retreat rate crystals dissolved in the cuvette are shown in Table 7.17. Final images were taken when the dissolution of the crystals

reached the point where further dissolution would result in rounding of the crystal faces.

Table 7.17: An example of the experimental crystal images obtained at the initial and final time points for paracetamol in FeSSIF at each temperature.

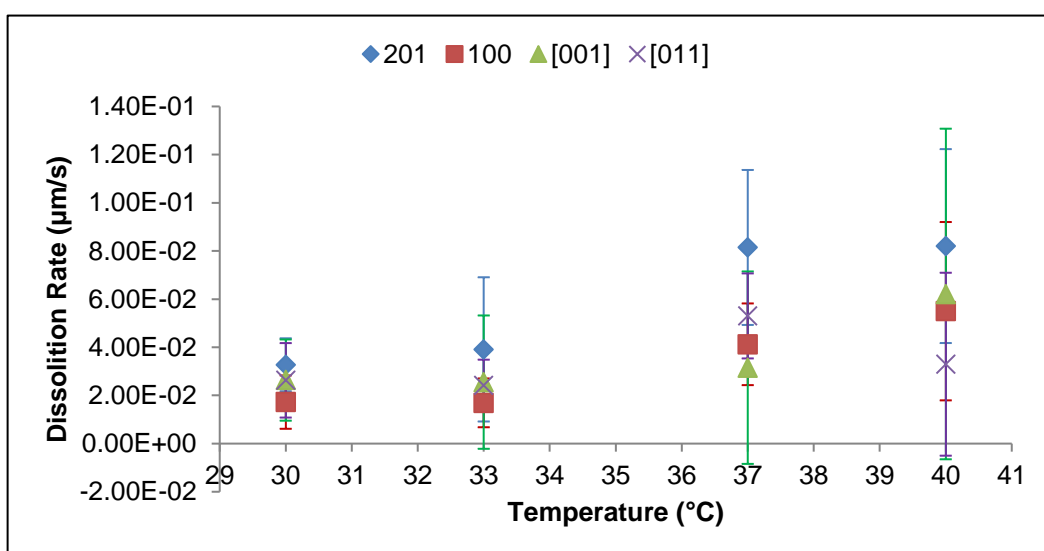
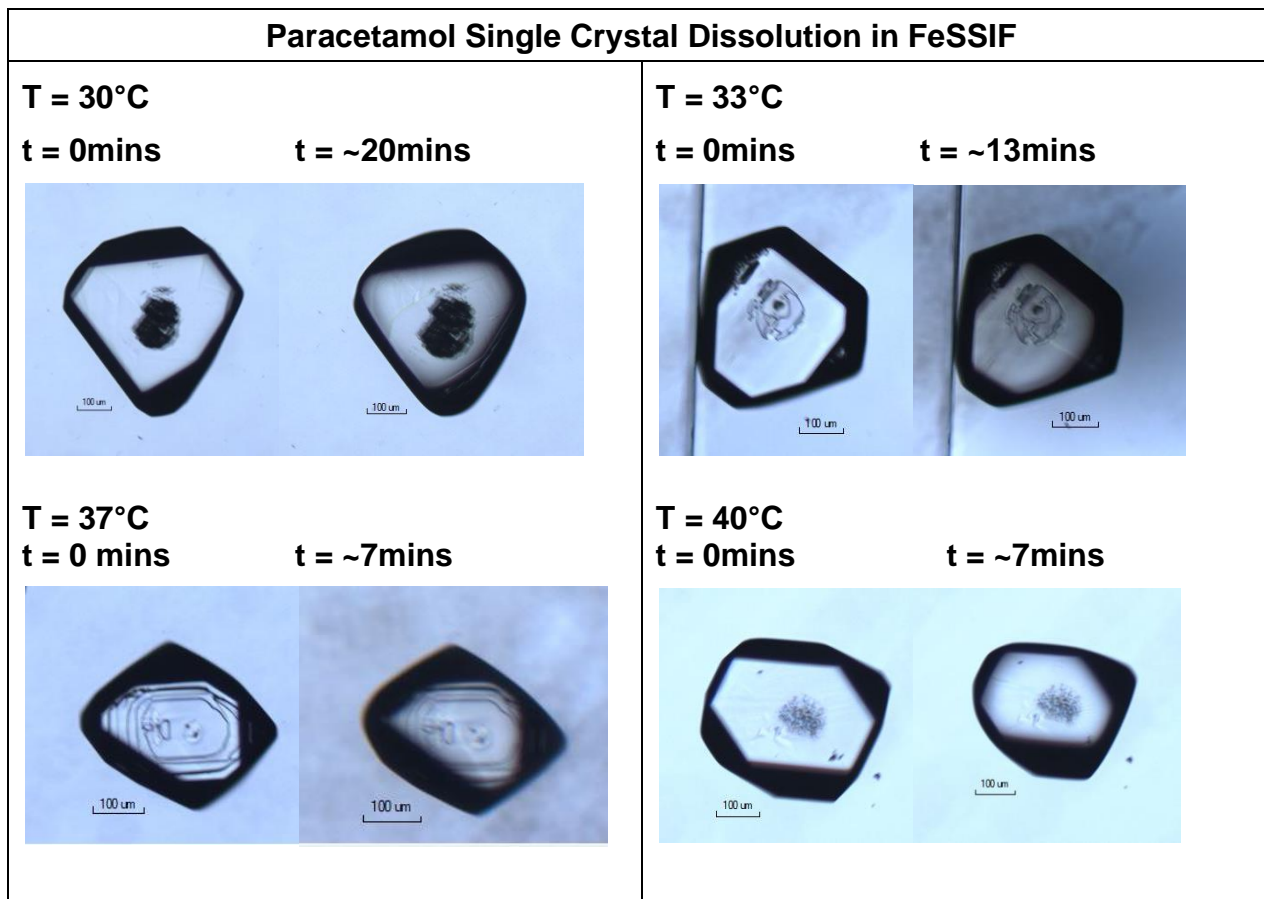


Figure 7.19: The relationship between dissolution rate and temperature for the faces of paracetamol in FeSSIF.

The dissolution rates of all faces under consideration showed that, in FeSSIF, the rates of all the faces followed a first order dependence with respect to temperature, with the mean dissolution rates increasing as temperature increased. However, this conclusion was made with caution due to the errors obtained, particularly at higher temperatures. There was found to be no significant solvent effect on any of the faces under consideration, and all of the faces were found to have similar dissolution rates.

7.6.2 Intermolecular Interactions of Paracetamol with FeSSIF

Surface characterisation of Paracetamol has been carried out previously, with the five main morphologically important faces being identified – {011}, {100}, {110}, {201}, and {001}. The interaction of FeSSIF with the crystal faces under consideration after having been grown from water could not be modelled through the systematic search function using Mercury VisualHabit as systematic search can only be used for the interaction of one solvent probe with the surface, and FeSSIF consists of multiple components. However, as the majority component of FeSSIF is water, this was used as the probe molecule in order to determine the interaction energies with the paracetamol surfaces under consideration.

7.6.2.1 {001}

The minimum interaction energy between a probe molecule of water and the {001} surface was found. This minimum interaction energy is the strongest and most stable interaction between the solvent and the solute.

The {001} surface was built of multiple unit cells surrounding the unit cell used for the grid search function in order to ensure that edge effects do not interfere with the calculation of interaction energies. It was ensured that grid rows closest to and furthest away from the surface contained white tetrahedrons only, as the interactions were found to be smaller than the defined minimum value, therefore were considered negligible. Removal of the grid shows that there were varying degrees of water interaction with the {001} surface, with the strongest of these interactions being shown in Figure 7.20.

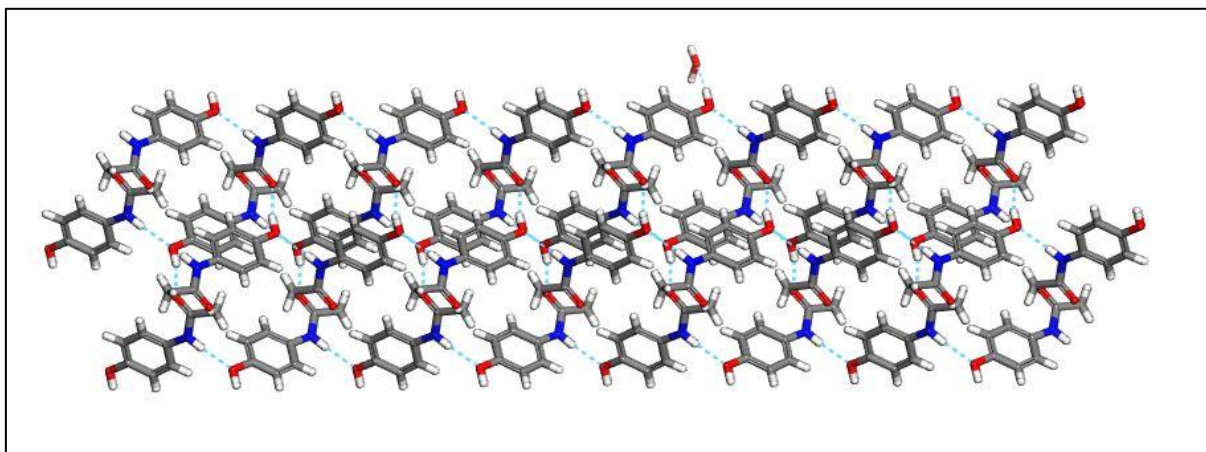


Figure 7.20: The strongest interaction of water with the {001} surface of paracetamol, with hydrogen bonding depicted.

Calculation of the interaction energy between the acetonitrile probe molecule and the {001} surface allowed for the determination of the total interaction energy, and also divided this total interaction energy figure into van der Waals (dispersive), hydrogen bonding, and electrostatic interactions. Thousands of interactions were calculated through the SystSearch function, however, for the purposes of clarity, the 100 strongest interactions have been presented.

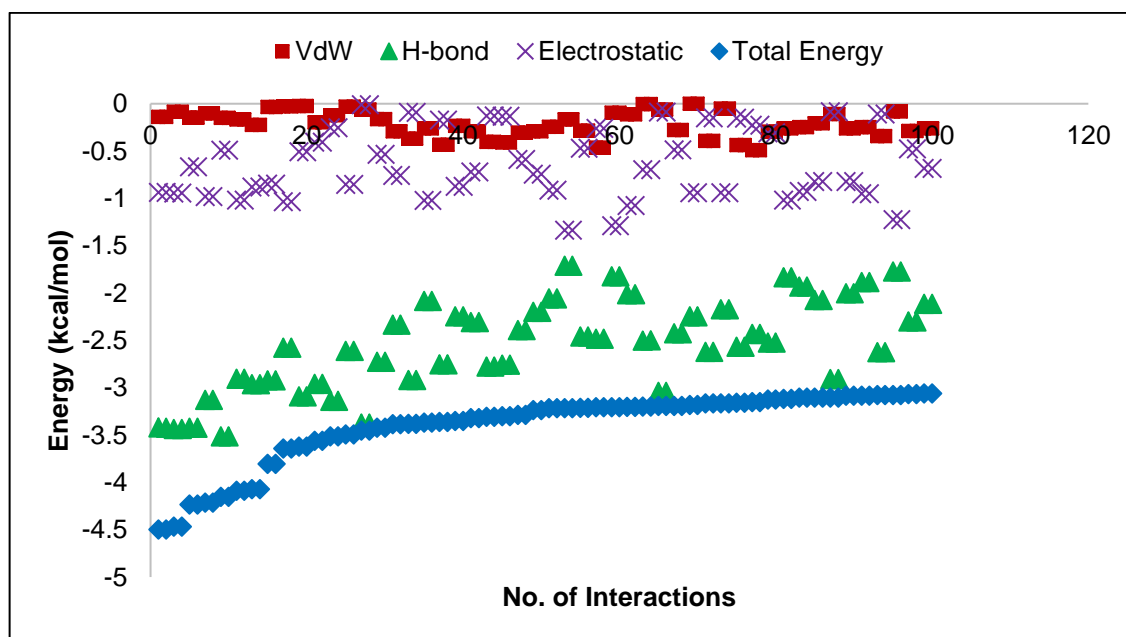


Figure 7.21: The top 100 interactions of water with the {001} surface, broken down into hydrogen bonding, van der Waals and electrostatic interactions.

This suggests that the majority of the total interaction energy of the water probe molecule with the {001} surface is due to hydrogen bonding, with van der Waals

dispersive interactions and electrostatic interactions making up a minimal amount of the total interaction energy.

7.6.2.2 {011}, {100} and {201}

The interaction energies of acetonitrile with the {011}, {100} and {201} faces were also determined, to allow for a comparison of the interaction energies between the faces under consideration. The same process as was carried out for the {011} surface was also used for the other surface calculations.

Removal of the grid after grid search calculations were carried out showed that there were varying degrees of water interaction with each of the faces, with the highest energy interactions of the {011}, {100} and {201} surfaces with the acetonitrile probe being shown in Figure 7.22, respectively.

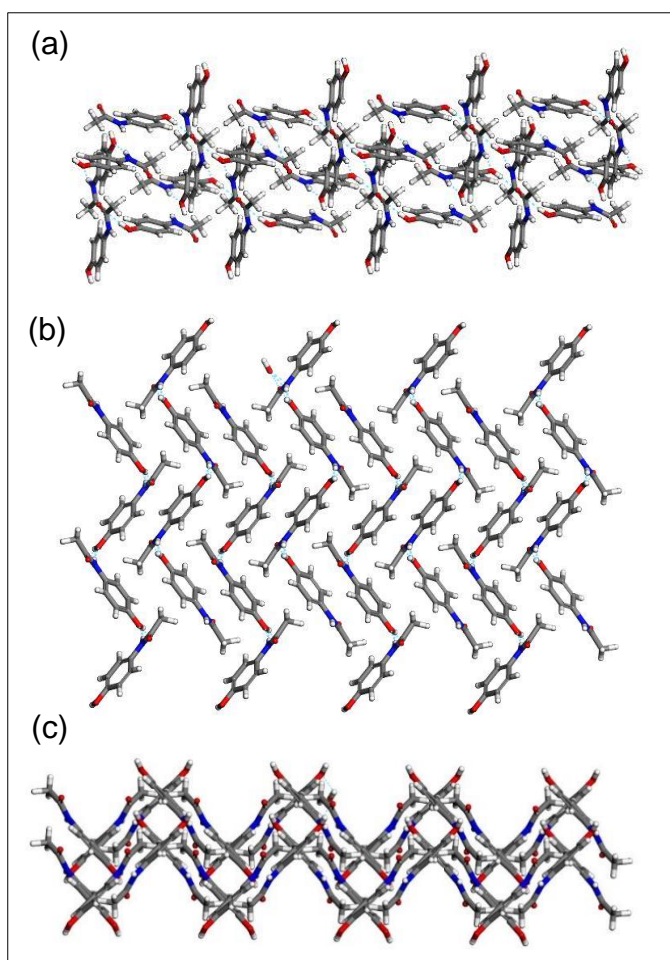


Figure 7.22: The strongest interactions of water with the (a) {011}, (b) {100} and (c) {201} surfaces, with hydrogen bonding depicted.

The calculation of these energy interactions between the water probe molecule and the surfaces under consideration allowed for the determination of the type of

interaction and the strength of these interactions. The number of interactions calculated through the SystSearch function were in the thousands, therefore for the purposes of clarity, the 100 strongest interactions have been presented.

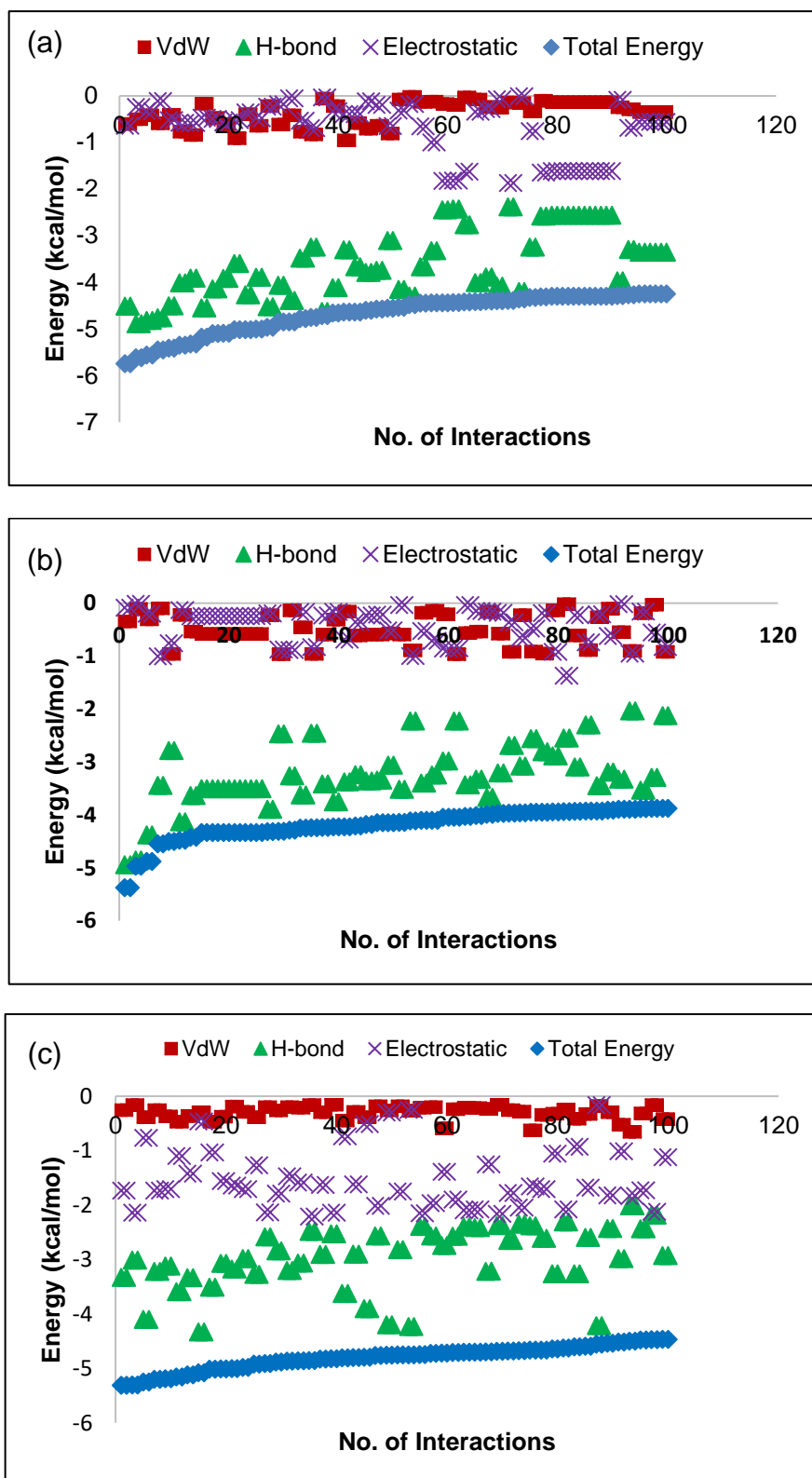


Figure 7.23: The top 100 interactions of water with the (a) {011}, (b) {100} and (c) {201} surfaces, broken down into hydrogen bonding, van der Waals and electrostatic interactions

These interactions suggest that the interaction of the water probe with the other surfaces under consideration are mostly due to hydrogen bonding, with van der Waals dispersive interactions and electrostatic interactions making up a minimal amount of the interaction.

7.6.2.3 Comparison of Surface Interactions

A comparison of the total interaction energies of the four surfaces under consideration are shown in Figure 7.24.

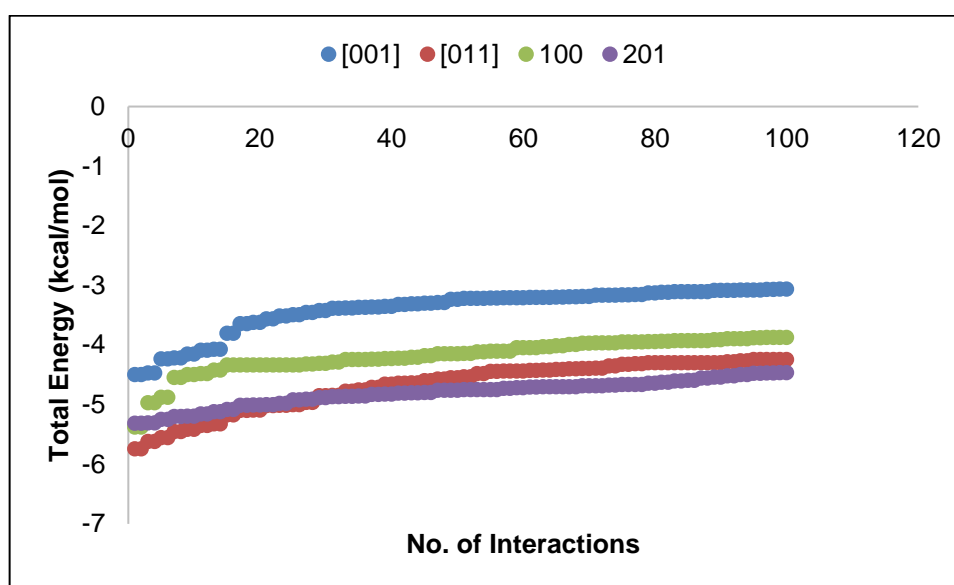


Figure 7.24: A comparison of the total energy interactions of water with all surfaces of paracetamol.

The water probe was found to have a similar energy interaction with all the faces under consideration. As a result of this comparison, the experimental results were validated in that the dissolution rates of all four faces in FeSSIF are comparable.

7.7 Dissolution Model Predictions for Paracetamol in FeSSIF

The Noyes-Whitney and Hintz-Johnson dissolution models were calculated to determine the predicted mass loss of a crystal of paracetamol in FeSSIF. These calculations were carried out in order to further validate the conclusions made in Chapter 6, as well as calculations carried out for Paracetamol in acetonitrile. These calculations therefore, will allow for the conclusion to be made as to whether current dissolution models can be used for in-vitro in-vivo dissolution comparison of pharmaceuticals.

As the Noyes-Whitney model states that boundary layer thickness is a function of particle size, a number of boundary layer thicknesses were used in order to determine the optimal thin-film thickness that corresponds best to the experimental data. Therefore, boundary layer thicknesses equal to 50%, 25%, 10% and 1% of the volume equivalent diameter of the particle were used.

7.7.1 Noyes-Whitney and Hintz-Johnson

An example of the Noyes-Whitney calculation of the mass loss as a function of time, with the boundary layer thickness equal to 50% of the volume equivalent diameter, at a temperature of 30°C is shown in Table 7.18:

Table 7.18: An example of the Noyes-Whitney calculation, at a temperature of 30°C, with a boundary layer equal to 50% of the volume equivalent diameter.

Time (s)	Diffusion Coefficient [D] (m ² /s)	Surface Area (m ²)	Boundary Layer Thickness [h] (m)	Cs (kg/L)	Ct (kg/L)	dM/dt (kg/s)	mass lost (kg)	Density of Solute (kg/m ³)	Volume of Crystal (m ³)	Mass of Crystal (µg)	V.E.D	50% V.E.D
0		1.27x10 ⁻⁷	8.99x10 ⁻⁵	0.011	0.0105			1290	3.04x10 ⁻¹²	3.92	179.75	89.87
	7.53x10 ⁻¹⁰					5.31x10 ⁻¹⁶	6.38x10 ⁻¹⁴					
120		1.27x10 ⁻⁷	8.99x10 ⁻⁵	0.011	0.0105			1290	3.04x10 ⁻¹²	3.92	179.75	89.87
	7.53x10 ⁻¹⁰					5.31x10 ⁻¹⁶	6.38x10 ⁻¹⁴					
240		1.27x10 ⁻⁷	8.99x10 ⁻⁵	0.011	0.0105			1290	3.04x10 ⁻¹²	3.92	179.75	89.87
	7.53x10 ⁻¹⁰					5.31x10 ⁻¹⁶	6.38x10 ⁻¹⁴					
360		1.27x10 ⁻⁷	8.99x10 ⁻⁵	0.011	0.0105			1290	3.04x10 ⁻¹²	3.92	179.75	89.87
	7.53x10 ⁻¹⁰					5.31x10 ⁻¹⁶	6.38x10 ⁻¹⁴					
480		1.27x10 ⁻⁷	8.99x10 ⁻⁵	0.011	0.0105			1290	3.04x10 ⁻¹²	3.92	179.75	89.87
	7.53x10 ⁻¹⁰					5.31x10 ⁻¹⁶	6.38x10 ⁻¹⁴					
600		1.27x10 ⁻⁷	8.99x10 ⁻⁵	0.011	0.0105			1290	3.04x10 ⁻¹²	3.92	179.74	89.87
	7.53x10 ⁻¹⁰					5.31x10 ⁻¹⁶	6.38x10 ⁻¹⁴					
720		1.27x10 ⁻⁷	8.99x10 ⁻⁵	0.011	0.0105			1290	3.04x10 ⁻¹²	3.92	179.74	89.87
	7.53x10 ⁻¹⁰					5.31x10 ⁻¹⁶	6.38x10 ⁻¹⁴					
840		1.27x10 ⁻⁷	8.99x10 ⁻⁵	0.011	0.0105			1290	3.04x10 ⁻¹²	3.92	179.74	89.87
	7.53x10 ⁻¹⁰					5.31x10 ⁻¹⁶	6.38x10 ⁻¹⁴					
960		1.27x10 ⁻⁷	8.99x10 ⁻⁵	0.011	0.0105			1290	3.04x10 ⁻¹²	3.92	179.74	89.87
	7.53x10 ⁻¹⁰					5.31x10 ⁻¹⁶	6.38x10 ⁻¹⁴					
1080		1.27x10 ⁻⁷	8.99x10 ⁻⁵	0.011	0.0105			1290	3.04x10 ⁻¹²	3.92	179.74	89.87
	7.53x10 ⁻¹⁰					5.31x10 ⁻¹⁶	6.38x10 ⁻¹⁴					
1200		1.27x10 ⁻⁷	8.99x10 ⁻⁵	0.011	0.0105	221		1290	3.04x10 ⁻¹²	3.92	179.74	89.87

Table 7.19: The calculated mass loss rate using the Noyes-Whitney equation, with a boundary layer equal to 50% of the volume equivalent diameter.

Temperature (°C)	Number of Crystals	Mass Loss Rate (µg/s)
30	5	$4.20 \times 10^{-7} \pm 8.37 \times 10^{-8}$
33	5	$1.60 \times 10^{-6} \pm 5.48 \times 10^{-7}$
37	5	$2.20 \times 10^{-6} \pm 4.47 \times 10^{-7}$
40	5	$4.20 \times 10^{-6} \pm 8.37 \times 10^{-7}$

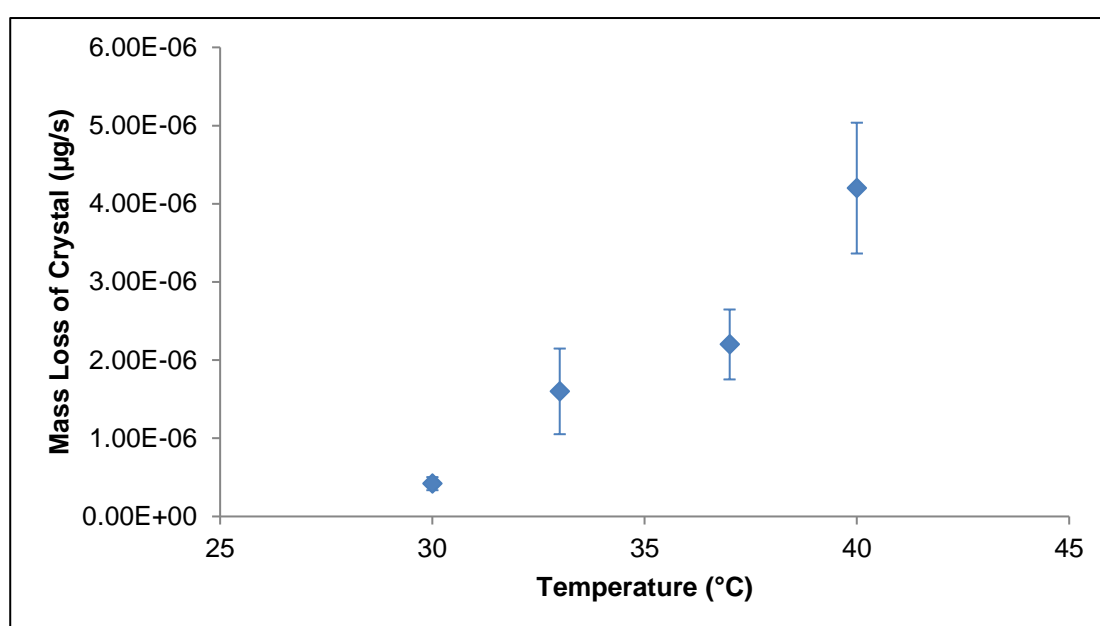


Figure 7.25: The relationship between the mass loss of a crystal of paracetamol and the temperature calculated using the Noyes-Whitney equation, with a boundary layer equal to 50% of the volume equivalent diameter.

The calculated mass loss using the Noyes-Whitney equation showed that the mass loss followed a linear trend with respect to temperature.

The mass loss rates calculated for the Noyes-Whitney model with the boundary layer thickness equal to 25% of the volume equivalent diameter over the range of experimental temperatures are shown in Table 7.20.

Table 7.20: The calculated mass loss rate using the Noyes-Whitney equation, with a boundary layer equal to 25% of the volume equivalent diameter.

Temperature (°C)	Number of Crystals	Mass Loss Rate (µg/s)
30	5	$8.20 \times 10^{-7} \pm 1.30 \times 10^{-7}$
33	5	$3.40 \times 10^{-6} \pm 1.14 \times 10^{-6}$
37	5	$4.60 \times 10^{-6} \pm 5.48 \times 10^{-7}$
40	5	$8.40 \times 10^{-6} \pm 1.52 \times 10^{-6}$

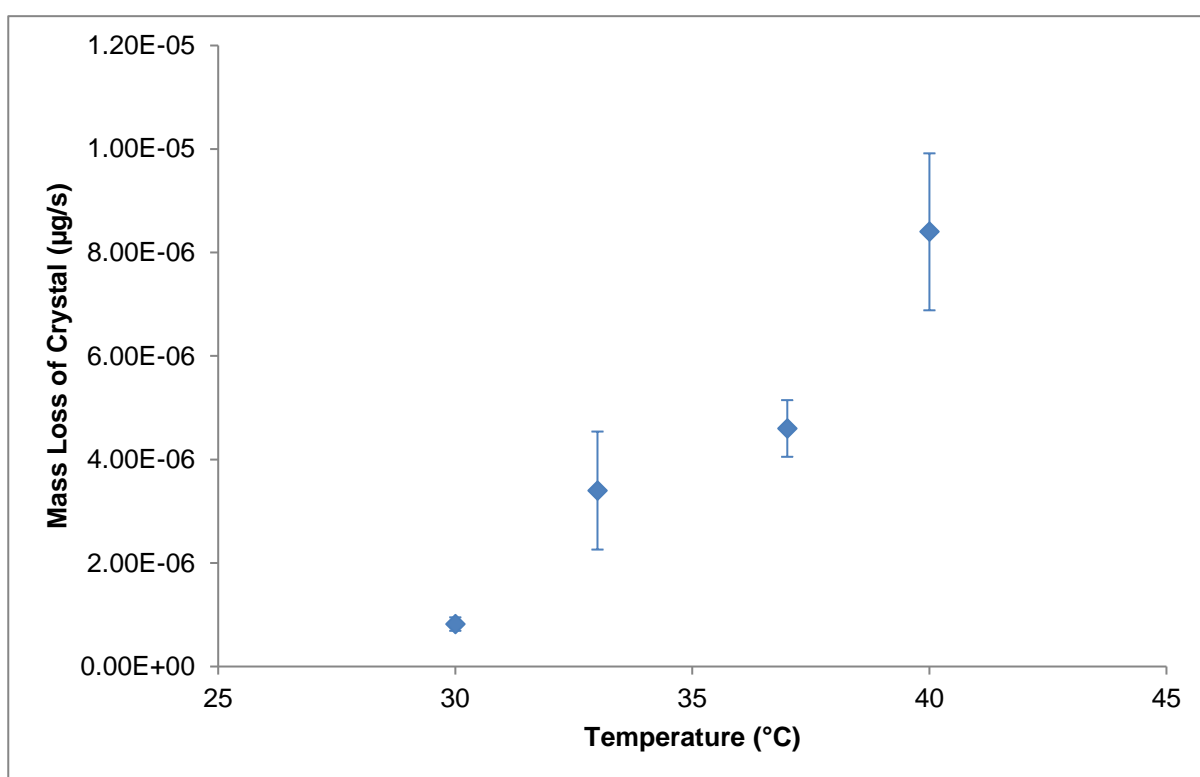


Figure 7.26: The relationship between the mass loss of a crystal of paracetamol and the temperature calculated using the Noyes-Whitney equation, with a boundary layer equal to 25% of the volume equivalent diameter.

The calculated mass loss using the Noyes-Whitney equation with a boundary layer thickness of 25% of the volume equivalent diameter also followed the same linear trend.

The mass loss rates calculated for the Noyes-Whitney model with the boundary layer thickness equal to 10% of the volume equivalent diameter, over the range of experimental temperatures is shown in Table 7.21.

Table 7.21: The calculated mass loss rate using the Noyes-Whitney equation, with a boundary layer equal to 10% of the volume equivalent diameter.

Temperature (°C)	Number of Crystals	Mass Loss Rate (µg/s)
30	5	$2.20 \times 10^{-6} \pm 4.47 \times 10^{-7}$
33	5	$7.80 \times 10^{-6} \pm 1.92 \times 10^{-6}$
37	5	$9.60 \times 10^{-6} \pm 5.48 \times 10^{-7}$
40	5	$2.00 \times 10^{-5} \pm 0$

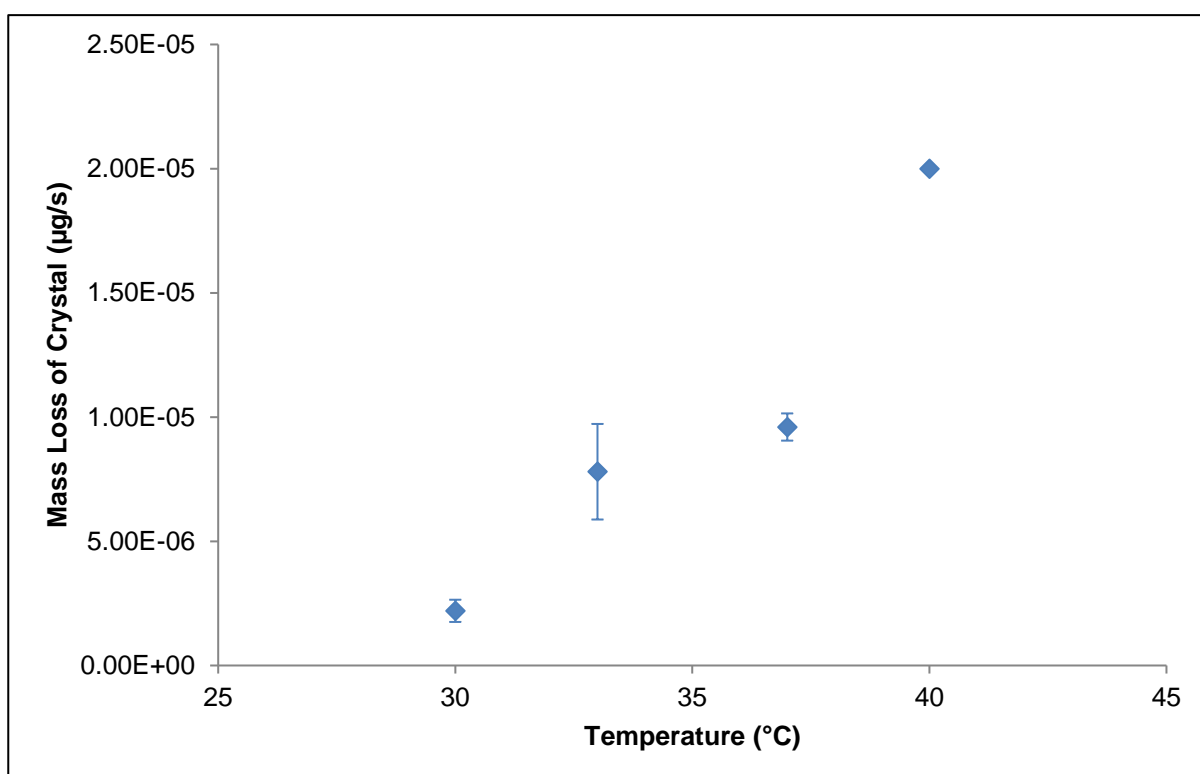


Figure 7.27: The relationship between the mass loss of a crystal of paracetamol and the temperature calculated using the Noyes-Whitney equation, with a boundary layer equal to 10% of the volume equivalent diameter.

The mass loss rates calculated for the Noyes-Whitney model with the boundary layer thickness equal to 1% of the volume equivalent diameter, over the range of experimental temperatures is shown in Table 7.22.

Table 7.22: The calculated mass loss rate using the Noyes-Whitney equation, with a boundary layer equal to 1% of the volume equivalent diameter.

Temperature (°C)	Number of Crystals	Mass Loss Rate (µg/s)
30	5	$2.20 \times 10^{-5} \pm 4.47 \times 10^{-6}$
33	5	$7.80 \times 10^{-5} \pm 1.92 \times 10^{-5}$
37	5	$9.60 \times 10^{-5} \pm 5.48 \times 10^{-6}$
40	5	$2.00 \times 10^{-4} \pm 0$

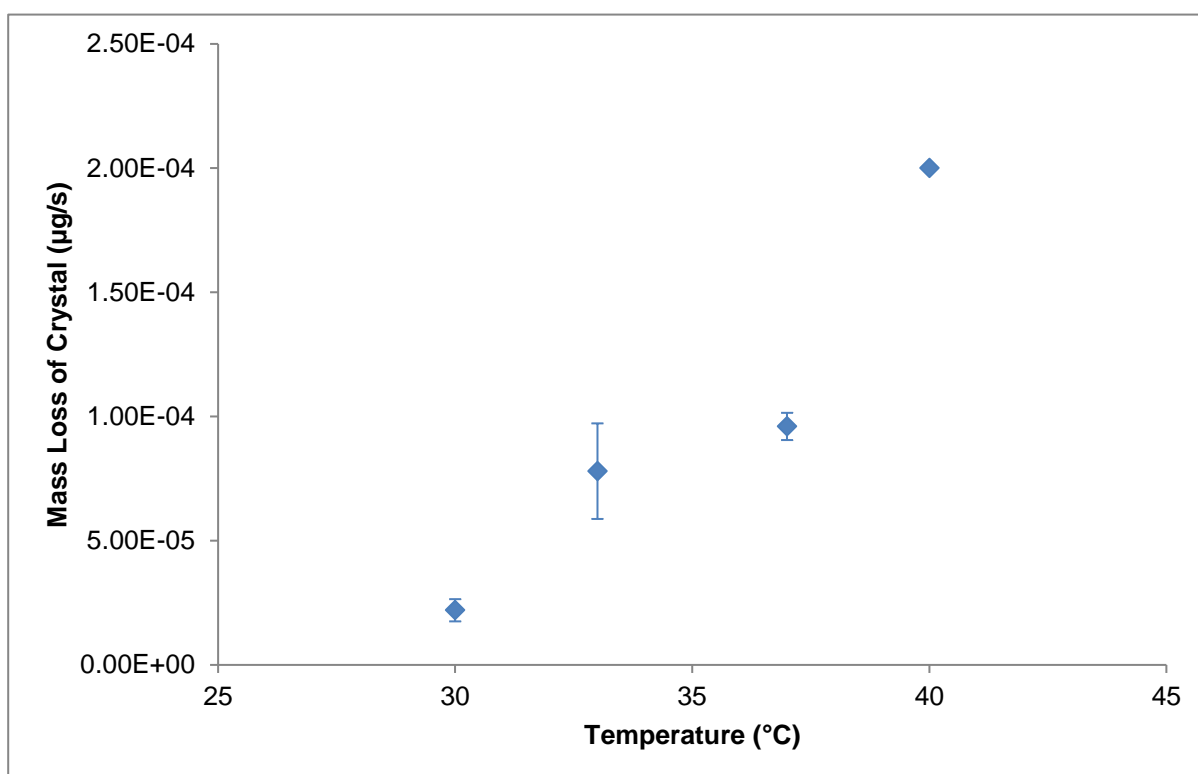


Figure 7.28: The relationship between the mass loss of a crystal of paracetamol and the temperature calculated using the Noyes-Whitney equation, with a boundary layer equal to 1% of the volume equivalent diameter.

Following on from this, the mass loss using the Hintz-Johnson dissolution model was also calculated. An example of the Hintz-Johnson calculation of the mass loss as a function of time, at a temperature of 30°C is shown in Table 7.23.

Table 7.23: An example of the Hintz-Johnson calculation, at a temperature of 30°C.

Time (s)	Diffusion Coefficient [D] (m ² /s)	Surface Area (m ²)	Boundary Layer Thickness [h] (m)	C _s (kg/L)	C _t (kg/L)	dM/dt (kg/s)	mass lost (kg)	Density of Solute (kg/m ³)	Volume of Crystal (m ³)	Mass of Crystal (μg)	V.E.D	Particle Radius
0		1.27x10 ⁻⁷	0.00003	0.011	0.0105			1290	3.04x10 ⁻¹²	3.92	179.75	89.87
	7.53x10 ⁻¹⁰					1.59x10 ⁻¹⁵	1.91x10 ⁻¹³					
120		1.27x10 ⁻⁷	0.00003	0.011	0.0105			1290	3.04x10 ⁻¹²	3.92	179.75	89.87
	7.53x10 ⁻¹⁰					1.59x10 ⁻¹⁵	1.91x10 ⁻¹³					
240		1.27x10 ⁻⁷	0.00003	0.011	0.0105			1290	3.04x10 ⁻¹²	3.92	179.74	89.87
	7.53x10 ⁻¹⁰					1.59x10 ⁻¹⁵	1.91x10 ⁻¹³					
360		1.27x10 ⁻⁷	0.00003	0.011	0.0105			1290	3.04x10 ⁻¹²	3.92	179.74	89.87
	7.53x10 ⁻¹⁰					1.59x10 ⁻¹⁵	1.91x10 ⁻¹³					
480		1.27x10 ⁻⁷	0.00003	0.011	0.0105			1290	3.04x10 ⁻¹²	3.92	179.74	89.87
	7.53x10 ⁻¹⁰					1.59x10 ⁻¹⁵	1.91x10 ⁻¹³					
600		1.27x10 ⁻⁷	0.00003	0.011	0.0105			1290	3.04x10 ⁻¹²	3.92	179.73	89.87
	7.53x10 ⁻¹⁰					1.59x10 ⁻¹⁵	1.91x10 ⁻¹³					
720		1.27x10 ⁻⁷	0.00003	0.011	0.0105			1290	3.04x10 ⁻¹²	3.92	179.73	89.87
	7.53x10 ⁻¹⁰					1.59x10 ⁻¹⁵	1.91x10 ⁻¹³					
840		1.27x10 ⁻⁷	0.00003	0.011	0.0105			1290	3.04x10 ⁻¹²	3.92	179.73	89.86
	7.53x10 ⁻¹⁰					1.59x10 ⁻¹⁵	1.91x10 ⁻¹³					
960		1.27x10 ⁻⁷	0.00003	0.011	0.0105			1290	3.04x10 ⁻¹²	3.92	179.73	89.86
	7.53x10 ⁻¹⁰					1.59x10 ⁻¹⁵	1.91x10 ⁻¹³					
1080		1.27x10 ⁻⁷	0.00003	0.011	0.0105			1290	3.04x10 ⁻¹²	3.92	179.72	89.86
	7.53x10 ⁻¹⁰					1.59x10 ⁻¹⁵	1.91x10 ⁻¹³					
1200		1.27x10 ⁻⁷	0.00003	0.011	0.0105			1290	3.04x10 ⁻¹²	3.92	179.72	89.86

Table 7.24: The calculated mass loss rate using the Hintz-Johnson model.

Temperature (°C)	Number of Crystals	Mass Loss Rate (µg/s)
30	5	$1.04 \times 10^{-6} \pm 5.59 \times 10^{-7}$
33	5	$3.60 \times 10^{-6} \pm 2.30 \times 10^{-6}$
37	5	$3.20 \times 10^{-6} \pm 1.10 \times 10^{-6}$
40	5	$8.20 \times 10^{-6} \pm 2.17 \times 10^{-6}$

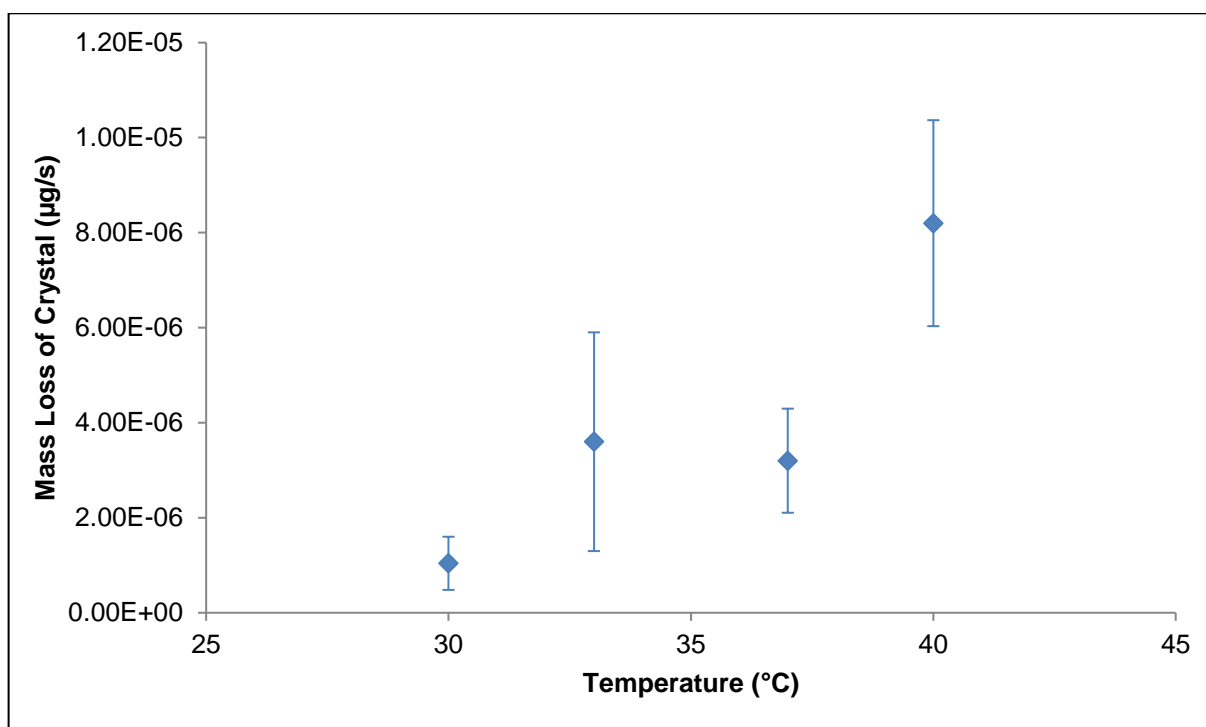


Figure 7.29: The relationship between the mass loss of a crystal of paracetamol and the degree of undersaturation calculated using the Hintz-Johnson model.

7.7.2 Comparison of Models with Experimental Data

The predictions calculated for paracetamol in FeSSIF using the Noyes-Whitney and Hintz-Johnson models were compared to the actual mass loss determined through dissolution experiments. The actual mass loss was calculated through the use of Heron's formula to determine the surface area, and the shape factor to determine the volume and hence the mass for each crystal.

An example of the calculation of actual mass loss as a function of time, at a temperature of 30°C is shown in Table 7.25.

Table 7.25: An example of the calculation of actual mass loss as a function of time, at a temperature of 30°C.

Time (s)	Surface Area (m ²)	Volume (m ³)	Density (kg/m ³)	Mass (µg)
0	1.27x10 ⁻⁷	3.04x10 ⁻¹²	1290	3.92
120	1.22x10 ⁻⁷	2.88x10 ⁻¹²	1290	3.72
240	1.16x10 ⁻⁷	2.66x10 ⁻¹²	1290	3.44
360	1.11x10 ⁻⁷	2.50x10 ⁻¹²	1290	3.22
480	1.09x10 ⁻⁷	2.40x10 ⁻¹²	1290	3.10
600	1.02x10 ⁻⁷	2.20x10 ⁻¹²	1290	2.84
720	9.71x10 ⁻⁸	2.04x10 ⁻¹²	1290	2.63
840	9.56x10 ⁻⁸	1.99x10 ⁻¹²	1290	2.56
960	9.00x10 ⁻⁸	1.81x10 ⁻¹²	1290	2.34
1080	8.84x10 ⁻⁸	1.77x10 ⁻¹²	1290	2.28
1200	8.36x10 ⁻⁸	1.63x10 ⁻¹²	1290	2.10

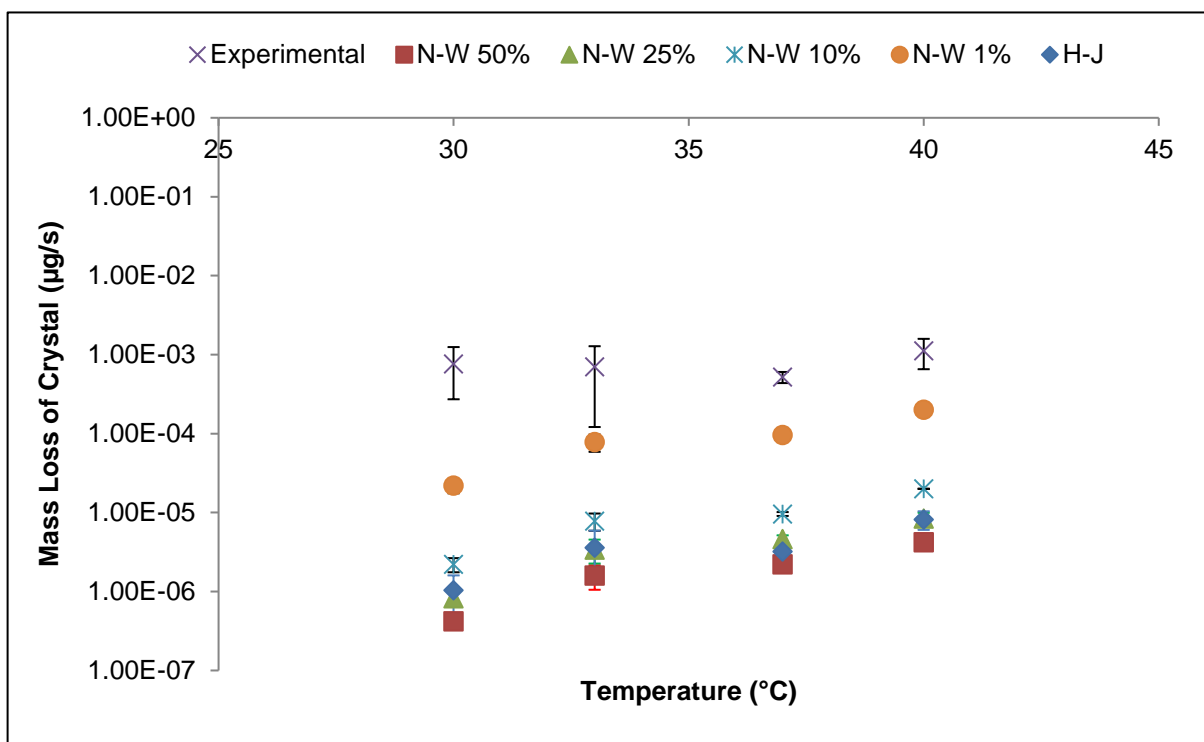


Figure 7.30: A comparison between the experimental mass loss and calculated mass losses using Noyes-Whitney and Hinz-Johnson.

The predicted mass loss of the crystal for all models is not an accurate prediction in comparison with the experimental mass loss. The percentage difference between the actual mass loss and predicted mass loss is shown in Table 7.26.

Table 7.26: The percentage difference between values of experimental mass loss and calculated mass loss.

Temperature (°C)	% difference				
	N-W (50%)	N-W (25%)	N-W (10%)	N-W (1%)	H-J
30	99.94	99.89	99.71	97.11	99.86
33	99.77	99.51	98.89	88.86	99.49
37	99.58	99.12	98.15	81.54	99.38
40	99.63	99.25	98.21	82.14	99.27

The percentage difference shows that the predicted values are inconsistent in comparison with the actual experimental mass loss. Therefore, current dissolution models could not be used in the pharmaceutical industry to predict in-vivo dissolution from in-vitro calculations.

The modification to the dissolution models carried out in Chapter 6, and for paracetamol in acetonitrile, where a fixed boundary layer thickness was used, was also carried out for the mass loss data for Paracetamol in FeSSIF. Therefore, the models were re-calculated using a fixed boundary layer of 0.1µm. An example of this calculation for a temperature of 30°C is shown in Table 7.27.

Table 7.27: An example of the Noyes-Whitney calculation with a fixed boundary layer parameter of 0.1 μm .

Time (s)	Diffusion Coefficient [D] (m ² /s)	Surface Area (m ²)	Boundary Layer Thickness [h] (m)	C _s (kg/L)	C _t (kg/L)	dM/dt (kg/s)	mass lost (kg)	Density of Solute (kg/m ³)	Volume of Crystal (m ³)	Mass of Crystal (μg)
0		1.27x10 ⁻⁷	0.0000001	0.011	0.0105			1290	3.04x10 ⁻¹²	3.92
	7.53x10 ⁻¹⁰					4.77x10 ⁻¹³	5.73x10 ⁻¹¹			
120		1.26x10 ⁻⁷	0.0000001	0.011	0.0105			1290	3.00x10 ⁻¹²	3.86
	7.53x10 ⁻¹⁰					4.73x10 ⁻¹³	5.68x10 ⁻¹¹			
240		1.24x10 ⁻⁷	0.0000001	0.011	0.0105			1290	2.95x10 ⁻¹²	3.81
	7.53x10 ⁻¹⁰					4.68x10 ⁻¹³	5.62x10 ⁻¹¹			
360		1.23x10 ⁻⁷	0.0000001	0.011	0.0105			1290	2.91x10 ⁻¹²	3.75
	7.53x10 ⁻¹⁰					4.64x10 ⁻¹³	5.56x10 ⁻¹¹			
480		1.22x10 ⁻⁷	0.0000001	0.011	0.0105			1290	2.87x10 ⁻¹²	3.70
	7.53x10 ⁻¹⁰					4.59x10 ⁻¹³	5.51x10 ⁻¹¹			
600		1.21x10 ⁻⁷	0.0000001	0.011	0.0105			1290	2.82x10 ⁻¹²	3.64
	7.53x10 ⁻¹⁰					4.55x10 ⁻¹³	5.45x10 ⁻¹¹			
720		1.20x10 ⁻⁷	0.0000001	0.011	0.0105			1290	2.78x10 ⁻¹²	3.59
	7.53x10 ⁻¹⁰					4.50x10 ⁻¹³	5.40x10 ⁻¹¹			
840		1.18x10 ⁻⁷	0.0000001	0.011	0.0105			1290	2.74x10 ⁻¹²	3.53
	7.53x10 ⁻¹⁰					4.45x10 ⁻¹³	5.35x10 ⁻¹¹			
960		1.17x10 ⁻⁷	0.0000001	0.011	0.0105			1290	2.70x10 ⁻¹²	3.48
	7.53x10 ⁻¹⁰					4.41x10 ⁻¹³	5.29x10 ⁻¹¹			
1080		1.16x10 ⁻⁷	0.0000001	0.011	0.0105			1290	2.66x10 ⁻¹²	3.43
	7.53x10 ⁻¹⁰					4.37x10 ⁻¹³	5.24x10 ⁻¹¹			
1200		1.15x10 ⁻⁷	0.0000001	0.011	0.0105			1290	2.62x10 ⁻¹²	3.37

A comparison of the mass loss values with a fixed boundary layer thickness with the experimental values obtained is shown in Figure 7.31.

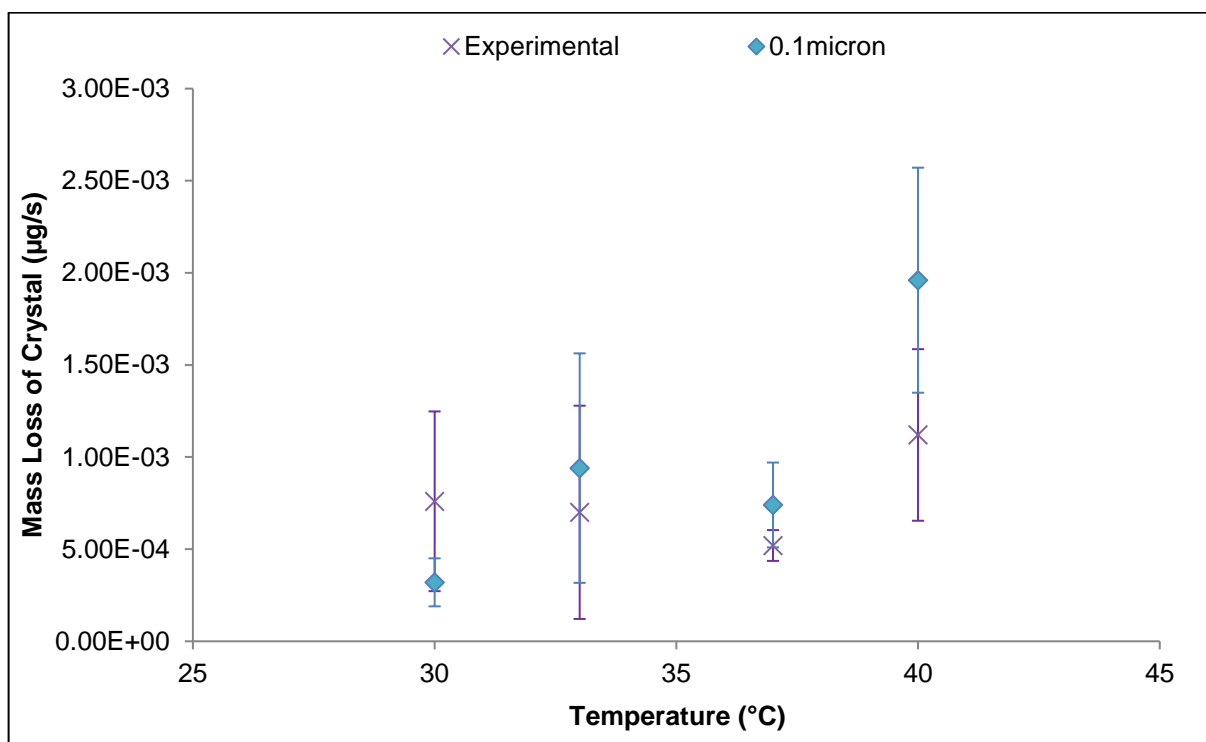


Figure 7.31: Comparison between the experimental mass loss and calculated values with a fixed boundary layer.

Table 7.28: The percentage difference between values of experimental mass loss and calculated mass loss with a fixed boundary layer.

Temperature (°C)	% difference
30	57.89
33	25.53
37	29.73
40	42.86

This modification resulted in a much more consistent prediction for the mass loss in comparison with the experimental mass loss. Upon comparison of the fixed boundary layers of paracetamol in acetonitrile and paracetamol in FeSSIF, the prediction of the modified model shows that for acetonitrile the boundary layer thickness should be 0.3µm for a consistent dissolution prediction, whereas for FeSSIF, the prediction of the modified model shows that the boundary layer thickness should be 0.1µm. These

values were found to be consistent with layer values found in literature determined by Bunn and Emmett (1949).

This can be explained through the interaction energies calculated, as a comparison of the dissolution of urea and paracetamol shows that as neither compound can form hydrogen bonding with acetonitrile, the majority of the total interaction energy with all surfaces is due to van der Waals interactions. Therefore, the boundary layer thickness for a dissolving molecule in acetonitrile can be concluded to be 0.3 μm . Based on the conclusions made in Chapter 6, it would be expected that the boundary layer thickness in FeSSIF would be larger than 0.3 μm , however although the majority component of FeSSIF is water, which can form hydrogen bonds with paracetamol, it is also made up of five other components, whose interaction with paracetamol, or each other, could not be determined.

7.8 Conclusions

This chapter aimed to present the solubility data of paracetamol in acetonitrile, water and FeSSIF. Comparison of the solubilities showed that acetonitrile had greater ideality, and that the solubility of paracetamol in the three solvents was found to be acetonitrile > water > FeSSIF.

Characterisation of paracetamol surfaces showed that there were five approximately equivalent morphologically important faces, which gave rise to a prismatic habit. This was explained through the surface chemistry of all the faces as they all have similar functional group contributions, with differences being attributed to the orientation of the functional groups at the surface.

The dissolution rate data of paracetamol in acetonitrile and paracetamol in FeSSIF were also presented. It was found that all morphologically important faces of paracetamol followed a first-order linear dependence with respect to undersaturation, and the dissolution rates of all the faces were comparable. The determination of interaction energies of all faces under consideration reinforced the experimental data obtained as all surfaces were found to have similar interaction energies with acetonitrile. It was also found that the dissolution rates of all face under consideration in FeSSIF followed a first order linear dependence with respect to temperature, with the mean dissolution rates increasing as temperature increased. The water probe

was found to have similar interaction energies with all faces under consideration, therefore the experimental results were validated.

Finally, calculation of the dissolution models to obtain theoretical overall mass loss data during dissolution experiments and comparing them to the experimental mass loss showed that the predicted values of the models were inconsistent, therefore current dissolution models could not be used to calculate mass loss in non-sink conditions. This was found to be the case for both solution systems.

Therefore, the dissolution models were modified, altering the boundary layer thickness as of the two models used for prediction calculations, both treated this parameter in different ways. A fixed boundary layer thickness was used for both solution systems, and a more consistent prediction was found for both systems, with boundary layer thicknesses of 0.3 μm and 0.1 μm for acetonitrile and FeSSIF, respectively. The boundary layer thicknesses for urea and paracetamol systems in acetonitrile were found to be the same. It was expected that the boundary layer thickness in FeSSIF would be larger than 0.3 μm , however although the majority component of FeSSIF is water, it is also made up of five other components, whose interaction with paracetamol, or each other, could not be determined.

References

- Bunn, C. W., H. Emmett. Crystal Growth from Solution: 1. Layer Formation on Crystal Faces. *Discuss. Faraday Soc.* **1949**. 5, 119-132.
- Finnie, S., K. V. R. Prasad, D. B. Sheen, J. N. Sherwood. Microhardness and Dislocation Identification Studies on Paracetamol. *Pharm. Res.* **2001**. 18(5), 674-681.
- Granberg, R. A., A. C. Rasmuson. Solubility of Paracetamol in Pure Solvents. *J. Chem. Eng. Data.* **1999**. 44(6), 1391-1395.
- Hammond, R. B., K. Pencheva, K. J. Roberts. A Structural-Kinetic Approach to Model Face Specific Solution/Crystal Surface Energy Associated with the Crystallisation of Acetyl Salicylic Acid from Supersaturated Aqueous/Ethanol Solution. *Cryst. Growth. Des.* **2006**. 6(6), 1324-1334.
- Heng, J. Y. Y., A. Bismarck, A. F. Lee, K. Wilson, D. R. Williams. Anisotropic Surface Energetics and Wettability of Macroscopic Form I Paracetamol Crystals. *Langmuir.* **2006**. 22(6), 2760-2769.
- Hintz, R. J., K. C. Johnson. The Effect of Particle Size Distribution on Dissolution Rate and Oral Absorption. *Int. J. Pharm.* **1989**. 51(1), 9-17.
- Khadka, P., Ro, J., Kim, H., Kim, I., Kim, J. T., Cho, J. M., Yun, G., Lee, J. Pharmaceutical Particle Technologies: An Approach to Improve Drug Solubility, Dissolution and Bioavailability. *Asian J. Pharm. Sci.* **2014**. 9(6), 304-306.
- McAllister, M. Dynamic Dissolution: A Step Closer to Predictive Dissolution Testing? *Mol. Pharm.* **2010**. 7(5), 1374-1387.
- Noyes, A. A., W. R. Whitney. The Rate of Solution of Solid Substances in their Own Solutions. *J. Am. Chem. Soc.* **1897**. 19(12), 930-934.
- Pickering, J., R. B. Hammond, V. Ramachandran, M. Soufian, K. J. Roberts. Synthonic Engineering Modelling Tools for Product and Process Design. *Engineering Crystallography: From Molecule to Crystal to Functional Form.* **2017**. NATO: Springer.
- Prasad, K. V. R., R. I. Ristic, D. B. Sheen, J. N. Sherwood. Dissolution Kinetics of Paracetamol Single Crystals. *Int. J. Pharm.* **2002**. 238(1-2), 29-41.
- Sudha, C., K. Srinivasan. Understanding the Effect of Solvent Polarity on the Habit Modification of Monoclinic Paracetamol in terms of Molecular Recognition at the Solvent Crystal Interface. *Cryst. Res. Technol.* **2014**. 49(11), 865-872.

Chapter 8: Conclusions and Future Work

8.1 Introduction

The work presented in the previous chapters aimed to extend the knowledge surrounding the influence of solution environment on the nucleation, growth and dissolution of anisotropic crystals, and the ability of computational or empirical modelling to predict these influences. The chapters in this thesis set out to ultimately develop a workflow to understand the nucleation, growth and dissolution of single crystals from supersaturated and undersaturated systems, along with a fundamental molecular approach to explain and an empirical approach to predict these processes.

The solubility studies of urea in Chapter 5 were vital to determine the nucleation and growth kinetics and provided an in-depth molecular understanding of urea interactions with biuret, as well as a starting point for urea interactions with a solvent. This foundation allowed for the dissolution experiments of urea as a model material in Chapter 6, building on solvent effect and molecular understanding and also allowed for a direct comparison between urea growth and dissolution.

Additionally, modification of empirical dissolution models in Chapter 6 for a model material paved the way for validating the model further in Chapter 7 with a pharmaceutical molecule, resulting in the ability to consistently predict bioperformance of an API. These studies are concluded in this chapter and with a focus on the link between nucleation, growth and dissolution of anisotropic single crystals, and hence the development of a workflow for the early stages of research and development of pharmaceuticals.

The aims and objectives of the thesis that have been initially set out to achieve during the course of this study are then reviewed, and finally suggestions have been made with initial experiments carried out and a method developed based on the findings of this research.

8.2 Conclusions of this Study

8.2.1 Solubility, Nucleation and Growth of Urea in the Presence and Absence of Biuret

Solubility studies and the van't Hoff evaluation suggested that the solubility behaviour of urea in absolute ethanol is less than ideal; therefore solute-solute interactions are generally more favoured than solute-solvent interactions. This was reinforced through

the calculation of the activity coefficient, which was greater than 1, however with increasing temperature the activity coefficient decreases, therefore becomes closer to the ideal scenario.

Determination of the MSZW using the slow cooling polythermal crystallisation method shows that the MSZW of urea in absolute ethanol decreases with increasing concentration due to the rapid onset of supersaturation, at lower concentrations $\Delta T = \sim 17^\circ\text{C}$, whereas at higher concentrations $\Delta T = 7^\circ\text{C}$. The addition of 1%w/w biuret widens the MSZW resulting in a more stable solution where $\Delta T = 5^\circ\text{C}-22^\circ\text{C}$, thereby affecting solute-solvent interactions.

The nucleation mechanism for urea in ethanol was found to be instantaneous at higher concentrations and progressive at lower concentrations. At lower concentrations, where progressive nucleation took place, the effective interfacial tension was found to decrease from 4.652 mJ/m^2 to 4.495 mJ/m^2 with an increase in concentration. This lower interfacial tension was also accompanied by a faster nucleation rate, with nucleation rates ranging from $9.22 \text{ nm}^{-3}\cdot\text{s}^{-1}$ - $20.48 \text{ nm}^{-3}\cdot\text{s}^{-1}$ for the lower concentration to $11.44 \text{ nm}^{-3}\cdot\text{s}^{-1}$ - $35.22 \text{ nm}^{-3}\cdot\text{s}^{-1}$ for the higher concentration at a progressive nucleation mechanism. The addition of 1%w/w biuret was not found to have an effect on the nucleation mechanism; however it did result in a significant increase in the nucleation rates with nucleation rates ranging from $9.25 \text{ nm}^{-3}\cdot\text{s}^{-1}$ - $67.73 \text{ nm}^{-3}\cdot\text{s}^{-1}$ for the lower concentration to $13.56 \text{ nm}^{-3}\cdot\text{s}^{-1}$ - $88.84 \text{ nm}^{-3}\cdot\text{s}^{-1}$ for the higher concentration.

At higher concentrations, where instantaneous nucleation took place, the crystallite growth shape factor was determined to be larger for crystals grown in the presence of 1%w/w biuret, resulting in crystals with a greater cross-sectional area. Therefore, biuret affects the morphology of crystallites grown, as they are less needle-like. Additionally, the values of the growth exponent 'n' was 2 for urea in absolute ethanol which suggested that the rate-limiting factor for urea in absolute ethanol was due to the rearrangement of the solute at the crystal-solution interface, however the addition of biuret into the system altered this process where at higher concentrations the rate-limiting factor changed to $n=1$, therefore was due to diffusion of a growth unit to the growing crystallite.

Solvent mediated growth rates of $\{110\}$ and $\{111\}$ faces of urea showed that the mean growth rates of both faces were found to have a linear dependence on

supersaturation, where the growth rates of both faces increased with increasing supersaturation. The growth rate of the {111} face was found to increase greater than that of the {110} face, and this difference was attributed to the difference in surface chemistry at both faces and the interaction of both faces with solvent molecules.

The growth mechanism for both the {110} and {111} faces was predicted through calculation of the α -factor, which suggested that the BCF mechanism was the predicted mechanism of growth for urea in absolute ethanol. The growth mechanism and kinetics were then calculated, where a value of $r=1$ was obtained through the power law model which was associated with the BCF mechanism for growth in the pure system. (Garside, 1985) As a result of this, the rate limiting step for growth of the {110} face was balanced between diffusion and surface integration of growth units, and for the {111} face was due to surface integration.

However, values of $r=0$ and $r=0.2$ were obtained through the power law model for the system containing biuret which did not correspond to either the BCF or B&S model. Therefore, values obtained from both models allowed for the conclusion that BCF mechanism was a better fit to the data, and the rate limiting step of the {110} face changed as the resistance to diffusion significantly increased with little effect on the resistance to surface integration. However, the rate limiting step for the {111} face stayed the same.

8.2.2 Surface Characterisation of Urea with Biuret

Crystals of urea exhibit three dominant faces, {110}, {111} and {001}, - {001} was found to be morphologically insignificant when crystallised under certain conditions. {111} was found to have a polar opposite face, {-1-1-1}, which had a different surface chemistry; with the {111} face having one additional hydrogen from the amide group at the surface. (Docherty et al., 1993)

The molecular interactions of biuret with the two faces under consideration was determined, as well as with the polar {-1-1-1} face. The majority of the total interaction energy of the biuret probe with all the faces under consideration were found to be due to hydrogen bonding, with van der Waals dispersive interactions and electrostatic interactions making up a minimal amount of the total interaction energy.

The biuret probe was found to have a stronger interaction with the {111} surfaces in comparison with the {110} surface. Calculation of these interactions reinforced

experimental data obtained showing that biuret had a greater effect in slowing down the growth of the {111} face in comparison with the {110} surface.

The addition of 1%w/w biuret was found to not have an effect on the linear relationship between growth rate and supersaturation, however biuret had a greater effect in slowing down the growth of the {111} face in comparison with the {110} face. This was found to be due to the interaction of biuret with both faces, as biuret has two distinct molecular interactions with the {111} face, a higher adsorption energy and a significantly larger surface coverage in comparison with the {110} face. (Singh et al., 2015)

8.2.3 Dissolution of Urea Single Crystals

The {110} and {111} surfaces of urea were found to follow a first-order linear dependence with respect to undersaturation in absolute ethanol, with the {111} surface dissolving faster than the {110} surface with increasing levels of undersaturation. Directly comparing dissolution rate data to growth rate data showed that the growth and dissolution rates of the surfaces of urea were the same, therefore growth and dissolution were found to be inverse processes.

A comparison of the dissolution rates of urea in absolute ethanol and acetonitrile showed that dissolution of urea in acetonitrile also followed a first-order linear dependence with respect to undersaturation, however, in acetonitrile, the dissolution rates of both surfaces were found to be comparable.

Calculation of the interaction energies of ethanol and acetonitrile probes with the urea surfaces under consideration showed that the majority of the total interaction energy of ethanol was due to hydrogen bonding with van der Waals dispersive interactions and electrostatic interactions making up a minimal amount of the total interaction energy. However, the majority of the total interaction energies of acetonitrile were due to hydrogen bonding with the {110} and {111} surfaces, but van der Waals dispersive interactions for the {-1-1-1} surface.

Total interaction energies were similar for both faces in both solvents, however the wetting energy for the {111} surface was found to be much higher than the wetting energies of the other surfaces. Calculation of these interactions reinforced experimental data where the dissolution rates of the {110} face for urea in absolute ethanol, and both faces in acetonitrile, had similar dissolution rates, however the

dissolution rate of the {111} surface in absolute ethanol was faster than the other surfaces.

Dissolution models were calculated to determine the theoretical overall mass loss of a single crystal of urea in ethanol and acetonitrile, and compared to experimental mass loss values. It was found that theoretical values were inconsistent and current models could not be used to predict mass loss in non-sink conditions. The models were modified in order to obtain a more consistent prediction through altering the boundary layer thickness, from a function of the particle size to a fixed value. It was found that a boundary layer thickness of 0.5 μm and 0.3 μm for ethanol and acetonitrile, respectively, resulted in a much more consistent prediction for the mass loss. These values were found to be in good agreement with those determined by Bunn and Emmett (1949). This difference in thickness was found to be due to interaction energies, as ethanol had a stronger interaction overall with the urea surfaces, and it can accept and donate hydrogen bonds, which are longer range interactions, therefore urea could interact with the bulk of the solution over a larger boundary layer.

8.2.4 Dissolution of Paracetamol Single Crystals

The solubility of Paracetamol in three solvents was found to be acetonitrile > water > FeSSIF. (Granberg et al., 1999) It was determined that the solubility of Paracetamol in all three solvents was less than ideal, reinforced by the calculation of the activity coefficient being greater than 1, with acetonitrile having a greater ideality than water or FeSSIF.

Characterisation of the surfaces of Paracetamol showed that there were five approximately equivalent morphologically important surfaces – {011}, {100}, {110}, {201} and {001}. This was due to the surface chemistry of the surfaces having similar functional group contributions with the differences being attributed to the orientation of functional groups at the surface. (Sudha et al., 2014; Prasad et al., 2002)

Dissolution of Paracetamol in acetonitrile was determined and it was found that all faces of Paracetamol followed a first-order linear dependence with respect to undersaturation and were comparable. Dissolution of Paracetamol in FeSSIF was also found to have a first-order linear dependence with respect to temperature, with

no significant solvent effect on any of the faces under consideration, so all faces were found to have comparable dissolution rates.

Calculation of the interaction energies of acetonitrile and water probes with the surfaces of Paracetamol showed that the majority of the total interaction energy was due to van der Waals dispersive interactions for acetonitrile, with hydrogen bonding and electrostatic interactions making up a minimal amount of the total interaction energy, and hydrogen bonding for water, with van der Waals dispersive interactions and electrostatic interactions making up a minimal amount of the total interaction energy. Total interaction energies of all surfaces were determined to be stronger for water than for acetonitrile, due to the water molecule being able to accept and donate hydrogen bonds with the surfaces.

Dissolution models were calculated to determine the theoretical overall mass loss of a single crystal of Paracetamol in acetonitrile and FeSSIF, and then compared to experimental mass loss values. It was found that theoretical values were inconsistent and the modification to the boundary layer thickness values were carried out to validate the results previously obtained. It was found that a boundary layer thickness of 0.3 μm and 0.1 μm for acetonitrile and FeSSIF, respectively, resulted in a much more consistent prediction for the overall mass loss. These values were found to be in good agreement with those determined by Bunn and Emmett (1949). It was expected that the difference in boundary layer thicknesses would be for the boundary layer thickness to be larger for FeSSIF in comparison with acetonitrile due to the hydrogen probe having stronger interactions with the surfaces. However, although the majority component of FeSSIF is water, it also consisted of five other components, whose interaction with paracetamol could not be determined.

8.3 Review of Thesis Aims and Objectives

Taking into consideration the core thesis aims and objectives at the beginning of this study, this study has provided an understanding between anisotropic crystal growth and dissolution and methods for predicting these processes. Polythermal studies have provided a new understanding of the nucleation mechanism and kinetics as a function of additive and concentration of urea.

The growth kinetics of {110} and {111} faces of spontaneously nucleated urea single crystals were measured under diffusion-limited conditions as a function of

supersaturation and additive, along with dissolution kinetics of single crystals of urea under the same, yet opposing, undersaturation conditions. Combining this data allowed for a direct comparison between growth and dissolution. Dissolution rates of paracetamol single crystals as a function of solvent, undersaturation and temperature were measured.

All experimental growth and dissolution data was linked to and rationalised through morphological analysis of surface chemistry and molecular modelling. Calculation of dissolution models have provided a new understanding of the inconsistency of current models at predicting dissolution and a modification of the models to consistently predict dissolution in solvents and FeSSIF to determine bioperformance in non-sink conditions.

However, some objectives were not met during this research, specifically understanding the scale-up between single crystal and powder dissolution and relating this to current dissolution models in order to predict bioperformance of pharmaceutical compounds, particularly those that are solubility or dissolution limited.

8.4 Suggestions for Future Work

The ultimate aim of this thesis was to either computationally or empirically predict growth and dissolution of anisotropic crystals. However, considering the importance of establishing an in-vitro in-vivo relationship to request a waiver of bioequivalency studies from regulatory authorities (Khadka et al., 2014), much more work will be required in order to provide a workflow to scale-up single crystal to powder dissolution in order to predict bioperformance. This can only be achieved through a thorough understanding of the dissolution process to the point of predicting bioperformance based on knowledge and understanding of the underlying crystal structure and surface interactions.

In order to develop this workflow preliminary experiments were carried out to develop a method for powder dissolution of Paracetamol in FeSSIF. Initially, UV-visible spectroscopy was planned for analysis in order to determine concentration of the solution, and hence determine the amount of FeSSIF that had dissolved. However, at 243nm, the wavelength needed to determine the absorbance of paracetamol, there was a significant overlap with one or more of the components of FeSSIF.

HPLC analysis was then considered for analysis in order to determine the concentration of Paracetamol in FeSSIF, however one or more components of FeSSIF were found to have a similar retention time causing overlapping of peaks. Therefore, one suggestion for future work would be to develop an analysis method for paracetamol in FeSSIF, in order to accurately determine the concentration.

Paracetamol in acetonitrile, therefore, was focussed on, and a HPLC method developed for the analysis of samples, which can be found below:

- Mobile Phase A: 90% Water, 10% Acetonitrile
- Stationary Phase: Acquity UPLC CSH Phenyl-Hexyl, 1.7 μ m, 2.1 x 100mm, Part #: 186005407, SN: 010734065166 10
- Diluent: Mobile Phase A
- Flow Rate: 0.5 mL/min
- Injection Volume: 2 μ L
- Needle Wash: 50% IPA in Water
- Injection Mode: Needle Wash with Flush time 10.0 seconds
- Detection: 243 nm UV
- Column Temperature: 40 °C
- Isocratic (100% mobile phase A for run time) methods for 3-minute run time
- Sample Preparation: 1 to 1000 dilution in diluent

Samples of a known amount of paracetamol in acetonitrile were prepared, to determine whether a calibration curve could be obtained using the method outlined above.

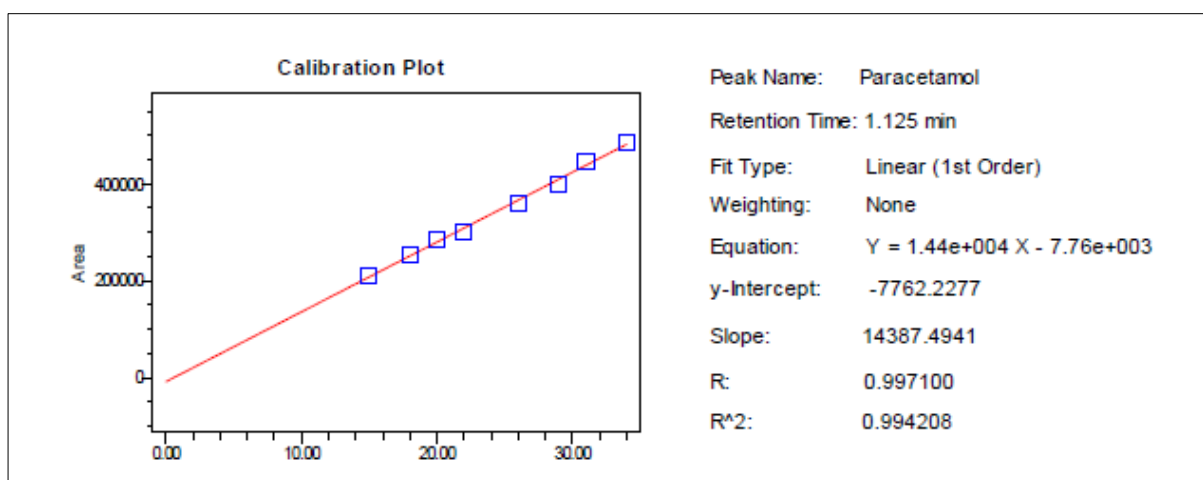


Figure 8.1: Calibration Plot for Paracetamol in HPLC.

This method allowed for a paracetamol peak to be determined, therefore preliminary experimentation was carried out in a 100mL jacketed vessel at the same levels of undersaturation as the single crystal experiments.

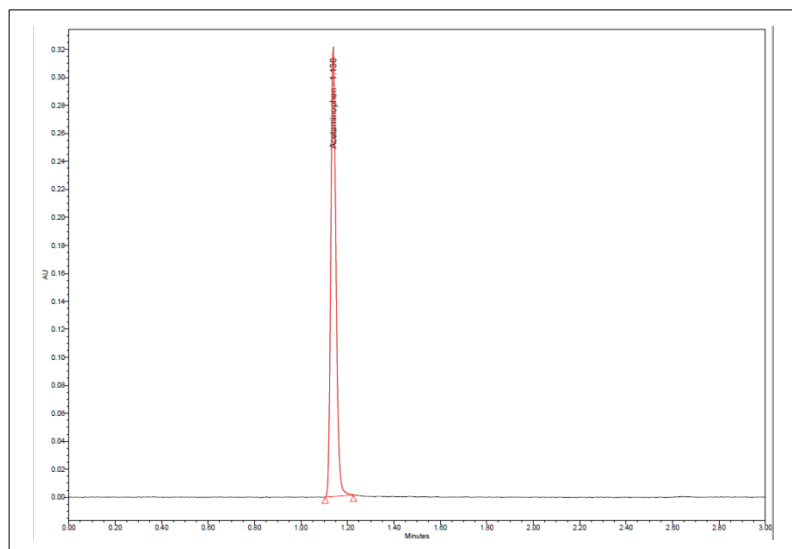


Figure 8.2: An example of a Paracetamol peak in HPLC.

1g of Paracetamol powder was added and the temperature of the vessel was controlled using a circulating water bath. Samples were taken at every interval corresponding to the images taken for single crystal experiments. Initially, after taking a sample, the powder was filtered through centrifuge filtration and the filtrate was diluted to determine the concentration, however it was realised that between collection and centrifugation of the sample, precipitation had taken place, therefore the concentration of the filtrate could not be determined accurately.

Hence, another suggestion for future work would be for this process to be refined further, perhaps using syringe filtration as a method to filter the powder upon collection of the sample and diluting the sample to ensure that no further precipitation can take place. Upon the development of an experimental and analytical method for paracetamol in solvent, and paracetamol in FeSSIF, which would allow for further modifications to dissolution models, this work could be taken further expanding to solubility or dissolution limited compounds.

The main limitation of this study is that all calculations have been carried out based on a two-dimensional image of a crystal, which may not necessarily be representative of the crystal facet which is being studied. With urea, for example, the errors associated with two-dimensional measurement of a 3D crystal may not be considerable due to it being a tetragonal system. With paracetamol, however, being a

prismatic crystal, considering the angle of the facets, measurements cannot be considered perpendicular for all the facets under consideration. Therefore, for future research, moving away from two-dimensional imaging to three-dimensional imaging using interferometry would provide a basis for calculations without having to rely on the assumption that all faces under consideration are perpendicular to the two-dimensional image. Additionally, with regards to the crystal itself, defects which can give rise to etching, have not been taken into consideration which would influence both the growth and dissolution of a crystal.

The data obtained in this study has been used for further collaborative work with the University of Leeds, initially through the simulation of a population balance model carried out by Dr. CaiYun Ma, and also through utilisation of the growth and dissolution data in opposing conditions to control the particle size distribution in crystallisers.

Additionally, a further way this study can be built upon is through the use of artificial intelligence to automate of the image analysis process. This is because pharmaceutical dissolution testing is usually carried out on the formulated drug product, however automating this study would mean the ability to carry out routine dissolution testing on the active pharmaceutical ingredient as it journeys through the manufacturing chain.

The 2020 vision for this work and onwards is, through careful particle engineering, a workflow from single crystal to powder, allowing for the design of precision particles modified for their bioavailability.

References

- Bunn, C. W., H. Emmett. Crystal Growth from Solution: 1. Layer Formation on Crystal Faces. *Discuss. Faraday Soc.* **1949**. 5, 119-132.
- Docherty, R., K. J. Roberts, V. Saunders, S. Black, R. J. Davey. Theoretical Analysis of the Polar Morphology and Absolute Polarity of Crystalline Urea. *Faraday Discuss.* **1993**. 95, 11-25.
- Garside, J. Industrial Crystallisation from Solution. *Chem. Eng. Sci.* **1985**. 40(1), 3-26.
- Granberg, R. A., A. C. Rasmuson. Solubility of Paracetamol in Pure Solvents. *J. Chem. Eng. Data.* **1999**. 44(6), 1391-1395.
- Khadka, P., Ro, J., Kim, H., Kim, I., Kim, J. T., Cho, J. M., Yun, G., Lee, J. Pharmaceutical Particle Technologies: An Approach to Improve Drug Solubility, Dissolution and Bioavailability. *Asian J. Pharm. Sci.* **2014**. 9(6), 304-306.
- Prasad, K. V. R., R. I. Ristic, D. B. Sheen, J. N. Sherwood. Dissolution Kinetics of Paracetamol Single Crystals. *Int. J. Pharm.* **2002**. 238(1-2), 29-41.
- Singh, M. K.; Tiwari, V. S. Uncovering the Mode of Action of Solvent and Additive Controlled Crystallisation of Urea Crystal: A Molecular-Scale Study. *Cryst. Growth Des.* **2015**. 15 (7), 3220-3234.
- Sudha, C., K. Srinivasan. Understanding the Effect of Solvent Polarity on the Habit Modification of Monoclinic Paracetamol in terms of Molecular Recognition at the Solvent Crystal Interface. *Cryst. Res. Technol.* **2014**. 49(11), 865-872.

Appendices

APPENDIX A: METASTABLE ZONE WIDTH DETERMINATION

A1: UREA IN ETHANOL

Concentration (g/mL)	Cooling Rate (°C/min)	Mean \pm St. Dev T_{cryst}	Mean \pm St. Dev T_{diss}
0.040	0.5	3.2 \pm 1.4	17.1 \pm 1.0
	1	-1.0 \pm 3.3	21.2 \pm 0.1
	2	-1.7 \pm 0.9	23.2 \pm 0.6
	5	-1.8 \pm 0.8	26.3 \pm 0.7
0.046	0.5	9.9 \pm 1.0	21.0 \pm 2.9
	1	8.7 \pm 1.1	26.3 \pm 0.2
	2	6.7 \pm 1.7	28.4 \pm 0.4
	5	3.7 \pm 0.8	30.1 \pm 1.3
0.050	0.5	17.9 \pm 1.9	25.8 \pm 3.8
	1	14.2 \pm 1.2	30.5 \pm 1.1
	2	11.5 \pm 1.1	33.1 \pm 0.4
	5	6.5 \pm 1.3	33.8 \pm 0.7
0.058	0.5	23.0 \pm 0.5	31.5 \pm 0.9
	1	20.4 \pm 1.0	35.1 \pm 0.9
	2	15.6 \pm 1.7	35.9 \pm 0.6
	5	13.3 \pm 0.7	39.8 \pm 1.4
0.066	0.5	27.4 \pm 2.7	34.4 \pm 2.7
	1	25.9 \pm 2.4	37.3 \pm 1.9
	2	25.0 \pm 1.1	42.8 \pm 0.6
	5	17.2 \pm 1.1	43.7 \pm 0.9

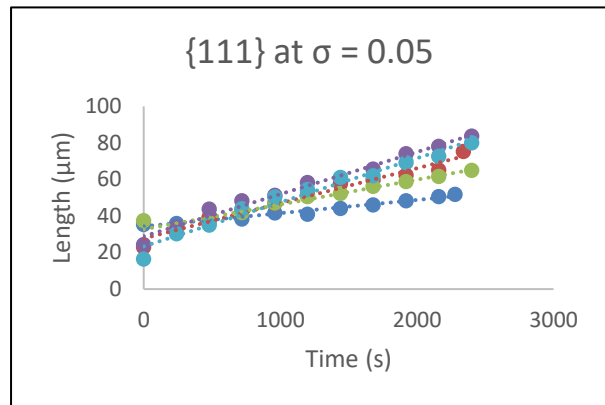
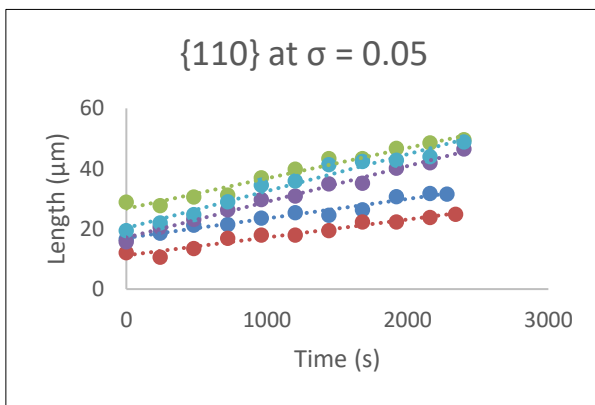
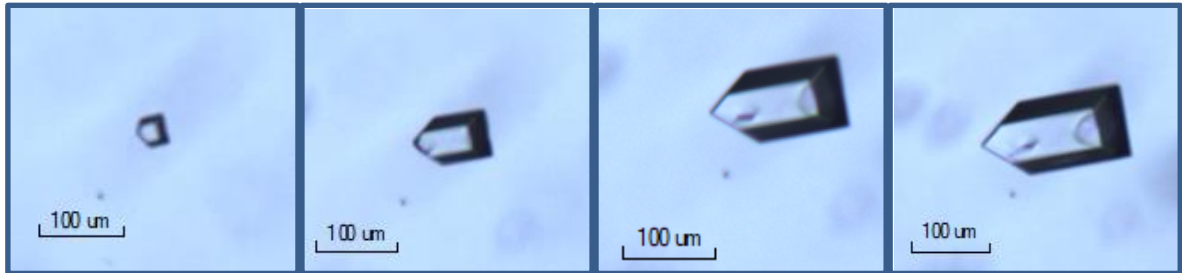
A2: UREA WITH 1% BIURET IN ETHANOL

Concentration (g/ml)	Cooling Rate (°C/min)	Mean \pm St. Dev T_{cryst}	Mean \pm St. Dev T_{diss}
0.04	0.5	4.6 \pm 3.3	26.1 \pm 0.3
	1	0.3 \pm 1.1	26.2 \pm 0.4
	2	-2.8 \pm 2.4	29.5 \pm 0.3
	5	-3.9 \pm 0.8	32.6 \pm 0.2
0.046	0.5	14.2 \pm 1.7	27.4 \pm 2.9
	1	11.7 \pm 3.8	29.8 \pm 0.5
	2	3.9 \pm 0.2	33.4 \pm 0.5
	5	3.0 \pm 2.1	36.0 \pm 0.7
0.05	0.5	20.8 \pm 1.0	30.9 \pm 2.0
	1	16.2 \pm 1.1	31.9 \pm 0.4
	2	14.8 \pm 0.9	33.4 \pm 0.5
	5	9.5 \pm 2.1	36.8 \pm 1.4
0.058	0.5	25.5 \pm 1.2	29.9 \pm 2.5
	1	22.6 \pm 1.7	35.0 \pm 0.5
	2	21.4 \pm 1.5	33.8 \pm 4.5
	5	16.8 \pm 2.5	39.5 \pm 3.8
0.066	0.5	26.0 \pm 1.8	30.2 \pm 1.0
	1	23.3 \pm 2.5	37.6 \pm 1.8
	2	20.5 \pm 1.3	40.3 \pm 0.3
	5	7.9 \pm 1.2	44.1 \pm 0.7

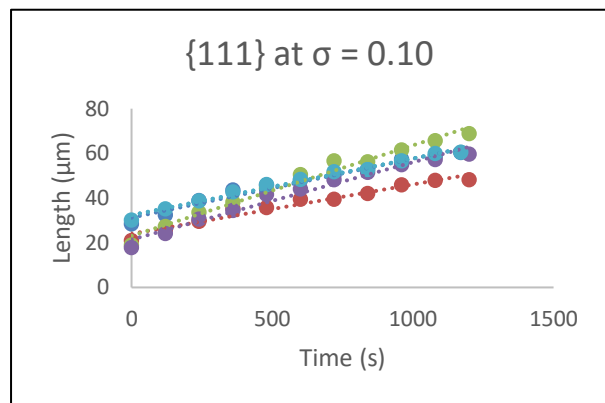
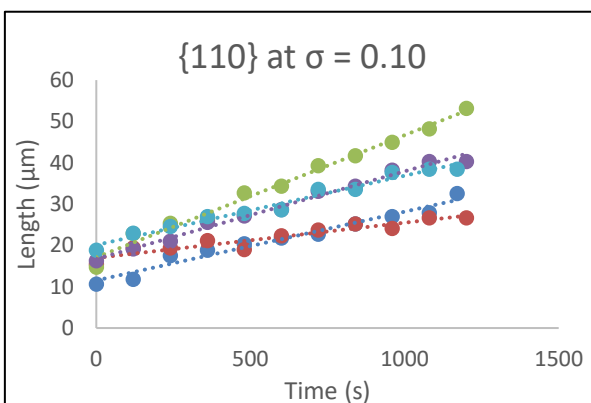
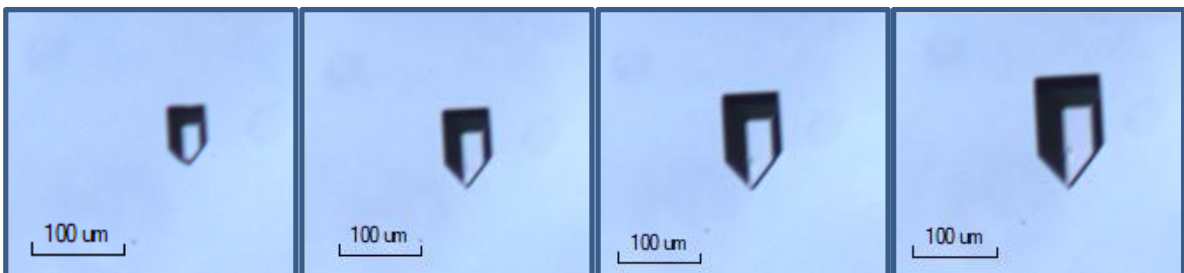
APPENDIX B: CRYSTAL GROWTH RATE MEASUREMENT

B1: UREA IN ETHANOL

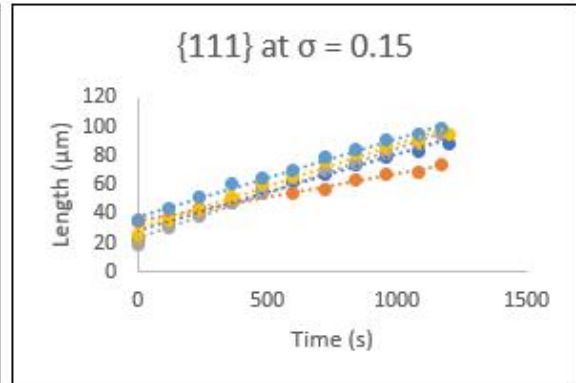
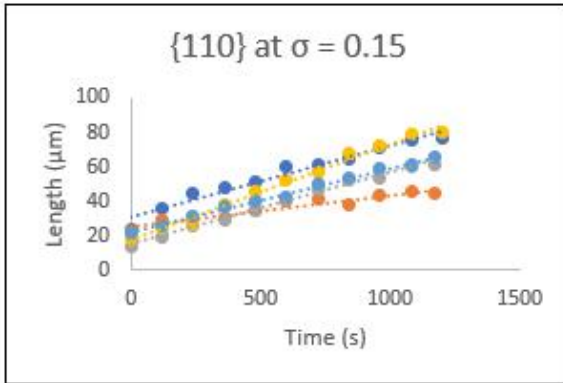
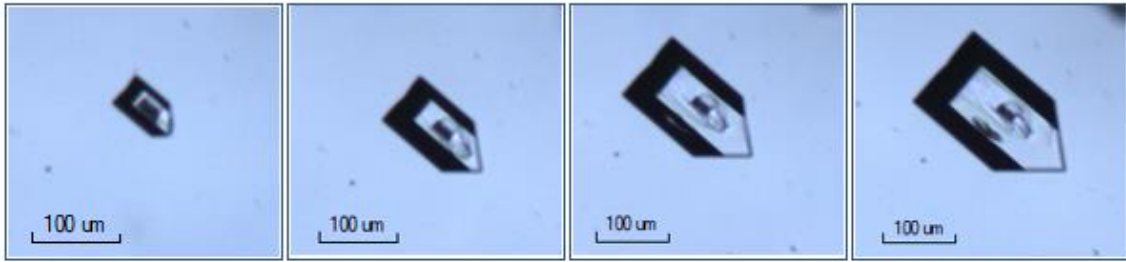
$\sigma = 0.05$



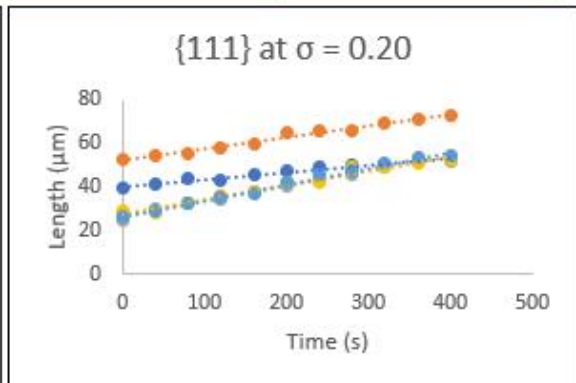
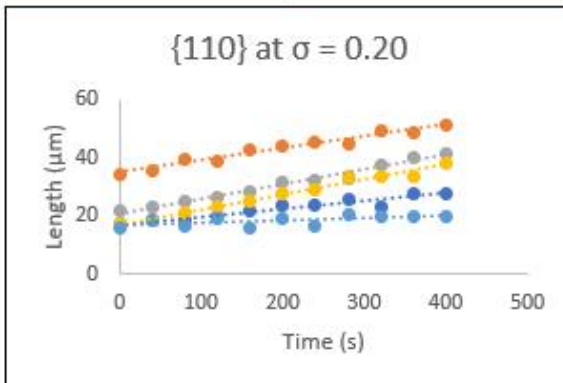
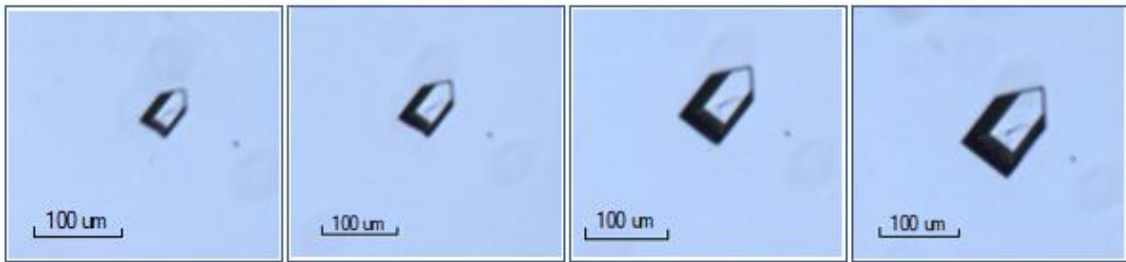
$\sigma = 0.10$



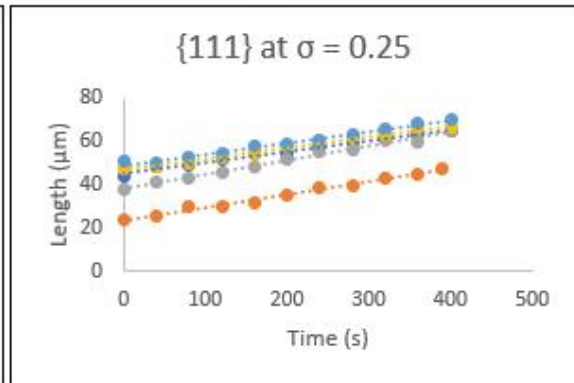
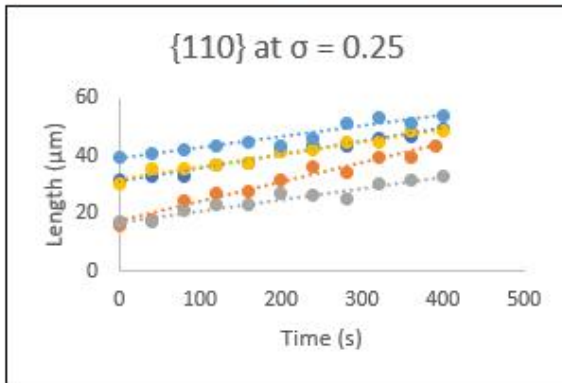
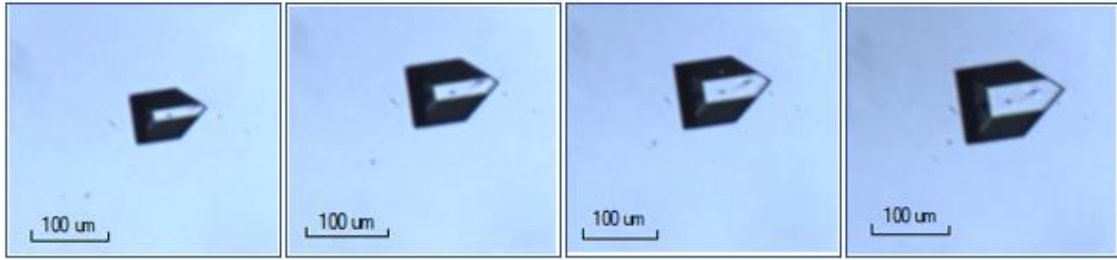
$\sigma = 0.15$



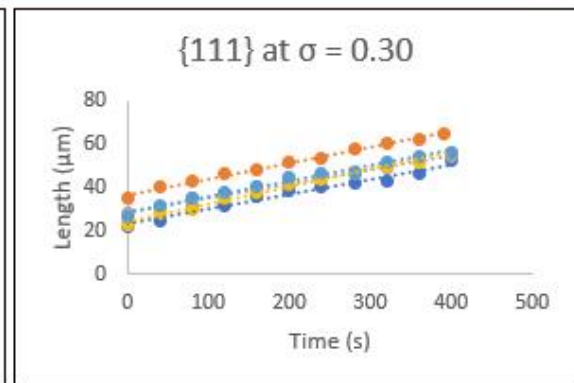
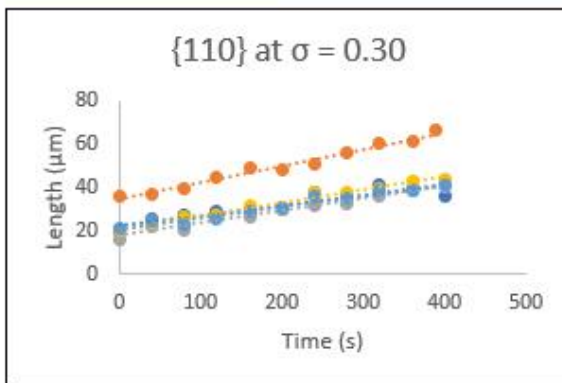
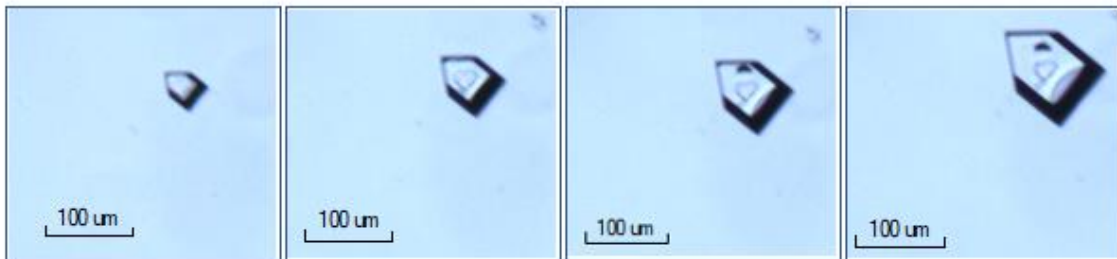
$\sigma = 0.20$



$\sigma = 0.25$

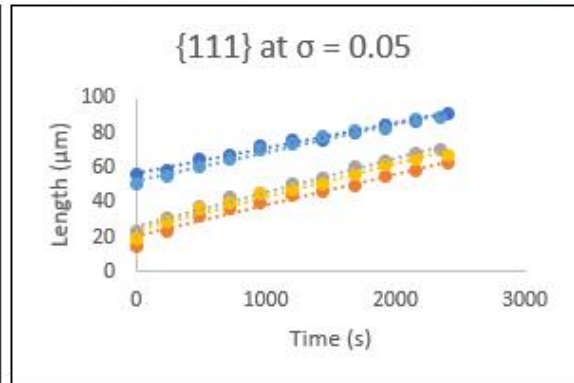
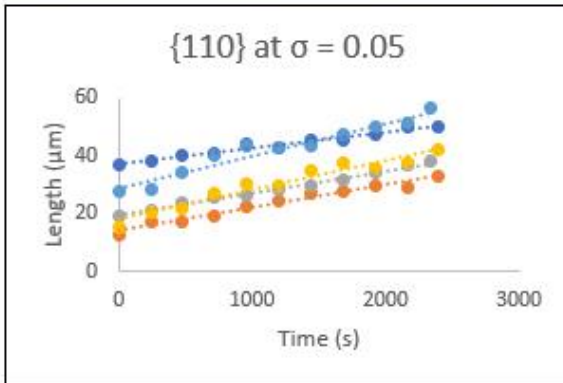
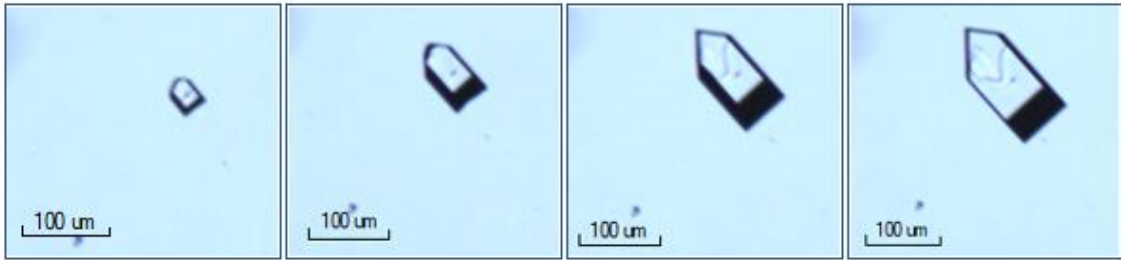


$\sigma = 0.30$

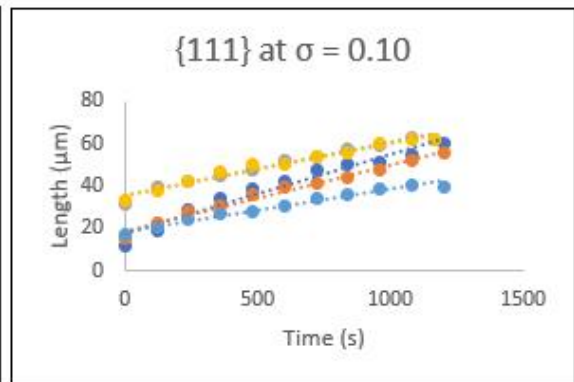
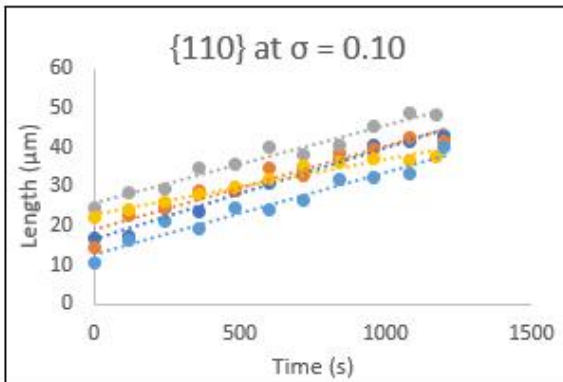
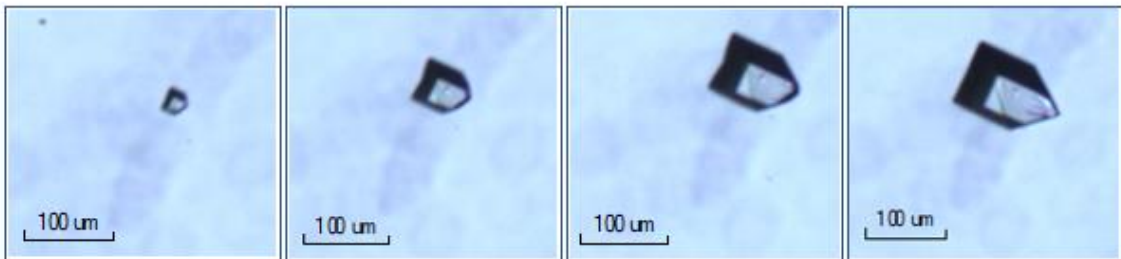


B2: UREA WITH 1% BIURET IN ETHANOL

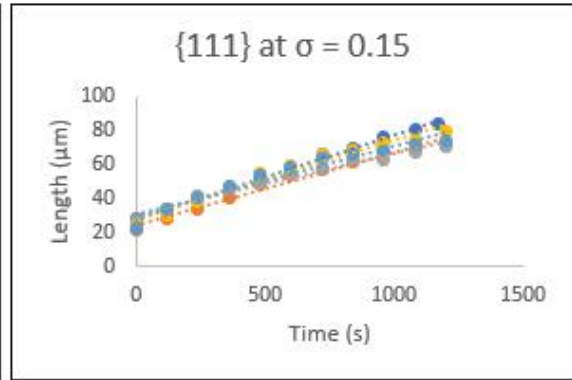
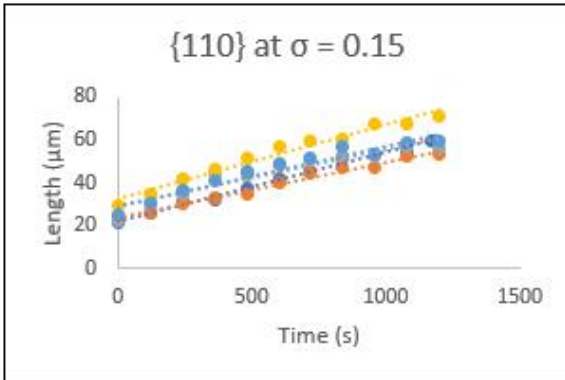
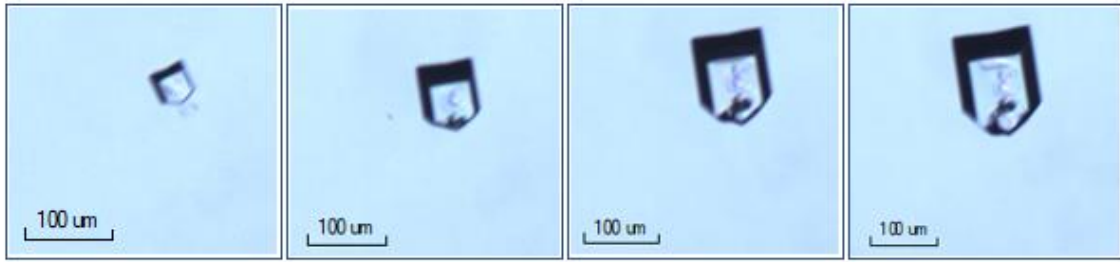
$\sigma = 0.05$



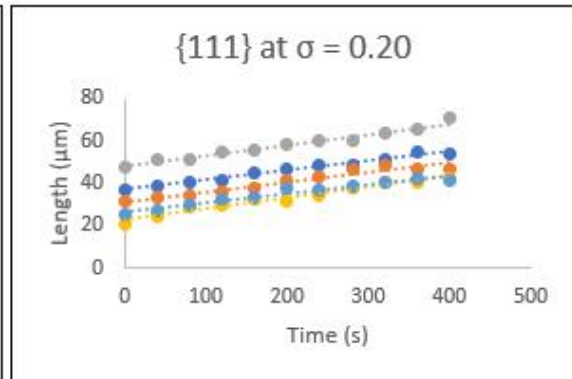
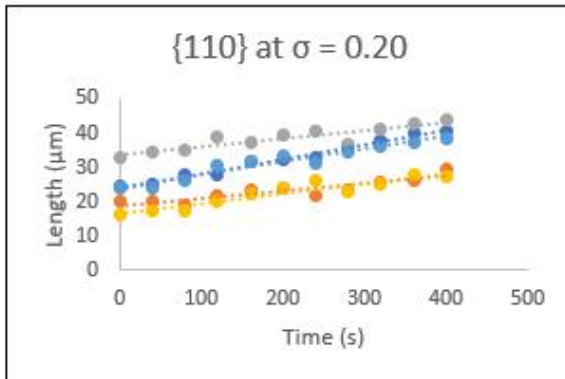
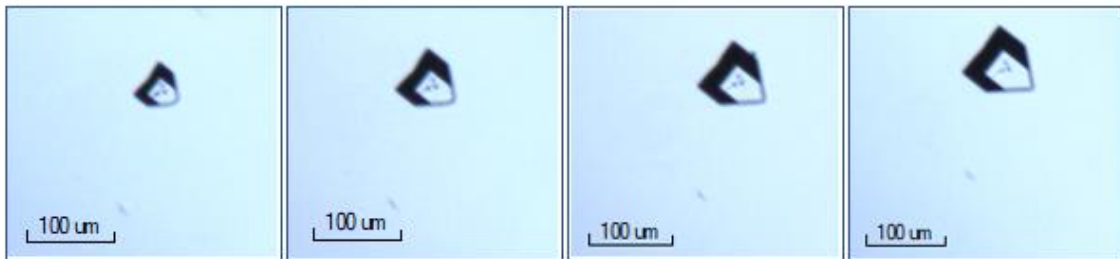
$\sigma = 0.10$



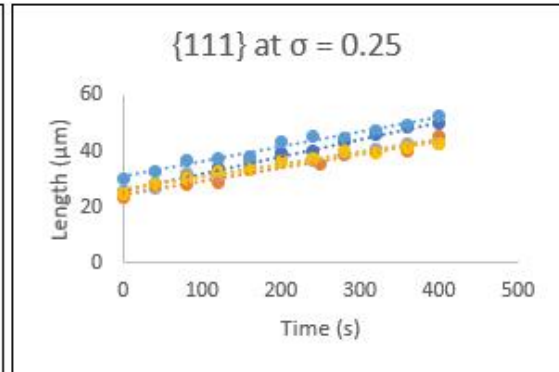
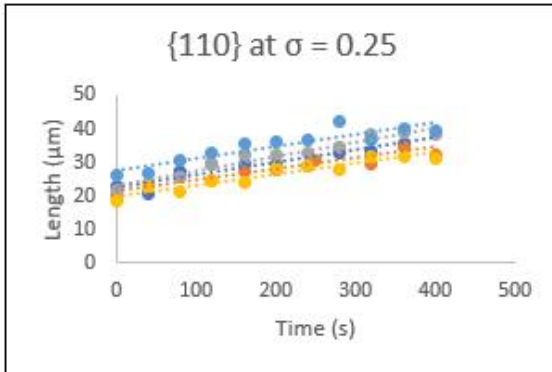
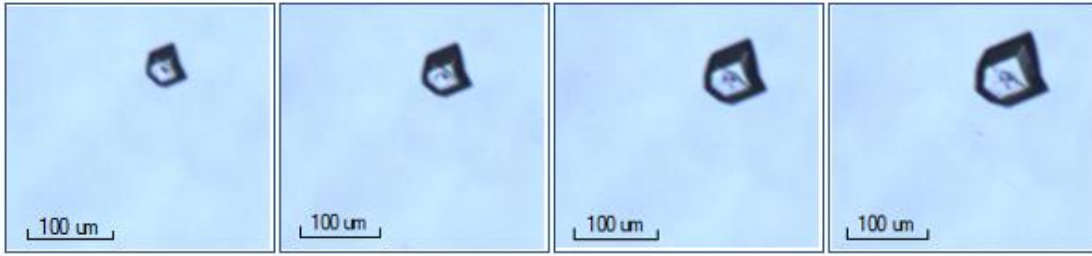
$\sigma = 0.15$



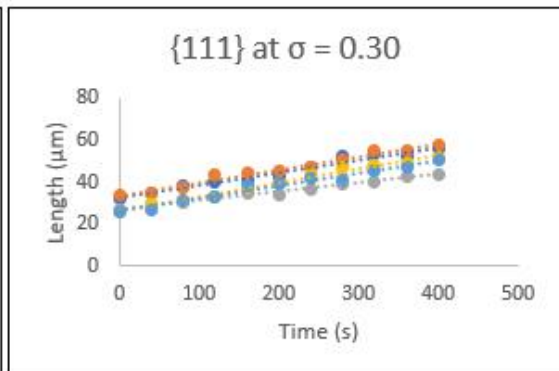
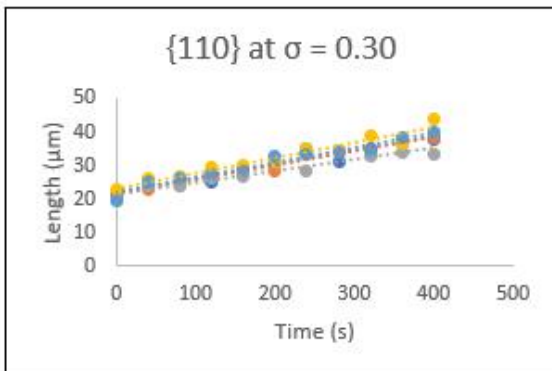
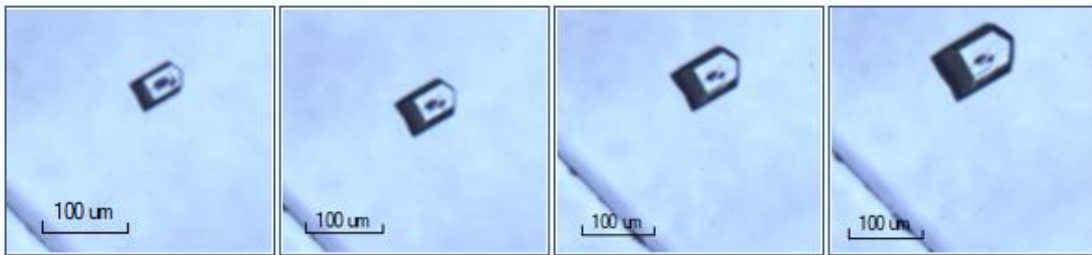
$\sigma = 0.20$



$\sigma = 0.25$



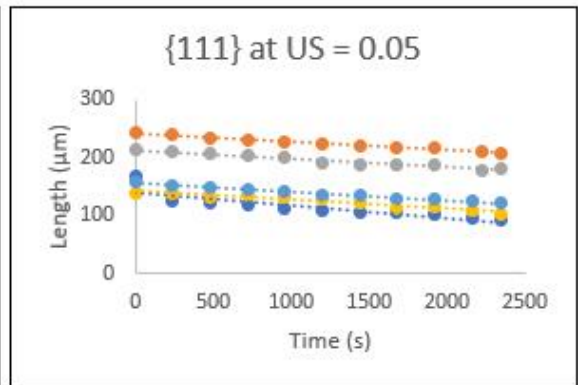
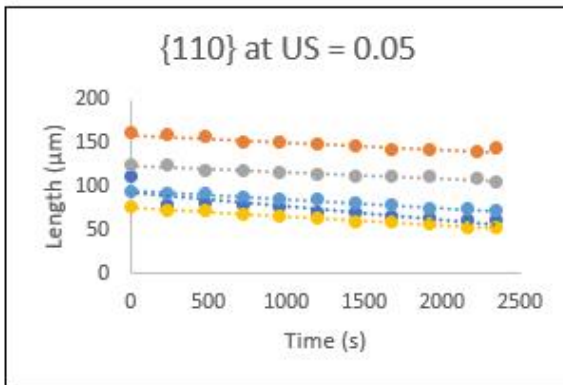
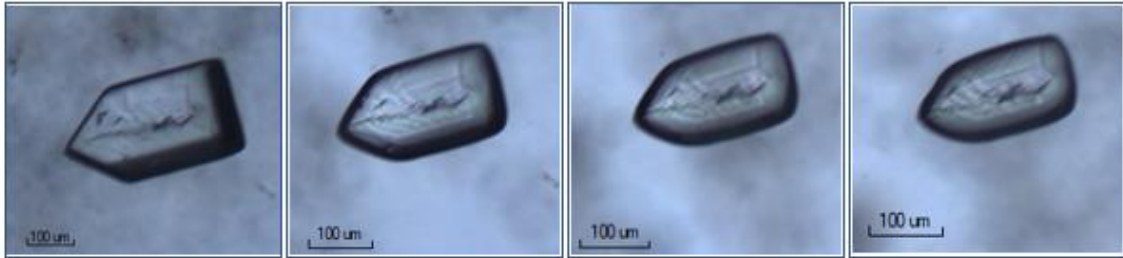
$\sigma = 0.30$



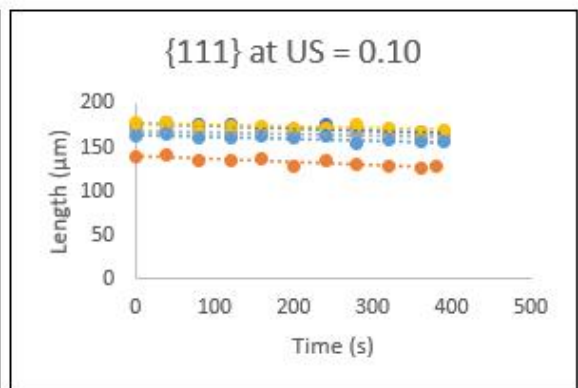
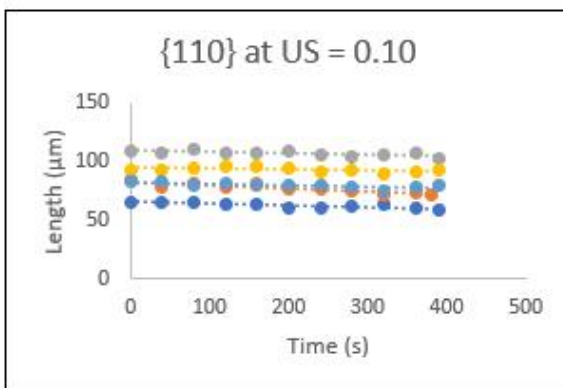
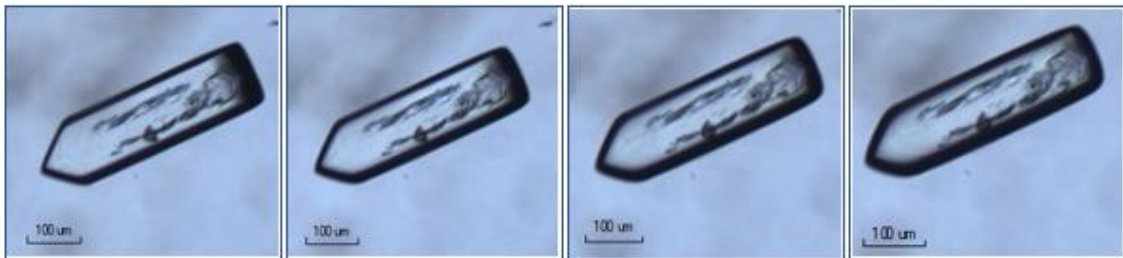
APPENDIX C: CRYSTAL DISSOLUTION RATE MEASUREMENT

C1: UREA IN ETHANOL

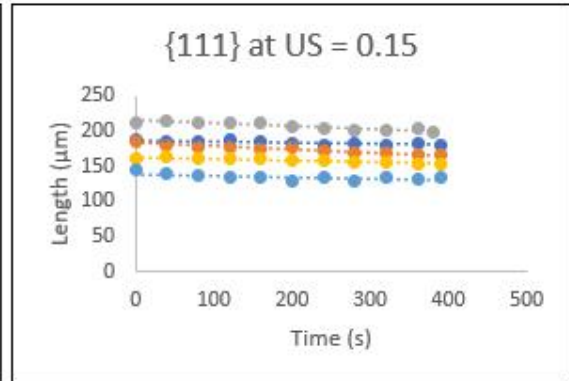
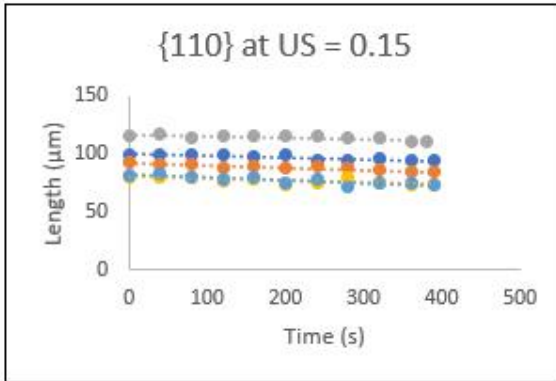
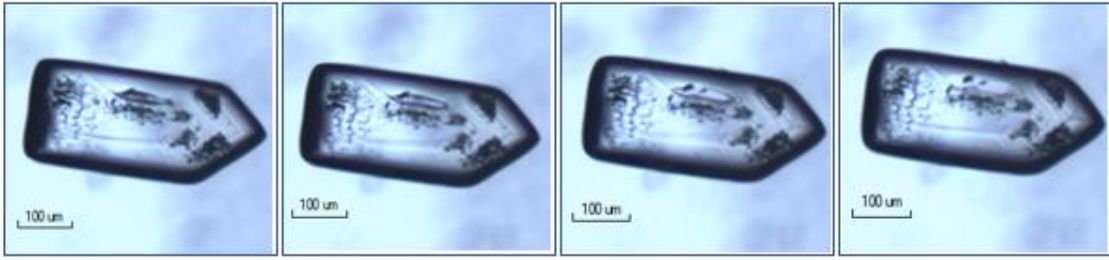
US = 0.05



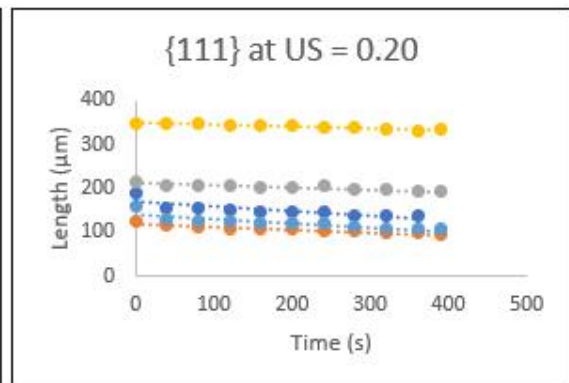
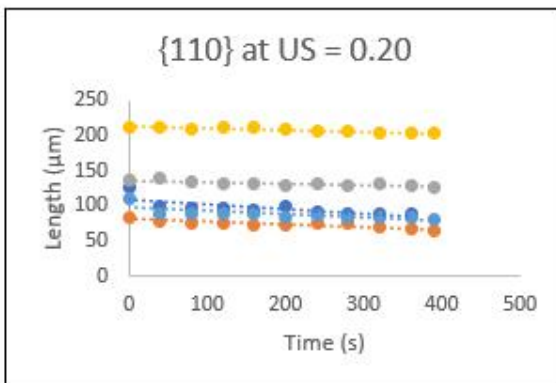
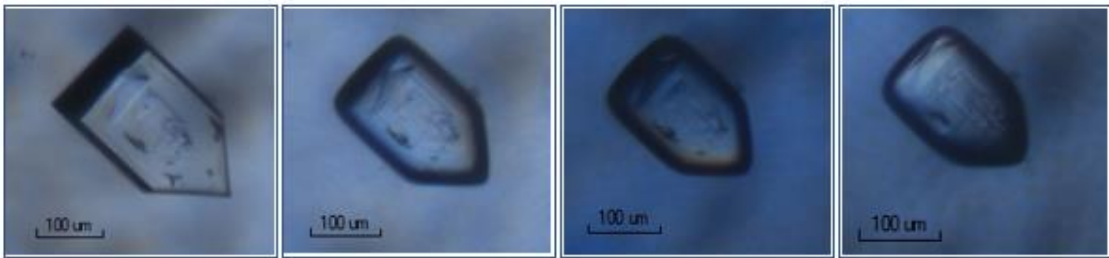
US = 0.10



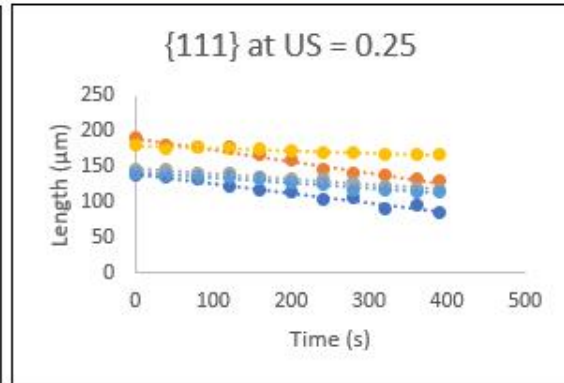
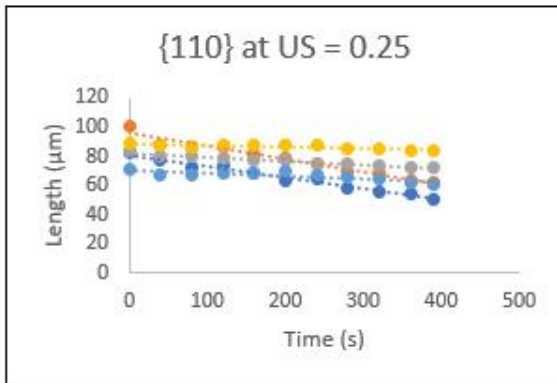
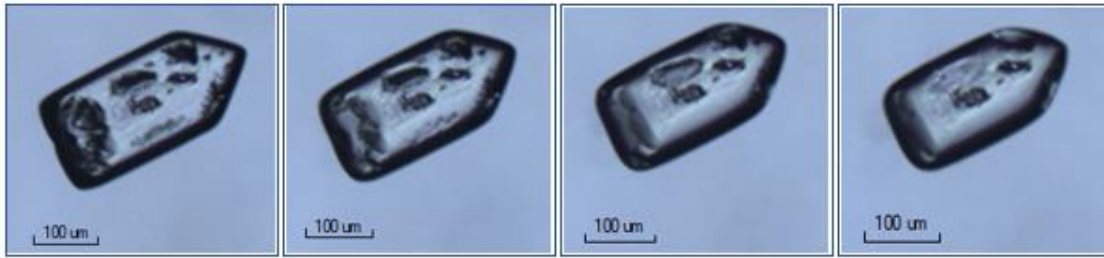
US = 0.15



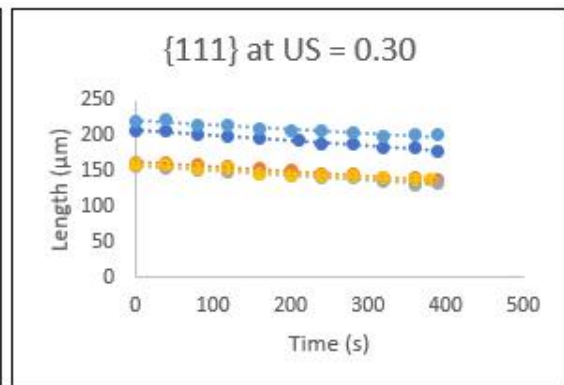
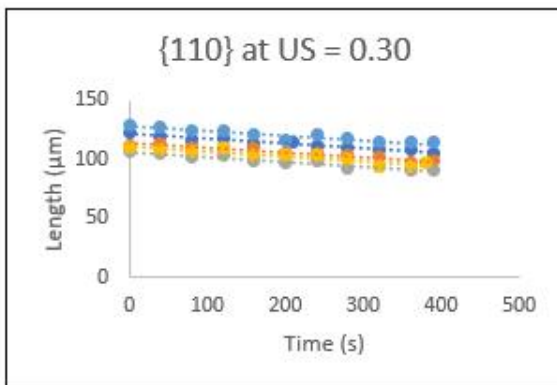
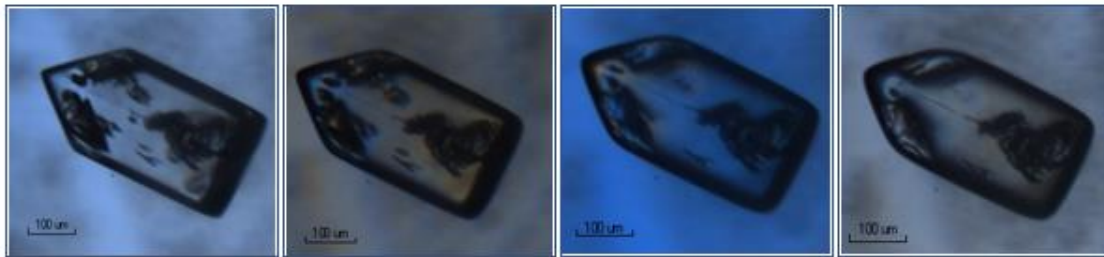
US = 0.20



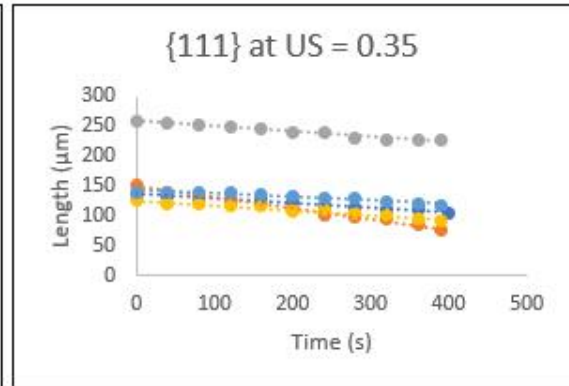
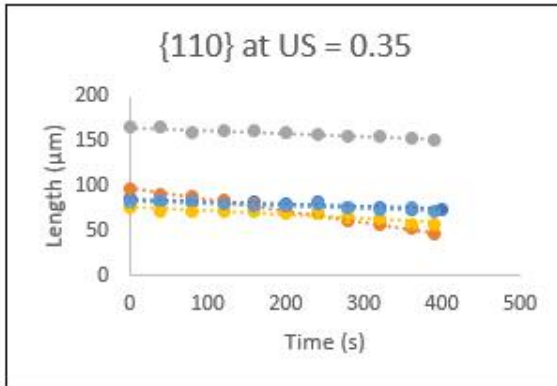
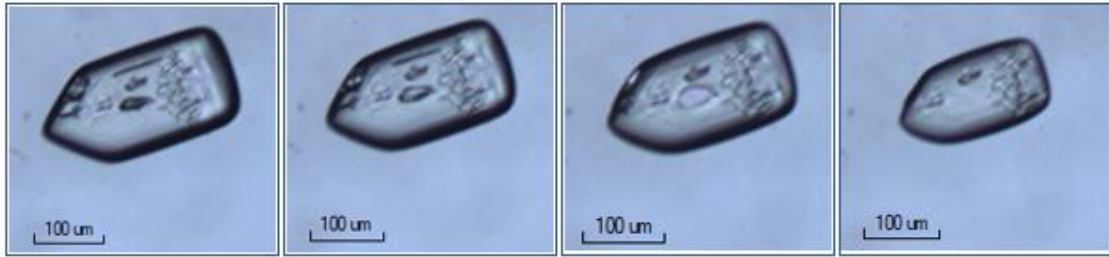
US = 0.25



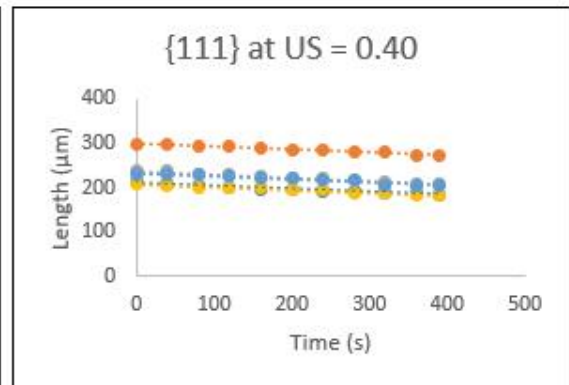
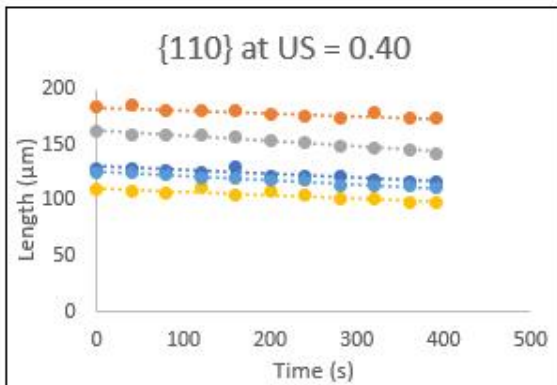
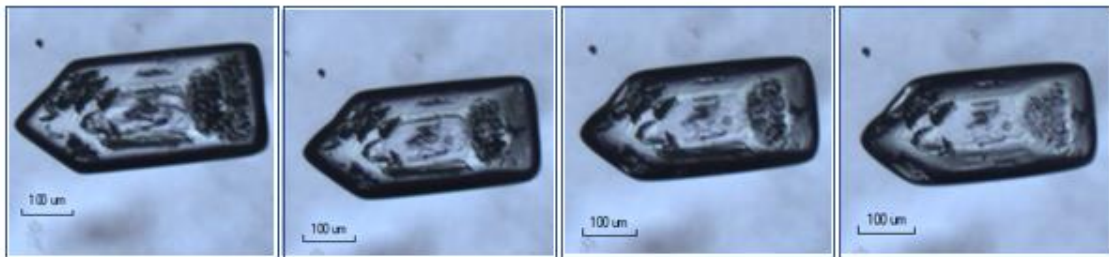
US = 0.30



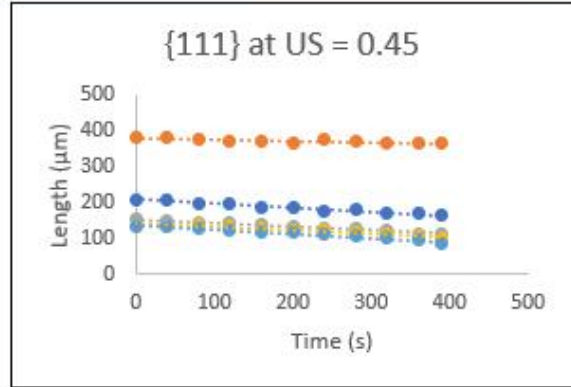
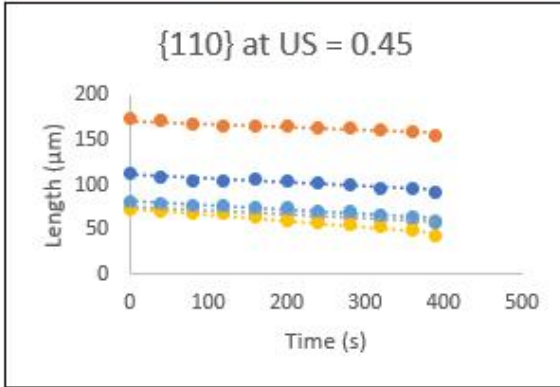
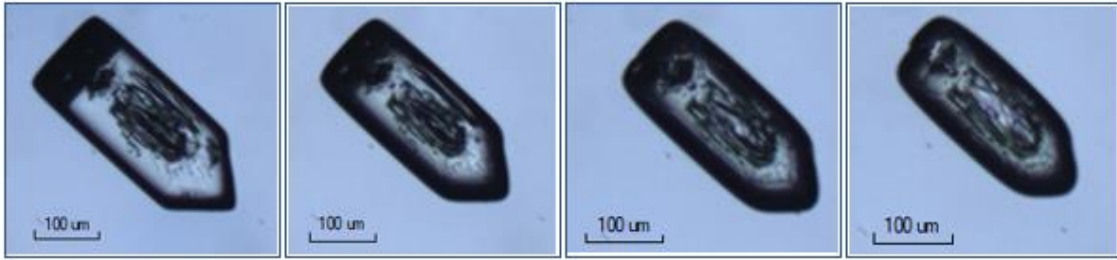
US = 0.35



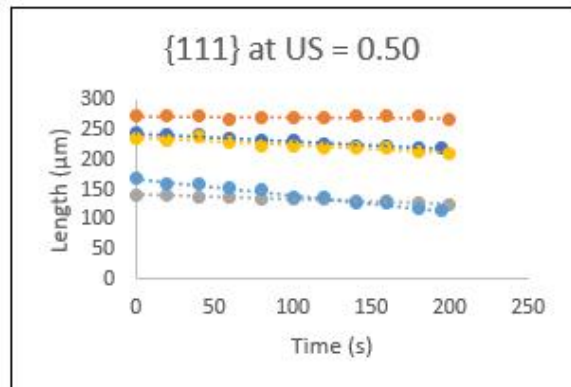
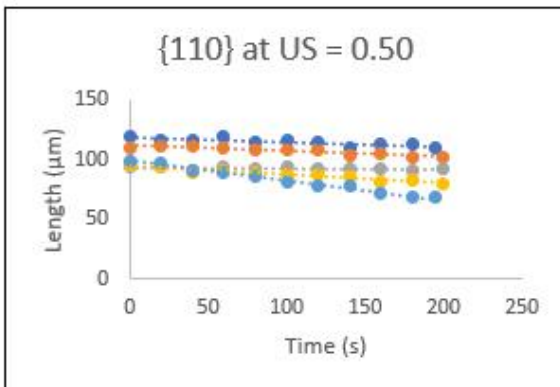
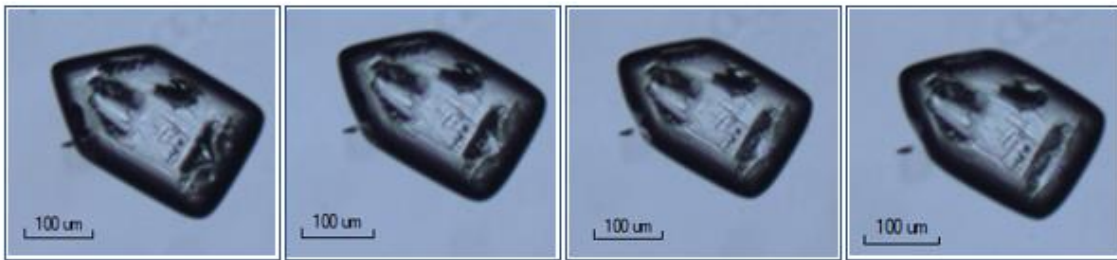
US = 0.40



US = 0.45

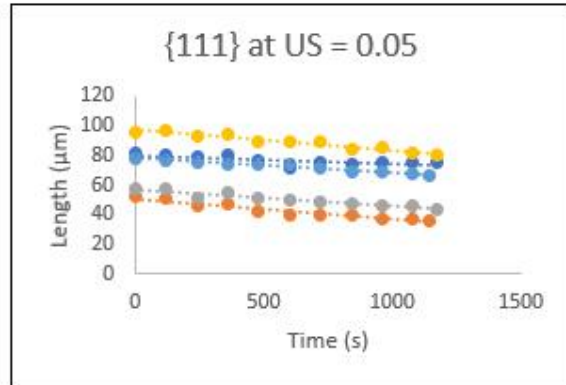
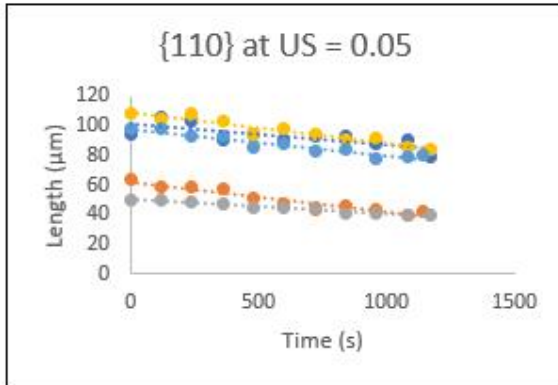
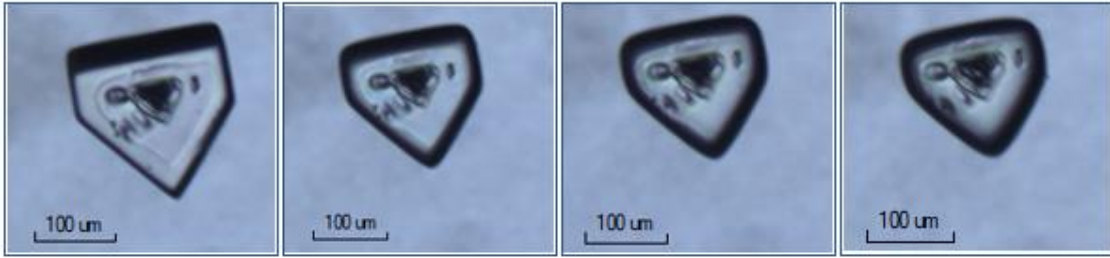


US = 0.50

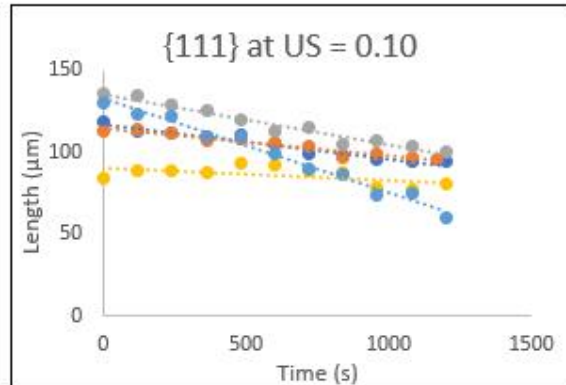
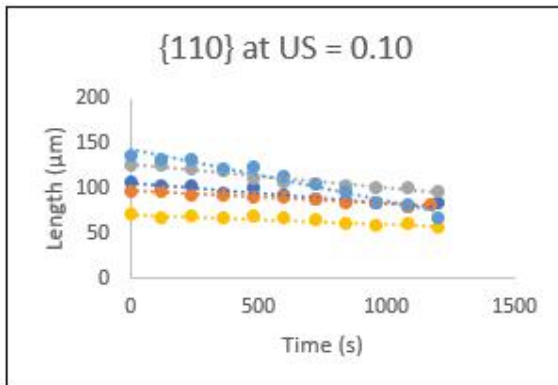
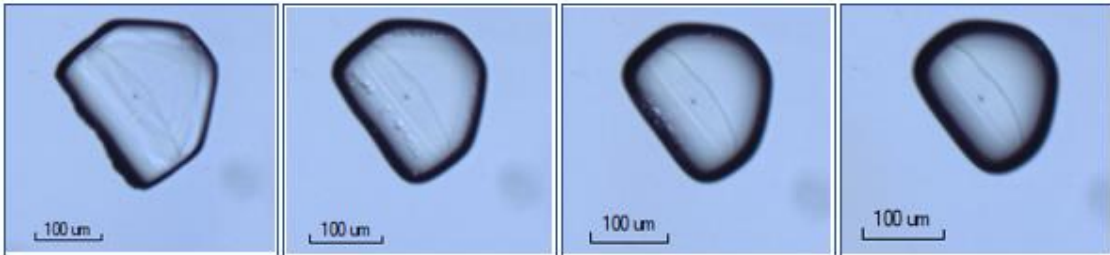


C2: UREA IN ACETONITRILE

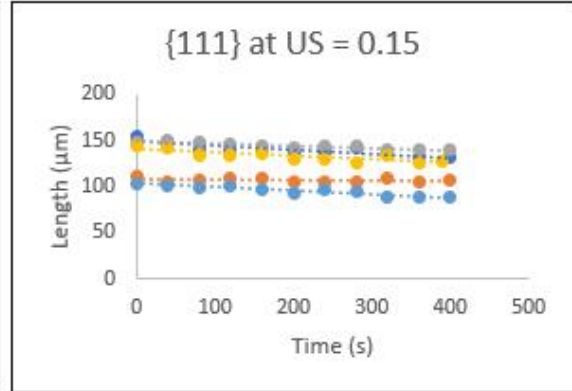
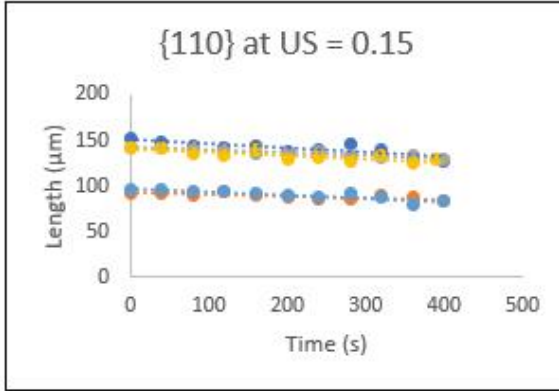
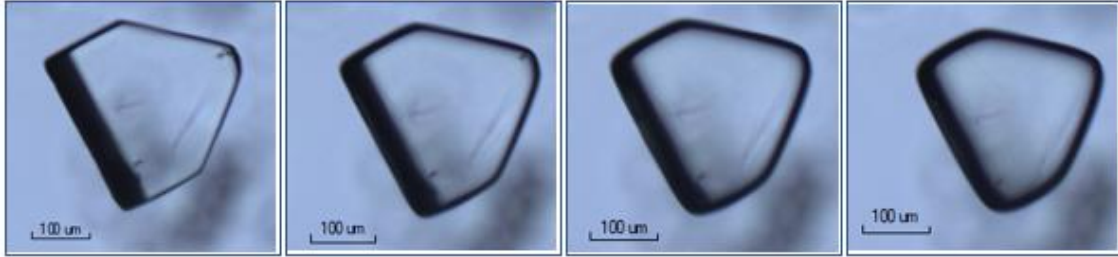
US = 0.05



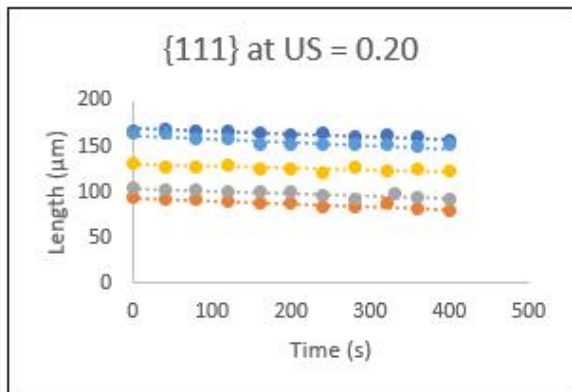
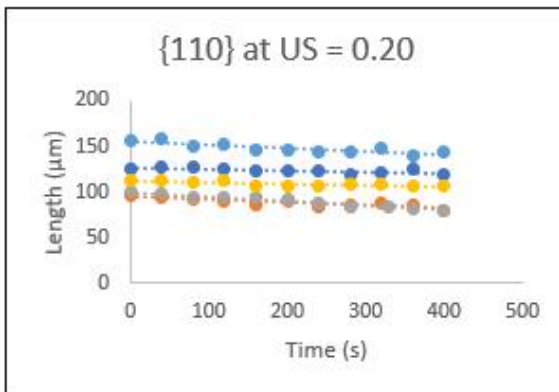
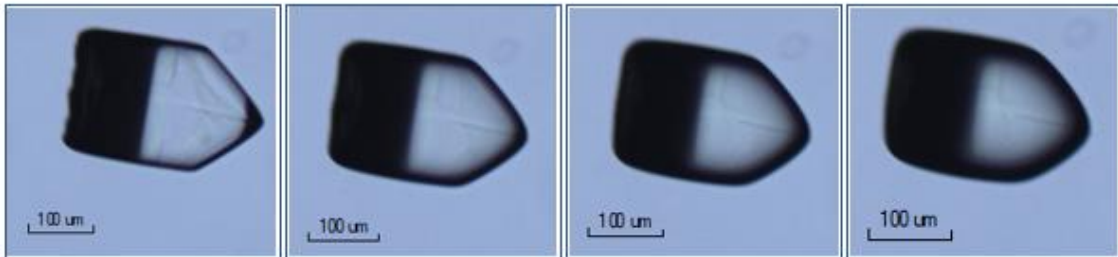
US = 0.10



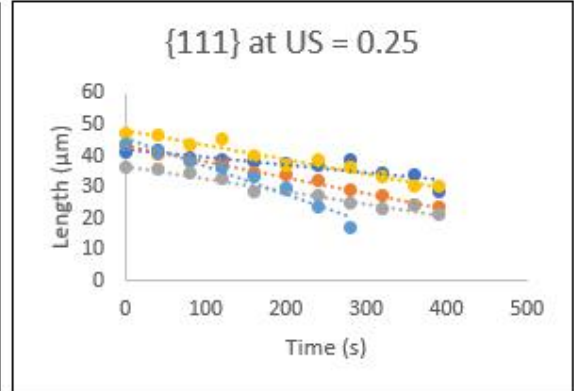
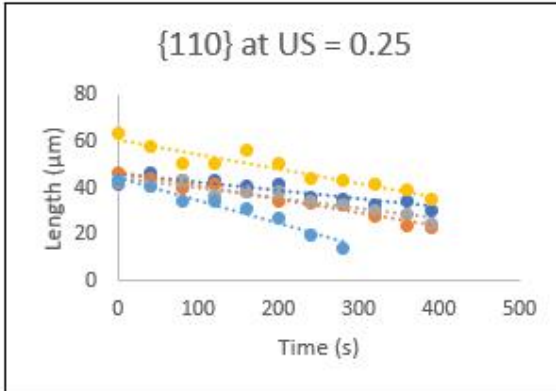
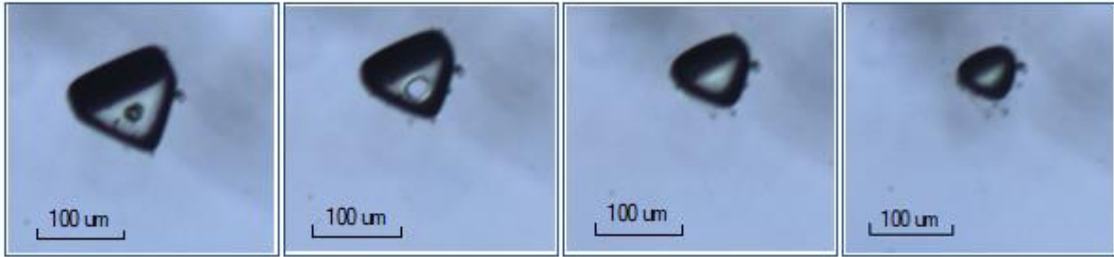
US = 0.15



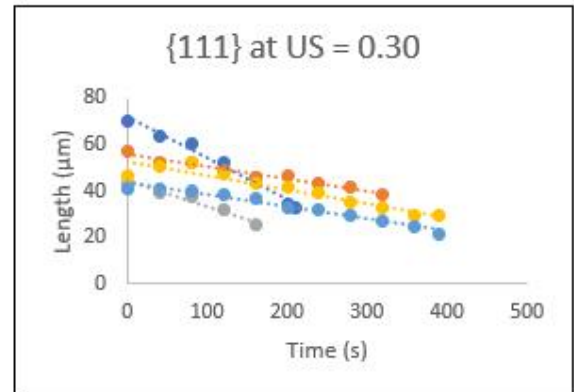
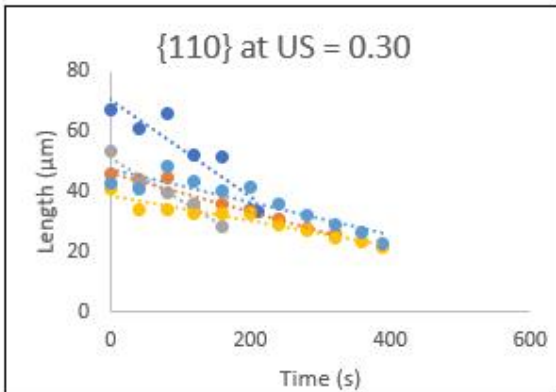
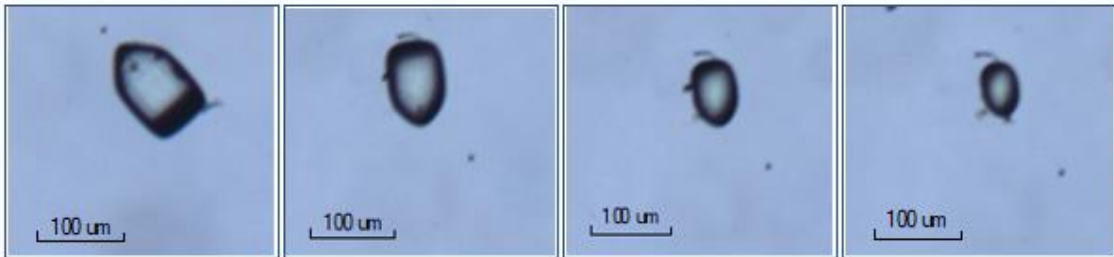
US = 0.20



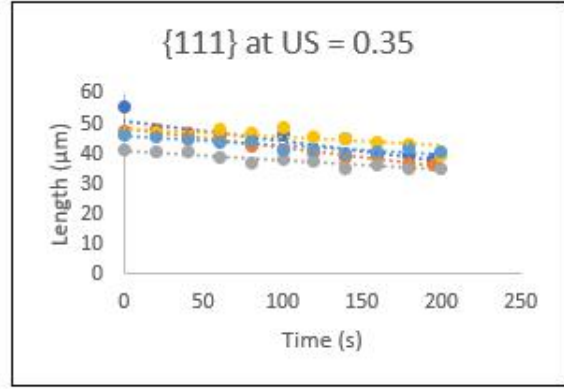
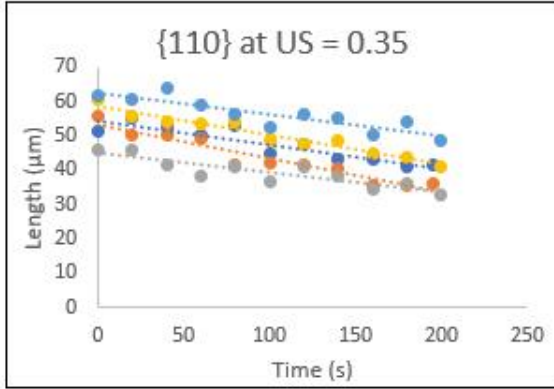
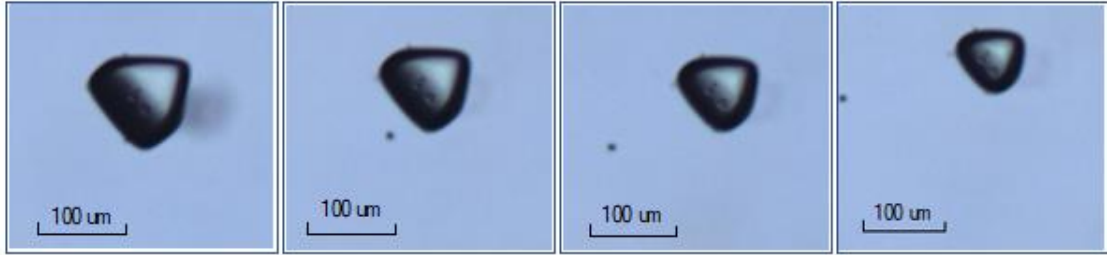
US = 0.25



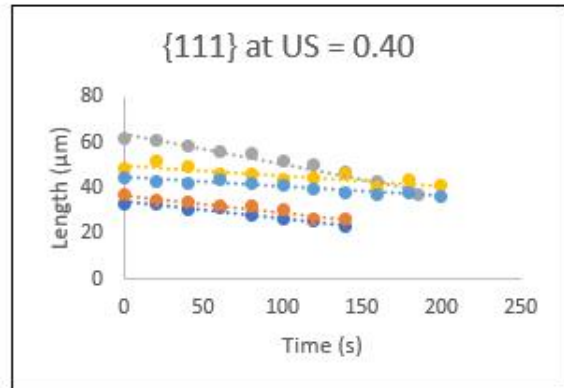
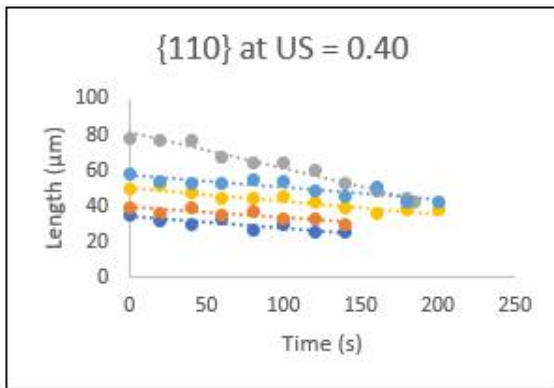
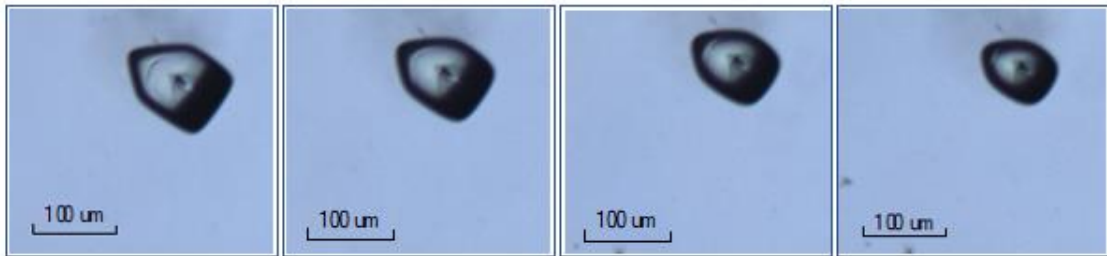
US = 0.30



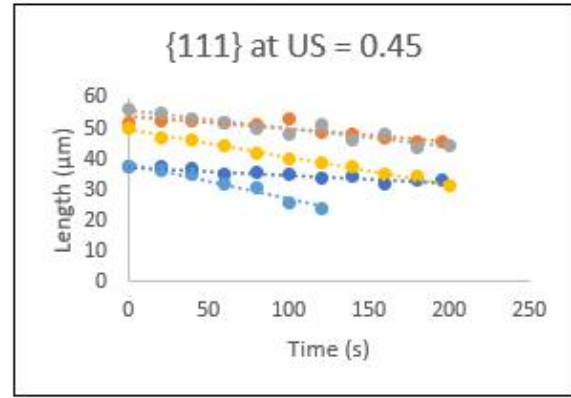
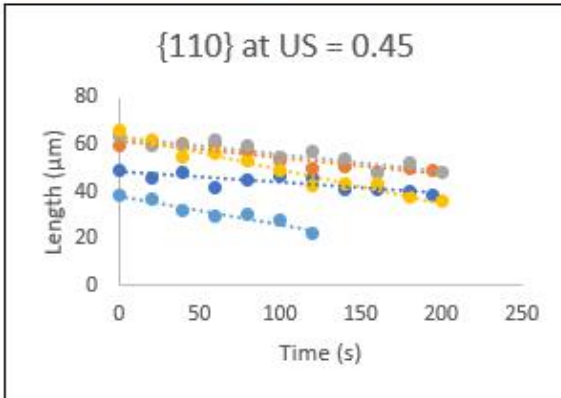
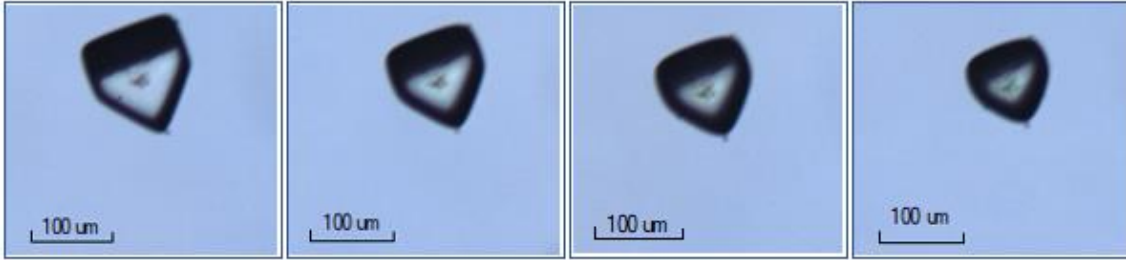
US = 0.35



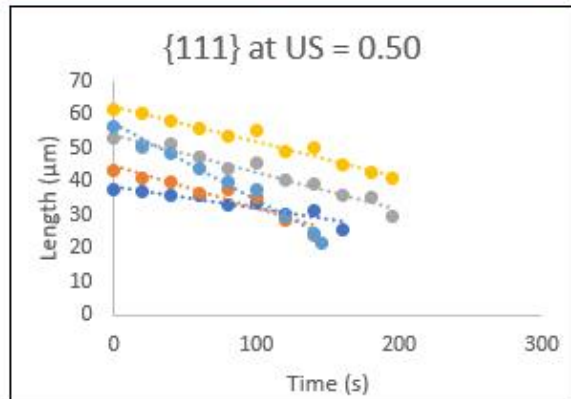
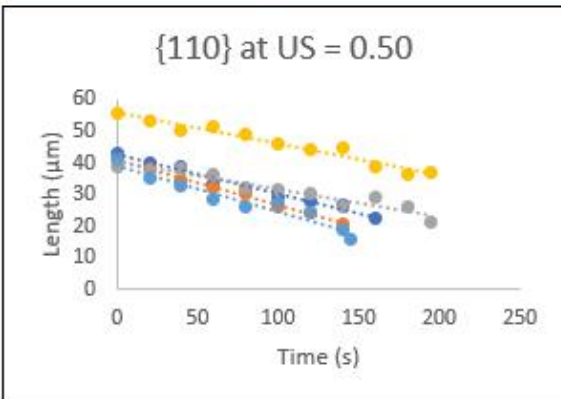
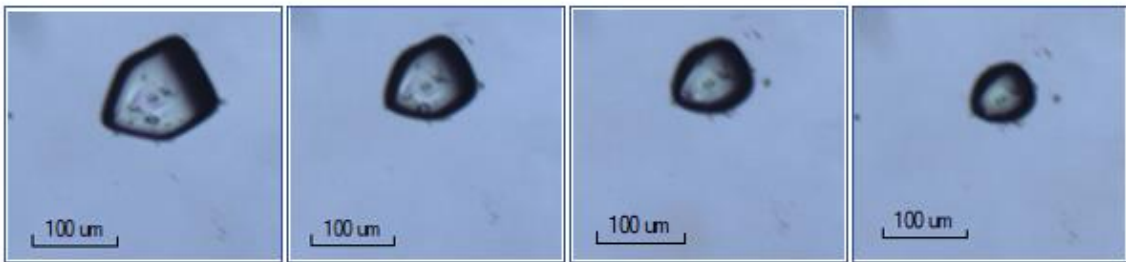
US = 0.40



US = 0.45

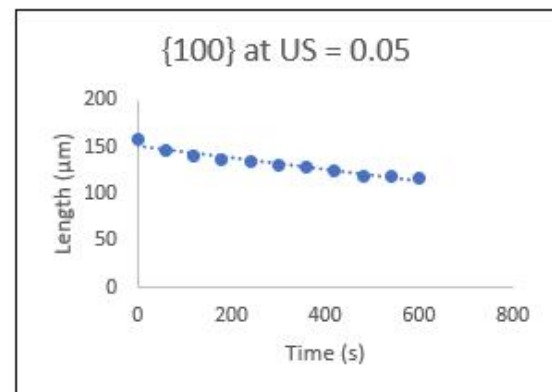
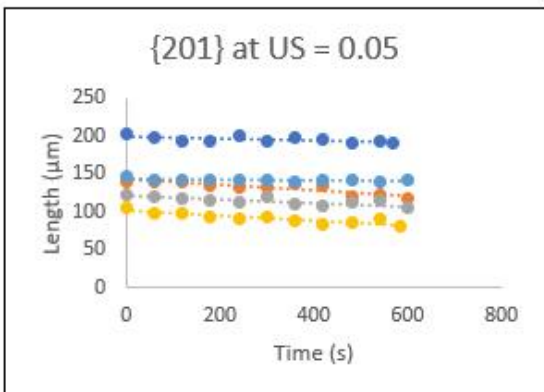
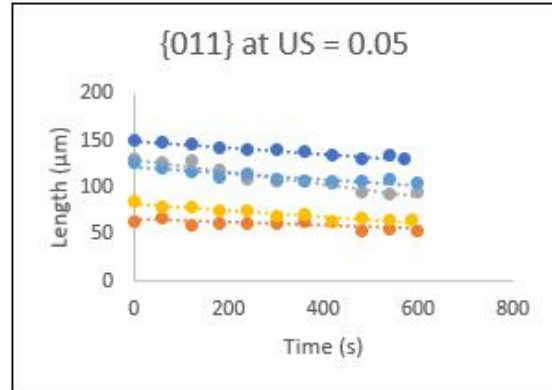
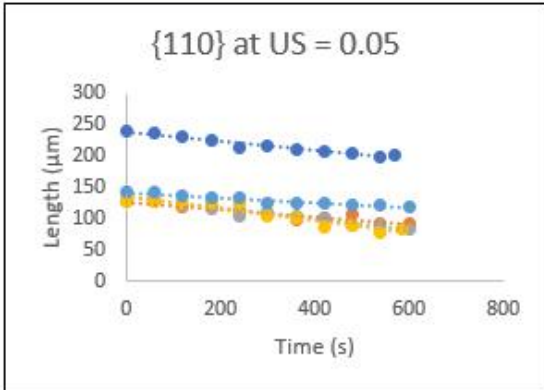
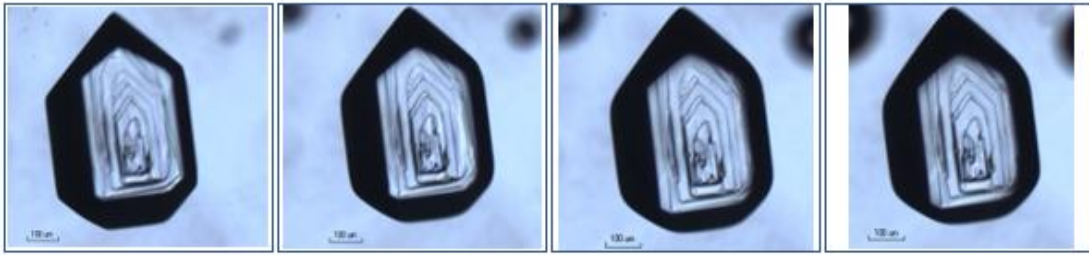


US = 0.50

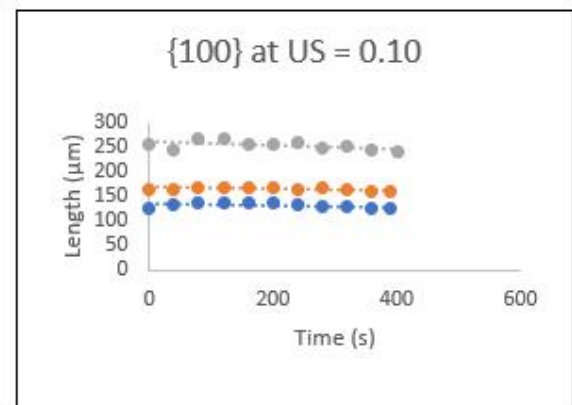
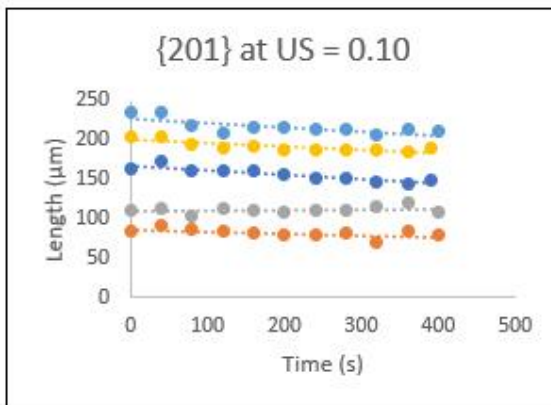
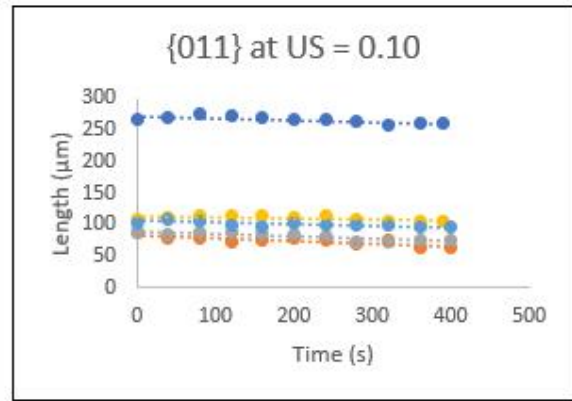
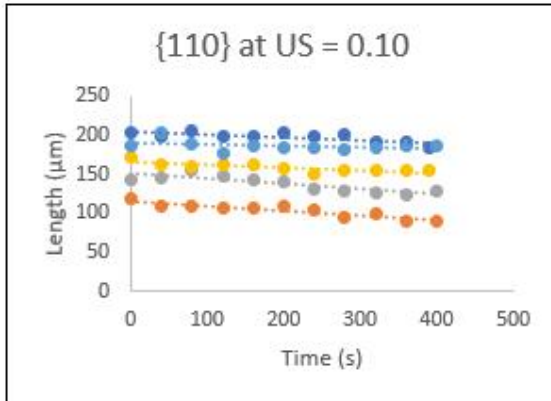
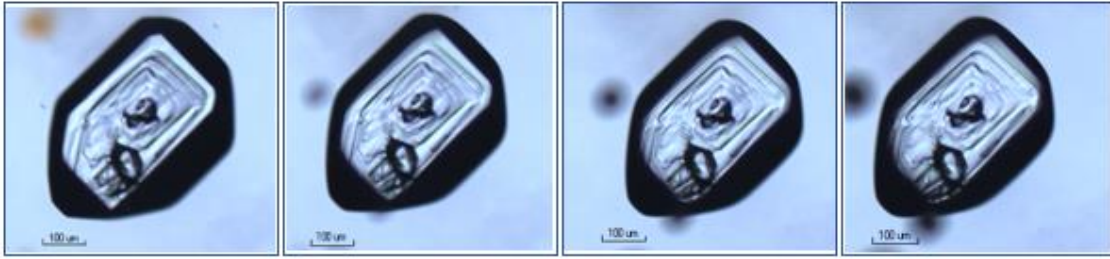


C3: PARACETAMOL IN ACETONITRILE

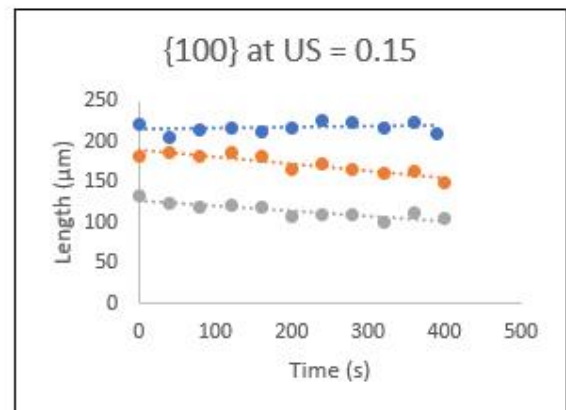
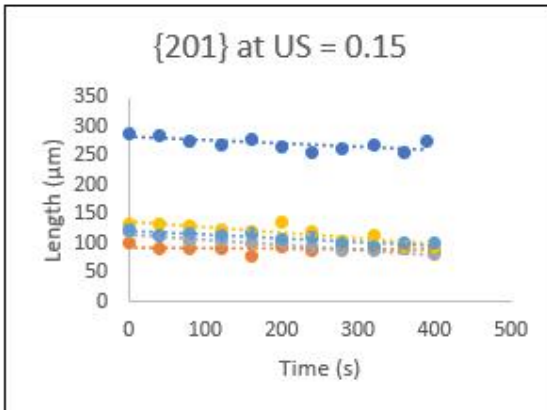
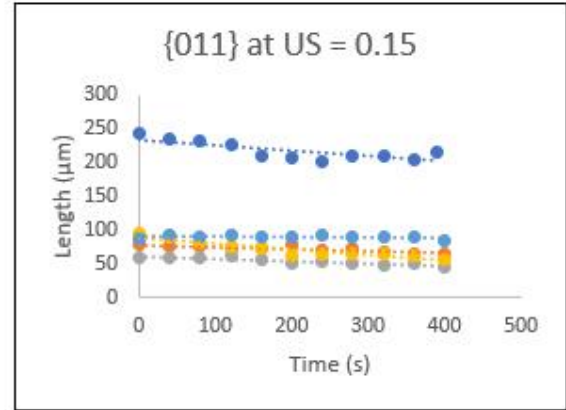
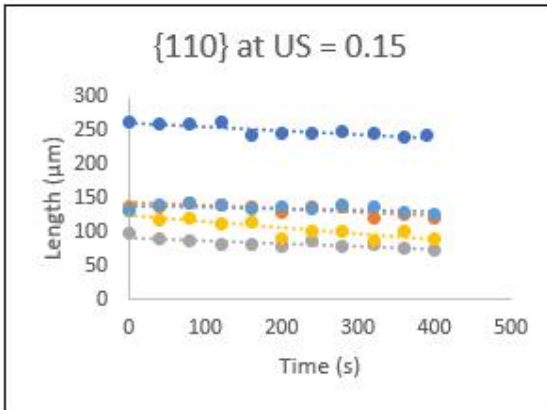
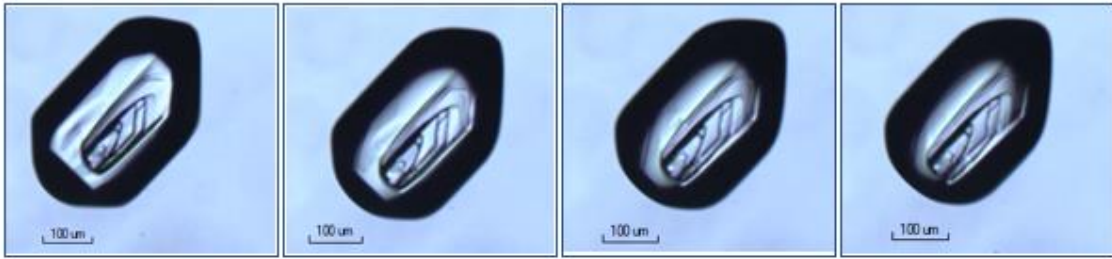
US = 0.05



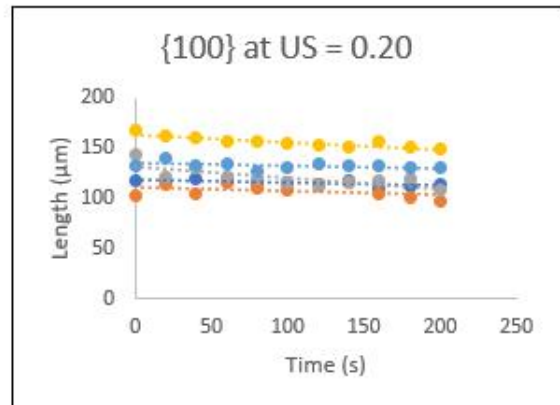
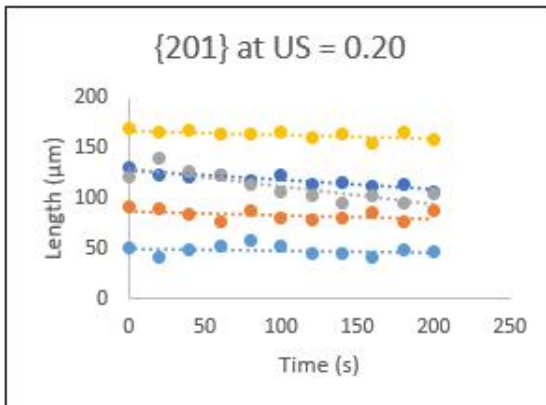
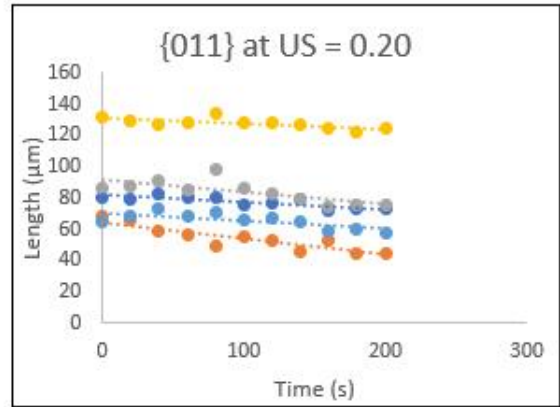
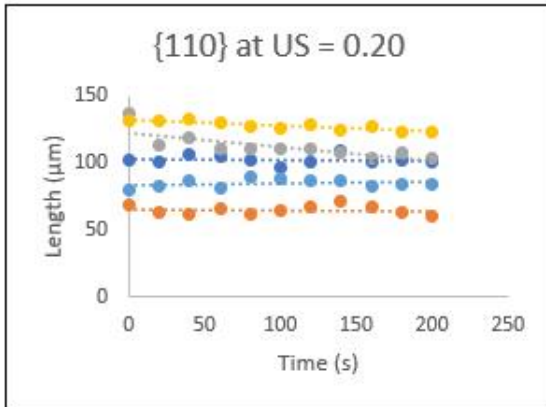
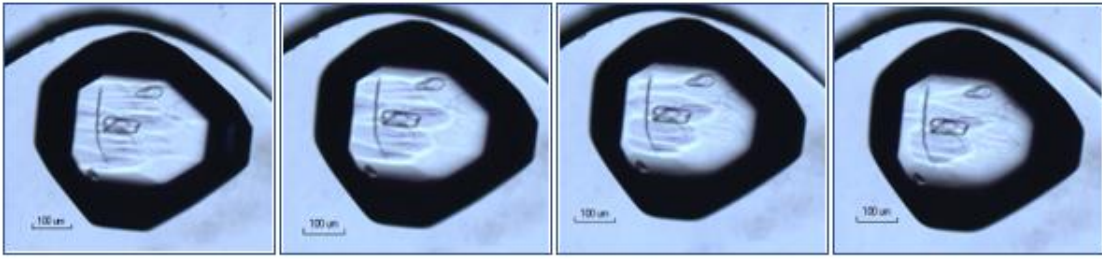
US = 0.10



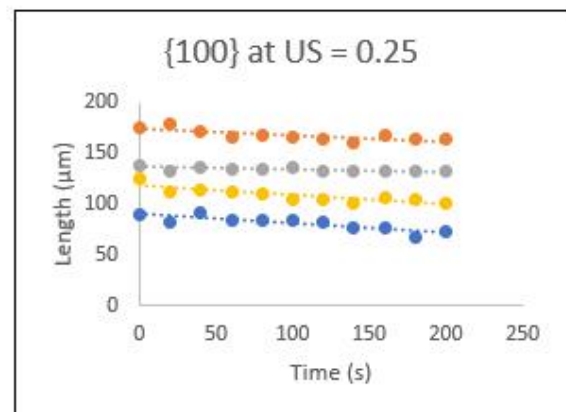
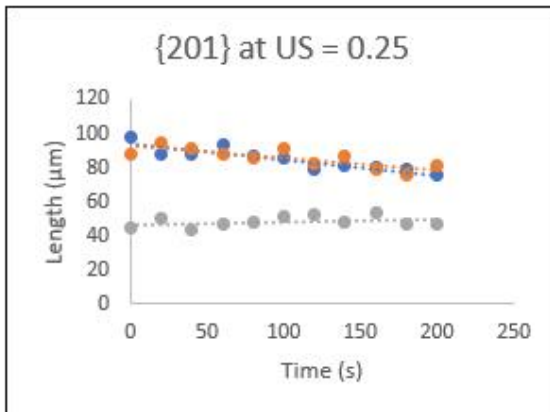
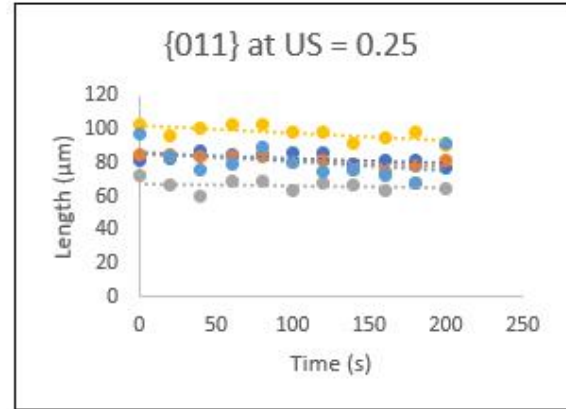
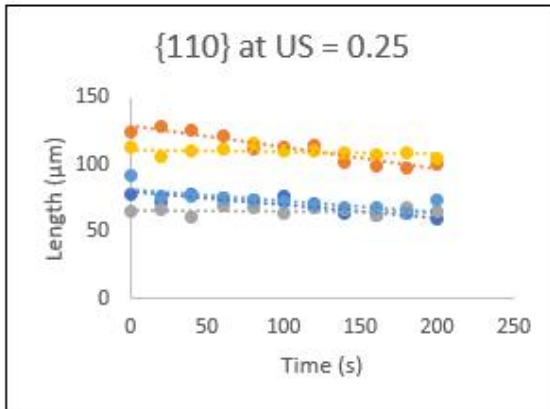
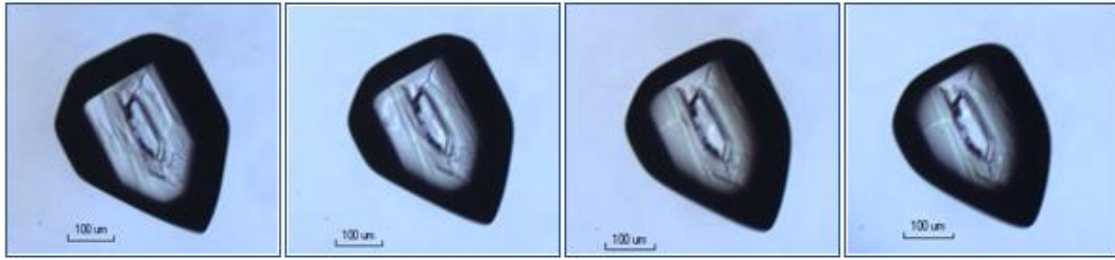
US = 0.15



US = 0.20

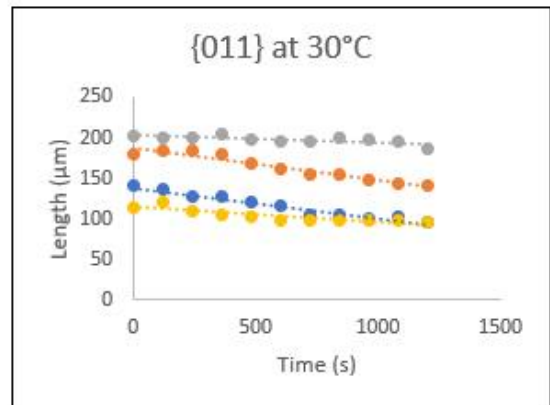
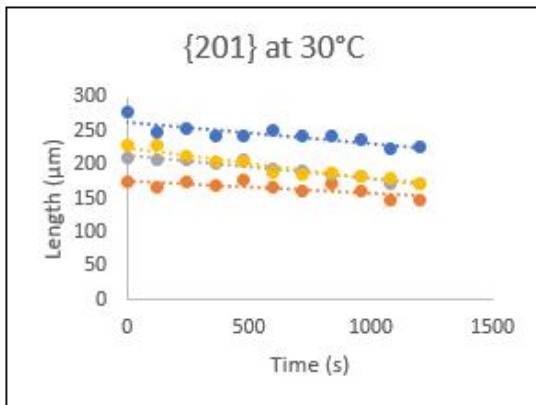
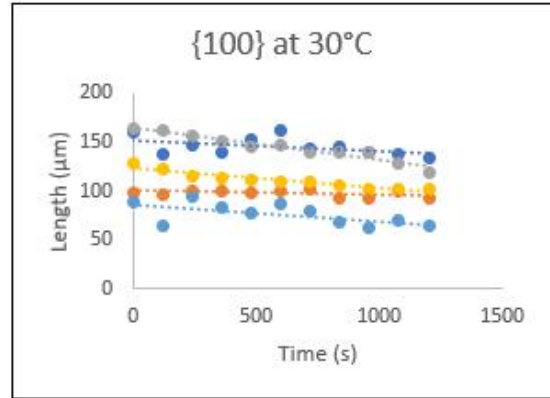
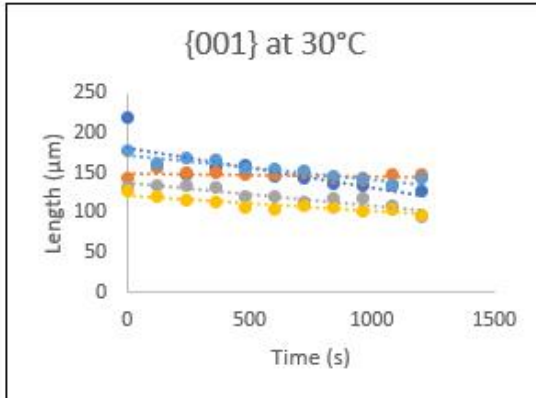
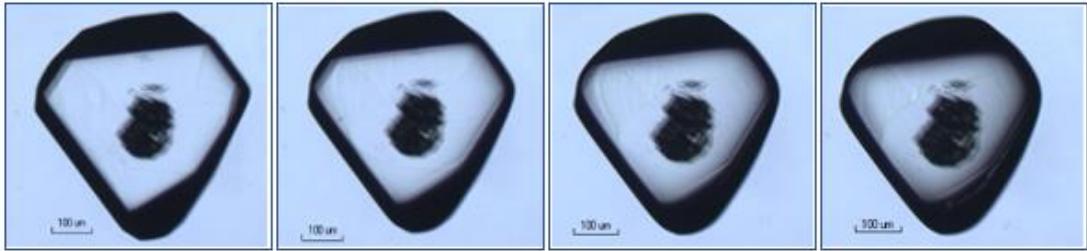


US = 0.25

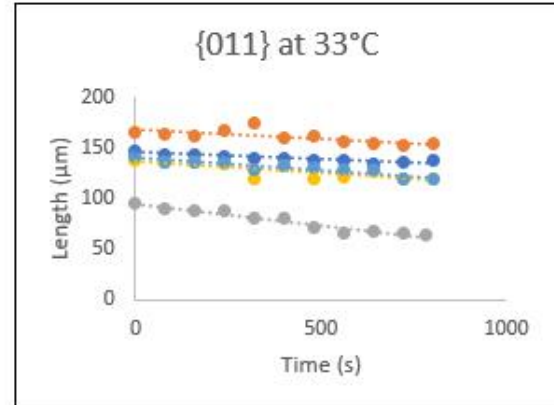
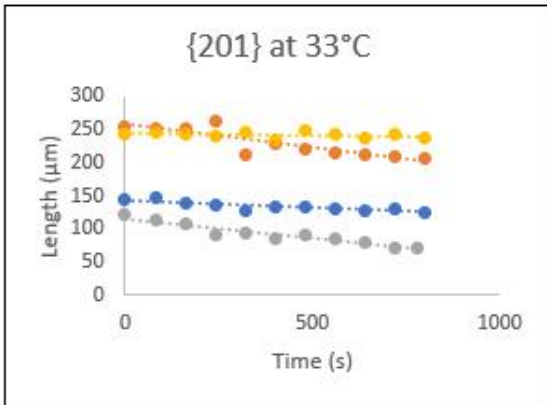
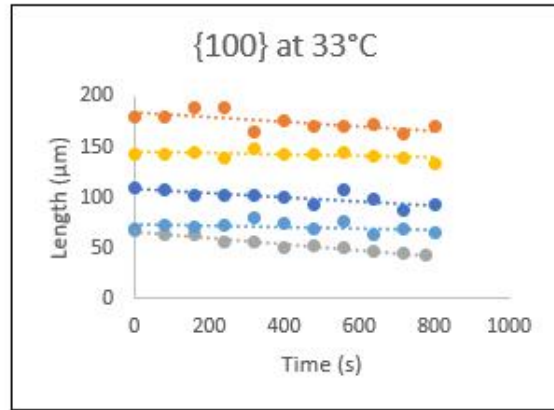
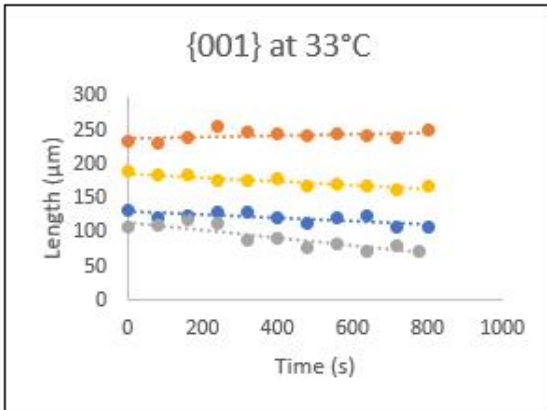
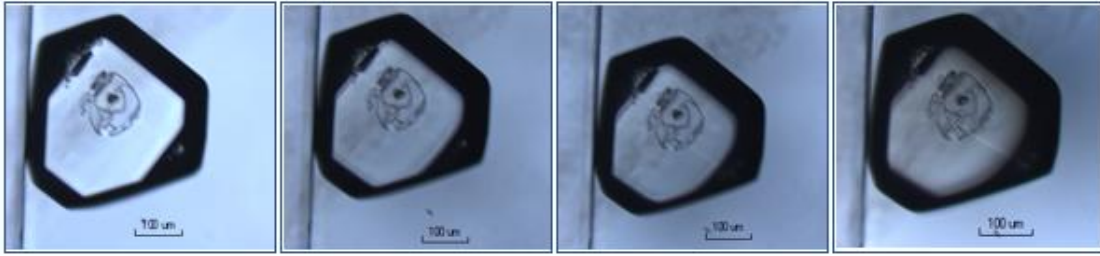


C4: PARACETAMOL IN FESSIF

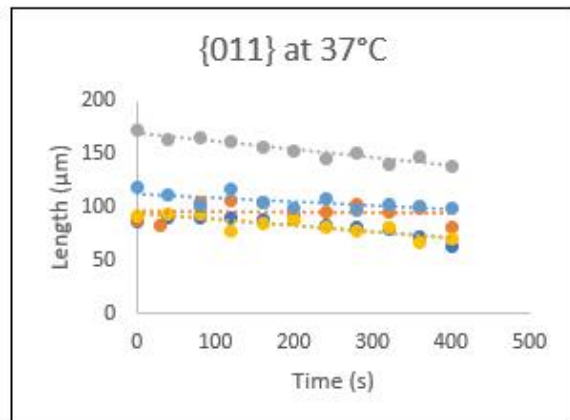
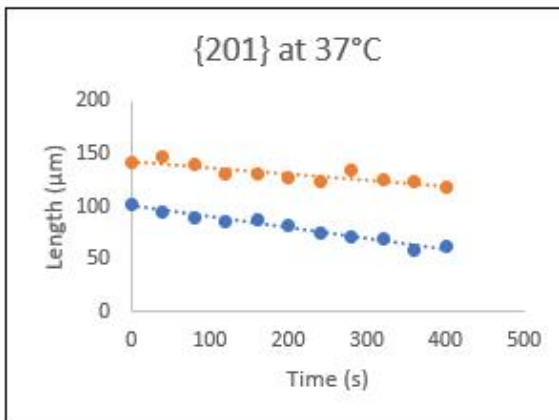
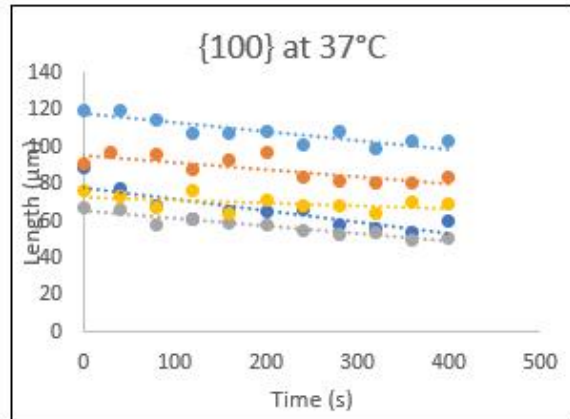
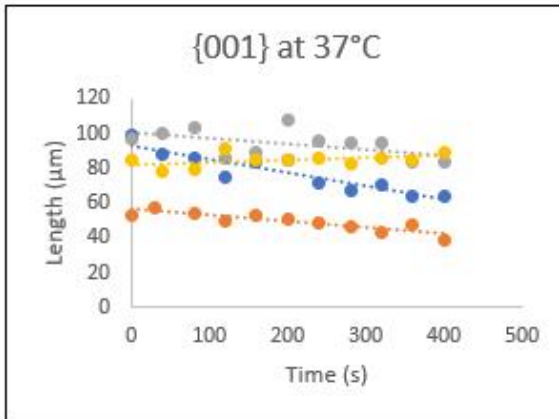
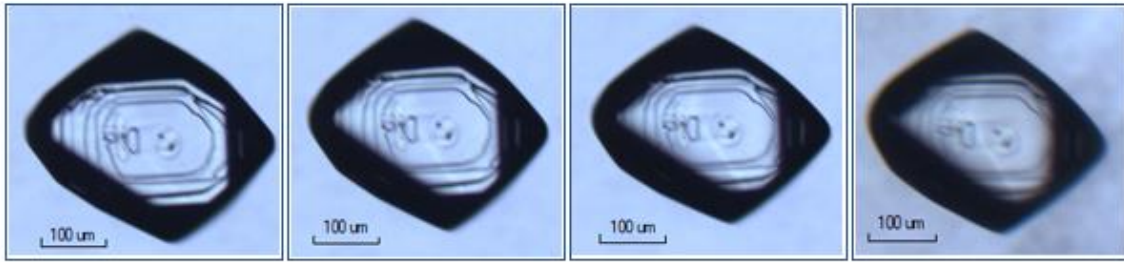
T = 30°C



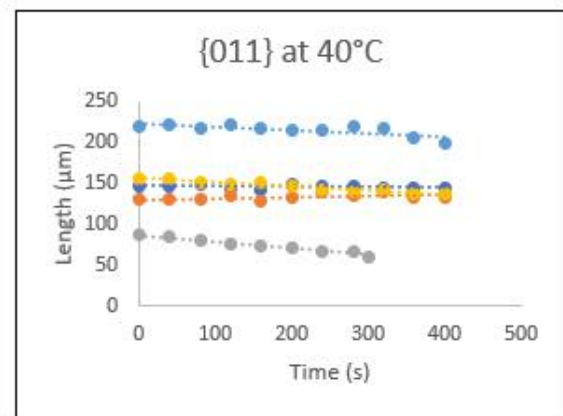
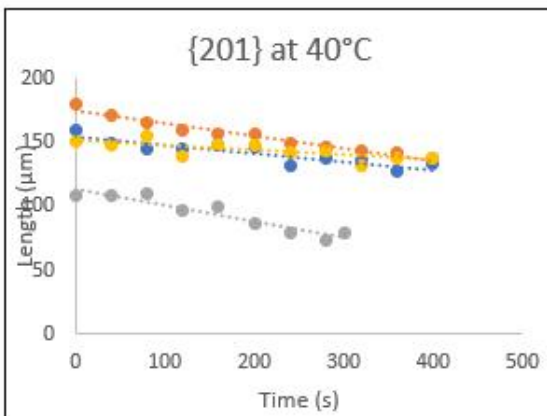
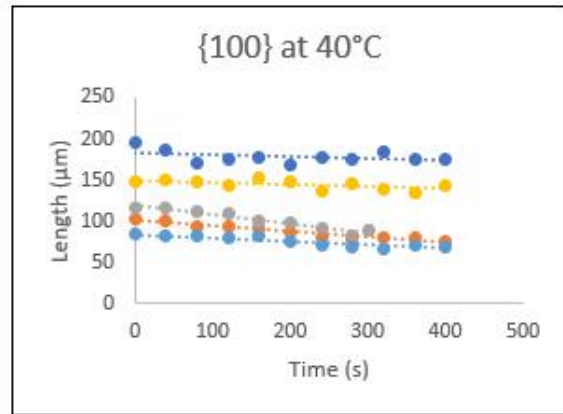
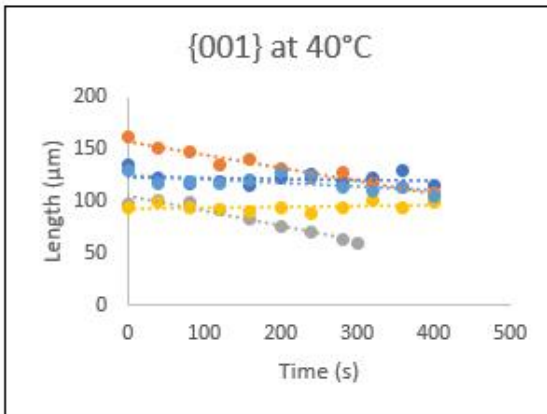
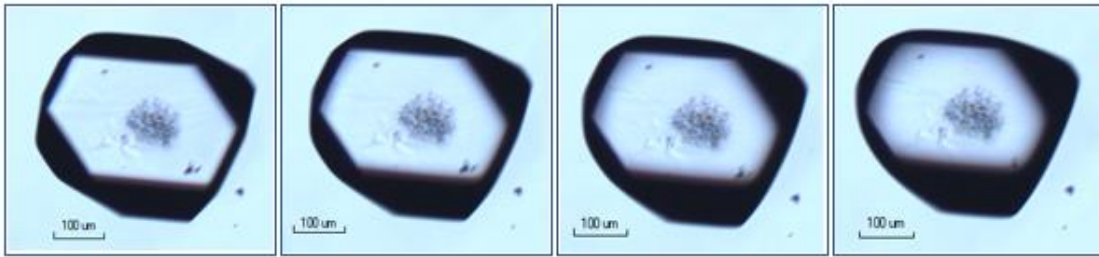
T = 33°C



T = 37°C



T = 40°C



APPENDIX D: CONFERENCE POSTERS

D1: THE INFLUENCE OF SOLUTION ENVIRONMENT ON THE NUCLEATION KINETICS AND GROWTH MECHANISM OF UREA

THE INFLUENCE OF SOLUTION ENVIRONMENT ON THE NUCLEATION KINETICS AND GROWTH MECHANISM OF UREA

AATIKA RIZVI¹, TOSHIKO IZUMI², KEVIN J. ROBERTS³

¹School of Engineering, Newcastle University, Newcastle Upon Tyne, NE1 7RU, UK
²Pfizer Global Research and Development, Ransgate Road, Sandvick, Kent, CT13 9NJ, UK
³Centre for the Digital Design of Drug Products, School of Process and Chemical Engineering, University of Leeds, Leeds, LS2 9JT, UK

INTRODUCTION

Crystallisation is an important purification, separation and pre-formulation process. It is the primary method applied for the intermediate and final stage production of a wide range of materials. A detailed understanding of crystallisation phenomena is not only required to design chemical separation and purification processes, but also to prevent the appearance of undesired crystals. Therefore, the fundamental process of nucleation and growth, and their associated kinetics need to be understood and characterised.

Supersaturation

• Fundamental driving force for crystallisation is the difference in chemical potential between crystallising substance and solution - more commonly used is concentration driving force.

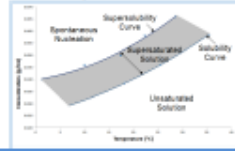
$$\Delta C = c - c^* = \frac{c - c^*}{c^*} \times 100\%$$

c : actual concentration; c^* : equilibrium saturation; ΔC : relative supersaturation

Metastable Zone Width (MSZW)

• MSZW indicates stability of solution - the larger the MSZW the more stable the solution. It is the preferred region in which to carry out controlled crystallisation processes through adjustment of system parameters.

- Three well-defined regions associated with solution crystallisation.
 1. Stable, undersaturated zone where crystallisation is impossible.
 2. Metastable zone between solubility and supersolubility curves, where crystallisation is improbable, although growth would occur if seeds were planted.
 3. Beyond supersolubility curve, where the system is said to be labile, and where spontaneous nucleation can occur.
- An increase in concentration of urea reduced the MSZW, resulting in a less stable solution, therefore spontaneous nucleation was more likely to occur.
- The addition of bulet resulted in an increase in the MSZW at lower concentrations - resulting in a more stable solution, therefore a greater degree of control and a slower crystallisation process would be expected.
- As urea is highly soluble in ethanol, at higher concentrations supersaturation is induced rapidly.



MSZW (°C)	Urea	Concentration (g/mL)			
		0.040	0.046	0.050	0.055
	Urea	15.9	13.1	10.4	9.9
	Urea & Bulet	22.6	13.3	12.7	5.5

NUCLEATION

Supersaturation alone is not sufficient cause for a system to begin to crystallise. Before crystals can develop, nuclei must exist in solution that act as centres of crystallisation. Nucleation may occur spontaneously, or be induced artificially.

- Nucleation parameters can be obtained by observing the effect of cooling rate on the measured achievable undercooling (KBHR)².
- KBHR methodology also provides insight into nucleation mechanism by differentiating between instantaneous (IN) and progressive (PN) nucleation.
 - IN: nuclei formed simultaneously and solution contains fixed number of crystallites of the same size - assumption that they all grow at the same rate.
 - PN: nuclei formed over extended period of time - nucleation and growth occur simultaneously and solution contains crystals of various sizes at any given point in time.

$$\ln q = \ln q_0 + (n+1) \ln \mu_c$$

$$\ln q = \ln \left(\frac{k_c \Gamma_c}{(n+1) \rho_c \rho_s} \right) + (n+1) \ln \mu_c$$

$$\ln q = \ln(k_c) + n \ln(\mu_c) - \frac{\ln(\rho_c \rho_s)}{(n+1)}$$

n : dimensionless molecular latent heat of crystallisation; k_c : molecular latent heat of crystallisation; k : Boltzmann constant; T_c : solution equilibrium temperature; μ_c : cooling rate; ρ_c : relative critical undercooling; ρ_s : ρ_s : free parameters; n and n_0 growth exponents for the growth mechanism of the crystallites; ρ_c : dimensionality of crystal growth; ρ_s : overall growth rate of the crystal; k_c : crystallite growth shape factor; ω : relative volume of crystals at the detection point; k_v : nucleus shape factor; v_0 : volume occupied by solute molecule in crystal; k_n : nucleus effective interfacial tension; V : volume of solution; k_d : nucleation rate constant; ρ : nucleation rate; r^* : critical nucleus radius; i^* : number of molecules in critical nucleus

Conc (g/mL)	q	Progressive Nucleation			Conc (g/mL)	q	Instantaneous Nucleation		
		$\ln q$	$\ln \mu_c$	$\ln \mu_c^2$			$\ln q$	$\ln \mu_c$	$\ln \mu_c^2$
Urea	0.04	0.52	0.22	0.22	0.52	0.52	0.22	0.22	
	0.046	1.75	0.88	0.88	1.75	1.75	0.88	0.88	
	0.05	2.45	1.25	1.25	2.45	2.45	1.25	1.25	
Urea & Bulet	0.04	0.52	0.22	0.22	0.52	0.52	0.22	0.22	
	0.046	1.75	0.88	0.88	1.75	1.75	0.88	0.88	
	0.05	2.45	1.25	1.25	2.45	2.45	1.25	1.25	

- The inclusion of bulet within the solution did not change the nucleation mechanism.
- For progressive nucleation: an increase in concentration resulted in a lower interfacial tension (γ_{eff}), and an increase in cooling rate (q) resulted in a lower critical nucleus radius (r^*). Therefore, an increase in nucleation rate (J) was expected for both systems with and without bulet, and this was also determined through KBHR calculations.
- For instantaneous nucleation: $n=2$ is indicative of system where growth is rate limited by rearrangement of the solute at the crystal/solution interface.
- Adding bulet and increasing concentration resulted in $n=1$, which is indicative of a system where the growth of crystallites is rate limited only by mass transfer i.e. the diffusion of the growth unit to the growing crystallites.

CRYSTAL GROWTH WITH AND WITHOUT ADDITIVE

- As soon as stable nuclei formed, they grow into crystals of visible size. The mechanism of crystal growth is thought to greatly influence the growth rate of a surface.
- Kossel model envisages that the crystal surface is made up of steps of monatomic height - containing kinks, loosely adsorbed growth units and vacancies on the surface.
- Burton, Cabrera and Frank (BCF): Incorporation of growth units onto the stepped surface provided by dislocations, leading to the formation of a growth spiral over the crystal surface.
- Birth and Spread (BS&S): In the absence of steps, surface develop through nucleation and growth of a monolayer.
- Rough Interface Growth (RIG): growth interface undergoes surface roughening providing abundant sites for surface integration with a large number of step and kink sites.
- Surface entropic α -factor can be used to predict how rough a surface may be.^{4,5}

Measured growth rates are influenced not only by the incorporation of growth units into the crystal surface, but also by the diffusion of growth units within the bulk of solution. As both effects take place consecutively, a rate limiting step for the growth of the crystal can be determined through the use of a growth model which combines the two effects acting in series.⁶

$$G = \frac{1}{\frac{1}{k'v} + \frac{1}{k''v} \tanh(A_0/a)}$$

G : growth rate; $k'v$: related to the coefficient of mass transfer; $k''v$: resistance to the diffusion of growth units in the bulk solution; k''_0 : growth rate constant; k''_0/a : k''_0/a : resistance to surface integration process; A_0 : thermodynamic parameter

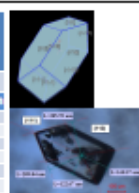
h	Urea		Urea & Bulet	
	$1/k'v$	$1/k''_0(a \tanh(A_0/a))$	$1/k'v$	$1/k''_0(a \tanh(A_0/a))$
(110)	0.04, 0.16, 0.19, 0.25, 0.32	2.74E+06	2.48E+06	4.11E+06
(111)	0.11, 0.16, 0.19, 0.25, 0.32	1.35E+06	2.82E+06	1.85E+06

$$E_{cr} = \frac{E_{int}}{RT} + E_{int}^*$$

E_{cr} : lattice energy; E_{int}^* : attachment energy; E_{int} : site energy; R : gas constant; T : absolute temperature; X_{int} : mole fraction of the solute as calculated for the supersaturation typically considered for crystal growth for a given solvent and temperature

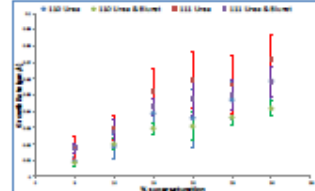
α -factor Range	Predicted Growth Mechanism
$\alpha < 2$	Rough interface, all growth units can be incorporated onto the growing surface (RIG)
$2 < \alpha < 5$	Interface is smoother, most probable mode of growth is B&S
$\alpha > 5$	Surface is very smooth, growth generally proceeds by screw dislocation (BCF)

h	α	Mechanism	h	α	Mechanism
(110)	5	BCF	(111)	5	BCF
	10	BCF		10	BCF
	15	BCF		15	BCF
	20	BCF		20	BCF
	25	BCF		25	BCF
	30	BCF		30	BCF



- Two morphologically important faces of urea were focussed on, (110) and (111) (shown in images above) and both faces were found to have α -factors greater than 5. Therefore, the growth mechanism at the levels of supersaturation studied was BCF.

- Resistance to the diffusion of growth units in the bulk solution ($1/k'v$) is greater than the resistance to the surface integration process ($1/k''_0(a \tanh(A_0/a))$) of the crystal for the (110) face, and this resistance is much greater with the addition of bulet.
- For the (111) face, the resistance to the surface integration process ($1/k''_0(a \tanh(A_0/a))$) of the crystal is the rate-limiting step, as it is much greater than the resistance to the diffusion of growth units in the bulk solution ($1/k'v$).



- Expectation would be that bulet has more of an effect on the growth rate of the (111) face, as it reduces the growth rate more than that of the (110) face. This was also observed experimentally as outlined in the figure above.

CONCLUSIONS

The addition of bulet did not affect the nucleation mechanism, however with increasing concentration, the rate limiting step changed from surface integration to mass transfer. The rate limiting step for the (110) face was found to be mass transfer, and for the (111) face was found to be interface kinetics. This did not change with the addition of bulet.

Acknowledgments: The authors gratefully acknowledge Pfizer for the funding and technical support of this research, and the EPSRC for their support in research at Newcastle University (Grant Reference EP/I037620/1).

References

[1] H. Osawa, 2011. Process Understanding: For Scale-Up and Manufacture of Active Ingredients. John Wiley and Sons.
 [2] D. M. C. Corzo, A. Borlaive, R. B. Hammond, D. Kashchav, K. J. Roberts, K. Lewtas, I. Mow. *CrystEngComm* 2014, 16, 974.
 [3] A. J. Blackie, M. T. Williams. 2011. *Pharmaceutical Process Development: Current Chemical and Engineering Challenges*.
 [4] T. T. H. Nguyen, I. Rowbottom, I. Marziano, R. B. Hammond, K. J. Roberts. *Cryst. Growth. Des.* 2017, 17 (8), pp 3088-3099.
 [5] S. N.A. Yusef. Characterisation of the Morphological and Surface Properties of Organic Micro-Crystalline Particles. Doctor of Philosophy (Chemical Engineering), Dec 2014, University of Leeds.
 [6] D. M. Camacho, K. J. Roberts, F. Muller, D. Thomas, I. Mow, K. Lewtas. *Cryst. Growth. Des.* 2017, 17, 563-575.



D2: THE INFLUENCE OF SOLUTION ENVIRONMENT ON FACE-SPECIFIC RETREAT RATES THAT ARE ASSOCIATED WITH THE DISSOLUTION OF UREA SINGLE CRYSTALS

THE INFLUENCE OF SOLUTION ENVIRONMENT ON FACE-SPECIFIC RETREAT RATES THAT ARE ASSOCIATED WITH THE DISSOLUTION OF UREA SINGLE CRYSTALS

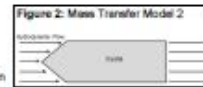
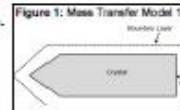
ASTIKA RIZUL¹, TOSHINO IZUMI², KEVIN J. ROBERTS³

¹ School of Engineering, Newcastle University, Newcastle Upon Tyne, NE1 7RU, UK
² Pfizer Global Research and Development, Ramsgate Road, Sandwich, Kent, CT13 9NJ, UK
³ Centre for the Digital Design of Drug Products, School of Process and Chemical Engineering, University of Leeds, Leeds, LS2 9JT, UK.

DISSOLUTION MODELS

Dissolution is defined as the release and diffusion of pharmaceutical molecules from the particle surface into the surrounding fluid medium¹. The dissolution rate of dosage form can strongly influence bioavailability, therefore there is significant interest in predicting, designing and controlling dissolution of pharmaceutical products during their development. Local concentrations of active pharmaceutical ingredients (API) in solution in the region of dissolving particles could get close to that of a saturated solution (non-sink conditions). The dissolution of particles in a solution environment which is close to that of the solubility limit of API would, in some cases, be expected to be relevant to overall bioperformance.

- APIs present in dosage forms are generally crystalline solids - crystals expected to be anisotropic.
- Anisotropic crystals have different functional chemistry's on the faces of the crystal, expectation would be that the faces would exhibit different wetting and dissolution properties.
- The shape of the crystal would influence the overall total surface area and hence, dissolution rate.
- Dissolution models are designed to predict bioperformance based on in-vitro information - a number of general assumptions are made:
 - All particles are spherical.
 - Surfaces of particles have a homogeneous dissolution rate.
 - Driving force for dissolution is directly proportional to the level of undersaturation (degree by which instantaneous concentration in solution is below saturation concentration).



Mass Transfer Models?

- Complexity of mass transfer arises from anisotropic surface properties - dissolution varies on face specific basis and characterisation is required of specific edges and vertices of each individual particle.
- Current dissolution models divided into 2 categories depending on how they incorporate mass transfer:
 - Models which envisage a boundary layer with a purely diffusion controlled rate-limiting process, operating across a boundary and into bulk solution (Figure 1).
 - Models which envisage surface renewal or disruption of solid-liquid interfaces due to hydrodynamic processes occurring in the solution (Figure 2).
- Due to conditions of single crystal experimental dissolution process, where dissolution occurs in a stagnant solution, mass transfer models of the first category have been focused on.
- Based on the governing assumptions of the models mentioned, the Noyes-Whitney/Herned-Strunger with the incorporation of Shape Factor, and the Hixson-Johnson models were considered to be most appropriate.

Noyes-Whitney/Herned-Strunger (NWS)

$$\frac{dM}{dt} = \frac{D \cdot A \cdot (C_s - C)}{h} \left(1 - \frac{C}{C_s} \right)$$

Accounting for factors upon which dissolution rate is dependent

1. Mass flux; D: diffusion coefficient; A: surface area; C: concentration difference over the diffusion layer of distance 'h'; C_s: saturation concentration; C: concentration of particles in bulk fluid; k: Boltzmann constant; μ: fluid viscosity; r_m: molecular radius of solute

Model	Year	Distinct Features / Governing Assumptions
Noyes-Whitney	1897	Overcomes the time dependency of surface area and determines that dissolution rate is governed by diffusional mass transfer
Herned-Strunger	1904	Introduces the dependence of the dissolution rate on the surface area and the presence of a stagnant boundary layer
Hixson-Crowell 1	1931	Considers sink conditions, the time dependency of surface area and the presence of agitation
Hixson-Crowell 2	1931	Considers non-sink conditions (concentration in solution is not constant), the time dependency of surface area and the presence of agitation
Higuchi-Hiesland	1963	Sink conditions, a spherical particle and boundary layer thickness is a function of the particle diameter
Nisbergall-Goyan	1963	Sink conditions, a spherical particle and boundary layer thickness is directly proportional to the square root of the diameter
Hixson-Johnson	1960	Non-sink conditions, spherical particle and boundary layer thickness is a function of the particle radius until a certain critical value
Shape Factor	1995	Accounts for the actual shape of a single crystal
Wang-Flanagan	1990	Considers the non-linearity of the concentration gradient of a spherical particle - boundary layer thickness independent of particle size
Fluid Dynamics	2008	Accounts for the fluid dynamics present in a flowagitated system - introduces fluid density, viscosity and velocity

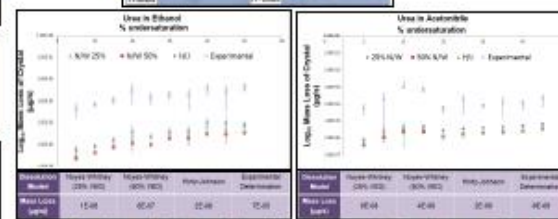
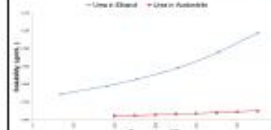
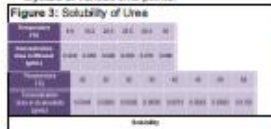
- Based on general assumptions:
 - Stagnant film layer with thickness 'h' surrounding surface particle.
 - Solid-liquid interface reaction is instantaneous, i.e. saturation is achieved almost immediately therefore it is not considered rate-limiting.
 - Dissolution rate is a function of the Brownian motion of diffusion of the molecules into the diffusion layer.
 - The boundary layer thickness was assumed to be between 25%-50% of the volume equivalent diameter (VED) of the single crystal - therefore, the extreme values of boundary layer thickness were taken into consideration.

- Hixson-Johnson (HJ)**
- Boundary layer thickness has been a point of debate for years.
 - 'h' defined as being equal to particle radius up to the point where the particle radius becomes 30μm. For particles with radii larger than 30μm, 'h' is considered to remain at a constant value.

DISSOLUTION OF UREA IN ETHANOL AND ACETONITRILE

A supersaturated solution at room temperature was heated, transferred to a cuvette, which was sealed and left to cool for a few hours in order to allow crystals to form. The cuvette was then sealed inside the measurement cell, and immersed in water. The temperature of the water was controlled through a heater/cooler unit. The measurement cell was placed on an inverted optical microscope, which was used to acquire images of single crystals at various time points.

- This may be due to acetonitrile being a polar aprotic solvent whereas ethanol is a polar protic solvent, therefore is able to form hydrogen bonds with urea.
- As a result of this, urea is less soluble in acetonitrile than ethanol almost by a factor of 10.
- Mercury Visual-Habit software was used to determine the shape factor, volume and surface area of the crystal through the use of Heron's formula², and hence the dissolution model predictions could be determined.



- Urea in Ethanol: (111) has a much faster dissolution rate with increasing undersaturation in comparison with (110) which was expected as (111) has much larger attachment energy³, therefore it would be expected to grow faster and also to dissolve faster.
- Urea in Acetonitrile: (110) and (111) have similar dissolution rates in acetonitrile, showing that the solvent has a great effect on the dissolution. This effect is also seen during the crystal growth process as the growth of the (110) and (111) faces are similar which can be determined from Figure 8.

- The dissolution models for the prediction of the mass loss of urea in ethanol are reasonable predictors at low levels of undersaturation, however with increasing undersaturation, the models become increasingly inaccurate.
- Therefore, dissolution models that were used are not a very good prediction of the mass loss associated with the dissolution of single crystals of urea in ethanol as some of the predicted values are lower by a factor of 10.
- This may be due to urea being highly soluble in ethanol, therefore the dissolution is a lot faster with increasing undersaturation.
- The dissolution models show that they are reasonable predictors that they are reasonable predictors of the mass loss of urea in acetonitrile at all levels of undersaturation - this may be due to urea being much more insoluble in acetonitrile.
- It can be hypothesised that the dissolution models chosen may be good predictors of the mass loss of a single crystal of API provided that the API is not highly soluble in the solvent, however further experimentation would need to be conducted in order to determine this.

CONCLUSIONS

The (110) face of urea had a much faster dissolution rate in ethanol than the (111) face, whereas in acetonitrile the dissolution rate of both faces was comparable. Therefore, the interaction of ethanol and acetonitrile with the functional groups at the surface of both faces would need to be determined.

Acknowledgments: The authors gratefully acknowledge Pfizer for the funding and technical support of this research, and the EPSRC for their support in research at Newcastle University (Grant Reference EP/R037820/1).



References

- [1] Y. Wang, B. Abnermarsson, L. Lindfors, J. G. Braessler. *Molecular Pharmaceutics* 2012, 9(5), 1052-1066.
- [2] J. Pickering, T. Kethyala, T. H. Nguyen, V. Ramachandran, M. Soufan, R. B. Hammond, K. J. Roberts, K. Parthasarathy, M. Tothhurst. *A Comparative Study of the Experimental and Theoretical Dissolution Kinetics of Ibuprofen in Ethanol*. (Submitted, *J. Pharm. Sci.*)
- [3] A. Noyes, W. R. Whitney. *J. Am. Chem. Soc.* 1897, 19(12), 930-934.
- [4] R. J. Hixson, K. C. Crowell. *Int. J. Pharm.* 1969, 5(1), 9-17.
- [5] A. Izumi, T. Izumi, K. J. Roberts. *The Influence of Solution Environment on the Nucleation Kinetics and Growth Mechanism of Urea*. Poster presented at 13th International Workshop on Crystal Growth of Organic Materials (CGOM13), Seoul, South Korea, 27-30 Aug 2019.
- [6] R. B. Hammond, K. Parthasarathy, K. J. Roberts. *Cry. Growth Des.* 2006, 6(5), 1324-1334.